

# Research Summaries Fiscal Years 2006-2007



Office of the Chief Scientist  
Science, Technology, and Management



U.S. Department of Energy  
Office of Civilian Radioactive Waste Management  
Washington, D.C.

## Contacts

This publication was produced by the U.S. Department of Energy  
Office of Civilian Radioactive Waste Management (OCRWM)

For further information, contact:

U.S. Department of Energy  
Office of Civilian Radioactive Waste Management  
1551 Hillshire Drive  
Las Vegas, Nevada 89134-6321  
or visit the OCRWM Home Page:  
<http://www.OCRWM.DOE.gov>

Cover photo by Roy Kaltschmidt, LBNL.



# Research Summaries Fiscal Years 2006-2007

This volume is dedicated to the memory of  
Gudmundur “Bo” Bodvarsson  
November 11, 1952 – November 29, 2006

*Einherjar*

(A term derived from the Old Norse, for  
“A great warrior who fought to bring order out of chaos”)

—John Wengle

# CONTENTS

■ **A Perspective from the Office of the Chief Scientist. . . . .** **1**  
Abraham Van Luik, Office of the Chief Scientist

**Thrust Areas:**

■ **Source Term Thrust . . . . .** **5**  
Rodney C. Ewing and Mark T. Peters, Source Term Thrust

**SNF Dissolution Mechanisms and Rates**

**Actinide Thermodynamics at Elevated Temperatures . . . . .** **11**  
Judah Friese, Linfeng Rao, Yuanxian Xia, Paula P. Bachelor, and Guoxin Tian

**Dissolution Mechanisms and Rates . . . . .** **13**  
Amanda Kline, Brady Hanson, and William Miller

**Implications of Deliquescence and Decay Heat on Source Term Degradation . . . . .** **15**  
James Jerden

**Formation and Properties of U<sup>6+</sup> Secondary Phases**

**Mitigation of the Release of <sup>129</sup>I from Spent Nuclear Fuel via Uptake by Uranyl Alteration Phases . . . . .** **19**  
Thomas E. Albrecht-Schmitt and Iain May

**Impact of Uranyl Alteration Phases of Spent Fuel on Mobility of Neptunium (Np) and Plutonium (Pu) in Yucca Mountain . . . . .** **21**  
Peter C. Burns

**Actinide Adsorption to U(VI) Silicates . . . . .** **23**  
S.B. Clark and Lawrence C. Hull

**Corrosion of Spent Nuclear Fuel: The Long-Term Assessment . . . . .** **25**  
Rodney C. Ewing

**Direct Determination of the Thermodynamic Properties of Uranyl Minerals Important for the Performance of the Proposed Geological Repository at Yucca Mountain . . . . .** **27**  
Jeremy B. Fein, Peter C. Burns, and Alexandra Navrotsky

**Chemical and Coordination Structure of Radionuclides in Spent Nuclear Fuel and Its Alteration Products: Understanding Release Pathways . . . . .** **29**  
Jeffrey A. Fortner, A. Jeremy Kropf, and James C. Cunnane



<b>An <i>In Situ</i> Spectroelectrochemical Study of Neptunium (Np) Redox, Dissolution, and Precipitation Behavior at the Corroding Spent Nuclear Fuel/Alteration Phase Interface . . . . .</b>	<b>31</b>
Artem Guelis, Jeremy Kropf, Christopher Johnson, Jeffrey Fortner, and Petr Vanysek	

<b>Natural Sequestration of Radionuclides In Volcanic Tuff . . . . .</b>	<b>33</b>
Jonathan Icenhower, Edgar Buck, Eric Pierce, Dawn Wellman, and Andreas Lüttge	

<b>Surface Charge and Radionuclide Adsorption Characteristics of U(IV,VI) Oxyhydroxides at 25–150°C . . . . .</b>	<b>35</b>
David J. Wesolowski, Laetitia Delmau, Lawrence M. Anovitz, Jorgen Rosenqvist, and Donald A. Palmer	

## **Waste Form–Waste Package Interactions in the Near Field**

<b>In-Package Sequestration of Radionuclides at Yucca Mountain: Waste Package Corrosion Studies Using Small Mockup Experiments . . .</b>	<b>41</b>
B. Elizabeth Anderson, Katheryn B. Helean, Patrick V. Brady, and Rodney C. Ewing	

<b>In-Package Sequestration of Radionuclides at Yucca Mountain: Neptunium Surface Complexation Subtask. . . . .</b>	<b>43</b>
James Jerden	

<b>Uptake of Technetium (Tc) by Iron-Based Materials . . . . .</b>	<b>45</b>
Kenneth M. Krupka, Christopher F. Brown, Steve M. Heald, H. Todd Schaef, Bruce Arey, and Michelle M. Valenta	

## **Integration of In-Package Chemical and Physical Processes**

<b>Computational Studies on the Corrosion of Spent Nuclear Fuel and the Adsorption and Incorporation of Radioactive Elements into Mineral Phases. . . . .</b>	<b>49</b>
Udo Becker	

<b>A Model for Radionuclide Release from Spent Nuclear Fuel. . . . .</b>	<b>51</b>
Carl I. Steefel, John Apps, Nicolas Spycher, and Eric Sonnenthal	

<b>■ Materials Performance Thrust . . . . .</b>	<b>55</b>
Joe H. Payer, Materials Performance Thrust	

## **Corrosion of Metal Surfaces Covered with Particulate and Deposits**

<b>Kinetics of the Cathodic Reduction of Oxygen on Passive Metals . . . . .</b>	<b>65</b>
David W. Shoesmith, Dmitrij Zagidulin, Xueyuan Zhang, and James J. Noël	

<b>Oxygen Electro-Reduction on Passive Metals . . . . .</b>	<b>67</b>
Dominic Gervasio and Stephen P. Rogers	

<b>Corrosion Cells Beneath Thin Films, Particulate, and Deposited Layers</b>	<b>69</b>
Joe H. Payer, Pallavi Pharkya, Xi Shan, Arun S. Agarwal, and Hongyi Yuan	

<b>Electrochemical Measurements of Corrosion under Thin Brine Layers. .</b>	<b>71</b>
Gerald S. Frankel, Rudolph G. Buchheit, Bastian Meier, and Shoichiro Taira	

<b>Mechanism of Mixed-Ion Effects on Corrosion in Thin Films. . . . .</b>	<b>73</b>
Roger C. Newman and Christopher Healey	

<b>Effect of Environmental Variables on the Structure and Composition of Passive Films . . . . .</b>	<b>75</b>
Tzipi Cohen-Hyams, Marcela Miyagusuku, Scott Harrington, and Thomas M. Devine	

---

## Evolution of Corrosion Damage by Localized Corrosion

<b>Crevice-Corrosion Electrochemistry of Ni-Cr-Mo Alloys . . . . .</b>	<b>79</b>
John R. Scully, Florent Bocher, and Francisco Presuel-Moreno	
<b>Modeling of Critical Chemistry for Crevice Corrosion . . . . .</b>	<b>81</b>
R.G. Kelly, Andrew J. Hodges, and F. Presuel-Moreno	
<b>Crevice-Corrosion Damage on Alloy-22 . . . . .</b>	<b>83</b>
David W. Shoesmith, Dmitrij Zagidulin, Pellumb Jakupi, and Jamie Noël	
<b>Localized Corrosion Stability in the Presence of Non-Chloride Anions . . . . .</b>	<b>85</b>
Roger C. Newman and David X. He	
<b>Metallurgical Effects on Localized Corrosion of Ni-Cr-Mo Alloys . . . . .</b>	<b>87</b>
Gerald S. Frankel, Rudolph G. Buchheit, Ajit Mishra, and Federico Gambina	
<b>Processes in Crevice-Corrosion Propagation, Stifling, and Arrest . . . . .</b>	<b>89</b>
Joe H. Payer, Xi Shan, Arun S. Agarwal, and Uziel Landau	
<b>Combinatorial Chemistry Approaches for Alloy Composition and Corrosion Behavior . . . . .</b>	<b>91</b>
Rudolph G. Buchheit, Gerald S. Frankel, and Fariaty Wang	
<b>Prediction of the Time Evolution of Localized Corrosion Damage . . . . .</b>	<b>93</b>
Digby D. Macdonald, Igor Nicic, and George R. Engelhardt (Consultant)	

## Evolution of Moisture Environment on Metal Surfaces

<b>Modeling Chemical Environments within Corroding Crevices for Ni-Cr-Mo-W-Fe Alloys . . . . .</b>	<b>97</b>
Peiming Wang, Ronald D. Springer, and Andre Anderko	
<b>Evolution of Solution Layer Chemistry in the Presence of Dust . . . . .</b>	<b>99</b>
R. G. Kelly and Zhuoyuan Chen	
<b>Modeling and Measurement of Current Distribution for Localized Corrosion in Thin Layers of Particulates and Electrolyte Films . . . . .</b>	<b>101</b>
Uziel Landau, Arun Agarwal, Xi Zhan, and Joe H. Payer	
<b>Microelectronic and MEMS Devices for Solution Properties and Corrosion Evaluations . . . . .</b>	<b>103</b>
Chung-Chiun Liu, Meijun Shao, and Laurie Dudik	
<b>Optical Probes and Sensors to Determine Concentration Distributions in Thin Films on Reactive Surfaces . . . . .</b>	<b>105</b>
William H. Smyrl and Francis Guillaume	
<b>High-Temperature Multi-Species Solution Properties and Behavior . . . . .</b>	<b>107</b>
David R. Cole, Lawrence N. Anovitz, Mirosław S. Gruszkiewicz, Donald A. Palmer, Jorgen Rosenqvist, David J. Wesolowski, Leslie L. Wilson, Andre Anderko, George Engelhardt, Peiming Wang, and Digby D. Macdonald	

## ■ Natural Barriers Thrust . . . . . |||

Yvonne Tsang, Natural Barriers Thrust

### Drift Seepage

<b>Thermal-Hydrological Near-Field Model Studies and Impact of Natural Convection on Seepage . . . . .</b>	<b>117</b>
George Danko and Jens T. Birkholzer	

<b>Integrated Assessment of Critical Chemical and Mechanical Processes Affecting Drift Performance: Laboratory and Modeling Studies . . . . .</b>	<b>119</b>
Derek Elsworth, Jonny Rutqvist, Ki-Bok Min, Abraham S. Grader, Chris J. Marone, and Eric Sonnenthal	

## **In-Drift Environment**

<b>Coupling Thermal-Hydrological-Chemical (THC) Models to Process Models for Waste Packages . . . . .</b>	<b>123</b>
Guoxiang Zhang, Nicolas Spycher, Eric Sonnenthal, and Carl Steefel	

## **Drift Shadow**

<b>Nature of Drift Shadows at Analogue Sites . . . . .</b>	<b>127</b>
Tim Kneafsey, Teamrat A. Ghezzehei, Grace Su, Paul Cook, and Brian Marshall	
<b>Testing the Concept of Drift Shadow. . . . .</b>	<b>129</b>
James Paces, Leonid Neymark, Teamrat Ghezzehei, and Patrick Dobson	
<b>Testing the Concept of Drift Shadow with X-Ray Absorption Imaging Experiments . . . . .</b>	<b>131</b>
Susan J. Altman, Clifford K. Ho, Aleeca Forsberg, and William Peplinski	

## **Unsaturated Zone Flow and Transport**

<b>Enhanced Retardation of Radionuclide Transport in Fractured Rock . .</b>	<b>135</b>
Hui-Hai Liu, Yinqi Zhang, Keni Zhang, and Fred J. Molz	
<b>Peña Blanca Natural Analogue . . . . .</b>	<b>137</b>
Schön S. Levy, Amr Abdel-Fattah, Paul Cook, John Dinsmoor, Patrick F. Dobson, Mostafa Fayek, Teamrat Ghezzehei, Steve Goldstein, Philip Goodell, Richard Ku, Shangde Luo, Michael T. Murrell, and Katrina Pekar	
<b>Matrix/Fracture Flow in Subrepository Units . . . . .</b>	<b>141</b>
Leonid Neymark, James Paces, David Vaniman, and Steve Chipera	
<b>Pore Connectivity, Episodic Flow, and Unsaturated Diffusion in Fractured Tuff . . . . .</b>	<b>143</b>
Qinhong Hu, Robert P. Ewing, and Liviu Tomutsa	

## **Saturated Zone Flow and Transport**

<b>Determining the Redox Properties of Yucca Mountain-Related Groundwater Using Trace-Element Speciation for Predicting the Mobility of Nuclear Waste . . . . .</b>	<b>147</b>
James Cizdziel, Vernon Hodge, and Karen H. Johannesson	
<b>Field Studies for the Determination of Transport Properties of Radioactive Solutes and Colloids Using Chemical Analogues. . . . .</b>	<b>149</b>
Barry Freifeld, Paul Reimus, M.J. Umari, and Kathy Gilmore	
<b>Improved Characterization of Radionuclide Retardation in Volcanics and Alluvium . . . . .</b>	<b>151</b>
Cynthia A. Dean, Mei Ding, Paul W. Reimus, Cheryl Sedlacek, Schon Levy, and Steve Chipera	
<b>Carbon-14 Groundwater Analysis . . . . .</b>	<b>153</b>
Gary L. Patterson and James Thomas	

<b>■ Advanced Technologies Thrust . . . . .</b>	<b>157</b>
Jeffrey Walker, Advanced Technologies Thrust	

---

<b>Applications in the Nuclear Industry for Corrosion-Resistant Amorphous-Metal Thermal-Spray Coatings . . . . .</b>	<b>161</b>
Joseph Collin Farmer and Jor-Shan Choi	
<b>Criticality-Control Applications in the Nuclear Industry for Thermal Spray Amorphous Metal and Ceramic Coating . . . . .</b>	<b>167</b>
Joseph Collin Farmer and Jor-Shan Choi	
<b>Evaluation of Structurally Amorphous Materials to Improve Tunnel Boring Machine Disc Cutters . . . . .</b>	<b>171</b>
Frank Wong and Craig Blue	
<b>Extreme Ground Motions . . . . .</b>	<b>173</b>
Lloyd Cluff	
<b>Reduced Pressure Electron Beam Closure Welding of Nuclear Waste Containers . . . . .</b>	<b>175</b>
T. James Dorsch and Christopher Punshon	

■ **Appendix A: OCRWM S&T Participating Organizations . . . . . 179**

---

This page intentionally left blank.







# A PERSPECTIVE FROM THE OFFICE OF THE CHIEF SCIENTIST

Abraham Van Luik  
Office of the Chief Scientist  
Policy and Technical Reviewer of Science and Technology  
Contact: [abe\\_vanluik@ymp.gov](mailto:abe_vanluik@ymp.gov)

In 2006, John Wengle, as Director of the Office of Science, Technology and International (OST&I) within the Office of Civilian Radioactive Waste Management, wrote about rapid change in the 2005 Annual Report for his OST&I program.

Just since that time, there has been a reorganization and a reduction in funding for the overall Yucca Mountain repository program, and therefore also for this work. As a consequence, the OST&I Office was made into a smaller Science and Technology (S&T) program to be managed within the Office of the Chief Scientist, and OST&I Director Wengle moved to another part of the Department of Energy. Director Wengle will be missed within OCRWM.

Also since that time, tragedy befell the leader of the Natural Barriers Thrust under this S&T program, Bo Bodvarsson, of Lawrence Berkeley National Laboratory. Bo passed away suddenly and unexpectedly in November 2006. He is greatly missed by his co-workers at the laboratory, within OCRWM, and by all who knew him. He was a scientific leader and visionary in his working life, and also had an extensive and exemplary nonprofessional life. The Natural Barriers Thrust was designed by Dr. Bodvarsson, with the capable help of his co-workers at LBNL and his collaborators in many other institutions.

Fiscal Year 2006 was a year of significant accomplishments in the S&T program. Fiscal Year 2007 continues to show progress and accomplishments, but now, due to a lack of funding, there will be a hiatus. The important thing to note is that the mission of the S&T program is one that will need to be returned to in the future. The foundation laid by Director Wengle for the overall program will be the basis for future work beyond 2008, when future funding will undoubtedly allow select portions of this work to be resumed. That selection will build on what was most promising in this report and in any additional accomplishments of Fiscal Year 2007.

The perspective of the Office of the Chief Scientist is that when funding is made adequate to move the repository program forward, the S&T program will be restarted, with funding allocated to what was most promising in the work completed by the end of Fiscal Years 2006 and 2007.

The mission of the S&T program is to promote the advancement of science and technology, with direct application to understanding the repository system and reducing its cost and operating duration without sacrificing safety. We are aware of the fact that the License Application currently in preparation is the highest priority in the Yucca Mountain effort. But we are also aware that this is a multigenerational project, and that building, operating, and closing this facility will span a century. To think that science and technology will stand still during this time is unrealistic. To not be continually seeking improvements in understanding and efficiency, while remaining focused on assuring safety, is not in keeping with the "continuous improvement" mindset that comes with a "nuclear culture" and its safety-conscious work ethic. Seeking to provide, as S&T did, direction to assure that science and technology improvements will be useful in increasing understanding and efficiency, while not adversely affecting safety, is living up to our societal mandate.

The Science Program within S&T, consisting of three major thrust areas (Source Term, Materials Performance, and Natural Barriers), is an effort, in the main, at seeking to advance understanding of the processes that control the release and transport of radionuclides at Yucca Mountain. This program aims to reduce the conservatisms in current approaches to modeling the behavior of the engineered and natural barriers within the repository system. Some conservatism is unavoidable because uncertainty is unavoidable, but with increased understanding, both can be reduced, which can have consequences in terms of increasing efficiency without adversely affecting safety.



Taken together, the work carried out under the three primary S&T science thrusts holds the key to dramatic improvement in our understanding of the potential effects of proposed changes in process modeling, designs, and materials. Figure 1 illustrates the integration of the three primary thrusts. A fourth Thrust, the Advanced Technologies Thrust, involving immediate development of focused advanced technology concepts, was also part of the original OST&I program, and selected portions of its scope of work have been moved into the main repository program's continuing technology development work, illustrating the immediate benefit from just a few years of S&T work. It is natural that the work in the other Thrust areas would take more time to

mature, but several efforts already show promise.

When significant progress has been made in S&T work and promise is demonstrated, the ideas will be handed off to the Chief Scientist's or Chief Engineer's programs for incorporation into the main effort under these offices.

Each of the aforementioned thrusts and their FY 2006 accomplishments are described and illustrated in this report. A brief introduction at the beginning of each Thrust section discusses the overall organization and goals of the Thrust, to be followed by individual papers describing the accomplishments achieved by participants within that Thrust.

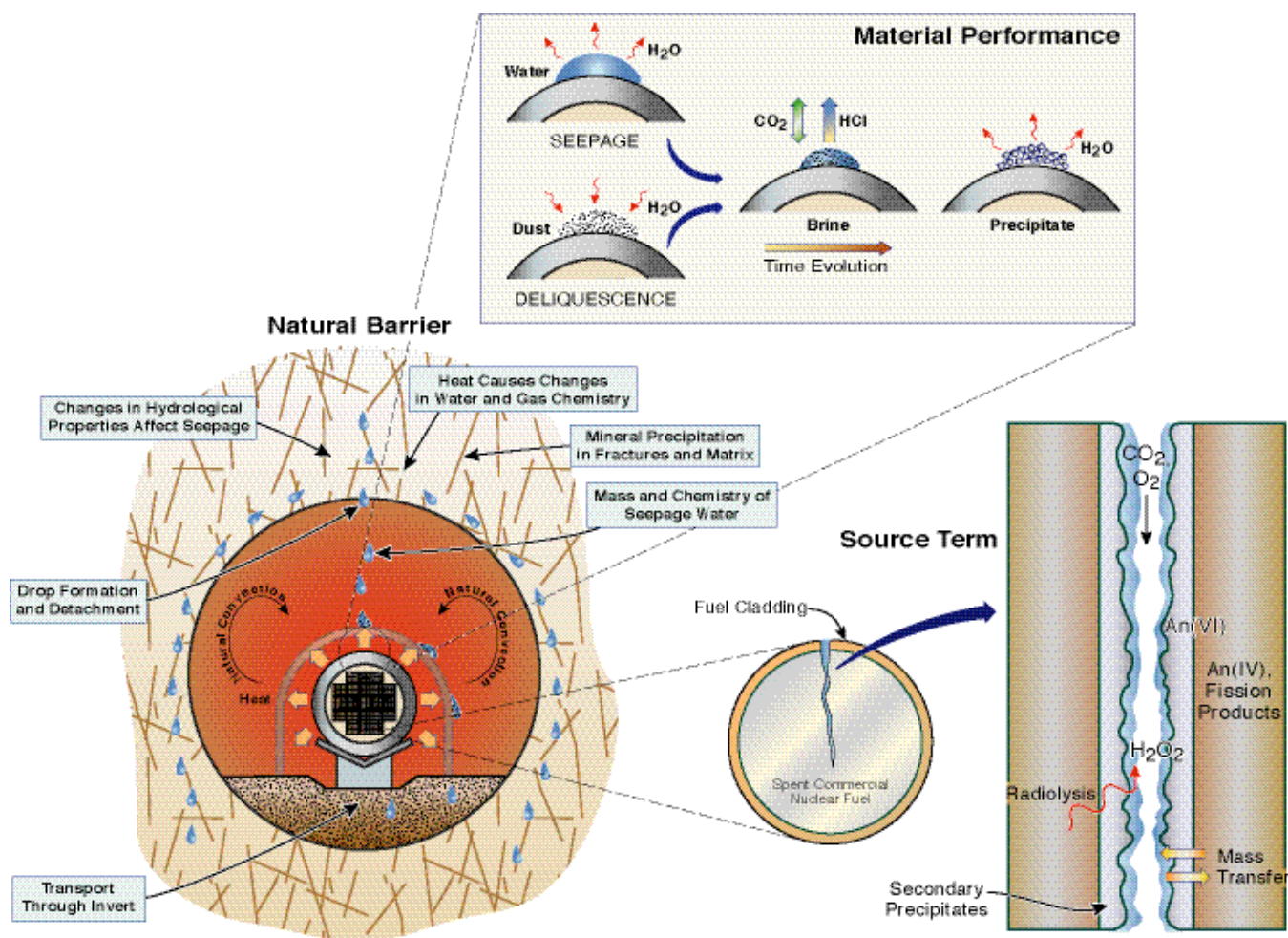


Figure 1. Integration of in-drift environment with contributions from Natural Barriers, Materials Performance, and Source Term Thrust Areas

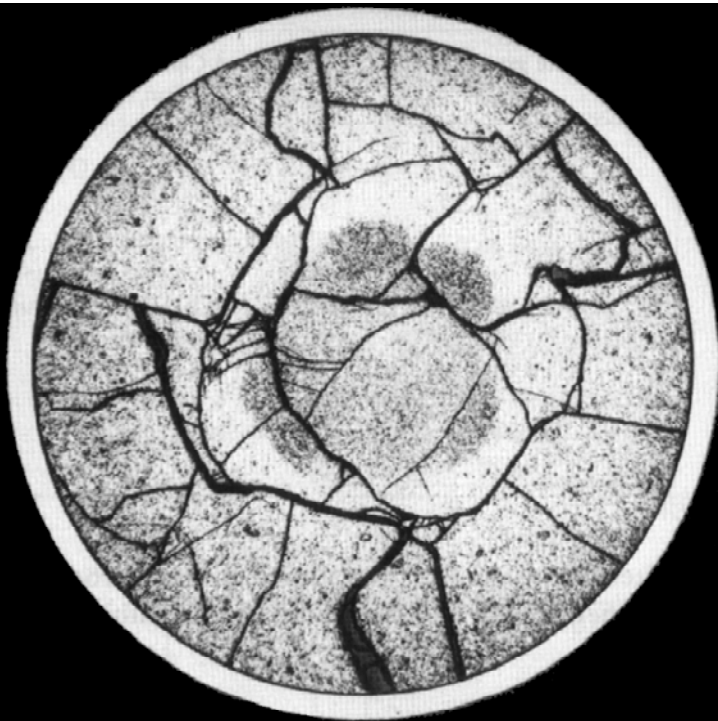
---

## Acknowledgments

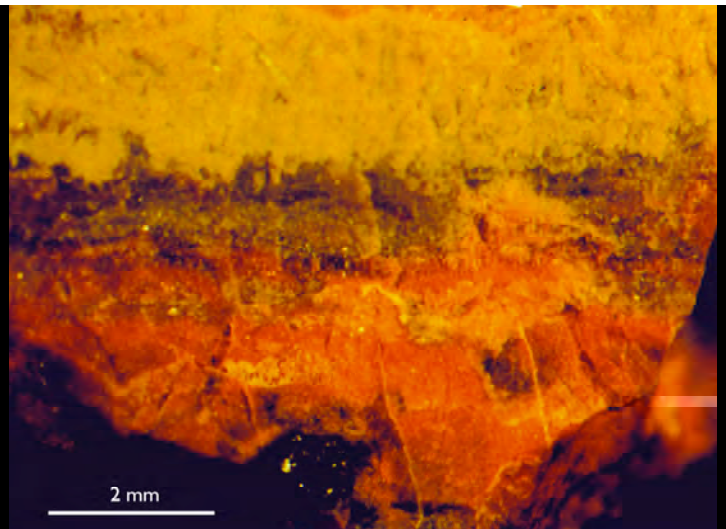
We gratefully acknowledge the contributions made by our program participants throughout Fiscal Years 2006 and 2007. Our principal investigators are drawn from Department of Energy national laboratories, the United States Geological Survey, the Defense Advanced Research Projects Agency, and other Federal agencies, local government agencies, academia, and industry. The talents and efforts of these individuals have set a firm foundation in bringing world-class science and technology to bear on the national priority of safe and efficient nuclear waste disposal—a foundation that will contribute to expanding the use of nuclear energy to meet our national needs.

Also deserving a special note of thanks are our thrust area

leaders: Rod Ewing, Mark Peters, Joe Payer, Yvonne Tsang, and Jef Walker. Each of these individuals is responsible, through their clarity of vision and depth and rigor of intellectual pursuit, for the robustness and vigor of their respective thrust areas. Certainly, I would be remiss if I failed to single out our collaborators at OCRWM as well: Russ Dyer, Bill Boyle, Debbie Barr, Claudia Newbury, Paige Russell, Scott Wade, Paul Harrington, Allen Benson, and Jane Summerson. All have been remarkably supportive, and intellectually challenging, in helping us to refine our S&T Program. The production of this report would not have been possible without the skillful, untiring, and always enthusiastic support of the following individuals: Diana Swantek, Dan Hawkes, Vivi Fissekidou, Cindy Lepouttre, Jim Jerden, and Robin Lynn Sampson.



Cross section of spent nuclear fuel with Zircaloy cladding.  
Diameter = 10 mm.



Photomicrograph of a corrosion rind on uraninite ( $\text{UO}_{2+x}$ ) formed under oxidizing conditions. The yellow material consists of U(VI) minerals formed by the alteration of the uraninite. The small black grain in the lower left edge of the sample is unaltered uraninite. (Finch and Ewing, 1992, Journal of Nuclear Materials).



# SOURCE TERM THRUST

Rodney C. Ewing<sup>1</sup> and Mark T. Peters<sup>2</sup>

Source Term Thrust

<sup>1</sup>University of Michigan | <sup>2</sup>Argonne National Laboratory (ANL)

Contact: Rod Ewing: [rodewing@umich.edu](mailto:rodewing@umich.edu)

Mark Peters: [mtpeters@anl.gov](mailto:mtpeters@anl.gov)

*The goal of the Source Term Thrust is to enhance the understanding of the performance of nuclear waste forms (mainly spent nuclear fuel [SNF] and nuclear waste glass) and to quantify the release of radionuclides in the evolving near-field environment expected at the proposed nuclear waste repository at Yucca Mountain, Nevada. The behavior of the source term, mainly SNF and vitrified waste, limits radionuclide releases, both initially and over the long term. Interactions of the source term with the near-field environment, such as corroded waste packages, place additional constraints on the long-term behavior, including retention and mobility of important radionuclides.*

This program is directed at developing a basic understanding of the fundamental mechanisms of radionuclide release and a quantification of the release as repository conditions evolve over time, particularly at longer times (>100,000 years). Radionuclide release will be critically sensitive to variations in temperature, radiation field, redox conditions, pH, pCO<sub>2</sub>, surface area-to-solution volume, and presence of near-field materials. Among the important processes that can control radionuclide release are: (1) kinetics of waste form corrosion, (2) formation of secondary, alteration phases, and (3) reduction and sorption onto the surfaces of near-field materials.

Predictions of the long-term behavior of nuclear waste forms cannot be based entirely on models of laboratory results that are then extrapolated to long periods. Hence, this program will integrate multiple lines of evidence (e.g., results from natural analogue studies) to clarify the scientific basis for waste-form-degradation mechanisms in relation to source term models. The program will evaluate the uncertainties introduced by parametric uncertainty, variations in environmental conditions, and the use of different conceptual models.

The present source term and near-field models in the Yucca Mountain performance assessment are conservative, but the uncertainties are large. To the extent that the mechanisms of release for specific radionuclides can be understood or the uncertainties decreased, the subsequent analysis of the far-field barriers becomes less important. In the

present performance assessment, important processes that will certainly occur are not explicitly included, such as the formation of secondary, U<sup>6+</sup> alteration phases. Very little credit is taken for the potential chemical interactions between released radionuclides and the alteration products of the SNF and metal waste packages, or their internal components. The conservatism of the present models may be reduced by an improved understanding of the fundamental geochemical/hydrologic processes that will control the corrosion of SNF under oxidizing conditions and the potential interactions that may occur among the corroded nuclear fuel, the high-level-waste (HLW)-borosilicate glass, and the waste package components. This focused and integrated research program will provide the scientific basis for the development of the next generation of more realistic models for source term and near-field processes. Although there has been considerable research on the corrosion of SNF and nuclear waste glasses, there has been much less work on developing models that are applicable to an oxidizing environment, such as that at the proposed Yucca Mountain repository.

There are two compelling reasons for the importance of understanding the source term and near-field behavior. First, essentially all radioactivity is initially in the waste form, mainly SNF or nuclear waste glass. An enhanced understanding and realistic estimates of the extent to which radionuclides will be retained in the waste form or near-field environment reduce demands on the performance of subsequent, far-field barriers. Realistic estimates of radionuclide release can also reduce uncertainties in the Total System Performance Assessment. Second, over long periods, as engineered barriers degrade, it is the waste forms that eventually provide the release of radioactivity to the environment. Thus, it is essential to predict with confidence the physical and chemical evolution of the waste form over hundreds of thousands of years.

Finally, the need to understand the corrosion and alteration of SNF and nuclear waste glasses is a research subject unique to the needs of the Office of Civilian Radioactive Waste Management (OCRWM) Science and Technology program. Other agencies and DOE offices, such as the National Science Foundation (NSF) or Office of Basic Energy Sciences (OBES), generally do not fund research on the properties or corrosion of SNF or nuclear waste glasses. Hence, OCRWM, by supporting this program, is creating a community of scientists and engineers who are actively working on and knowledgeable in this field. An important component of this program is the connection to international efforts, particularly to the European Community (EC) programs. We are in the process of connecting our research program to NF-Pro, a four-year integrated project (2004–2007) supported by the EC, as part of their Sixth Framework Program. NF-Pro brings together 40 nuclear research and waste management organizations

with the aim of integrating European research on the near field. We have also initiated contact with the EU MICADO (Model uncertainty for the mechanism of dissolution of spent fuel in a nuclear waste repository) program. Through these collaborations, we will leverage present U.S. funding for increased understanding and enhance the international knowledge and reputation of the U.S. program.

The present program, summarized in the following pages, consists of 15 separate programs that involve five national laboratories and five universities (one in Great Britain). In many instances, university investigators have programs closely tied to national laboratories in order to utilize unique facilities for handling highly radioactive materials. Three of the graduate students in this program are supported by OCRWM Fellowships and have completed practica at national laboratories this past summer.

The research programs address four critical areas:

#### SNF Dissolution Mechanisms and Rates

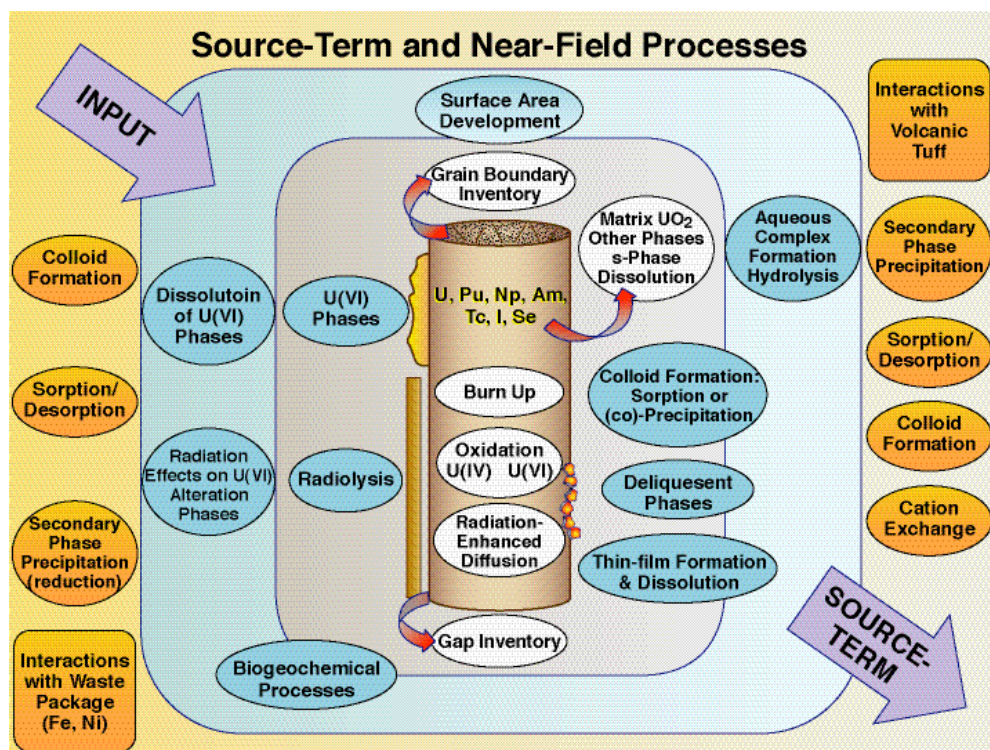
The initial release of radionuclides is governed by the specific mechanisms and rates of dissolution, which in turn, vary as a function of pH, dissolved oxygen concentration, temperature, solution composition, fuel chemistry (i.e., burn-up), and mode of contact with water. Systematic

studies are being conducted of radionuclide release from SNF as a function of these parameters, with special attention being paid to the effects of radiolysis on matrix dissolution rates and the formation of secondary phases. The program also investigates the effects of water that may condense and accumulate on failed SNF pins. By the process of deliquescence of hygroscopic fission product phases, alteration products may form on the surfaces of the SNF.

Descriptions of this individual program area are provided in the two-page summaries on pp. 9–16.

#### Formation and Properties of $U^{6+}$ Secondary Phases

Under an oxidizing environment, the corrosion of SNF leads to the formation of a complicated array of  $U^{6+}$  secondary phases that may retard release of radionuclides either by co-precipitation/incorporation, sorption, or by forming a physical barrier to the continued contact with water or release of radionuclides. We have established a multi-pronged approach that includes carefully controlled experiments to determine the means and extent of radionuclide incorporation (e.g.,  $^{237}\text{Np}$ ,  $^{239}\text{Pu}$ , and  $^{129}\text{I}$ ) and sorption into and onto the structures of  $U^{6+}$  secondary phases. The experimental work is supported by the application of advanced techniques (x-ray absorption spectroscopy at the Advanced Photon Source at Argonne



Schematic illustration of the potentially important processes in the Source Term Thrust research program.

National Laboratory, laser-ablation inductively coupled plasma mass spectroscopy, and *in situ* spectroelectrochemical techniques) in order to determine the extent of incorporation and sorption of radionuclides in/on U<sup>6+</sup>- secondary phases. The stability of these phases is being determined by high-temperature oxide-melt solution calorimetry and reversible solubility measurements, as well as systematic irradiation experiments. Computational simulations involving quantum mechanical calculations are being used to investigate the energetics of the incorporation and sorption processes. In addition, actinide complex stability constants at elevated temperatures are being measured using potentiometry, solvent extraction, spectrophotometric, and nuclear magnetic resonance measurements. The experimental and modeling studies are supported and confirmed by studies of natural occurrences of SNF, namely at the Oklo natural reactors.

Descriptions of this individual program area are provided in the two-page summaries on pp. 17–37.

#### **Waste Form–Waste Package Interactions in the Near Field**

The SNF will corrode and release radionuclides in an environment dominated by the presence of uranium, iron, and solutions whose compositions are the result of interactions with the waste forms, waste packages, and the surrounding volcanic tuff. These interactions buffer the environment in which the SNF corrodes and also offer additional opportunities for reduced mobility of radionuclides. We have research programs to investigate the types and behaviors of waste package corrosion products, and their potential for reduction and sorption of key

radionuclides (e.g., uptake of <sup>99</sup>Tc onto iron oxyhydroxides). We also will investigate the interactions of UO<sub>2</sub> with solutions in contact with volcanic tuff using the pressurized unsaturated flow (PUF) system and *in situ* analytical techniques to investigate and characterize the secondary phases that form. Again, computational simulations of atomic-scale interactions will be used to interpret and support the experimental results.

Descriptions of this individual program area are provided in the two-page summaries on pp. 39–46.

#### **Integration of In-Package Chemical and Physical Processes**

The greatest challenge for this program is to integrate the scientific results into a larger scale model of the source term and near-field interactions. To accomplish this, we have immediately begun creating numerical models that capture the important physical and chemical processes that lead to radionuclide release from SNF. The source term model will be coupled to a drift/near-field-scale model that captures the relevant thermal-hydrologic-chemical regimes as a function of time. This integrated model will be used to establish the scientific links among our science programs and provide a basis for understanding the behavior of SNF at different time frames: (1) prior to breach of the waste package; (2) at the time of early breaches of the waste package at elevated temperature; and (3) after breach at long periods, greater than 100,000 years, but at essentially ambient conditions.

Descriptions of this individual program area are provided in the two-page summaries on pp. 47–52.

---

This page intentionally left blank.

# SNF DISSOLUTION MECHANISMS AND RATES

## **Actinide Thermodynamics at Elevated Temperatures**

Judah Friesse, Yuanxian Xia, and Paula P. Bachelor, Pacific Northwest National Laboratory (PNNL)

Linfeng Rao and Guoxin Tian, Lawrence Berkeley National Laboratory (LBNL)

## **Dissolution Mechanisms and Rates**

Amanda Kline and William Miller, University of Missouri-Columbia

Brady Hanson, Pacific Northwest National Laboratory (PNNL);

## **Implications of Deliquescence and Decay Heat on Source Term Degradation**

James Jerden, Argonne National Laboratory (ANL)



---

This page intentionally left blank.

# Actinide Thermodynamics at Elevated Temperatures

Judah Friese<sup>1</sup>, Linfeng Rao<sup>2</sup>, Yuanxian Xia<sup>1</sup>, Paula P. Bachelor<sup>1</sup>, and Guoxin Tian<sup>2</sup>

<sup>1</sup>Pacific Northwest National Laboratory (PNNL) | <sup>2</sup>Lawrence Berkeley National Laboratory (LBNL)

## Research Objectives

The postclosure chemical environment in the proposed Yucca Mountain repository is expected to experience elevated temperatures. Predicting potential migration of actinides would be more robust if sufficient reliable thermodynamic data on hydrolysis and complexation are available for these temperatures. Data are scarce and scattered for 25°C, and nonexistent for elevated temperatures. Current modeling of actinide migration makes conservative assumptions to compensate for this lack of data, particularly at elevated temperatures.

This collaborative project between LBNL and PNNL collects thermodynamic data at elevated temperatures on actinide complexes with inorganic ligands that may be present in Yucca Mountain. The ligands include hydroxide, fluoride, sulfate, phosphate, and carbonate. Thermodynamic parameters of complexation, including stability constants, enthalpy, entropy, and heat capacity of complexation, are measured with a variety of techniques, including solvent extraction, potentiometry, spectrophotometry, and calorimetry.

## Approach

Acid-base potentiometry measures electromotive force (*emf*) as a function of the concentration of hydrogen ion that in turn depends on reactions in solution, including ligand protonation and metal complexation. Thus, the measured *emf* can be used to calculate the stability constants of actinide complexes. Solvent extraction uses the change of distribution coefficients with the ligand concentration to determine metal complexation stability constants. With spectrophotometric methods, the oxidation states and nature of actinide species are identified by characteristic absorption bands (e.g., Np(V) at 980 nm and Pu(VI) at 830 nm). From the change of absorbance as a function of concentrations of reagents, the stability constants of actinide complexes are determined. Nuclear magnetic resonance (NMR) spectroscopy measures chemical shifts in species of nuclei present according to fractional populations. Since the magnitude of chemical shifts depends on the values of the equilibrium constant, the chemical shift becomes a function determined analogous to the potentiometric case.

Titration calorimetry directly measures reaction heat released (or absorbed) when a solution is titrated with a titrant. Since the reaction heat in a complexation titration is a function of the concentrations of reagents, the stability constant(s) of complex(es), and the enthalpy of complexation, the latter can be calculated from calorimetric titrations.

## Accomplishments

### Complexation of Pu(IV) and Pu(VI) at Elevated Temperatures

Thermodynamic studies of actinide complexation at elevated temperatures were extended from uranium and neptunium to plutonium, another important transuranic element of great concern in environmental transport. Complexation of Pu(IV) with F<sup>-</sup> was studied at 25–55°C by solvent extraction (Figure 1). The equilibrium constants of the reactions,  $\text{Pu}^{4+} + i\text{HF} = \text{PuF}_i^{(4-i)+} + i\text{H}^+$  where  $i = 1$  and 2, were found to decrease with increasing temperature.

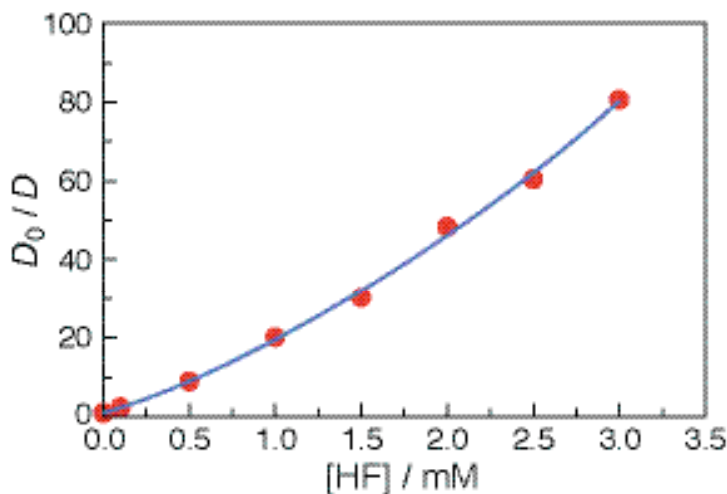


Figure 1. Solvent extraction of Pu(IV) in the presence of HF: Plot of  $D_0/D$  vs.  $[\text{HF}]$ , solid symbol—experimental, curve—calculated. Aqueous phase—Pu(IV) in 2.0 M  $\text{HClO}_4 + \text{HF}$ ; organic phase—0.05 M TTA in toluene;  $t = 55^\circ\text{C}$ .

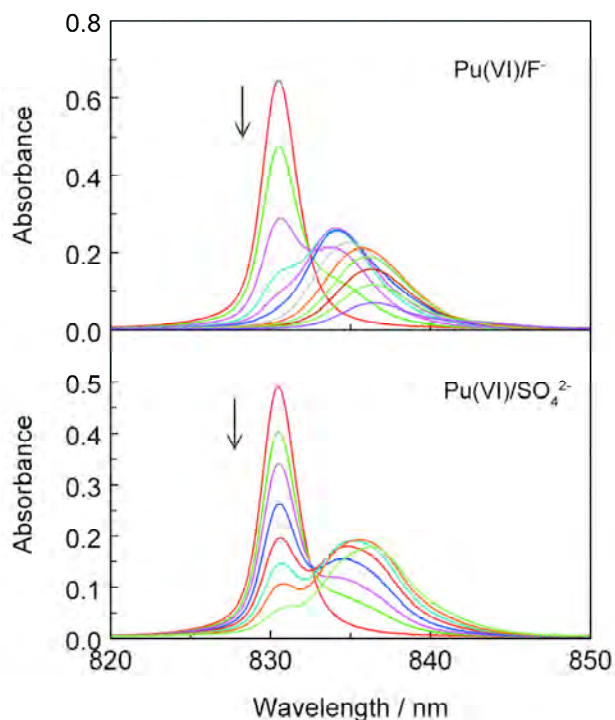


Figure 2. Spectrophotometric titration of Pu(VI) complexation with fluoride and sulfate ( $I = 1.0$  M NaClO<sub>4</sub>,  $t = 25^\circ\text{C}$ , optical path = 1.00 cm). Top—Pu(VI)/fluoride:  $V^0 = 2.50$  mL,  $C_{\text{Pu}}^0 = 1.18 \times 10^{-3}$  M,  $C_{\text{H}^+}^0 = 1.51 \times 10^{-3}$  M; titrant: 1.00 M NaF, 3.29 mL added. Bottom—Pu(VI)/sulfate:  $V^0 = 2.50$  mL,  $C_{\text{Pu}}^0 = 8.93 \times 10^{-4}$  M,  $C_{\text{H}^+}^0 = 1.14 \times 10^{-3}$  M; titrant: 0.50 M Na<sub>2</sub>SO<sub>4</sub>, 1.50 mL added.

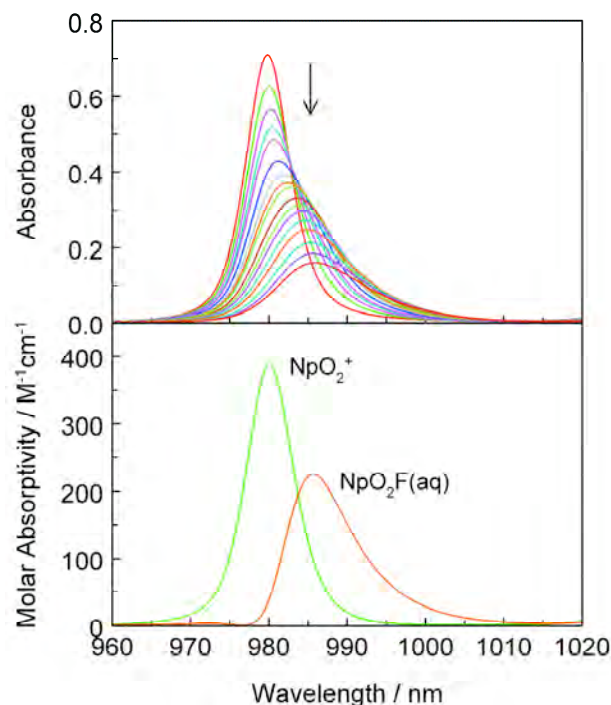


Figure 3. Spectrophotometric titration of Np(V) fluoride complexation ( $I = 1.0$  M NaClO<sub>4</sub>,  $t = 25^\circ\text{C}$ , optical path = 1.00 cm). Top—17 spectra,  $V^0 = 2.50$  mL,  $C_{\text{Np}}^0 = 1.82 \times 10^{-3}$  M,  $C_{\text{H}^+}^0 = 1.0 \times 10^{-6}$  M; titrant: 1.00 M NaF, a total of 2.40 mL added in 16 additions. Bottom—calculated molar absorptivities of Np(V) species.

Complexation of Pu(VI) with F<sup>-</sup> and SO<sub>4</sub><sup>2-</sup> was studied at 25°C by spectrophotometry using the characteristic absorption band of Pu(VI) at 830 nm (Figure 2). Calculations of stability constants are in progress.

#### Spectrophotometric Measurements on Np(V) and U(VI) at Elevated Temperatures

Spectrophotometric titrations were performed to measure the stability constants of U(VI)/F<sup>-</sup>, U(VI)/SO<sub>4</sub><sup>2-</sup>, Np(V)/F<sup>-</sup> and Np(V)/SO<sub>4</sub><sup>2-</sup> complexes at 25–70°C (Figure 3). It was found that all these complexes become stronger at higher temperatures.

#### Microcalorimetric Measurements on Np(V) and Pu(VI)

Calorimetric titrations of Np(V)/F<sup>-</sup> and Np(V)/SO<sub>4</sub><sup>2-</sup> complexes were completed, and data processing with new stability constants obtained by spectrophotometry is in progress. A representative calorimetric titration is shown in Figure 4. Calorimetric titrations of Pu(VI) systems have been started.

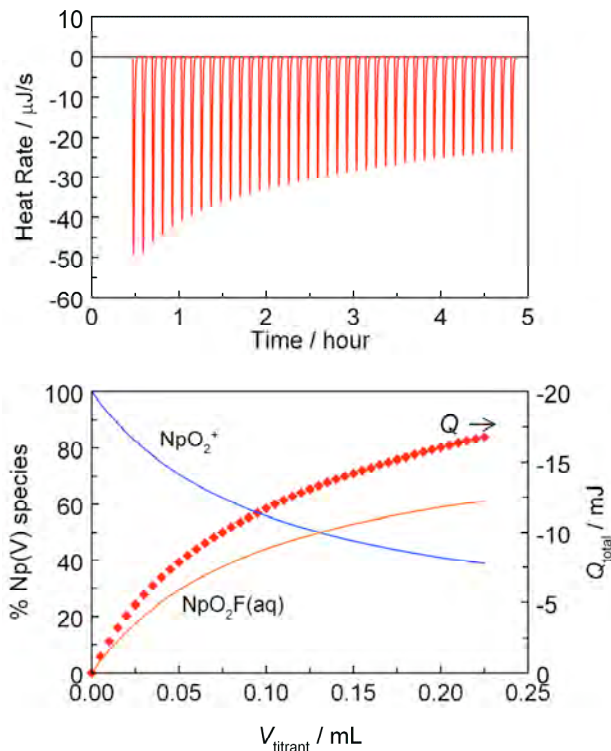


Figure 4. Calorimetric titration of Np(V) fluoride complexation ( $I = 1.0$  M NaClO<sub>4</sub>,  $t = 25^\circ\text{C}$ ).  $V^0 = 0.900$  mL,  $C_{\text{Np}}^0 = 1.78 \times 10^{-3}$  M,  $C_{\text{H}^+}^0 = 3.0 \times 10^{-7}$  M; titrant: 1.0 M NaF, 5 microL/addition.

# Dissolution Mechanisms and Rates

Amanda Kline<sup>1</sup>, Brady Hanson<sup>2</sup>, and William Miller<sup>1</sup>

<sup>1</sup>University of Missouri-Columbia | <sup>2</sup>Pacific Northwest National Laboratory (PNNL)

## Research Objectives

This research focuses on the examination of the variables associated with spent nuclear fuel (SNF) dissolution. The project consists of both theoretical and experimental techniques in order to achieve a better understanding of parameters affecting dissolution, such as temperature, dissolved O<sub>2</sub> concentrations, flow rates, fuel chemistry, and radiolysis of the solution in contact with the fuel.

## Approach

The rate of dissolution of SNF is dependent upon many factors, and the extent to which each variable affects the dissolution rate varies greatly. Recently, the effect of radiolysis on fuel dissolution has become the focus of international attention. However, most of this attention is on how radiolysis alters otherwise reducing environments. Since radiolysis produces radicals and molecules (e.g., H<sub>2</sub>O<sub>2</sub>) that are more oxidizing than dissolved oxygen, the effects of radiolysis even under oxidizing conditions may be significant. Modeling is used to calculate the radiation dose to water from SNF, allowing a more accurate depiction of the water chemistry in contact with the fuel. Experimental work utilizing single-pass flowthrough (SPFT) tests were used to determine the dependence of the dissolution rate on each parameter and to validate the models.

The primary objective of our research is to determine the effect  $\beta$ - and  $\gamma$ -radiolysis has on SNF dissolution rates, especially when determining their contribution to the dissolution rate on fresh (i.e., <30 years old) SNF, as has been performed in support of geologic disposal. The effect of each type of radiation on water radiolysis and subsequent fuel dissolution will be examined by preparing sintered UO<sub>2</sub> pellets doped with single radionuclides and testing the specimens using SPFT. Non-uranium dopants, such as fission products and actinides, that alter the fuel chemistry and dissolution rates must also be examined, so that fuel chemistry and radiolysis effects can be determined separately. The chemistry effect can be determined using the same fuel preparation and SPFT techniques, but utilizing nonradioactive isotopes.

## Accomplishments

Two models have been developed and presented to deter-

mine the effects of radiolysis on SNF dissolution. First, a systematic dosimetry model to determine the dose to water from SNF was developed (Miller et al., 2006). MCNP5 and a random-walk Monte Carlo model implemented in Mathematica were used to calculate the dose as a function of parameters such as radiation type and energy, distance from the fuel, fuel particle size (e.g., surface-to-volume ratio) and fuel-to-water ratios. The second model (Kline et al., 2006) uses the dose obtained by the first model for SNF of specific burnup and decay time. A Fortran code and the simultaneous differential equation solver ODEPACK were used in the second model to calculate the concentrations of species that make up the water chemistry, by first determining the initial radiolytic yields, as determined by the G-values, and then solving 129 simultaneous reactions for the 32 species included. Figure 1 shows the large effect of radiation dose on the concentration of the main oxidizers by comparing the model results from 23-year-old SNF to those surrounding unirradiated UO<sub>2</sub> in an oxidizing environment without any bicarbonate in solution. H<sub>2</sub>O<sub>2</sub> shows approximately a 4-order-of-magnitude increase, and O<sub>2</sub><sup>-</sup> and OH each show approximately a 2-order-of-magnitude increase for SNF.

Dissolution rates are being measured using SPFT, where the flow rate is sufficiently high to minimize back reactions and to maintain the uranium concentration well below solubility limits, in order to prevent alteration phase formation. The

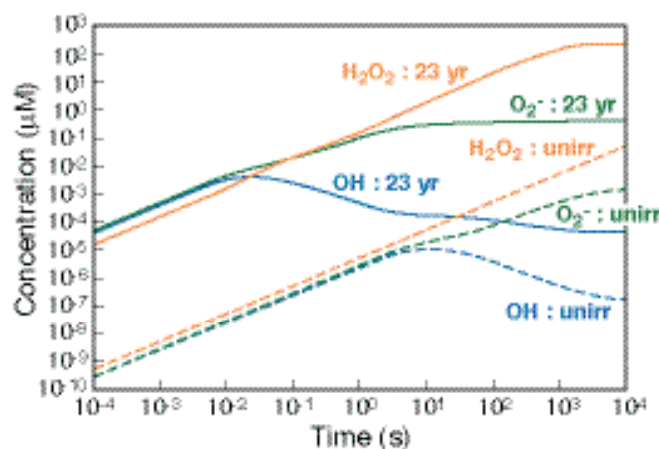


Figure 1. Comparison of the predicted concentration of main oxidizers contacting unirradiated UO<sub>2</sub> and 23-year-old SNF.

system has been designed to maintain a well-mixed solution equilibrated at operating temperature, with a sparge gas containing 20.9% O<sub>2</sub> and enough CO<sub>2</sub> to maintain a total carbonate concentration of  $2 \times 10^{-3}$  M and constant pH. The pre-equilibration at temperature is an important design feature by which to precisely control dissolved oxygen concentrations and minimize effects of exsolved oxygen. At 25°C, 50°C, and 75°C, the dissolved oxygen concentrations are 8.7 ppm, 5.9 ppm, and 4.2 ppm, respectively. Dissolved oxygen concentrations and pH are measured continuously with on-line sensors. The fuels used for the initial tests are from reactor-grade pellets procured from a commercial vendor. SPFT tests on two fuels, one being natural enriched UO<sub>2</sub> and the second being 4.6% enriched UO<sub>2</sub> containing 8 wt% Gd, are ongoing (Kline et al., 2007). Figure 2 shows the results from the tests on these two fuels, each conducted at three different flow rates.

Based on the model results, one would expect the dissolution rate of fresh SNF to be significantly higher than for unirradiated UO<sub>2</sub>, due to the increased concentration of radiolytically-produced highly oxidizing species. Over the first 500 years after irradiation, the contribution of  $\beta$  and  $\gamma$  radiation decreases by approximately four orders of magnitude (Miller et al., 2006). The long-term radiolysis contribution will be from  $\alpha$  decay of long-lived actinides. This suggests that the dissolution rates reported on fresh SNF are significantly higher than they will be for aged fuel under repository conditions. Similarly, the results on doped fuels suggest that in the absence of the radiolytic field, SNF will have smaller dissolution rates than unirradiated UO<sub>2</sub> as a result of the changes in fuel chemistry. Both the reduction in radiolysis effect over time and the chemical stabilization effect are expected to show that current dissolution rates for both fresh SNF and unirradiated UO<sub>2</sub> are higher than the long-term dissolution rates will be for SNF under geologic conditions. Initial results such as in Figure 2 suggest that the dependence on dissolved oxygen may be underestimated and the temperature dependence overestimated in current models, owing to exsolved oxygen issues.

The work of Amanda Kline was performed under appointment of the Office of Civilian Radioactive Waste Management Fellowship Program administered by Oak Ridge Institute for Science and Education under a contract between the U.S. Department of Energy and the Oak Ridge Associated Universities.

## Related Publications

Miller, W., A. Kline, and B. Hanson, Dosimetry modeling

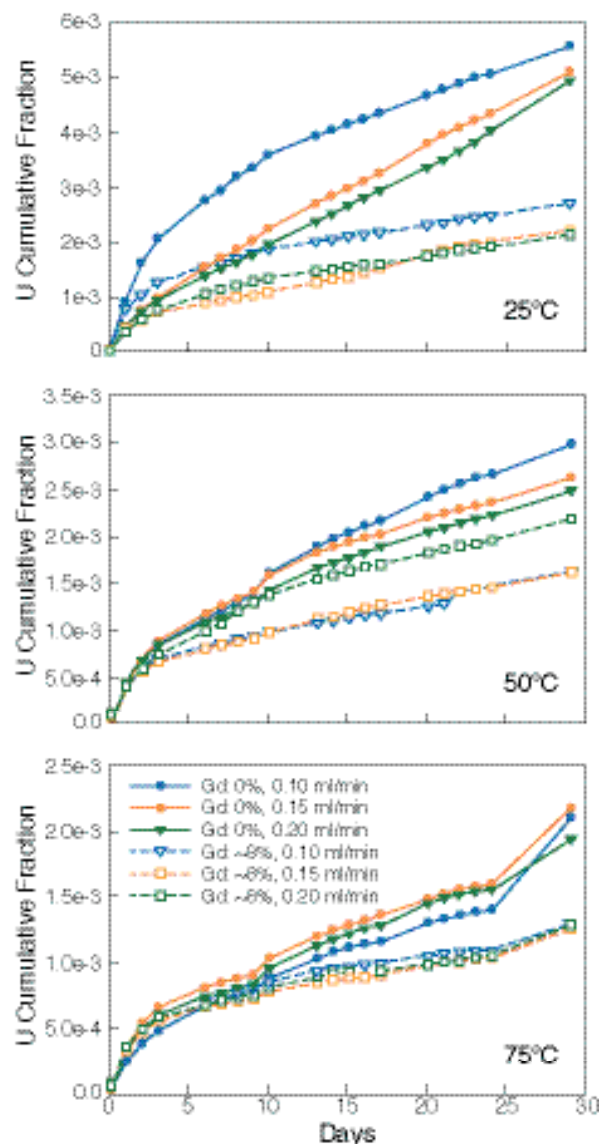


Figure 2. Results from SPFT tests on UO<sub>2</sub> and 8wt% Gd-doped UO<sub>2</sub> at 25°C, 50°C, and 75°C at 0.1, 0.15 and 0.2 mL min<sup>-1</sup>.

at the fuel-water interface. Proceedings of the 11th International High-Level Radioactive Waste Management Conference (IHLRWM), American Nuclear Society, Las Vegas NV, pp. 698–711, 2006.  
Kline, A., B. Hanson, W. Miller, and R. Wittman, Modeling the radiolysis effect on CSNF dissolution kinetics. Transactions of the American Nuclear Society Winter Meeting, 95, 177–178, Albuquerque, New Mexico, 2006.  
Kline, A., B. Hanson, and W. Miller, Characteristics of UO<sub>2</sub> dissolution as determined by SPFT Tests. American Nuclear Society Winter Meeting 2007 (submitted).



# Implications of Deliquescence and Decay Heat on Source Term Degradation

James Jerden

Argonne National Laboratory (ANL)

## Research Objectives

The goal of this project was to quantify processes that could cause water to condense and accumulate on failed spent nuclear fuel (SNF) pins. A particularly important process in this regard is the deliquescence of hygroscopic fission product minerals present within fuel grain boundaries and the fuel/cladding gap. Deliquescence could lead to the accumulation of water, despite the fact that the fuel assemblies will be the hottest material in the waste packages. The specific experimental objectives were to: (1) develop a predictive understanding of the onset of deliquescence on SNF by quantifying the deliquescence thresholds (as a function of temperature) of hygroscopic primary phases in the fuel or fuel/cladding gap, (2) develop a predictive understanding of how the aqueous films that form from deliquescence evolve

chemically as the SNF corrodes at relevant temperatures and relative humidities, (3) determine the paragenesis, mineral chemistry, and deliquescence behavior of alteration phases that form as SNF corrodes in aqueous films formed by deliquescence.

## Approach

The deliquescence behavior of key fission-product salts has been quantified using an isopiestic method. This approach was based on the fact that in a closed system—consisting of a hygroscopic salt, an aqueous salt solution, and a gas phase—water will partition via evaporation or condensation until its chemical potential is equal in all phases. Our experiments involved reacting a dry powder of the hygroscopic mineral(s) of interest, with air of a known relative humidity at a

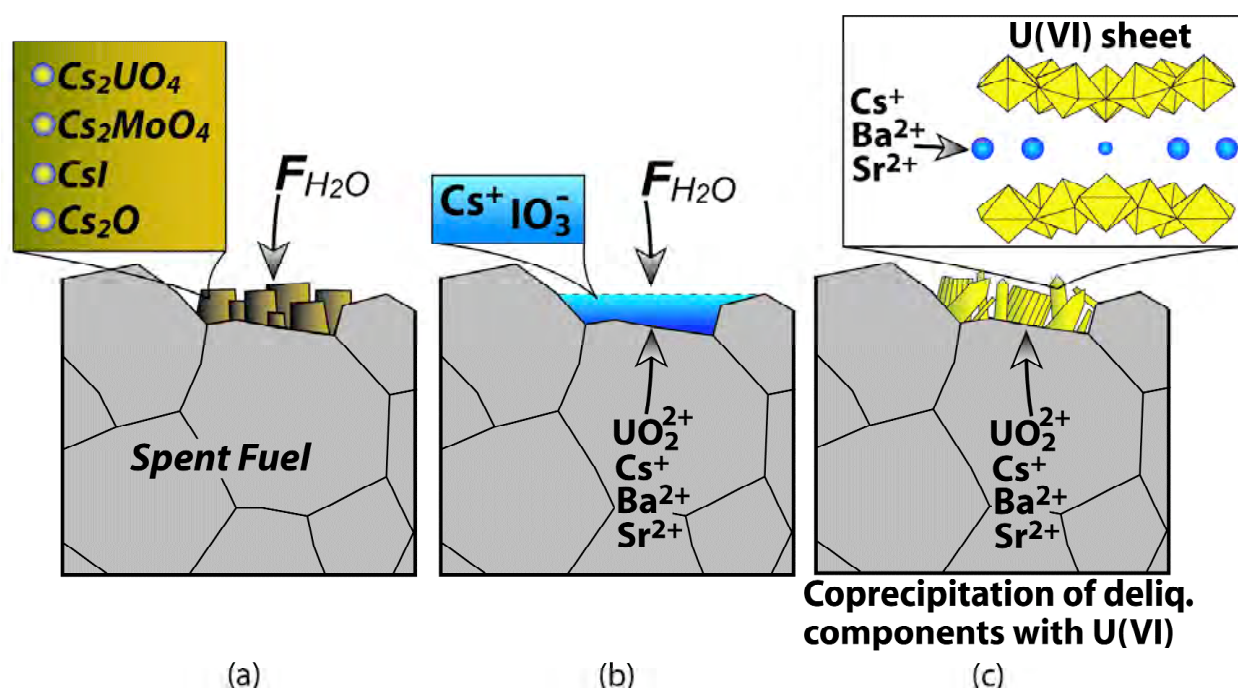


Figure 1. A summary of the processes involved in fission-product mineral deliquescence: (a) If the ambient relative humidity increases above approximately 80%, deliquescence will occur despite the fact that the fuel is 1°C–5°C hotter than the surrounding environment; (b) water will continue to condense as long as the activity of water in the deliquescent brine is lower than the ambient relative humidity; (c) the precipitation of uranyl corrosion phases counteracts deliquescence (increases the activity of water in the deliquescent brine) as deliquescent components are incorporated into the nondeliquescent uranyl minerals. Thus, the precipitation of uranyl minerals promotes evaporation of water from the SNF surface.

controlled temperature in a sealed system. The initial relative humidity was controlled using a sodium chloride salt solution. When the deliquescence threshold (relative humidity at which water will condense) of the sample is exceeded, the amount of water that accumulates due to deliquescence was measured gravimetrically. The amount of water that accumulates as the deliquescent solution equilibrates with the surrounding gas phase was also measured gravimetrically.

## Accomplishments

The deliquescence behavior of the hygroscopic fission product minerals cesium iodide (CsI), cesium molybdate ( $\text{Cs}_2\text{MoO}_4$ ) and selected cesium uranates ( $\text{Cs}_2\text{UO}_4$  and  $\text{Cs}_2\text{U}_2\text{O}_7$ ) have been studied over temperatures ranging from 40°C to 90°C. We have also completed experiments investigating how the deliquescence process, and subsequent chemical evolution of brines, is influenced by SNF corrosion. These were performed by reacting SNF surrogates (uranium oxides) containing hygroscopic fission product minerals ( $\text{Cs}_2\text{UO}_4 \pm \text{Cs}_2\text{U}_2\text{O}_7 \pm \text{CsI} \pm \text{Cs}_2\text{MoO}_4$ ) with humid air in a sealed isopiestic apparatus. Our experimental results have been used to quantify the conditions under which deliquescence could initiate SNF corrosion and how corrosion reactions may counteract deliquescent water accumulation.

Results indicate that fission product deposits containing cesium iodide, cesium molybdate, and the cesium uranate  $\text{Cs}_2\text{UO}_4$  will deliquesce at relative humidities greater than 80% and temperatures ranging from 40°C to 90°C. This process will occur even if the SNF is up to 5°C hotter than the surrounding environment. Once the

deliquescence process has started, water will continue to condense on the surface of the fuel as long as the activity of water in the brine is lower than the ambient relative humidity. However, our results also show that once SNF corrosion phases (uranyl minerals) begin to form, the deliquescence process becomes self-limiting, owing to the incorporation of deliquescent components into these stable alteration phases. The paragenesis of the alteration products is important in the sequestration of deliquescent components. Results from the SNF surrogate tests suggest that nondeliquescent uranyl minerals such as Cs-compreignacite [ $(\text{Cs}_6[(\text{UO}_2)_{12}(\text{OH})_{10}\text{O}_{10}](\text{H}_2\text{O})_{3.5})$ ] and billietite [ $(\text{Ba})(\text{UO}_2)_6\text{O}_4(\text{OH})_6(\text{H}_2\text{O})_8$ ] play key roles in increasing the activity of water in the brine formed by deliquescence by sequestering barium and cesium. There was also evidence that iodine released from the deliquescence of CsI may be sequestered by the formation of other nondeliquescent uranyl iodate minerals of the general type  $\text{M}(\text{II})[(\text{UO}_2)_2(\text{IO}_3)_2\text{O}_2](\text{H}_2\text{O})$  or  $\text{M}(\text{I})_2[(\text{UO}_2)_3(\text{IO}_3)_4\text{O}_2]$ . The key finding of this project was that, while deliquescence may lead to a transient accumulation of water and incipient corrosion of SNF, this process will be counteracted (effectively “turned-off”) by the sequestration of deliquescent components into nondeliquescent minerals (Figure 1).

## Related Publications

Jerden, J.L. Jr., M. Goldberg, J. Cunnane, T. Bauer, R. Wigeland, and R. Nietert, Can spent nuclear fuel decay heat prevent radionuclide release? In: Scientific Basis for Nuclear Waste Management XXVIII, J.M. Hanchar, S. Stroes-Gascoyne, and L. Browning, eds., Materials Research Society Symposium Proceedings, 824, pp.101–106, Warrendale, PA, 2004.

## FORMATION AND PROPERTIES OF $U^{6+}$ SECONDARY PHASES

### **Mitigation of the Release of $^{129}I$ from Spent Nuclear Fuel via Uptake by Uranyl Alteration Phases**

Thomas E. Albrecht-Schmitt, Auburn University; Iain May, The University of Manchester, Great Britain

### **Impact of Uranyl Alteration Phases of Spent Fuel on Mobility of Neptunium (Np) and Plutonium (Pu) in Yucca Mountain**

Peter C. Burns, University of Notre Dame

### **Actinide Adsorption to U(VI) Silicates**

S. B. Clark, Washington State University; Lawrence C. Hull, Idaho National Laboratory

### **Corrosion of Spent Nuclear Fuel: The Long-Term Assessment**

Rodney C. Ewing, University of Michigan

### **Direct Determination of the Thermodynamic Properties of Uranyl Minerals Important for the Performance of the Proposed Geological Repository at Yucca Mountain**

Jeremy B. Fein, Peter C. Burns, University of Notre Dame; Alexandra Navrotsky, University of California, Davis

### **Chemical and Coordination Structure of Radionuclides in Spent Nuclear Fuel and Its Alteration Products: Understanding Release Pathways**

Jeffrey A. Fortner, A. Jeremy Kropf, and James C. Cunnane, Argonne National Laboratory (ANL)

### **An *In Situ* Spectroelectrochemical Study of Neptunium (Np) Redox, Dissolution, and Precipitation Behavior at the Corroding Spent Nuclear Fuel/Alteration Phase Interface**

Artem Guelis, Jeremy Kropf, Christopher Johnson, and Jeffrey Fortner, Argonne National Laboratory (ANL); Petr Vanysek, Northern Illinois University

### **Natural Sequestration of Radionuclides In Volcanic Tuff**

Jonathan Icenhower, Edgar Buck, Eric Pierce, and Dawn Wellman, Pacific Northwest National Laboratory (PNNL); Andreas Lüttge, Rice University

### **Surface Charge and Radionuclide Adsorption Characteristics of U(IV,VI) Oxyhydroxides at 25–150°C**

David J. Wesolowski, Laetitia Delmau, Lawrence M. Anovitz, Jorgen Rosenqvist, and Donald A. Palmer, Oak Ridge National Laboratory (ORNL)

---

This page intentionally left blank.

# Mitigation of the Release of $^{129}\text{I}$ from Spent Nuclear Fuel via Uptake by Uranyl Alteration Phases

Thomas E. Albrecht-Schmitt<sup>1</sup> and Iain May<sup>2</sup>

<sup>1</sup>Auburn University | <sup>2</sup>The University of Manchester, Great Britain

## Research Objectives

Iodine-129 ( $^{129}\text{I}$ ) is a long-lived ( $t_{1/2} = 1.7 \times 10^7$ )  $\beta$ -emitting fission product present in spent nuclear fuel (SNF). In groundwater, such as that from the J-13 well near Yucca Mountain, it is expected to exist as both iodate,  $\text{IO}_3^-$ , and iodide. The objective of this program is to study the potential incorporation of  $^{129}\text{IO}_3^-$  into uranyl alteration phases that will likely form as the result of the interaction of SNF with groundwater at the proposed repository in Yucca Mountain. We propose that the trigonal pyramidal iodate anion can substitute in trace amounts in the place of tetrahedral  $[\text{SiO}_3(\text{OH})]^{3-}$  and  $\text{PO}_4^{3-}$ , as well as for trigonal planar  $\text{CO}_3^{2-}$ . Experiments will be performed whereby uranyl silicates, phosphates, and carbonates are synthesized in the presence of trace amounts of  $^{129}\text{IO}_3^-$ . Previously made uranyl alteration phases will also be equilibrated with  $^{129}\text{IO}_3^-$ . The uptake of  $^{129}\text{IO}_3^-$  will be studied by counter-methods, x-ray diffraction, inductively coupled plasma-mass spectroscopy (ICP-MS), and inductively coupled plasma-atomic emission spectroscopy (ICP-AES). In the case of uranyl carbonates such as rutherfordine,  $\text{UO}_2(\text{CO}_3)$ , charge balance requirements may allow for the simultaneous incorporation of both  $^{129}\text{IO}_3^-$  and  $^{237}\text{NpO}_2^+$ . Experiments to test for this concomitant uptake will also be performed. We anticipate that the formation of uranyl alteration phases will indeed act as a mechanism for the retardation of the release of  $^{129}\text{I}$ . The data that we generate will be used to modify current models for the release of  $^{129}\text{I}$  into the environment from SNF.

## Approach

Most of the exploratory syntheses in recent uranyl chemistry have either been performed under ambient conditions or under hydrothermal conditions near 200°C. Conditions relevant to the Yucca Mountain repository are expected to be near 70–90°C. We will approach the incorporation of  $^{237}\text{Np}$  and  $^{129}\text{I}$  in two different ways. First, experiments will be performed whereby uranyl silicates, phosphates, and carbonates are crystallized in the presence of  $^{237}\text{Np}$  and  $^{129}\text{I}$ . Second, we will allow previously crystallized uranyl alteration phases to equilibrate with solutions containing trace amounts of  $\text{NpO}_2^+$  and  $\text{IO}_3^{1-}$ . Bulk product composition will be determined using powder x-ray diffraction. The uptake of radionuclides will be

measured using a scintillation counter, ICP-MS, and ICP-AES. It will be important to determine the structures of actinyl iodates that crystallize at near neutral pH to show whether or not the structures of these compounds can lend some guidance in terms of which uranyl alteration products are likely to uptake  $\text{IO}_3^{1-}$ . Finally, while the solution complexation of uranyl by iodate has been studied at 25°C at low pH, data for complexation at elevated temperatures and at pH conditions similar to those expected at Yucca Mountain have not been performed. We will determine the complexation thermodynamic parameters of  $\text{UO}_2^{2+}$  with iodate at 90°C. The complexation of  $\text{NpO}_2^+$  by iodate in solution has not been addressed at all and will also need to be done.

## Accomplishments

The reactions of  $^{237}\text{NpO}_2$  with excess iodate under acidic hydrothermal conditions result in the isolation of the Np(IV), Np(V), and Np(VI) iodates,  $\text{Np}(\text{IO}_3)_4$ ,  $\text{Np}(\text{IO}_3)_4 \cdot n\text{H}_2\text{O} \cdot n\text{HIO}_3$ ,  $\text{NpO}_2(\text{IO}_3)$ ,  $\text{NpO}_2(\text{IO}_3)_2(\text{H}_2\text{O})$ , and  $\text{NpO}_2(\text{IO}_3)_2 \cdot \text{H}_2\text{O}$ , depending on both the pH and the amount of water present in the reactions. Reactions with less water and lower pH favor reduced products. While the initial redox processes involved in the reactions between  $^{237}\text{NpO}_2$  or  $^{242}\text{PuO}_2$  and iodate are similar, the low solubility of  $\text{Pu}(\text{IO}_3)_4$  dominates product formation in Pu iodate reactions to a much greater extent than  $\text{Np}(\text{IO}_3)_4$  does in the Np iodate system.  $\text{UO}_2$  reacts with iodate under these conditions to yield U(VI) iodates solely. The isotopic structures of the An(IV) iodates,  $\text{An}(\text{IO}_3)_4$  (An = Np, Pu) consist of one-dimensional chains of dodecahedral An(IV) cations bridged by iodate anions. The structure of  $\text{Np}(\text{IO}_3)_4 \cdot n\text{H}_2\text{O} \cdot n\text{HIO}_3$  is constructed from  $\text{NpO}_9$  tri-capped trigonal prisms that are bridged by iodate into a polar three-dimensional framework structure. In uranyl iodate chemistry, we demonstrated the direct intercalation of iodic acid into the layered structure of  $\text{UO}_2(\text{IO}_3)_2(\text{H}_2\text{O})$ . When  $\text{UO}_2(\text{NO}_3)_2 \cdot 6\text{H}_2\text{O}$  is reacted with a two- to five-fold excess of iodic acid under mild hydrothermal conditions, the only compound that results is  $\text{UO}_2(\text{IO}_3)_2(\text{H}_2\text{O})$ . When the amount of iodic acid is increased to tenfold, a mixture of  $\text{UO}_2(\text{IO}_3)_2(\text{H}_2\text{O})$  and  $\text{UO}_2(\text{IO}_3)_2(\text{H}_2\text{O}) \cdot 2\text{HIO}_3$  is found.

We have also prepared several new phosphate phases, such as  $\text{Na}(\text{UO}_2)(\text{PO}_4) \cdot \text{H}_2\text{O}$ ,  $\text{K}(\text{UO}_2)(\text{PO}_4) \cdot 2\text{H}_2\text{O}$ , and

$\text{Cs}_2(\text{UO}_2)_2(\text{PO}_4)_2 \cdot 3\text{H}_2\text{O}$ , that have the desired structural motifs that we need for studying the uptake of iodate. These compounds have been characterized by single crystal x-ray diffraction and other spectroscopic techniques. These compounds are similar in structure with sklodowskite,  $\text{Mg}[(\text{UO}_2)(\text{SiO}_3\text{OH})]_2(\text{H}_2\text{O})_6$ , and phurcalite  $\text{Ca}_2[(\text{UO}_2)_3(\text{PO}_4)_2\text{O}_2](\text{H}_2\text{O})_7$ .

Our findings on the unusual redox chemistry of Np and Pu iodates under water-limiting hydrothermal conditions points to the importance of understanding actinide chemistry when trace amounts of water are present, as opposed to reactions when water is present in bulk amounts. The pH dependence of these reactions is also of importance in determining which oxidation state of the actinide will dominate product formation. Trace water represents a more realistic early scenario in the lifetime of a repository.

Our findings on the preparation of new phosphate phases will allow us to pursue iodate uptake studies in the final year of this grant. These studies are under way.

## References

- Bray, T.H., J. Ling, E.-S. Choi, J.S. Brooks, J.V. Beitz, R.E. Sykora, R.G. Haire, D.M. Stanbury, and T.E. Albrecht-Schmitt, Critical role of water content in the formation and reactivity of uranium, neptunium, and plutonium iodates under hydrothermal conditions: Implications for the oxidative dissolution of spent nuclear fuel. *Inorganic Chemistry*, 46, 3663–3668, 2007.
- Ling, J., and T.E. Albrecht-Schmitt, Intercalation of iodic acid into the layered uranyl iodate,  $\text{UO}_2(\text{IO}_3)_2(\text{H}_2\text{O})$ . *Inorganic Chemistry*, 46, 346–347, 2007.
- Bray, T. H.; J.V. Beitz, A.C. Bean, Y. Yu, and T.E. Albrecht-Schmitt, Structural polarity induced by cooperative hydrogen bonding and lone-pair alignment in the molecular uranyl iodate,  $\text{Na}_2[\text{UO}_2(\text{IO}_3)_4(\text{H}_2\text{O})]$ . *Inorganic Chemistry*, 45, 8251–8257, 2006.



# Impact of Uranyl Alteration Phases of Spent Fuel on Mobility of Neptunium (Np) and Plutonium (Pu) in Yucca Mountain

Peter C. Burns

University of Notre Dame

## Research Objectives

Uranyl alteration phases of spent nuclear fuel (SNF) that form in a repository such as Yucca Mountain will likely incorporate a variety of radionuclides, and will thus impact their mobility. An understanding of radionuclide incorporation mechanisms into relevant uranyl phases, as well as the structures, chemistry, and thermochemical properties of the key uranyl phases, is needed to better understand the repository source term. Ongoing research at the University of Notre Dame is mostly focused on factors that impact incorporation of  $^{237}\text{Np}$  into selected uranyl phases that are likely to form as alteration products of SNF under moist oxidizing conditions.

## Approach and Accomplishments

### Synthesis and Structure of $\text{Np}_2\text{O}_5$

The phase  $\text{Np}_2\text{O}_5$  has been identified as a potential solubility-limiting phase for  $\text{Np}^{5+}$  in a geological repository under oxidizing conditions. Despite its importance and simple chemistry, its structure has remained unknown. Within the framework of a detailed study of Np crystal chemistry, we developed a new synthesis technique that provides single crystals of  $\text{Np}_2\text{O}_5$  via a mild hydrothermal route and determined its structure using single-crystal X-ray diffraction. The details of this study have been published in Forbes et al. (JACS 129, 2760–2761). The structure, shown in Figure 1, contains neptunyl square and pentagonal bipyramids that are linked into a layered framework. The formation of this compound under such mild conditions should have a significant impact on modeling the fate and transport of this radionuclide in the environment. These results for  $\text{Np}_2\text{O}_5$  will also allow further characterization in terms of thermodynamic stability and ultimately a reassessment of its role in the environmental chemistry of Np.

### Incorporation of $\text{Np}^{5+}$ Into Single Crystals of Uranyl Phases

Our earlier studies have examined incorporation of  $\text{Np}^{5+}$  into synthetic powders of uranyl phases. The results of these studies indicate that Np is incorporated into some structures, whereas others (those containing electroneutral

sheets and no interlayer cations) largely exclude Np.

We have synthesized single crystals of 10 uranyl phases using solutions containing 500 ppm  $\text{Np}^{5+}$ . These phases were selected to provide a substantial range of crystal structure connectivities, as well as multiple sites for potential incorporation of  $\text{Np}^{5+}$ . Recovered crystals were analyzed initially by single crystal x-ray diffraction to verify their identities. Subsequently, each was analyzed using laser-ablation inductively coupled plasma mass spectrometry (LA-ICP-MS), which was used to measure the ratio of mass 237 (Np) to 235 (U) (U-235 is present at about 0.2%). Analyses of crystals that were synthesized in the absence of Np consistently gave a background ratio of 0.0004. Analyses of the ten compounds all revealed substantial incorporated Np. These results show unequivocally that the Np is located within the crystals of the uranyl phases. The level of incorporation

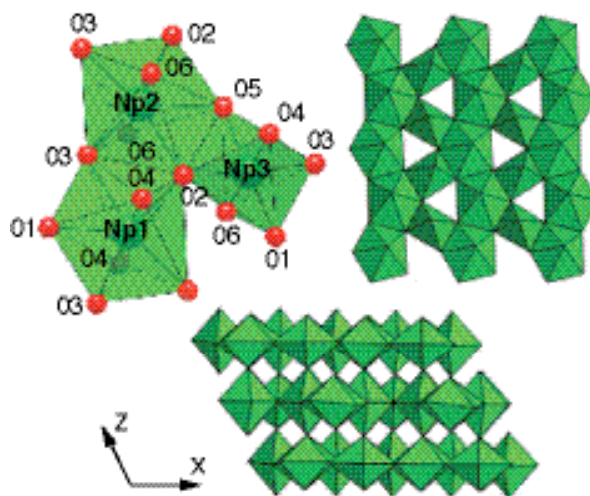


Figure 1. Polyhedral representation of the crystal structure of  $\text{Np}_2\text{O}_5$

was found to vary considerably over the compounds studied, and there was no apparent correlation with the synthesis conditions utilized in each case. Rather, the connectivity of the crystal structure and the availability of different types of cation sites appear to be the factors that impact incorporation. Ongoing studies of additional phases are currently under way to further elucidate the

structural controls on  $\text{Np}^{5+}$  incorporation. A representative crystal and ICP-MS data are given in Figure 2.

### Crystal Chemistry of Perrhenate as an Analogue for Pertechnetate

It has often been assumed that pertechnetate will not complex uranyl ions in solution, and that pertechnetate cannot coordinate uranyl ions in crystal structures, owing to the bond-valence requirements of the pertechnetate group (e.g., Chen, Burns, and Ewing, *J. Nucl. Mater.* 2000, v.278, 290–300). It is therefore assumed that pertechnetate will not be incorporated into uranyl phases that form when SNF is altered in a geological repository. However, over the past three years, several studies have appeared in the literature that unequivocally show that perchlorate, perrhenate, and pertechnetate can all coordinate uranyl ions. These studies have been a combination of spectroscopic and diffraction analysis, and have focused on compounds containing uranyl ions and a range of organic molecules.

We developed techniques for the synthesis of single crystals of uranyl perrhenates, as crystal-chemical analogues for uranyl pertechnetates. Thus far, these techniques have yielded the crystal structures of the compounds  $(\text{UO}_2)_2(\text{ReO}_4)_4(\text{H}_2\text{O})_3$ ,  $[(\text{UO}_2)_4(\text{ReO}_4)_2\text{O}(\text{OH})_4(\text{H}_2\text{O})_7](\text{H}_2\text{O})_5$ , and  $\text{Na}(\text{UO}_2)(\text{ReO}_4)_3(\text{H}_2\text{O})_2$ . Each of these compounds contain uranyl ions that are coordinated by perrhenate

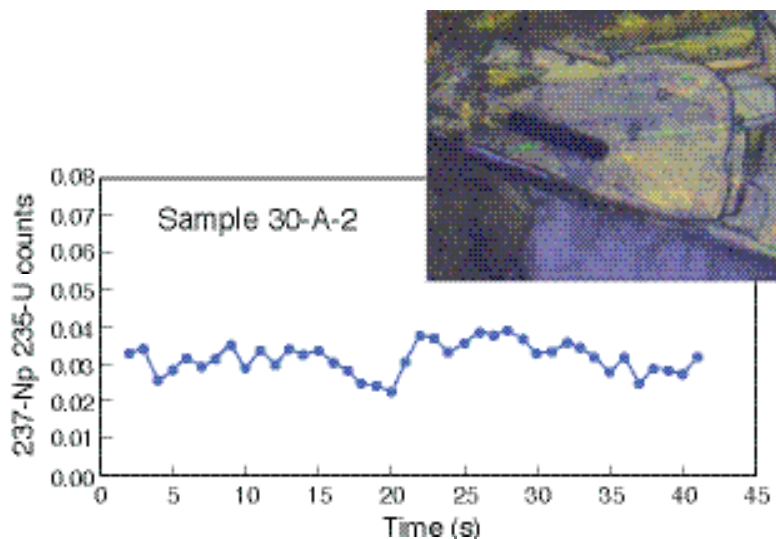


Figure 2. Representative example of a single crystal of a uranyl phase synthesized in the presence of  $\text{Np}^{5+}$ , and the corresponding LA-ICP-MS data showing the ratio of counts for mass 237 (Np) and 235 (U).

groups. The first contains chains of uranyl pentagonal bipyramids that are bridged by the sharing of equatorial vertices with perrhenate groups, whereas the latter two contain isolated clusters of uranyl pentagonal bipyramids that share vertices with perrhenate groups. These structures firmly establish the possibility of coordination of uranyl by perrhenate, and strongly suggest that pertechnetate can also coordinate uranyl. This suggests that pertechnetate may be incorporated into some uranyl minerals by substitution for tetrahedrally coordinated cations, and experimental studies of such incorporation are warranted.



# Actinide Adsorption to U(VI) Silicates

S. B. Clark<sup>1</sup> and Lawrence C. Hull<sup>2</sup>

<sup>1</sup>Washington State University | <sup>2</sup>Idaho National Laboratory

## Research Objectives

Recent work by us and others indicates that actinide adsorption to the U(VI) solids expected in the waste package may play a key role in the reduction of dissolved concentrations of radionuclides such as Np(V). However, little is known about the mechanism(s) of adsorption, nor is there sufficient knowledge or data to represent the phenomenon in predictive modeling codes. Unfortunately, this situation makes it impossible to consider actinide adsorption to the U(VI) silicates in either geochemical or performance assessment (PA) predictions.

The goal of this project, initiated on August 15, 2005, is to develop a thermodynamic description of the adsorption of key actinide cations to relevant U(VI) silicates using a surface complexation approach. Our objectives are to:

1. Study the surface charge associated with well-characterized U(VI) silicate solids under chemical conditions representing the waste package after corrosion.
2. Develop thermodynamic data to describe the adsorption of actinide cations to well-characterized U(VI) silicate solids. Adsorption and desorption experiments are conducted under conditions designed to address the complexity of the waste package chemistry.
3. Verify surface charge behavior and adsorption processes/mechanisms with appropriate spectroscopic tools. We are developing a molecular description of surface roughness and actinide sequestration at U(VI) silicate surfaces.
4. Use experimental results to parameterize a geochemical model to describe actinide sorption to U(VI) silicate solids. This surface complexation approach will use the diffuse double layer model that can be incorporated into geochemical codes such as EQ3/6.

## Approach

Our overall approach is to assume that the interaction of the positively charged actinide cations to the surface of U(VI) silicates is driven by electrostatics. Thus, one of the most important parameters for understanding the sorption

of contaminants to surfaces is the electrostatic charge of that surface as a function of pH and ionic strength. Our conceptual model for the U(VI) silicate surfaces available as complexation sites for the actinide cations is shown in Figure 1. Similar to the approach used routinely for clay minerals, we are considering both surface sites and edge sites. These are the sites that can be protonated or deprotonated, thereby leading to surface charge, and also sites that can complex actinide cations.

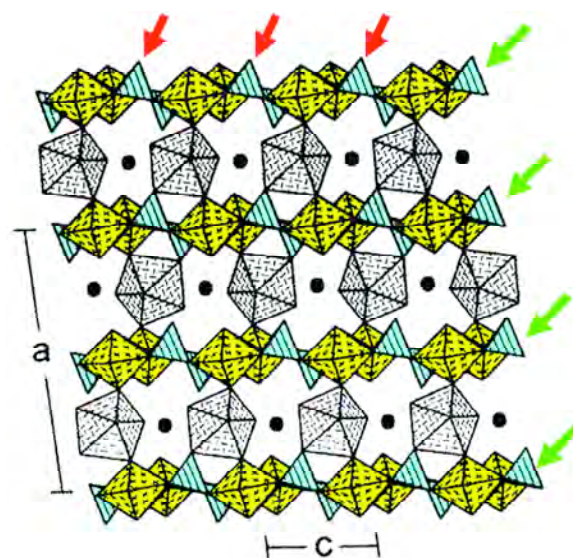


Figure 1. Possible sites for surface complexation of  $\text{NpO}_2^+$  or other actinide cations to the  $\alpha$ -uranophane structure. The green arrows show locations at the edge of each sheet; the blue tetrahedral are the silicate moieties, which can complex actinide cations. The red arrows show another possibility for coordination to the silicate tetrahedra located within the sheet.

## Accomplishments

We have begun to measure the surface charge of the U(VI) silicate series uranophane ( $\text{Ca}[(\text{UO}_2)(\text{SiO}_3\text{OH})]_2(\text{H}_2\text{O})_5$ ), Na-boltwoodite ( $\text{Na}[(\text{UO}_2)(\text{SiO}_3\text{OH})](\text{H}_2\text{O})_5$ ), and sklodowskite ( $\text{Mg}[(\text{UO}_2)(\text{SiO}_3\text{OH})]_2(\text{H}_2\text{O})_6$ ). Our preliminary results are shown in Figure 2. In the pH region of 5–7, the surface charge changes significantly, as expected. Interestingly, our initial results suggest that these surfaces are negatively charged at all pH values, although at pHs

below 5, the charge is only slightly negative. Above pH 7, the surface has a relatively high negative charge. In the region between pH 5–7, the surface charge varies markedly. Also, although all the U(VI) silicate surfaces show very similar behavior, note that the sklodowskite surface is less negatively charged at a given pH than uranophane or boltwoodite.

Based on these results, we have begun experiments to determine Np(V) adsorption isotherms to these U(VI) solids. We expect that adsorption at pH values less than 5 will be quite low, that it will increase above pH 5, and that it should reach 100% by pH 7. As the simple dissolved cation,  $\text{NpO}_2^+$  has a low cationic charge, which we suspect will limit its overall ability to sorb to the surface. We will consider changes in the Np(V) speciation as a function of pH over that region.

The sorption isotherms will be treated with a two-site model, as described above. We intend to use x-ray absorption spectroscopy to verify our assumptions about the molecular level interaction of the actinide cation to the U(VI) silicate surface.

Adsorption of Np and other actinides to U(VI) solids likely reduces their dissolved concentrations significantly. Unfortunately, little is known about actinide adsorption to these solids, and consequently, this phenomenon is not currently considered in the Yucca Mountain performance

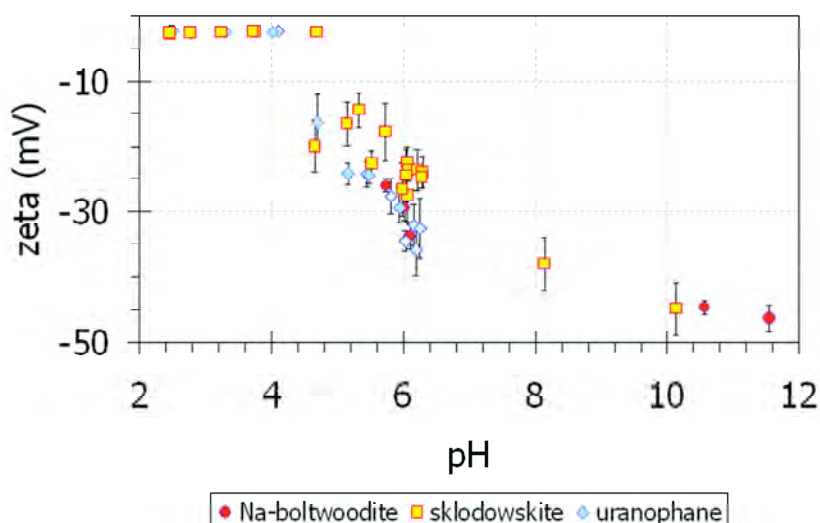


Figure 2. The measured zeta potential for Na-boltwoodite, sklodowskite, and uranophane as a function of pH. Note that in all cases, the zeta potential is negative. In the pH region of 5–7, sklodowskite is less negative at a given pH value than Na-boltwoodite or uranophane.

assessment. Our initial results suggest that while all of these solids have a capacity to sorb actinide cations at all pH ranges, sklodowskite at near neutral pH values is less negatively charged than the other U(VI) silicates. This indicates that in this pH region, boltwoodite and uranophane may be more important solids than sklodowskite for sorption of the actinides. The knowledge and data gained by this science project will address this opportunity to improve the Yucca Mountain performance assessment.

# Corrosion of Spent Nuclear Fuel: The Long-Term Assessment

Rodney C. Ewing  
University of Michigan

## Research Objectives

Spent nuclear fuel (SNF), essentially  $\text{UO}_2$ , accounts for over 95% of the total radioactivity of all of the radioactive wastes in the United States that require disposal, disposition, or remediation. The alteration of SNF results in the formation of new uranium phases that can cause the release or retardation of actinide and fission-product radionuclides. Over the long term, and depending on the extent to which the secondary uranium phases incorporate fission products and actinides, *these alteration phases become the near-field source term.*

This research program is a broadly based effort to understand the long-term behavior of SNF and its alteration products in a geologic repository. This research program addresses the following questions: (1) What are the *long-term* corrosion products of natural  $\text{UO}_{2+x}$ , uraninite, under oxidizing and locally reducing conditions? (2) What is the sequence of formation of the phases during alteration? (3) What is the radionuclide content of the corrosion products, as compared with the original  $\text{UO}_{2+x}$ ? and (4) What are the effects of ionizing radiation and alpha-decay on the stability and composition of the U(VI)-phases?

## Approach

The research program at the University of Michigan was initiated in July of 2004. At present we have one graduate student, Elizabeth Anderson (OCRWM Fellowship; NSF Fellowship) and three post-doctoral fellows, Satoshi Utsunomiya, Artur Deditius, and Veronique Pointeau (CEA). We have initiated studies in three areas: (1) studies of the alteration phases of  $\text{UO}_2$  under oxidizing and reducing conditions; (2) evaluation of the role of colloids in radionuclide transport; (3) heavy-particle and ionizing radiation damage of U(VI)-phases; (4) experiments that use mockups to study the interactions of radionuclides with the corrosion products of the waste packages (in collaboration with Sandia National Laboratory).

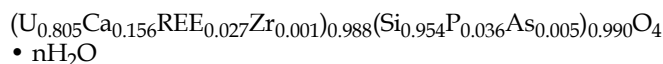
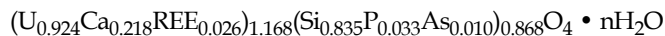
## Accomplishments

### Alteration of Coffinite ( $\text{USiO}_4$ ) Under Reducing and Oxidizing Conditions

Coffinite ( $\text{USiO}_4 \cdot n\text{H}_2\text{O}$ ,  $I_{41}/amd$ ,  $Z=4$ ) is a major alteration

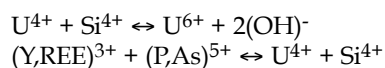
phase of uraninite,  $\text{UO}_{2+x}$ , under reducing conditions. This work is focused on (1) characterization of the alteration of coffinite under reducing and oxidizing conditions, and (2) determination of the role of organic matter during precipitation and alteration of coffinite. We have examined natural, coarse-grained coffinite from the Grants uranium region, New Mexico. The coffinite samples have been analyzed in detail at the submicron scale, in order to understand the microscale evolution of texture and chemistry during alteration under reducing and oxidizing conditions.

Two different populations of coffinite were identified. The primary coffinite grows on the mixed layers of organic matter and V-mica, mainly roscoelite  $[\text{K}(\text{V},\text{Al},\text{Mg})_2\text{AlSi}_3\text{O}_{10}(\text{OH})_2]$ , while secondary coffinite is present on the surfaces of the primary coffinite. Based on the electron-microprobe analyses (EMPA), chemical formulas of primary and secondary coffinites are:



The concentrations of U, Ca, and As decreased, whereas Si, P, and REEs were incorporated into the structure during the recrystallization of secondary coffinite under reducing conditions. Analysis totals by EMPA for both primary and secondary coffinite are variable and high (93.7–99.1 wt% and 91.9–99.7 wt%, respectively), indicating that  $\text{H}_2\text{O}$  is not an essential component of the coffinite structure. Under oxidizing conditions, coffinite altered to form (Na,K)-boltwoodite  $[(\text{Na},\text{K})(\text{UO}_2)(\text{SiO}_3\text{OH})(\text{H}_2\text{O})_{1.5}]$  and subsequently to uranyl sulfates. In a few cases, coffinite was directly altered to U-sulfate, which is tentatively identified as jáchymovite  $[(\text{UO}_2)(\text{SO}_4)(\text{OH})_{14}(\text{H}_2\text{O})_{13}]$ .

Based on charge-balance calculations using EMPA data, the coffinite can incorporate small amounts of  $\text{U}^{6+}$  up to 0.2 [apfu]:  $(\text{U}^{4+}_{1-x}\text{U}^{6+}_x)\text{Si}_{1-x}\text{O}_4 \cdot n\text{H}_2\text{O}$ ,  $0 < x < 0.2$ . In order to balance the charge,  $(\text{OH})^-$  groups can be introduced into the Si position. These substitution mechanisms are expressed as:



### Colloid Transport of Actinides

Sorption of actinides, particularly plutonium, onto submicron-sized colloids increases their mobility in the environment. Because of their low concentrations (<ppm), their occurrence and speciation on colloids in the “far field” have not yet been described. Based on the systematic analyses of the solid and the solution, we have investigated actinides on colloids in the groundwater from the Mayak Production Association, Urals, Russia, where at “ground zero” the Pu-activity is ~1000 Bq/l. Pu-activities are still 0.16 Bq/l (3 km) with 70–90 mol% of the Pu sorbed onto nanocolloids, confirming the significant role of colloids in the transport of Pu over long distances. Nano-SIMS elemental maps reveal that amorphous Fe-oxide colloids adsorb Pu(IV)-hydroxides or -carbonates along with U-carbonates.

### Radiation Effects on U<sup>6+</sup> Phases

U(VI) phases are common alteration products of SNF under oxidizing conditions, and they may potentially incorporate actinides, such as long-lived <sup>239</sup>Pu and <sup>237</sup>Np, delaying their transport to the biosphere. In order to evaluate the effects of ballistic interactions of  $\alpha$ -decay events and ionizing radiation by  $\beta$ -decay on the stability of the U<sup>6+</sup>-phases, we have conducted ion-beam (1.0 MeV Kr<sup>2+</sup>) and electron-beam irradiations on six different structures of U(VI) phases: uranophane, kasolite, boltwoodite, saleeite, carnotite, and liebigite, in addition to uranyl oxide hydrate, schoepite. Under ion-beam irradiation, nanocrystals of UO<sub>2</sub> formed at doses as low as 0.006 dpa, which is slightly less than the accumulated dose in pure U<sup>6+</sup> phases due to self  $\alpha$ -decay after 100,000 years, 0.009 dpa, and much less than the estimated dose after 10,000 years for the case that 1 wt. % <sup>239</sup>Pu is incorporated. During electron irradiation of schoepite, the amorphization dose (D<sub>a</sub>) was only  $0.51 \times 10^{10}$  Gy, and randomly oriented uraninite nanocrystallites formed at  $7.8 \times 10^{10}$  Gy, which is approximately the same dose as compared with the D<sub>a</sub>s for the other U<sup>6+</sup>-phases. Because the predicted cumulative dose from ionizing radiation in SNF is  $\sim 10^7$ – $10^8$  Gy during the first  $10^2$ – $10^3$  years after discharge, U<sup>6+</sup>-phases are not expected to amorphize during this time.

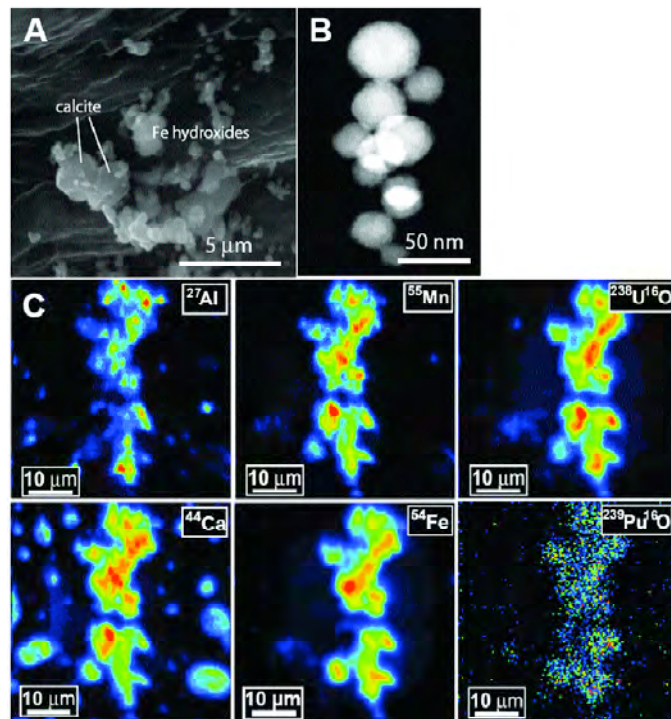


Figure 1. Direct evidence of Pu-adsorption onto amorphous Fe-hydroxyoxide. (A), SEM micrograph of typical colloids from well #1/69. Many spherical particles were observed with a size of < 1  $\mu$ m. (B), high-angle annular dark-field scanning TEM image of the spherical colloids. Electron diffraction patterns from these particles indicate that they are amorphous. (C), Contrast-enhanced, nano-SIMS elemental maps. (The intensity of the color does not correspond to the concentrations of the different elements [after Novikov et al., 2006].)

### References

- Novikov, A.P., S.N. Kalmykov, S. Utsunomiya, R.C. Ewing, F. Horreard, S.B. Clar, V.V. Tkachev, and B.F. Myasoedov, Colloid transport of plutonium in the far-field of the Mayak Production Association, Russia. *Science*, 314, 638–641, 2006.
- Utsunomiya, S., and R.C. Ewing, Radiation-induced decomposition of U(VI) alteration phases of UO<sub>2</sub>. *Proceedings of the Material Research Society Symposium*, 932, 465–472, 2006.

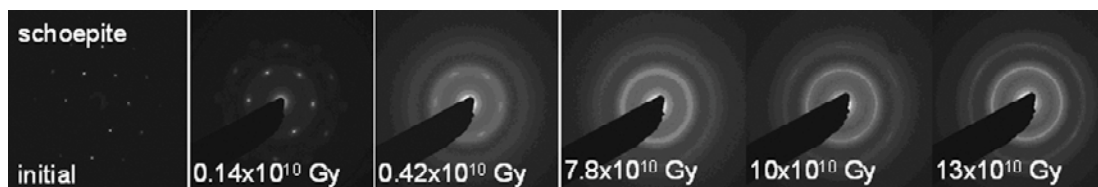


Figure 2. Selected area electron diffraction patterns showing the transition in schoepite as a function of the cumulative ionizing dose. After Utsunomiya and Ewing (2006).





# Direct Determination of the Thermodynamic Properties of Uranyl Minerals Important for the Performance of the Proposed Geological Repository at Yucca Mountain

Jeremy B. Fein<sup>1</sup>, Peter C. Burns<sup>1</sup>, and Alexandra Navrotsky<sup>2</sup>

<sup>1</sup>University of Notre Dame | <sup>2</sup>University of California, Davis

## Research Objectives

The objective of this study is to determine the thermodynamic properties for a broad range of environmentally important uranyl mineral phases using solubility and calorimetric measurements, producing an internally consistent dataset that is useful in modeling spent nuclear fuel (SNF) alteration and U mobility behavior in near-surface environments.

We are using solubility and calorimetry measurements in order to provide rigorous constraints on the Gibbs free energies of formation, enthalpies of formation, and standard entropies for these solids. These parameters are needed not only to determine which uranyl phases will become stable as a function of conditions as SNF alters in a repository setting, but also to calculate the mobility of U in equilibrium with these alteration phases. Solubilities of representative members of the uranyl oxide hydrates, uranyl silicates, and uranyl carbonates are being measured both for the end-member phases as well as for selected phases containing a range of substituted Np within the crystal structure.

## Approach

In the experimental research program, we are synthesizing and measuring the solubility of a wide range of uranyl mineral phases. In order to improve the accuracy and precision of the thermodynamic interpretation of the data, solubility measurements are being conducted primarily under the low pH conditions at which  $\text{UO}_2^{+2}$  is the dominant aqueous uranyl species. The solubility experiments are being conducted as functions of pH, ionic strength, and temperature, and will yield Gibbs free energies of formation of the phases of interest. The calorimetric data will enable determination of the enthalpies of formation for these phases, so together the standard entropies can be determined as well.

The mineral syntheses and solubility measurements are being conducted at University of Notre Dame under the supervision of Burns and Fein, respectively; the calorimetry measurements are being conducted at University of California-Davis under the supervision of Navrotsky.

## Solubility Experiments

Successful extraction of thermodynamic data from solubility measurements requires a range of measurements or controls on the experimental systems: (1) rigorous demonstration of equilibrium reversal; (2) measurements of the equilibrium pH and the total equilibrium concentrations of all mineral-forming cations in the system; (3) ionic strength control or measurement; and (4) determination that secondary mineral phases do not form during experimentation. In each batch solubility experiment, a synthesized uranyl mineral powder is placed in contact with a fixed ionic strength solution, and the pH of the suspension is adjusted to a desired value using minute volumes of concentrated perchloric acid or sodium hydroxide solution. Samples are taken as a function of time and analyzed for dissolved cations using an inductively coupled plasma optical emission spectroscopy approach. The solids used in each experiment are analyzed using x-ray diffraction and Fourier-transform infrared spectroscopy to check for secondary precipitates that may have formed during the experiments. In some experiments, solubility reversals are conducted by spiking the starting solutions with uranium and any other mineral-forming cations, so that equilibrium is approached from supersaturation.

## Calorimetry Experiments

High-temperature oxide melt solution calorimetry uses a Calvet-type high temperature custom-built calorimeter. Solution enthalpies for each sample are measured by dropping ~5 mg pressed pellets of material from room temperature, 298 K, into the molten oxide solvent,  $3\text{Na}_2\text{O}\cdot 4\text{MoO}_3$ , at calorimetric temperature, 976 K. The calorimeter, calibrated using the heat content of  $\alpha\text{-Al}_2\text{O}_3$ , is flushed continuously with  $\text{O}_2$  throughout the experiments to ensure an oxidizing atmosphere. Prior to the calorimetric experiments, complete dissolution in the solvent at calorimetric conditions is established in a furnace at 976 K. A large and rapidly generated endothermic enthalpy of drop solution for each phase, return of the calorimetric signal to its baseline value, and a solvent color change from white to yellow indicates that the uranyl minerals dissolve fully in the melt. The high density of the sample assures that the pellets drop quickly and sink in the solvent, so that the sam-

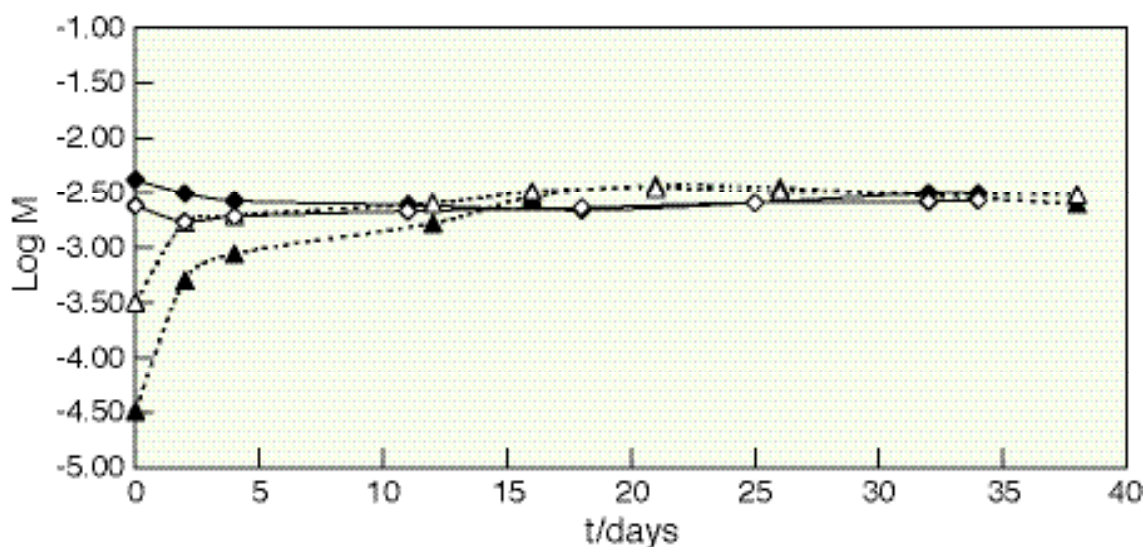


Figure 1. . Plot of logarithm of solubility of soddyite against time for experiments at pH 3.67 from supersaturation (filled diamonds U and open diamonds Si) and undersaturation (filled triangles U and open triangles Si). These results, in conjunction with calorimetry measurements, place tight constraints on the thermodynamic properties that define soddyite stability and solubility under a range of repository conditions.

ple does not float on the surface of the melt. Calorimetry is straightforward and problem-free. We are conducting calorimetry measurements on each of the phases used for solubility experiments that have not previously been examined using calorimetry.

## Accomplishments

Over the past year, we have perfected synthesis techniques for a number of uranyl oxide hydrates, uranyl silicates, and uranyl carbonates, and solubility and calorimetry measurements have been conducted on several of these phases. Solubility measurements indicate that solubility reversals can be measured and equilibrium attained over the course of 10–20 days, depending on pH and the uranyl phase present. We have also begun synthesis and solubility experiments to study the effect of Np-incorporation in soddyite on the concentrations of U and Np in equilibrium with the mixed neptunyl/uranyl phase. Our solubility and calorimetry measurements for pure soddyite are reported in the first publication from this project in *Journal of Chemical Thermodynamics* (Figure 1). Five additional papers are in preparation: one which will review what is known about solubilities and thermodynamic properties of uranyl minerals; one experimental

paper on each of the following groups of minerals—the uranyl silicates, the uranyl hydrates, and the uranyl carbonates—and a publication on the solubility of soddyite with incorporated Np. All papers should be completed and submitted this year.

The results from this project will dramatically improve our understanding of the thermochemical parameters of uranyl minerals, thereby improving our ability to model radionuclide mobility in the subsurface. The experiments in this study are valuable as direct indications of the concentration of uranium and other elements in solution in equilibrium with environmentally important uranyl mineral phases. In addition and perhaps more importantly, the experiments yield an internally consistent dataset of the thermodynamic properties for a wide range of uranyl minerals of repository and general environmental interest.

## Project Publication

Gorman-Lewis, D., L. Mazeina, J.B. Fein, J.E.S. Szymanowski, P.C. Burns, and A. Navrotsky, Thermodynamic properties of soddyite from solubility and calorimetry measurements. *Journal of Chemical Thermodynamics*, 39, 568–575, 2007.





# Chemical and Coordination Structure of Radionuclides in Spent Nuclear Fuel and Its Alteration Products: Understanding Release Pathways

Jeffrey A. Fortner, A. Jeremy Kropf, and James C. Cunnane  
Argonne National Laboratory (ANL)

## Research Objectives

Knowledge of the chemical states of trace fission products and transuranium actinides in spent nuclear fuel (SNF) and related materials from the nuclear fuel cycle provide insight that may benefit both modeling and design considerations for waste disposal in a geologic repository. Owing to the overall complexity of the repository system, it is important to establish multiple lines of evidence for a proposed mechanism to describe radionuclide behavior. To this end, this project examining SNF materials was designed to complement independent thermodynamic and solution chemistry experiments. Of the available techniques, x-ray absorption spectroscopy (XAS) was found to be uniquely suited for determining oxidation states and structural environments of elements in solids, particularly within challenging radioactive specimens. This project was initiated to investigate the solid state chemistry of radioactive fission products (e.g., technetium) and activation products (neptunium, plutonium) in SNF by using advanced XAS techniques, many of which were developed as part of this project. The objective is to provide definitive information about the crystal chemistry of these key radionuclides and to determine the possible impact on release behavior during SNF corrosion. We also address possible sequestration of these radionuclides in more stable minority phases (e.g., exsolved, metallic 5-metal “epsilon” particles) and secondary alteration phases. Technetium-99 ( $^{99}\text{Tc}$ ) is an important radionuclide in repository models, owing to its relatively long half-life and the high aqueous solubility of its compounds where it is in the heptavalent state. As oxide SNF undergoes fission in a reactor, a portion of the technetium is incorporated into an exsolved intermetallic “epsilon particle” alloy that forms in the fuel from the 5th-period noble metal fission products molybdenum, technetium, ruthenium, rhodium, and palladium.

By strengthening the science underlying models developed to predict the long-term performance of SNF in the planned repository, we hope to provide insight that is expected to benefit both modeling and design considerations for waste disposal in a geologic repository.

## Approach

In order to obtain spectroscopic information from elements

present in SNF at the trace level and in the presence of an intense x-ray fluorescence background from the uranium oxide matrix, an energy discriminating detector based upon diffractive optics, the “bent-Laue analyzer” (BLA) detector, was chosen. At the time this project was initiated, the BLA concept had been demonstrated, but needed further improvements to be developed under the auspices of this project. Among the improvements developed were refined optics to achieve microprobe x-ray spot size to smaller than 2 microns at 19 keV, using new mirrors that were specifically designed to be used with the BLA, and a quad-analyzer array to obtain simultaneous, independent tuning and data acquisition. Using this approach, detailed XAS information from technetium and other trace elements in specimens of SNF has been obtained. By analyzing XAS extended fine structure (EXAFS) data from a particular absorption edge, we can determine the local environment of a specific atomic species, including distances to near-neighbors, types and numbers of neighboring atoms, and details of the radial distribution function. The energy of the absorption threshold and near-edge absorption features also can be used to obtain information about the charge state of the central atom and the site symmetry.

## Accomplishments

Several XAS measurements from SNF and separate epsilon-phase alloys were performed at the Materials Research Collaborative Access Team (MR-CAT) insertion device beamline, located at the Advanced Photon Source (APS), a third-generation x-ray synchrotron source at Argonne National Laboratory. The brightness of the APS in the high-energy x-ray regimes makes it ideal for investigating these materials, which have relatively high-energy absorption edges for key elemental components, and which must be carefully encapsulated for radiological safety. Specimens were obtained from SNF used in testing for the Yucca Mountain Project; from SNF-derived epsilon metal particles that had been chemically separated from fuel by Daqing Cui of Studsvik Nuclear AB, Sweden, with whom we have an ongoing collaboration (Figure 1); and from synthetic epsilon metal prepared by arc-melting Mo, Ru, Rh, and Pd (with Re as a stand-in for Tc) provided by David Wronkiewicz of the University of Missouri-Rolla (Figure 2). Among the observations is that the epsilon phase in SNF has been found to persist relatively intact in corroded SNF,

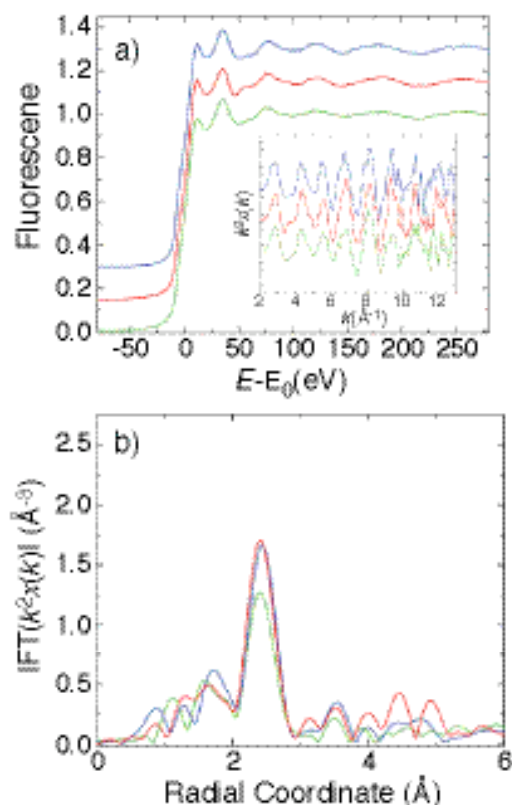


Figure 1. EXAFS from epsilon metal particles extracted from spent fuel by Daqing Cui et al. a) Spectral edges from Mo (blue) Tc (red) and Ru (green) with fine structure (inset). b) Fourier transform modulus with color key as in a). Note the striking similarity of the near-edge and fine structure, suggesting a very well-mixed alloy.

with little evidence of de-alloying (loss of less-noble metals molybdenum and technetium). This suggests that the corrosion potential of the bulk fuel is fixed below the de-alloying potential of the epsilon metal. Also, the epsilon phase may be difficult to simulate in detail outside of the irradiated fuel (Figure 2). This may be owing to the conditions of high irradiation and prolonged time at temperature under which the epsilon phase forms in the fuel.

## References

- Cui, D., J. Low, C.J. Sjöstedt, and K. Spahiu, On Mo-Ru-Tc-Pd-Rh-Te alloy particles extracted from spent fuel and their leaching behavior under Ar and H<sub>2</sub> atmospheres. *Radiochim. Acta*, 92, 551–555, 2004.
- Fortner, J.A., A.J. Kropf, J.L. Jerden, and J.C. Cunnane, Chemical effects at the reaction front in corroding spent nuclear fuel. In: *Scientific Basis for Nuclear Waste Management XXX*, D.S. Dunn, C. Poinssot, and B. Begg, eds., Mater. Res. Soc. Symp. Proc. 985 Paper 0985-NN01-03, Warrendale, PA, 2007.
- Fortner, J.A., A.J. Kropf, R.J. Finch, and J.C. Cunnane, Technetium and molybdenum in oxide spent nuclear fuel: Impact on release estimates. In: *Scientific Basis for*

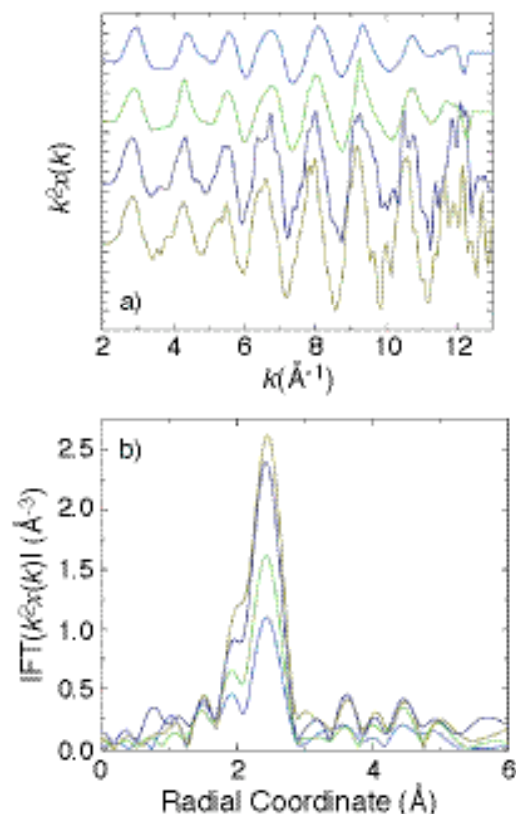


Figure 2. a) X-ray absorption fine structure from Mo, Ru, Rh, and Pd (in order from top to bottom) in a synthetic epsilon particle sans Tc from the University of Missouri-Rolla (courtesy D. Wronkiewicz). b) Fourier transform moduli, with peak amplitude in order of decreasing intensity representing Pd (olive) Rh (navy) Ru (green) and Mo (blue). In this specimen, the Mo appears substantially less well-ordered than the more noble metals, and less ordered than the Mo in the CSNF-derived epsilon phase (Figure 1).

- Nuclear Waste Management XXVIII, J.M. Hanchar, S. Stroes-Gascoyne, and L. Browning, eds., Mater. Res. Soc. Symp. Proc. 824, Paper CC2.11 Warrendale, PA, 2004.
- Fortner, J.A., R.J. Finch, A.J. Kropf, and J.C. Cunnane, Re-evaluating neptunium in uranyl alteration phases from corroded spent fuel. *Nuclear Technology*, 148 (2), 174–180, 2004.
- Fortner, J.A., A.J. Kropf, R.J. Finch, C.J. Mertz, J.L. Jerden, M.G. Goldberg, and J.C. Cunnane, Analysis of trace elements in commercial spent nuclear fuel using X-ray absorption spectroscopy. In: *Global 2003*, ANS Proceedings, 2003.
- Kropf, A.J., J.A. Fortner, R.J. Finch, J.C. Cunnane, and C. Karanfil, A bent silicon crystal in the Laue geometry to resolve X-ray fluorescence for X-ray absorption spectroscopy. *Physica Scripta*, T115, 998–1000, 2005.
- Wronkiewicz, D.J., C.S. Watkins, A.C. Baughman, F.S. Miller, and S.F. Wolf, Corrosion testing of a simulated five-metal epsilon particle in spent nuclear fuel. In: *Scientific Basis for Nuclear Waste Management XXV*, B.P. McGrail and G.A. Cragolino, eds., Mat. Res. Soc. Symp. Proc., 713, Paper JJ14.4.2., 2002.

# An *In Situ* Spectroelectrochemical Study of Neptunium (Np) Redox, Dissolution, and Precipitation Behavior at the Corroding Spent Nuclear Fuel/Alteration Phase Interface

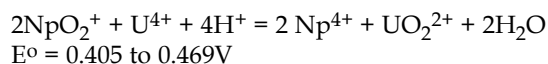
Artem Guelis<sup>1</sup>, Jeremy Kropf<sup>1</sup>, Christopher Johnson<sup>1</sup>, Jeffrey Fortner<sup>1</sup>, and Petr Vanysek<sup>2</sup>

<sup>1</sup>Argonne National Laboratory (ANL) | <sup>2</sup>Northern Illinois University

## Research Objectives

The objective of this project is to examine the oxidative dissolution of Np(IV) and the reductive precipitation of aqueous Np(V) species at  $U_{(1-x)}Np_xO_2$  [ $0 \leq x < 0.1$ ] and other surfaces under applied oxidation potential conditions relevant to the range of corrosion potentials expected for the surface of corroding spent  $UO_2$  fuels in air-saturated solutions (i.e., at applied potentials near the fuel's corrosion potential).

In spent  $UO_2$  fuels Np is expected to be present as a solid solution of  $NpO_2$  in the  $UO_2$  fluorite structure, with which it is compatible. Np may be released from the spent  $UO_2$  fuels matrix when the matrix degrades by oxidative dissolution. Available data in acidic solutions indicate that the standard potential for the  $UO_2^{2+}/U^{4+}$  is significantly lower than the standard potential for the  $NpO_2^+/Np^{4+}$  couple, and indicate that reduction of Np(V) by U(IV) as the fuel corrodes is thermodynamically favored, as shown by the following reaction:



Although this equilibrium equation is not valid for the solid-liquid interface, the spent nuclear fuel (SNF) corrosion potential is expected to be lower than the potential of the Np(V)/Np(IV) couple, so one could expect the reduction of Np(V) at the SNF surface. This indicates that oxidation of Np(IV) in the fuel's lattice may not occur under the pertinent potential conditions at the fuel's surface. In short, the oxidative dissolution behavior of Np at the corroding fuel surface remains uncertain.

## Approach

The work included the following objectives: (1) determine the applied potential range for reductive precipitation of Np(V) onto  $U_{(1-x)}Np_xO_2$  [ $0 \leq x < \sim 10^{-1}$ ] and inert (e.g., Pt, carbon or pyrolytic graphite) electrode surfaces; (2) identify the applied potential ranges for congruent and incon-

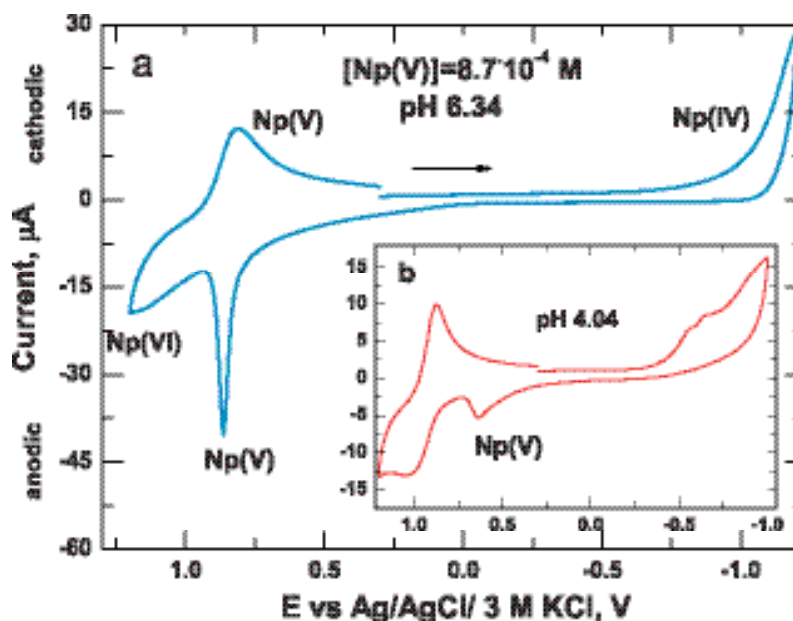


Figure 1. Cyclic voltamogram of Np in 0.1 M NaCl on glassy carbon electrode (a) pH 6.34, (b) pH 4.04.

gruent release of Np(V) and U(VI) from  $U_{(1-x)}Np_xO_2$  surfaces; and (3) design electrochemical cells suitable for performing the Np oxidative dissolution and reductive precipitation measurements *in situ* at Argonne's Advanced Photon Source (APS) Materials Research-Collaborative Access Team (MR-CAT) beamline; and (4) conduct x-ray absorption near-edge structure (XANES) and extended x-ray absorption fine structure (EXAFS) analyses of solution species and precipitated solids at  $U_{(1-x)}Np_xO_2$  solid-liquid interfaces.

## Accomplishments

Using cyclic voltametry of the Np solution at neutral pH, we have determined the potential range for the reductive precipitation of Np(V) to Np(IV) on the glassy carbon and Pt working electrodes, with consecutive oxidation of Np(IV) oxo-hydroxy species from the electrode surface to soluble  $NpO_2^+$  species (Figure 1).

As expected, a significant overpotential is observed for the electron transfer between Np(V) and Np(IV), due to

the changes in the chemical structures. The Np(VI)/Np(V) couple, on the other hand, reveals reversible behavior at lower pH and quasi-reversible behavior in neutral solutions.

The reduction of Np(V) at the UO<sub>2</sub> surface without applied potential was demonstrated by allowing the <sup>238</sup>UO<sub>2</sub> pellet to react with air-saturated neutral Np(V) solution for 4 days. XANES analysis showed the presence of a mixture of Np(IV) and Np(V) precipitated at the UO<sub>2</sub> surface (Figure 2). The Np concentration in the solution decreased from  $1 \times 10^{-4}$  to  $3.3 \times 10^{-5}$  M.

We have designed and built an electrochemical cell for laboratory and synchrotron use. In addition to standard fluid and electrode ports for electrochemistry, two inline x-ray windows allow beam access at glancing incidence to the electrode surface. A third larger window parallel to the electrode surface may be used as a beam port or as a fluorescence/scattering exit. *In situ* x-ray glancing incidence and reflectivity measurements, as well as x-ray absorption spectroscopy and limited x-ray diffraction measurements, are possible using this cell with this window configuration. The positioning of the electrode with respect to the larger window was expected to inhibit electrical current and ion transport at small separations that may be required for x-

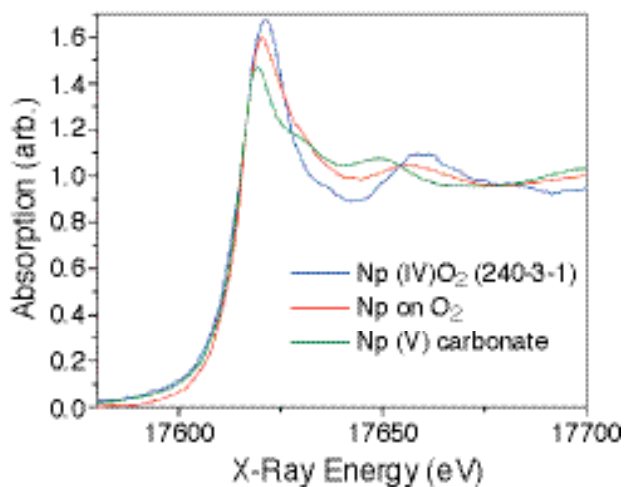


Figure 2. XANES of the Np on the UO<sub>2</sub> surface (red spectrum) and spectra of Np(IV) (blue) and Np(V) (green). Initial pH 6.5.

ray measurements. Cyclic voltammetry measurements indicate that the electrode current does not decrease until the electrode approaches within ~0.5 mm of the window. The typical separation will be larger than 1.5 mm. This cell has been tested in different orientations for satisfactory fluid flow.

# Natural Sequestration of Radionuclides In Volcanic Tuff

Jonathan Icenhower<sup>1</sup>, Edgar Buck<sup>1</sup>, Eric Pierce<sup>1</sup>, Dawn Wellman<sup>1</sup>, and Andreas Lüttge<sup>2</sup>

<sup>1</sup>Pacific Northwest National Laboratory (PNNL) | <sup>2</sup>Rice University

## Research Objectives

The cardinal goal of this investigation has been to gain an understanding of the mobility of dissolved elements in a dynamic geochemical environment, in which sequestration of elements may occur due to secondary mineral precipitation. A dynamic geochemical environment is present at the proposed Yucca Mountain repository site, because of the inherent thermodynamic instability of the matrix that is the source of dissolved radionuclide elements— $U_2$ —and the porous lithologies through which the solution migrates—the volcanic tuff. Previous experimental and modeling studies have shown that pore fluids interacting with volcanic tuff that makes up the bedrock in the disposal setting results in massive displacement of soluble elements in spent nuclear fuel (SNF) and the growth of secondary phases. We studied secondary phase growth and element mobility on the  $UO_2$  surface and in the tuff to form the basis of mechanistic and predictive models. These data will establish source-term and retention parameters, and will underpin a more precise model of radionuclide migration and retention that will refine existing models.

## Approach

Because of interruptions in the funding for this work, many of the key experiments are still ongoing and will continue through FY07 and into FY08. Accordingly, what is reported herein is only a fragmentary picture of the complete set of data that we are gathering. The four main thrusts of the experiments are to quantify: (1) the dissolution behavior of the volcanic tuff, (2) the transport of elements through the tuff, (3) the corrosion/dissolution of  $UO_2$  at repository conditions, and (4) the combined dissolution/reaction behavior of  $UO_2$  and volcanic tuff in a single experiment. The dissolution of volcanic tuff and  $UO_2$  was carried out in traditional flow-through experiments over a range of  $T$ , pH, flow rate, and groundwater compositions. Concentrations of dissolved constituents were determined by inductively coupled plasma-optical emission spectroscopy (ICP-OES) and -mass spectroscopy (-MS) methods, and run products were examined using vertical scanning interferometry (VSI) and atomic force microscopy (AFM). Transport of elements (Ba, Cs, I, Mo, Sr, Se, and Re) was quantified in hydraulically saturated columns. Concentrations of elements from these ongoing

experiments that have taken place over the last two years are not yet available. The reaction behavior of  $UO_2$  and volcanic tuff is being determined in a hydraulically unsaturated column (pressurized unsaturated flow, or PUF) test that consists of  $UO_2$  powder overlying tuff powders. The input solution is a synthetic groundwater solution doped with trace amounts of nonradiogenic elements (Ba, Cs, I, Mo, Sr, and Se) or a nonradiogenic substitute (Re for Tc). Effluent solutions are being analyzed using ICP-OES and -MS methods, and run products will be scrutinized by SEM and HRTEM methods. No data are currently available from this experiment.

## Accomplishments

### Volcanic Tuff Dissolution

Dissolution kinetics of volcanic tuff powders as a function of pH and temperature are shown in Figure 1. Dissolution rates based on Si release to dilute solution at 40° and 90°C

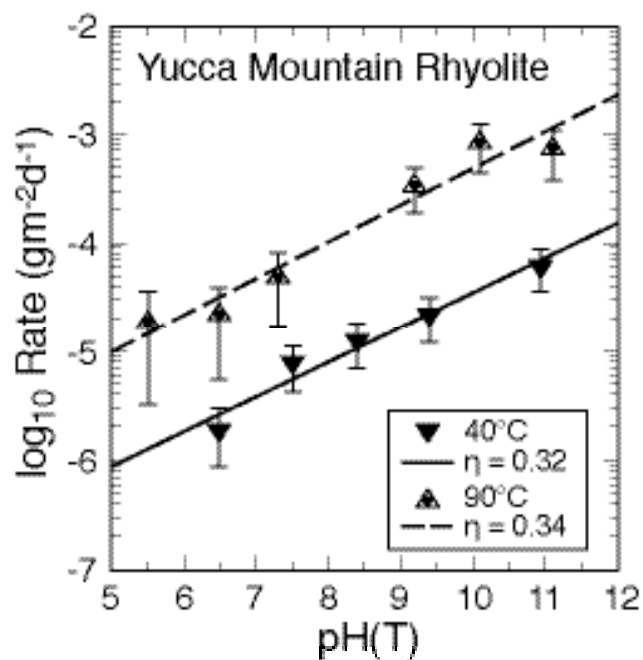


Figure 1. Plot of  $\log_{10}$  rate v. solution pH at temperature for Yucca Mountain tuff at 40° and 90°C. The power law coefficient,  $\eta$ , was measured as 0.3 at both temperatures.



indicate a strong dependence on solution pH. The power law coefficient for the rate dependence on dissolution, or the exponent to which the rate is raised, was measured as  $\eta = 0.3$  at both temperatures. At high pH values, the effluent chemistry data indicate formation of secondary phases. Run products from experiments with tuff coupons were examined by VSI methods, and a representative image is shown in Figure 2. The figure shows that devitrified matrix—consisting of feldspar and silica polymorphs—dissolves more rapidly than feldspar phenocrysts. Run products were also viewed using AFM, and representative images are shown in Figure 3. These images show the nature of the dissolution surface in the tuff matrix and the formation of nascent secondary phases. A thick reaction layer was not observed in these experiments. These data are included in a manuscript that is being written for the *American Journal of Science*.

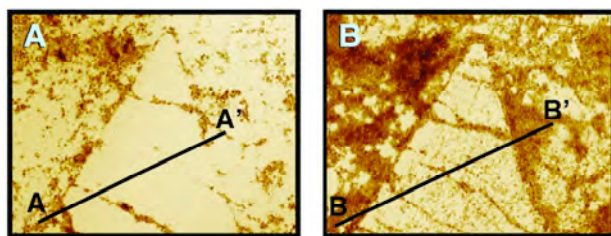


Figure 2. Vertical scanning interferometer (VSI) image of alkali feldspar phenocryst in volcanic tuff matrix before (A) and after (B) dissolution test. The increase in brownish “grunge” in (B) indicates a greater degree of dissolution in the matrix compared to the phenocryst.

### Dissolution of $\text{UO}_2$

Although the dissolution behavior of  $\text{UO}_2$  has been widely reported in the literature, we were surprised by some of the new surface features that we observed from our experiments. Dissolution experiments were carried out in flow-through reactors at a variety of temperatures and input solution chemistries. We found that once a pH, temperature, and bicarbonate threshold is crossed, dissolution rates rapidly decline. The reason for this is unclear, but it

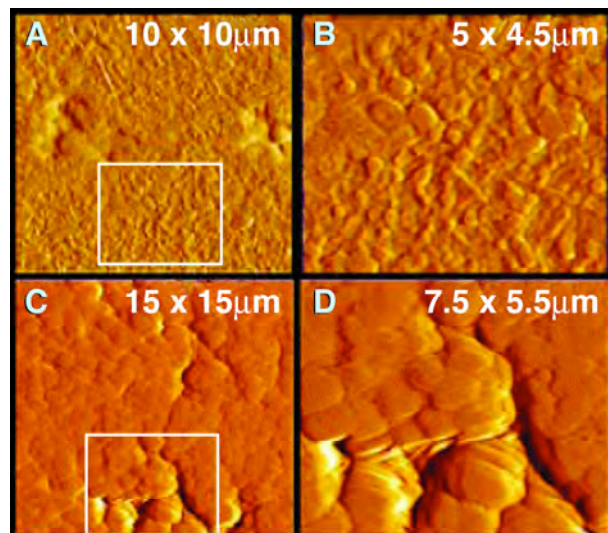


Figure 3. AFM images of volcanic tuff matrix after subjected to dissolution test—the matrix compared to the phenocryst.

appears that a secondary sodium uranyl carbonate mineral forms a continuous film across the  $\text{UO}_2$  surface. We are laboring to determine if this result is repeatable and to identify the film on the  $\text{UO}_2$  surface. We have a pending manuscript in *Journal of Nuclear Materials* that includes these results.

Transport and reaction mechanisms from  $\text{UO}_2$  into volcanic tuff that affect the entire suite of radioactive elements are being determined in detail. If it can be shown that important radioactive elements are less mobile than presently assumed, and that aqueous corrosion rates of SNF (presently assumed to be at the forward rate of reaction) are far slower than current models imply, more realistic source-term and attenuation values can be utilized in repository performance assessments. In addition, a decision to utilize less exotic and expensive engineered barriers, with potential savings of hundreds of millions of dollars, may be supported by newer, more meaningful experimental strategies.



# Surface Charge and Radionuclide Adsorption Characteristics of U(IV,VI) Oxyhydroxides at 25–150°C

David J. Wesolowski, Laetitia Delmau, Lawrence M. Anovitz, Jorgen Rosenqvist, and Donald A. Palmer  
Oak Ridge National Laboratory (ORNL)

## Research Objectives

Uraninite is the primary spent nuclear fuel (SNF) matrix, and until oxidized, it is the surface most likely to come in contact with aqueous solutions that might mobilize radionuclides. The objectives of this project are to determine, in NaCl brines at 25° to 150°C: (a) the pH and temperature dependencies of the proton-induced surface charge density of  $\text{UO}_2$  (uraninite); and (b) the sorption affinities of actinide and analog ions on uraninite surfaces. This information can be used to develop surface site complexation models to describe ion adsorption on SNF materials under near-field repository conditions.

## Approach

We and our collaborators have pioneered experimental investigations of metal oxide solubility, surface charging and pH-dependent ion adsorption at temperatures ranging from 10° to >250°C, using our unique high-temperature pH-measurement and electrophoresis systems (Wesolowski et al., 2000; Machesky et al., 2001; Zhou et al., 2003; Fedkin et al., 2003). Oxide surfaces are positively charged at pH's below the  $\text{pH}_{\text{pzc}}$  and negatively charged at higher pH. This charge accumulation attracts ions of opposite sign, which adsorb on the surface. We have also developed thermodynamically rigorous surface complexation models (cf. Ridley et al., 2004; 2005) that quantitatively predict the equilibrium adsorption constants of protons, monovalent anions, and mono-, di-, and trivalent cations on metal oxide surfaces to high temperatures. These experimental and modeling approaches enable useful investigation of the sorptive properties of uranium oxide phases found within breached radioactive waste packages at the elevated temperatures predicted in the near-field environment.

## Accomplishments

### Uraninite Surface Charge and Ion Adsorption at Elevated Temperatures

Nearly stoichiometric uraninite ( $\text{UO}_{2.08}$ ) was synthesized by reacting  $^{235}\text{U}$ -depleted  $\text{UO}_3$  in low-density steam at 600°C, with the  $\text{H}_2$  partial pressure fixed within the uraninite stability field by the Mn/MnO buffer sys-

tem, similar to an approach previously used to synthesize pure magnetite (Wesolowski et al., 2000). The point of zero charge of the uraninite powder was determined at 25° and 50°C in 0.1 and 1.0 molal NaCl solutions, using a glass-electrode autotitrator system and data reduction scheme as described by Ridley et al. (2002). The pH of zero net surface charge of this uraninite is shown to be similar to that of rutile ( $\alpha\text{-TiO}_2$ ) over the temperature range studied. Experimental problems were encountered in attempts to

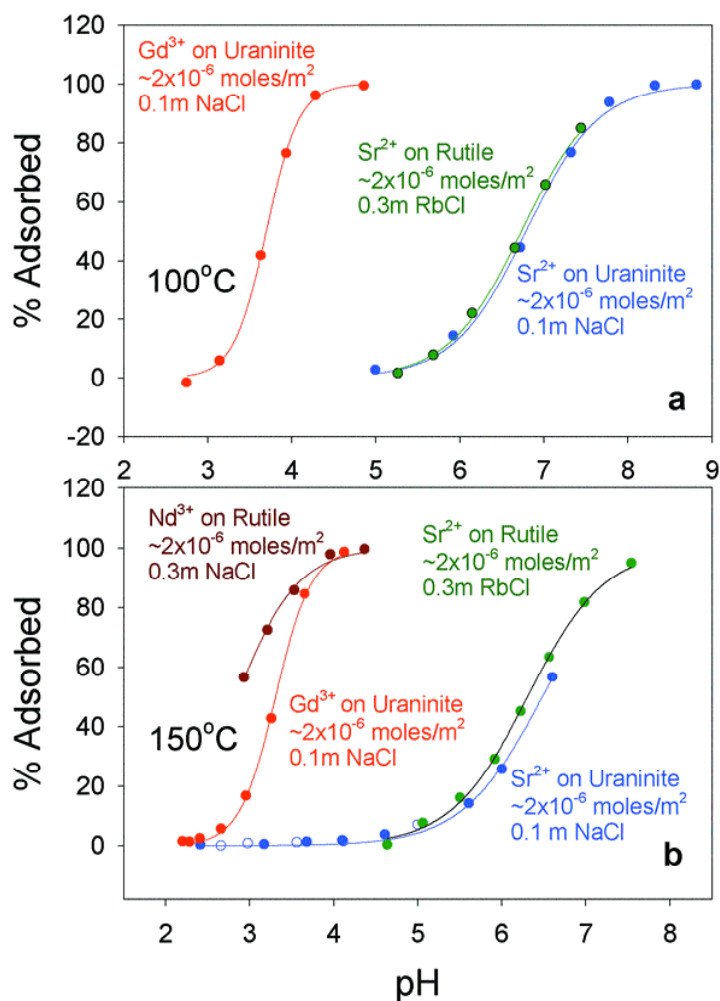


Figure 1. Sorption of  $\text{Sr}^{2+}$  and  $\text{Gd}^{3+}$  on uraninite compared with  $\text{Sr}^{2+}$  and  $\text{Nd}^{3+}$  adsorption on rutile powder surfaces from pH titrations at 100 and 150°C.

extend the  $\text{pH}_{\text{pzc}}$  to higher temperatures in our hydrogen-electrode pH cells, due presumably to protolytic side-reactions associated with  $\text{H}_2$  interaction with the uraninite surface. However, the hydrogen-electrode cells could be used to determine sorption isotherms (Figure 1) for the uptake of nonradioactive analog ions ( $\text{Sr}^{2+}$ ,  $\text{Gd}^{3+}$ ) by uraninite powder surfaces at 100° and 150°C, since these measurements do not require highly-precise proton-balance calculations. As can be seen in Figure 1, the sorption of  $\text{Sr}^{2+}$  and  $\text{Gd}^{3+}$  on uraninite is similar to the sorption of  $\text{Sr}^{2+}$  and  $\text{Nd}^{3+}$  on rutile powder surfaces, at similar surface loadings and ionic strengths in NaCl solutions.

### Actinide and Analog Adsorption on Uraninite at Room Temperature

This series of experiments was designed to measure the adsorption of trace levels ( $<10^{-5}$  molal) of radioactive isotopes of  $\text{Sr}^{2+}$ ,  $\text{Gd}^{3+}$  and  $\text{Am}^{3+}$  onto the same uraninite powder described above, at 25°C in NaCl solutions. As a comparison,  $\text{Gd}^{3+}$  sorption on rutile was also measured. A series of aqueous solutions at constant ionic strength (0.03m, NaCl), with calibrated pHs, and containing a known amount of the sorbing ion of interest, were mixed with a carefully weighed amount of uraninite. Results with  $\text{Sr}^{2+}$  and  $\text{Gd}^{3+}$  indicated that the adsorption only reached 100% when these elements were originally present in very low concentrations. Otherwise, the sorption isotherms had the expected sigmoidal shape (see Figure 1), but with a plateau lower than 100%. Experiments were conducted with different amounts of uraninite and different concentrations of  $\text{Sr}^{2+}$  and  $\text{Gd}^{3+}$ . They all indicated that the uranium oxide surface was saturated at a lower sorbent concentration than expected. Also, the pH at which the adsorption starts appears to be somewhat lower than expected, based on our results obtained using the hydrogen electrode cell. However, the order of the pH values at 50% of adsorption is correct – i.e., 2.83 for  $\text{Gd}^{3+}$  and 3.05 for  $\text{Sr}^{2+}$ .

Carrying out these experiments radiometrically allowed the comparison between a trivalent lanthanide ( $\text{Gd}^{3+}$ ) and a trivalent actinide ( $\text{Am}^{3+}$ ). These experiments were done with these elements at trace level ( $<10^{-5}$  molal). Results are presented in Figure 2. Because of the large amount of information already available for adsorption of cations onto rutile, we carried out a series of experiments

showing the similarities and differences. Figure 3 presents the results obtained with  $\text{Gd}^{3+}$ , showing that uraninite and rutile adsorb gadolinium at somewhat different pH values for the same conditions. While the pH for uraninite is lower in both cases, the difference seems to be less when the cation is initially present at concentrations of approximately  $10^{-3}$  molal.

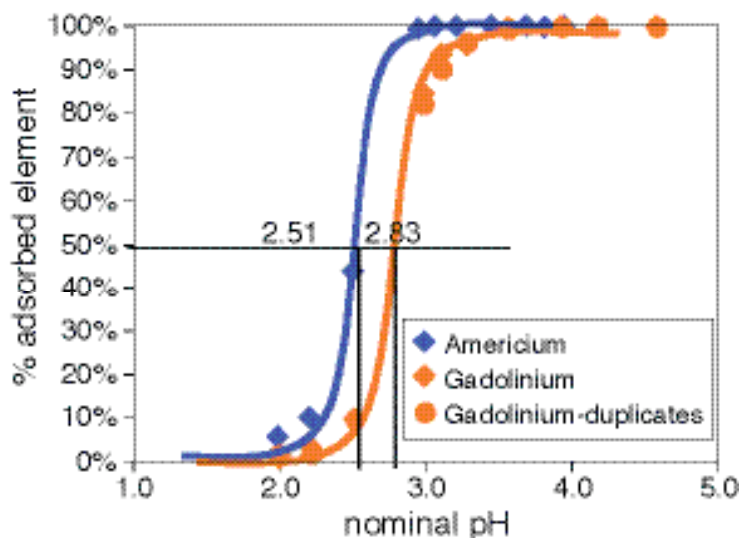


Figure 2. Comparison between Gd and Am adsorption on uranium oxide. Am and Gd are present at trace level, ionic strength of the aqueous phase I = 0.03 m (NaCl).

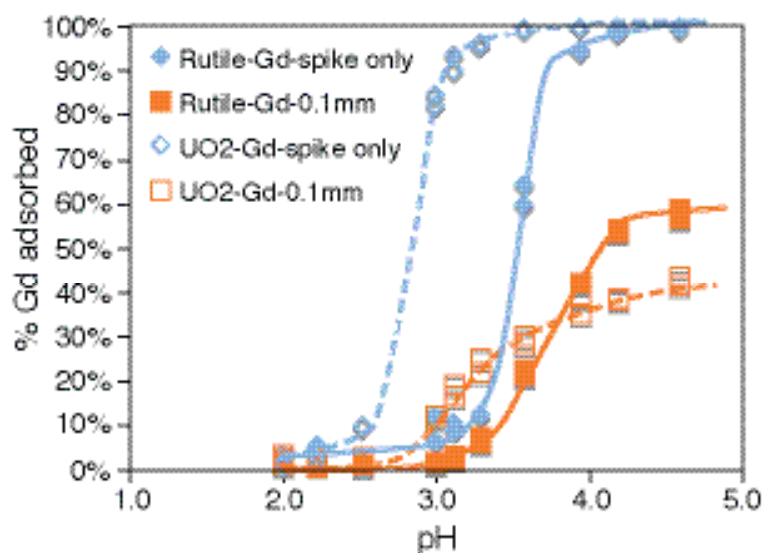


Figure 3. Comparison between  $\text{Gd}^{3+}$  adsorption on uranium oxide and rutile.  $\text{Gd}^{3+}$  is present either at trace level or at a concentration of 0.1 millimolal, ionic strength of the aqueous phase I = 0.03 molal (NaCl).

## Summary

Despite some experimental difficulties, we have observed that the surface charging and ion ( $\text{Sr}^{2+}$ ,  $\text{Gd}^{3+}$ ,  $\text{Am}^{3+}$ ) adsorption characteristics of near-stoichiometric uraninite ( $\text{UO}_{2.08}$ ) are similar to those of rutile ( $\alpha\text{-TiO}_2$ ) in NaCl brines (0.03–1.0 molal) at temperatures of 25° to 150°C. These preliminary results demonstrate that additional studies would be useful in better defining the surface chemistry of uraninite, but that surface charge development and ion sorption characteristics of rutile can probably be used as a surrogate for modeling the interaction of uraninite with dissolved radionuclide cations, until more information is made available on uraninite. This is a very useful finding, since rutile is one of the most widely studied mineral phases, in terms of its surface chemistry and ion adsorption properties, particularly at elevated temperatures in high-chloride brines.

## Related Publications

Fedkin, M.V., X.Y. Zhou, J.D. Kubicki, A.V. Bandura, S.N. Lvov, M.L. Machesky, and D.J. Wesolowski, High temperature microelectrophoresis studies of the rutile/aqueous solution interface. *Langmuir*, 19, 3797–3804, 2003.

Machesky, M.L., D.J. Wesolowski, D.A. Palmer, and M.K. Ridley, On the temperature dependence of

intrinsic surface protonation equilibrium constants: An extension of the revised MUSIC model. *J. Colloid Interface Sci.*, 239, 314–327, 2001.

Ridley, M.K., Machesky, M.L., Palmer, D.A. and Wesolowski, D.J., Potentiometric studies of the rutile-water interface: Hydrogen-electrode concentration-cell versus glass-electrode titrations. *Colloids and Surfaces A*, 204, 295–308, 2002.

Ridley, M.K., Machesky, M.L., Wesolowski, D.J. and Palmer, D.A., Modeling the surface complexation of calcium at the rutile-water interface to 250°C. *Geochim. Cosmochim. Acta*, 68, 239–251, 2004.

Ridley, M.K., M.L. Machesky, D.J. Wesolowski, and D.A. Palmer, Surface complexation of neodymium at the rutile-water interface: A potentiometric and modeling study in NaCl media to 250°C. *Geochim. Cosmochim. Acta*, 69, 63–81, 2005.

Wesolowski, D.J., M.L. Machesky, D.A. Palmer, and L.M. Anovitz, Magnetite surface charge studies to 290°C from in situ pH titrations. *Chemical Geology* 167, 193–229, 2000.

Zhou, X.Y., X.J. Wei, M.V. Fedkin, K.H. Strass, and S.N. Lvov, Zetameter for microelectrophoresis studies of the oxide/water interface at temperatures up to 200°C. *Rev. Scientific Instru.* 74, 2501–2506, 2003.

---

This page intentionally left blank.

## WASTE FORM—WASTE PACKAGE INTERACTIONS IN THE NEAR FIELD

### **In-Package Sequestration of Radionuclides at Yucca Mountain: Waste Package Corrosion Studies Using Small Mockup Experiments**

B. Elizabeth Anderson, Katheryn B. Helean, and Patrick V. Brady, Sandia National Laboratories (SNL); Rodney C. Ewing, University of Michigan

### **In-Package Sequestration of Radionuclides at Yucca Mountain: Neptunium Surface Complexation Subtask**

James Jerden, Argonne National Laboratory (ANL)

### **Uptake of Technetium (Tc) by Iron-Based Materials**

Kenneth Krupka, Christopher F. Brown, Steve M. Heald, H. Todd Schaefer, Bruce W. Arey, and Michelle M. Valenta, Pacific Northwest National Laboratory (PNNL)

---

This page intentionally left blank.



# In-Package Sequestration of Radionuclides at Yucca Mountain: Waste Package Corrosion Studies Using Small Mockup Experiments

B. Elizabeth Anderson<sup>1</sup>, Kathryn B. Helean<sup>1</sup>, Patrick V. Brady<sup>1</sup>, and Rodney C. Ewing<sup>2</sup>

<sup>1</sup>Sandia National Laboratories (SNL) | <sup>2</sup>University of Michigan

## Research Objectives

Knowledge of the corrosion processes and products of spent nuclear fuel (SNF) in a geological repository allows a more thorough understanding of the subsequent release of radionuclides. Corroding A516 steel within the proposed waste packages may create locally reducing conditions, thus changing the likely corrosion products of  $\text{UO}_2$ , which forms the bulk of SNF. Also, ferrous iron,  $\text{Fe}^{2+}$ , has been shown to reduce  $\text{UO}_2^{2+}$  to  $\text{UO}_2(\text{s})$ , and some ferrous iron-bearing ion-exchange materials absorb radionuclides and heavy metal. Therefore, high electron availability of the steel corrosion products may inhibit corrosion of  $\text{UO}_2$  and reduce and immobilize problematic species such as  $\text{TcO}_4^-$ ,  $\text{NpO}_2^+$ , and  $\text{UO}_2^{2+}$ . The focus of this study is on the nature of Yucca Mountain-relevant steel corrosion products and their effects on local redox state, SNF corrosion, and radionuclide transport.

## Approach

Six small-scale (~1:40 by length) waste package mockups were constructed using 316 stainless steel, the same material as the inner layer of the proposed Yucca Mountain waste packages. Twenty-five 1 x 10 x 0.2 cm strips of A-516 carbon steel, the material used as guides for SNF inside proposed waste packages at Yucca Mountain, were inserted into each waste package. The mockups differed with respect to water input, access to the atmosphere, and temperature, and two of the mockups also contain 0.1 g powdered  $\text{UO}_2$ . Simulated Yucca Mountain process water (YMPW) was injected into the mockups at a rate of 200  $\mu\text{L}$  per day five days a week, using a calibrated needle syringe. The YMPW consists of 50 mg/L silica as sodium metasilicate (and thus, 38.3 mg/L Na), enough HCl to lower the pH to 7.6, and an excess of powdered calcite. The solution was allowed to equilibrate with the atmosphere for an additional five days. The final pH stabilized at 7.5.

Characterization of corrosion products was by x-ray powder diffraction (XRD), scanning electron microscopy (SEM), and, where appropriate, transmission electron microscopy (TEM), x-ray photoelectron spectroscopy (XPS), and sequential leaching for uranium. The ferrous to ferric iron ratio ( $\text{Fe}^{2+}/\text{Fe}^{3+}$ ) was measured in the effluent

using colorimetry and in the solids using either a standard  $\text{K}_2\text{Cr}_2\text{O}_7$  titration (Sandia ASTM D 3872-86) or acid digestion followed by colorimetry. These ratios and measured water pH were input into the geochemical modeling program EQ3/6 to estimate the oxygen fugacity inside of the waste package.

## Accomplishments

Although the generally poor crystallinity of the corrosion products precludes reliable quantitative analysis by XRD, major phases were identified in the high-temperature scoping study at 30 and 90 days and in two significantly corroded  $\text{UO}_2$ -free mockups. The waste package exposed only to humid air showed no significant corrosion after one year. Magnetite,  $\text{Fe}_3\text{O}_4$ , possibly along with the structurally identical but fully oxidized maghemite, was the major corrosion phase present in all cases. The presence of  $\text{Fe}^{2+}$  was confirmed by wet chemistry. Hematite was identified as a minor phase in the high-temperature scoping study at both 30 and 90 days, and in the 90-day sample a diffraction peak corresponding to a d-spacing of 12.87 Å was also evident in x-ray data from the solids. This phase could not be identified from a single XRD peak. However, subsequent SEM with energy dispersive spectroscopy (EDS) on a polished cross section indicates a “fibrous” phase into which Cl is preferentially incorporated, and micrographs suggest a layered structure (Figure 1). A backscattered electron micrograph shows oxidation “blisters” pock-marking the steel surface and clear zones that can be described as anodic (oxidizing) and cathodic (reducing). Solids analysis from the one-year tests are ongoing, but show similar results.

The effluent analysis from both mockup experiments indicate that *in situ*  $\text{O}_2$  fugacities were of the order  $10^{-36}$  bar. It is important to note that even after a year of exposure to moist air, the majority of the low alloy steel remained uncorroded and shiny, indicating that anaerobic corrosion is significantly slower than oxidative corrosion processes.

The presence of reduced iron in magnetite in waste package mockup studies suggests not only that radionuclide-sorbing minerals will be present in Yucca Mountain waste packages, but also that the in-package environment will be reducing. This is confirmed by the effluent analyses that

constrain  $fO_2$  to  $10^{-36}$  bar, well below ambient. Hematite is also expected to be present in significant amounts at elevated temperatures, which may be the case at the repository, and possibly also a layered chloride phase. If this layered phase does form in a real waste package, it could be important for the uptake of radionuclides and in maintaining reducing conditions, particularly if it is related to another layered phase, green rust. Ongoing experiments with  $UO_2$  will provide further insight into the effects of steel corrosion on radionuclide transport. This study suggests that steel and its corrosion products may retard transport of U and other radionuclides in Yucca Mountain waste packages and the environment.

## Publications

Husler, J.W., B.E. Anderson, K.B. Helean, C.R. Bryan, and P.V. Brady, Ferrozine micro-method for the determination of iron in solids. In preparation, 2007.  
Anderson, B.E., K.B. Helean, J.W. Husler, C.R. Bryan, P.V. Brady and R.C. Ewing, Waste package corrosion studies using small mockup experiments. In preparation, 2007.

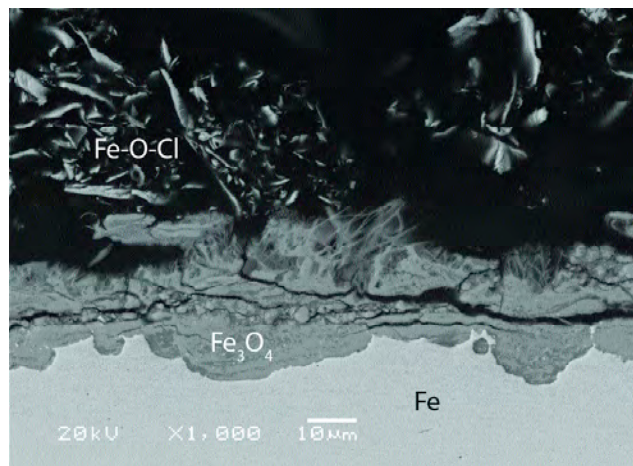


Figure 1. Backscattered electron micrograph of corroded steel in the heated mockup after ninety days. The loosely consolidated fibers, which are consistent with the layered structure noted in the XRD data, are enriched with chlorine relative to the other corrosion products.

# In-Package Sequestration of Radionuclides at Yucca Mountain: Neptunium Surface Complexation Subtask

James Jerden

Argonne National Laboratory (ANL)

## Research Objectives

This subtask of the Source Term In-Package Sequestration Project had three main objectives: (1) to quantify the distribution of neptunium between common iron oxide minerals [goethite ( $\alpha\text{-FeOOH}$ ), magnetite ( $\text{Fe}_3\text{O}_4$ )] and aqueous solutions as a function of pH, ionic strength, sorbent/sorbate ratio, reaction time (aging), and solution composition; (2) to use synchrotron based x-ray absorption and fluorescence techniques to obtain molecular-scale information (e.g., local coordination environment, oxidation state) on how neptunium is bound to mineral surfaces; and (3) to quantify the reversibility of neptunium sorption onto the iron oxide mineral surfaces. Goethite and magnetite were chosen as sorbents for this study, because they are anticipated to be important corrosion phases within a breached waste package containing steel.

## Approach

The sorption experiments were performed in stirred batch reaction vessels. Neptunium-bearing solutions with known pH, ionic strength, and composition were reacted with powders of goethite or magnetite for specific time intervals. Uranium was added to some tests to study possible competition between uranium and neptunium for sorption sites. The vessels were constantly stirred, and contained air filled headspaces that were regularly replenished by opening the vessel and blowing clean air into the bottle before recapping. All solution concentrations were measured by inductively coupled plasma mass spectrometry (ICPMS). Sorbate solutions consisted of either 0.001 molar sodium chloride or a simulated Yucca Mountain pore water. The simulated pore water was a calcite equilibrated, sodium silicate solution containing:  $5.0\text{E-}3$  molal  $\text{Na}^+$ ,  $8.0\text{E-}4$  molal  $\text{SiO}_2(\text{aq})$ ,  $5.0\text{E-}4$  molal  $\text{Ca}^{2+}$ , and approximately  $6.0\text{E-}3$  molal  $\text{HCO}_3^- + \text{CO}_3^{2-}$ . Neptunium-loaded goethite sorbent samples from selected tests were resuspended in the simulated pore-water solution for 21 days to measure neptunium desorption. The pH of the desorption tests was adjusted to approximately 5.8 using HCl. Selected sorbent samples were analyzed by x-ray absorption spectroscopy (XAS) to determine the oxidation state and coordination environment of the

adsorbed neptunium. Extended x-ray absorption fine structure (EXAFS) spectroscopy and x-ray absorption near-edge structure (XANES) spectroscopy measurements were made at the Materials Research Collaborative Access Team (MRCAT) 10ID beam line at the Argonne National Laboratory Advanced Photon Source (APS).

## Accomplishments

Results from the sorption experiments are shown in Figure 1. Distribution coefficients for neptunium sorption on goethite and magnetite in 0.001 NaCl range from less than 1000 mL/g at low pH to over 10,000 mL/g at pH > 6.5. Distribution coefficients as high as 100,000 mL/g were measured for the sorption test performed in the simulated pore waters. XAS results show that neptunium complexes with the goethite surface as  $\text{Np(V)}$ . The neptunium adsorbed to goethite shows Np-O bond length of approximately 1.8 angstroms, which is representative of the Np-O axial bond in the neptunyl(V) complex. The neptunyl(V) ion is coordinated to 5 or 6 equatorial oxygens with Np-O bond lengths of 2.45 angstroms. The absence of a clearly recognizable Np-Fe interaction for the sodium chloride sorption tests suggests that neptunium in these solutions adsorbs as an outer-sphere complex. XAS results from the calcium-bearing sodium silicate sorption tests show evidence for a neptunyl(V) inner-sphere surface complex with a Np-Fe interaction at 3.5 angstroms and a possible Np-Ca interaction. This possible Np-Ca bond may indicate the presence of neptunium-bearing calcite at the goethite surface. XAS results from the magnetite sorption tests show that both  $\text{Np(IV)}$  and  $\text{Np(V)}$  are present on the mineral surface, indicating that some fraction of the  $\text{Np(V)}$  in solution was reduced to  $\text{Np(IV)}$  by the magnetite. Desorption tests indicate that samples in which neptunium was bound as inner-sphere complexes show significant sorption hysteresis (greater than 90% of sorbed neptunium was not desorbed).

Our results indicate that under certain conditions, neptunium will be sequestered by waste package corrosion products as tightly bound (not readily desorbed) inner-sphere complexes, or by a co-precipitation process involving the incorporation of neptunium into a carbon-

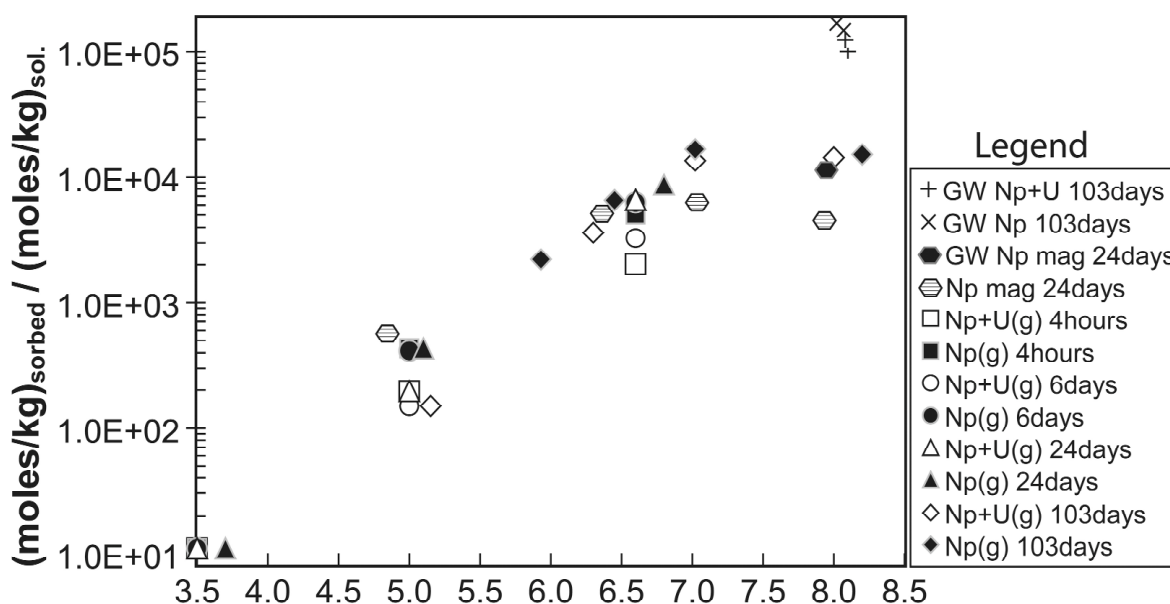


Figure 1. Results from Np sorption tests on goethite showing distribution coefficients for Np sorption (moles of Np adsorbed per kg of sorbent / moles Np per kg of solution in contact with sorbent). The samples labeled GW are from sorption tests performed in simulated groundwater; all other tests were done in  $\sim 0.001$  molal sodium chloride solutions—(g) denotes goethite sorbent, (mag) denotes magnetite sorbent.

ate mineral. The reduction of neptunium on magnetite could potentially catalyze the precipitation of the sparingly soluble neptunium solid  $\text{NpO}_2$ . These results represent an important new data set for optimizing surface complexation models for neptunium sorption.

### Related Publications

Jerden, J.L. Jr., and A.J. Kropf, Surface complexation of neptunium(V) with goethite. In: Scientific Basis

for Nuclear Waste Management XXX, D.S. Dunn, C. Poinssot, and B. Begg, eds. (Mater. Res. Soc. Symp. Proc. 985), Warrendale, PA, 2007.

Jerden, J.L. Jr., J. Kropf, and Y. Tsai, Surface complexation of actinides with iron oxides: implications for radionuclide transport in near-surface aquifers. Eos Trans. AGU, 86(52), Fall Meet. Suppl., Abstract 0800h-H31B-1290, 2005.

# Uptake of Technetium (Tc) by Iron-Based Materials

Kenneth M. Krupka, Christopher F. Brown, Steve M. Heald, H. Todd Schaefer, Bruce W. Arey, and Michelle M. Valenta  
Pacific Northwest National Laboratory (PNNL)

## Research Objectives

This work focuses on characterizing the surface-mediated, heterogeneous reduction/sorption reactions that affect the sequestration of  $^{99}\text{Tc}$  by Fe oxide/hydroxide solids, which precipitate during corrosion of Fe-based materials used in the waste package, such as A 516 carbon steel used in the fuel basket.

## Approach

Batch reaction experiments were used to examine the sorption of dissolved pertechnetate [ $\text{Tc(VII)}$ ] on Fe oxide/hydroxide solids that precipitate during the corrosion of A 516 carbon steel coupons reacted with  $^{99}\text{Tc(VII)}$  [0 (blank), 0.001, 0.1, and 1.0 mmol/L] spiked simulated Yucca Mountain pore water or dilute water (i.e., undersaturated with respect to carbonate). Test vials were sacrificed and sampled at various time points. The resulting solutions were analyzed potentiometrically for pH and by inductively coupled plasma-optical emission spectroscopy (ICP-OES) for the concentrations of major cations and some trace metals. Concentrations of other trace metals and  $^{99}\text{Tc}$  were measured by inductively coupled plasma-mass spectrometry (ICP-MS). Bulk x-ray diffraction (XRD) and scanning electron microscopy (SEM), in conjunction with energy dispersive spectroscopy (EDS), were used to characterize the unreacted and corroded steel coupons and Fe corrosion products, as well as to determine the location of sorbed  $^{99}\text{Tc}$ . Synchrotron-based x-ray analyses, including x-ray microfluorescence ( $\mu\text{XRF}$ ), x-ray absorption near-edge structure (XANES), extended x-ray absorption fine structure (EXAFS), and x-ray microdiffraction ( $\mu\text{XRD}$ ), were used to determine the speciation and redox state of  $^{99}\text{Tc}$  incorporated Fe oxides present on the corroded carbon steel coupons.

## Accomplishments

Results of the  $^{99}\text{Tc}$  studies suggest that  $^{99}\text{Tc}$  would sorb during the formation of steel corrosion products, and would, during this process, be reduced from  $^{99}\text{Tc(VII)}$  to the sparingly soluble  $^{99}\text{Tc(IV)}$  oxidation state. As a result of this surface-mediated, heterogeneous reduction/sorption process, the inventory of  $^{99}\text{Tc}$  released from breached waste packages would be expected to be lower than what

is now conservatively estimated.

Earlier results from similar batch reaction experiments and characterization studies conducted with dissolved permanganate [ $\text{Re(VII)}$ ], as a surrogate for  $^{99}\text{Tc(VII)}$ , are presented in Krupka et al. (2006a,b). Although the Re experiments also demonstrated that Re would sorb with Fe oxides/hydroxides that precipitate during the corrosion of steel, the XANES and EXAFS analyses indicated, unlike the results from the  $^{99}\text{Tc}$  studies, that Re was not reduced from the +7 to the +4 oxidation state during this reaction, as originally expected (Krupka et al., 2006a,b). The results from the Re and  $^{99}\text{Tc}$  studies suggest that the standard potential for the  $\text{Re(VII)}/\text{Re(IV)}$  redox couple may be significantly lower than that for the  $^{99}\text{Tc(VII)}/^{99}\text{Tc(IV)}$  couple. Thus, Re may not be an adequate surrogate for studying the geochemical behavior of  $^{99}\text{Tc}$  at environmentally relevant reducing conditions.

The solution analyses from the  $^{99}\text{Tc}$  experiments and direct characterization of the steel coupons contacted by both  $^{99}\text{Tc}$ -spiked solution matrices, using SEM/EDS and synchrotron-based x-ray analyses, confirmed the uptake of  $^{99}\text{Tc(VII)}$  during the formation of steel corrosion products. Less corrosion had occurred in the experiments spiked with  $^{99}\text{Tc(VII)}$  compared to those spiked with  $\text{Re(VII)}$ . The extent of corrosion in the  $^{99}\text{Tc(VII)}$  experiments also decreased with increasing concentrations of dissolved  $^{99}\text{Tc(VII)}$ , especially at 1.0 mmol/L  $^{99}\text{Tc(VII)}$ . These results are consistent with results of other studies that show pertechnetate [ $^{99}\text{Tc(VII)}$ ] to be effective at inhibiting the corrosion of iron and steel (Cartledge, 1966). Additionally, the amount of corrosion on the coupons reacted with simulated pore water versus those reacted with dilute water was considerably less after 175 days of reaction time. XRD results for the corroded steel coupons and the filter samples showed that the corrosion products consisted primarily of magnetite ( $\text{Fe}_3\text{O}_4$ ) and lepidocrocite [ $\gamma\text{-FeO(OH)}$ ], sometimes goethite [ $\alpha\text{-FeO(OH)}$ ], and possibly maghemite ( $\gamma\text{-Fe}_2\text{O}_3$ ). SEM/EDS analyses of the corrosion products on the reacted coupons revealed the presence of  $^{99}\text{Tc}$  in the corrosion product (Figure 1). Because the reacted coupons were rinsed several times with their respective  $^{99}\text{Tc}$  free starting solutions prior to storage and solid-phase characterization, the  $^{99}\text{Tc}$  associated with the corrosion products is



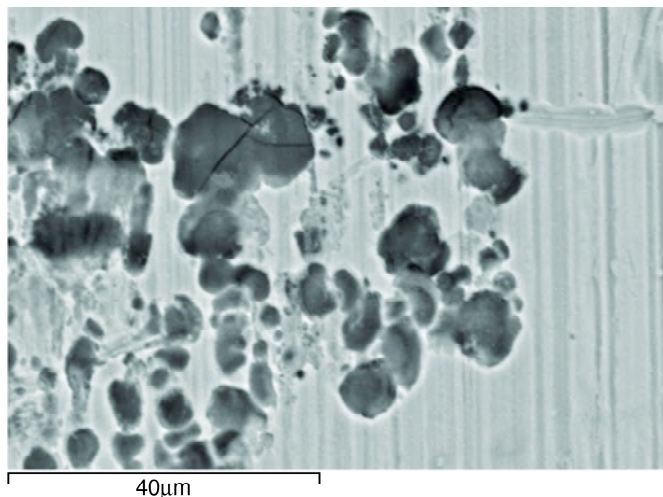


Figure 1. SEM micrograph of typical corrosion pits (dark areas) that formed after 175 days on the A 516 carbon steel coupons reacted in 0.1 mmol/L  $^{99}\text{Tc(VII)}$ -spiked simulated pore water. (EDS identified the presence of Tc in these corrosion pits.)

currently assumed to be co-precipitated with the corrosion product, rather than surface adsorbed. XANES analyses of  $^{99}\text{Tc}$  present on the reacted coupons show that >80% of the sorbed  $^{99}\text{Tc}$  was reduced from the +7 to +4 oxidation state upon incorporation into the Fe corrosion products (Figure 2). The EXAFS data were fit by a

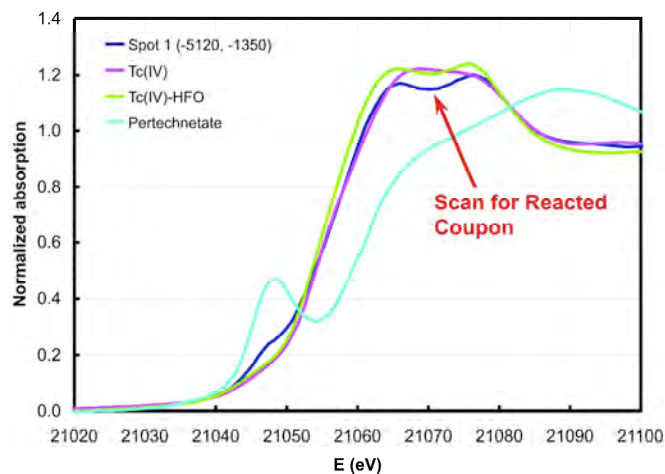


Figure 2.  $^{99}\text{Tc}$  near edge data (dark blue) for a typical spot on corroded coupon reacted in dilute water spiked with 0.1-mmol/L dissolved  $^{99}\text{Tc(VII)}$  compared to spectra for  $^{99}\text{Tc(VII)}$  (light blue) and  $^{99}\text{Tc(IV)}$  (green and pink spectra) standards.

linear combination of the spectra for  $^{99}\text{TcVIIIO}_4^-$  and  $^{99}\text{TcIV-HFO}$  (amorphous hydrous Fe(III) oxide) standards. A preliminary evaluation indicates that the EXAFS had a better fit using the  $^{99}\text{Tc-HFO}$  standard (Zachara et al., 2007) for  $^{99}\text{Tc(IV)}$  rather than hydrated  $^{99}\text{TcIVO}_2$  solid. These results indicate that the sorbed  $^{99}\text{Tc(IV)}$  is in an octahedral environment, sharing an edge with a single neighboring Fe-O octahedron.

The Pacific Northwest National Laboratory is operated by Battelle for the U.S. Department of Energy under Contract DE-AC05-76RLO 1830. The synchrotron-based x-ray analyses were completed at the Advanced Photon Source (APS) beamlines 20 BM and 20 ID (PNC-CAT) at the Argonne National Laboratory. Use of APS is supported by the DOE Office of Science, Office of Basic Energy Sciences, under Contract No. W-31-109-Eng-38.

## References

- Cartledge, G. H., The passivation of iron in the presence of pertechnetate and chromate ions. *Journal of the Electrochemical Society*, 113, 328–333, 1966.
- Krupka, K.M., C.F. Brown, H.T. Schaef, S.M. Heald, M.M. Valenta, and B.W. Arey, Rhenium uptake as analogue for  $^{99}\text{Tc}$  by steel corrosion products. In: *Proceedings of the 11th International High-Level Radioactive Waste Management Conference (IHLR-WM)*, April 30–May 4, 2006, Las Vegas, pp. 905–912, American Nuclear Society, La Grange Park, IL, 2006a.
- Krupka, K.M., C.F. Brown, M.M. Valenta, H.T. Schaef, and B.W. Arey, Uptake of technetium (Tc) by iron-based materials. In: *Office of Science and Technology and International (OST&I) Annual Report 2005*, pp. 43–44, DOE/RW-0581, U.S. Department of Energy, Office of Civilian Radioactive Waste Management, Washington, DC, 2006b.
- Zachara, J.M., S.M. Heald, B.-H. Jeon, R.K. Kukkadapu, C. Liu, J.P. McKinley, A.C. Dohnalkova, and D.A. Moore, Reduction of pertechnetate [ $\text{Tc(VII)}$ ] by aqueous Fe(II) and the nature of solid phase redox products. *Geochimica et Cosmochimica Acta*, 71, 2137–2157, 2007.

# INTEGRATION OF IN-PACKAGE CHEMICAL AND PHYSICAL PROCESSES

**Computational Studies on the Corrosion of Spent Nuclear Fuel and the Adsorption and Incorporation of Radioactive Elements into Mineral Phases**  
Udo Becker, University of Michigan

**A Model for Radionuclide Release from Spent Nuclear Fuel**  
Carl I. Steefel, John Apps, Nicolas Spycher, and Eric Sonnenthal, Lawrence Berkeley National Laboratory (LBNL)

---

This page intentionally left blank.

# Computational Studies on the Corrosion of Spent Nuclear Fuel and the Adsorption and Incorporation of Radioactive Elements into Mineral Phases

Udo Becker

University of Michigan

## Research Objectives

Reaction mechanisms and the thermodynamics of incorporating radioactive elements on minerals and secondary phases during the alteration of waste products often cannot be adequately investigated using experimental or field approaches. However, quantum mechanical computational approaches can often help in determining reaction pathways, as well as the thermodynamics and kinetics of corrosion processes and mobilization (and re-immobilization) of radioactive elements in the environment of nuclear waste repositories. Computational approaches allow us to study the oxidation mechanism of spent nuclear fuel (SNF) and the role of water and temperature in the corrosion process. The atomic, electronic, and spin structure of the bulk material and specific surfaces are evaluated, and the thermodynamics of the adsorption of radioactive complexes are calculated as a function of adsorbing mineral and specific surface features (such as steps, kinks, and defect sites). In all of these reactions, electron transfer and, thus, potential redox mechanisms are monitored. Finally, computational studies are often the only tool that can investigate whether radioactive elements can be incorporated into mineral phases or corrosion products. Structural changes can be analyzed together with the energy of substitution, which is an important measure of the amount and long-term fate of radionuclides in their host phases.

## Approach

At present, we have three graduate students involved in these projects: Frances N. Skomurski (OCRWM Fellowship), Lindsay Shuller (OCRWM Fellowship), and Elizabeth Anderson (OCRWM Fellowship; NSF Fellowship). In our research group, we have focused our efforts in three research areas: (1) The corrosion of  $\text{UO}_2$  in dry and wet environments, associated transition states, and their influence on the long-term stability of SNF; (2) the incorporation of Np into  $\text{U}^{6+}$  alteration phases as a possible long-term sink for this radioactive element; and (3) the adsorption and redox behavior of Tc complexes on mineral surfaces.

## Accomplishments

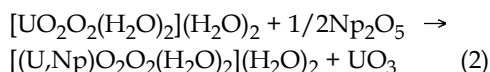
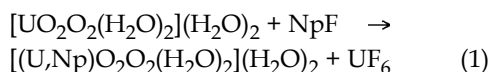
### The Corrosion of $\text{UO}_2$

The initial corrosion of  $\text{UO}_2$  was studied computationally

in dry and wet conditions. While water makes adsorption of oxygen thermodynamically more stable, more important is its influence on the energy lowering of activated complexes upon  $\text{O}_2$  approach. Water dramatically increases the adsorption kinetics from ~1000 years for the oxidation of one monolayer of  $\text{UO}_2$  in dry conditions to immediate oxidation of  $\text{UO}_2$  in a wet atmosphere.

### Np Incorporation into $\text{U}^{6+}$ Alteration Phases

Understanding the behavior of Np is important, because Np is a potential contributor to long-term dose due to the half-life of Np-237 of ~2.1 million years, and because  $\text{Np}^{5+}$  is mobile as neptunyl complexes. This study uses quantum-mechanical calculations to determine the most energetically favorable Np-incorporation mechanism into studtite,  $[\text{UO}_2\text{O}_2(\text{H}_2\text{O})_2](\text{H}_2\text{O})_2$ , and boltwoodite,  $\text{HK}(\text{UO}_2)(\text{SiO}_4)(\text{H}_2\text{O})_{1.5}$ . For studtite, we compare  $\text{Np}^{5+}$ -incorporation (Equation 1; here  $\text{Np}^{5+} \leftrightarrow \text{U}^{6+}$  substitution is charge-balanced by the addition of  $\text{H}^+$ ) to  $\text{Np}^{6+}$ -incorporation (Equation 2).



While Equation (1) preserves oxidation states of all elements and results in a low substitution energy (0.93 eV), the hexafluoride reference phases are not expected to play a major role in a repository environment. Equation (2) requires the correct modeling of spin ordering in  $\text{Np}_2\text{O}_5$ . In addition to the mechanism in Equations 1+2,  $\text{Np}^{5+}$  incorporation has been evaluated, requiring optimization of additional  $\text{H}^+$  ions in different locations. For this latter case, the lowest incorporation energy found so far is 4.57 eV, which is too high for studtite to be considered a major Np sink.

Boltwoodite, a uranyl sheet silicate with  $\text{Na}^+/\text{K}^+$  ( $+\text{H}_2\text{O}$ ) interlayer cations, is a common alteration phase observed in SNF dissolution studies.  $\text{Np}^{5+}$  incorporation for  $\text{U}^{6+}$  was tested, and the system was charge-balanced by adding  $\text{H}^+$  (Figure 1) in different locations, by replacing  $\text{K}^+$  in the

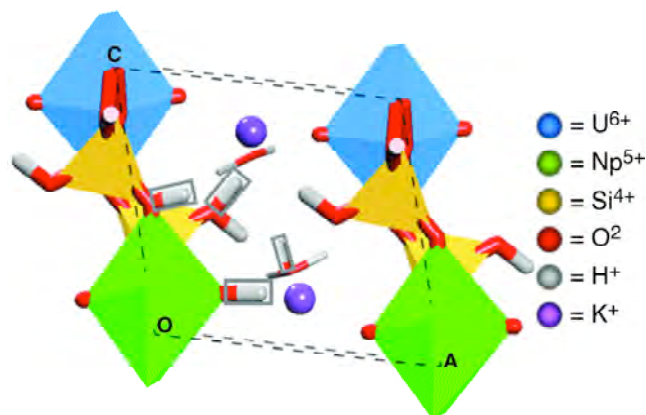


Figure 1.  $\text{Np}^{5+}$  incorporated into the boltwoodite structure with all the possible  $\text{H}^+$  positions labeled with a box around the  $\text{H}^+$  atom.

interlayer by  $\text{Ca}^{2+}$ , or  $\text{Si}^{4+}$  by  $\text{P}^{5+}$ . The first two substitution mechanisms result in substitution energies of  $\sim 1.4$  eV. Due to the unit cell size of the reference phases (feldspars), a mixture of quantum mechanical (uranyl phases) and experimental thermodynamic data (feldspars) were used for these calculations.

### Tc and Re Adsorption/Reduction onto Different Mineral Phases

Technetium is of interest because its radioactivity and high mobility as pertechnetate ( $\text{TcO}_4^-$ ) suggest it being a major contributor to long-term dose on release from a nuclear waste repository.  $\text{ReO}_4^-$  is often used as a chemical analogue for  $\text{TcO}_4^-$ , which is justified by the elements' similar radii and major oxidation states of +7 and +4, as well as their similar ranges over Eh-pH space of  $\text{TcO}_4^-$  and  $\text{ReO}_4^-$ . However, this analogy may fail in a variety of conditions—conditions being tested in this study.

A series of batch sorption experiments allows a more direct comparison between the elements adsorbed to a suite of nine redox-sensitive materials: hematite, galena, pyrite, goethite, magnetite,  $\text{Fe}^0$ , hydroxyapatite doped with 10% Fe, sphalerite, and pyrrhotite. Relative adsorption are compared by measuring the remaining  $\text{ReO}_4^-$  or  $\text{TcO}_4^-$  in solution and oxidation states of Re or Tc in the solids. Batch experiments performed using Re in air resulted in measurable uptake only by Fe.

As a complement to these tests, optimized geometries, adsorption energies, and electronic structures of Tc and Re complexes on galena clusters are calculated quantum-mechanically, including changes in hydration energies. These calculations show that the adsorption of  $\text{TcO}_4^-$  to a galena terrace is similar to that of  $\text{ReO}_4^-$  in both energy and geometry. Two potentially stable geometries were found for adsorption to step edges (Figure 2). For the second configuration, we observe a reduction of the anions from total charge of -1 to -2, indicating a transfer of one electron from the galena cluster to pertechnetate or perrhenate. This position is favorable for  $\text{TcO}_4^-$  but unfavorable for  $\text{ReO}_4^-$ , suggesting that  $\text{TcO}_4^-$  will be reduced by galena step edges, but  $\text{ReO}_4^-$  will not.

### References

- Anderson, B.E., U. Becker, K.B. Helean, and R.C. Ewing, Perrhenate and pertechnetate behavior on iron and sulfur-bearing compounds. Proceedings of the Materials Research Society, 985 (in press), D.S. Dunn, C. Poinssot, and B. Begg, eds., 2007.
- Shuller, L.C., R.C. Ewing and U. Becker, Np-incorporation into uranyl phases: A quantum-mechanical approach. Proceedings of the Materials Research Society, 985 (in press), D.S. Dunn, C. Poinssot, and B. Begg, eds., 2007.
- Skomurski, F.N., R.C. Ewing, A.L. Rohl, J.D. Gale, and U. Becker, Quantum mechanical vs. empirical potential modeling of uranium dioxide ( $\text{UO}_2$ ) surfaces: (111), (110), and (100). American Mineralogist, 91, 1761-1772, 2006.
- Skomurski, F.N., L.C. Shuller, R.C. Ewing, and U. Becker, The corrosion of  $\text{UO}_2$  versus  $\text{ThO}_2$  and the role of electron transfer. Journal of Nuclear Materials (submitted), 2007.
- Skomurski, F.N., U. Becker, and R.C. Ewing, Computational investigation of the formation of hyperstoichiometric uranium dioxide ( $\text{UO}_{2+x}$ ). Proceedings of the Materials Research Society, 985 (in press), D.S. Dunn, C. Poinssot, and B. Begg, eds., 2007.

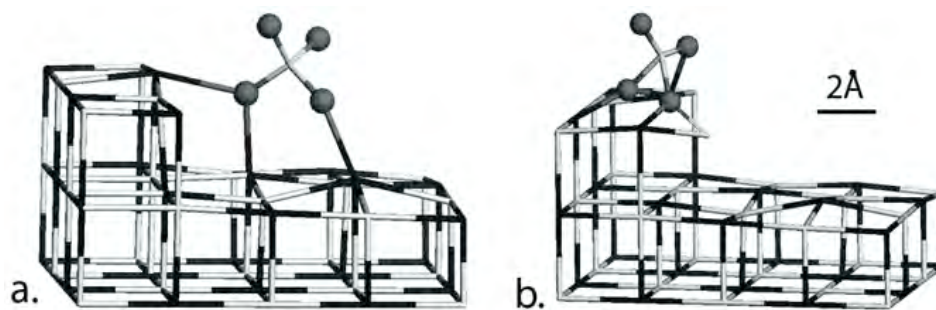


Figure 2. Two possible final positions for  $\text{TcO}_4^-$  and  $\text{ReO}_4^-$  are a galena step edge.  $\text{ReO}_4^-$  prefers position (a), while  $\text{TcO}_4^-$  prefers position (b).



# A Model for Radionuclide Release from Spent Nuclear Fuel

Carl I. Steefel, John Apps, Nicolas Spycher, and Eric Sonnenthal  
Lawrence Berkeley National Laboratory (LBNL)

## Research Objectives

The primary objective of this project was to develop conceptual and numerical models for the prediction of the progressive release of radionuclides from a breached spent nuclear fuel (SNF) container when exposed to seepage and condensate water. The model incorporates the partial oxidation and dissolution of uranium oxide, the precipitation of alteration products, the solid solution substitution and/or adsorption of other actinides (e.g., Np, Pu, and Am) during precipitation of the secondary uranyl phases, radionuclide decay, and alpha particle and gamma radiation on aqueous phase radiolysis. The SNF model is then coupled to thermal-hydrologic-chemical (THC) processes occurring in the near field and drift environment, including  $O_2$  and  $CO_2$  transport and flow and evaporation of seepage water, so as to provide a more realistic description of the total environment within which SNF degradation occurs.

## Approach

The technical approach reflects the current conceptualization of a hypothetical waste package failure, in which ingress of either seepage water or condensate leads to contact with SNF along cladding cracks. The environment may be fully saturated (liquid only), or (more likely) may include a gas phase in which relatively rapid transport of the reactive gas species  $O_2$  and  $CO_2$  can occur. Given this physical setting, the principal focus was on developing a kinetic model for the degradation of U(IV) oxides and the subsequent precipitation of a variety of secondary U(VI) phases according to the Ostwald Rule of Stages (Steefel and Van Cappellen, 1990). The kinetic treatment of the Ostwald Rule of Stages was found to be necessary to capture the rapid release of uranium over short time scales (~1–2 years), followed by a much lower uranium flux as more stable U(VI) oxide phases come to dominate with time (Wronkiewicz et al., 1992).

## Accomplishments

In order to develop a validated numerical model, drip tests conducted at 90°C at Argonne National Laboratory, using uranium oxide wafers (summarized by Wronkiewicz et al., 1992), were simulated (Figure 1).

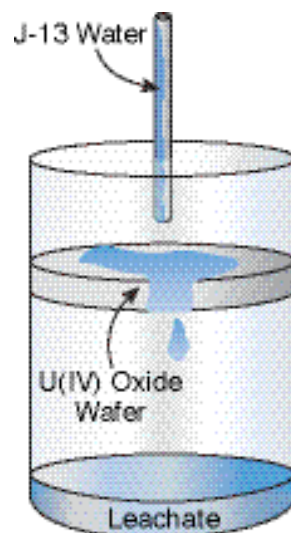


Figure 1. Schematic illustration of Argonne drip tests with U(IV) oxide wafers (Wronkiewicz et al, 1992) that were used for model validation.

The SNCF degradation was considered to take place by the oxidative dissolution of uraninite ( $UO_2$ ) coupled to the precipitation of a soluble precursor-phase schoepite ( $UO_3 \cdot 2H_2O$ ), followed by the growth of more stable becquerelite ( $CaU_6O_{19} \cdot 10H_2O$ ) on the schoepite mineral surface over time. The kinetic rate laws considered include the precipitation of schoepite without a nucleation barrier, according to

$$R_{\text{Schoepite}} = -A_{\text{Schoepite}} k \left( 1 - \frac{Q}{K_{eq}} \right),$$

where  $R$  is the rate,  $A$  is the surface area of the schoepite,  $k$  is the rate constant,  $Q$  is the ion activity product, and  $K_{eq}$  is the equilibrium constant. This is followed by the irreversible growth of becquerelite on the schoepite surface:

$$R_{\text{Becquerelite}} = -A_{\text{Schoepite}} k_{\text{Ostwald}}$$

According to this model, the nucleation of becquerelite is inhibited, and the mineral can only form by effectively cannibalizing the schoepite surface. As the mass of the more-stable-phase becquerelite increases with time, its rate

of formation eventually becomes dominated by growth on its own surface, according to

$$R_{\text{Becquerelite}} = -A_{\text{Becquerelite}} k \left( 1 - \frac{Q}{K_{eq}} \right).$$

Simply decreasing the rate of precipitation of becquerelite by a small amount leads to a very-short-term suppression of its formation (days), while a larger decrease leads to its complete suppression altogether. Simple manipulation of the rate constants for becquerelite therefore cannot produce a match of the observations in the Argonne drip tests, and a kinetic model incorporating the Ostwald Rule of Stages along the lines of the formulation presented above is necessary. The results are summarized in Figure 2.

This Ostwald Rule of Stages model developed here and implemented in the code CrunchFlow captures the approximately 1-year period in which only schoepite was observed in the Argonne drip tests, followed by the appearance of becquerelite and other stable phases in Year 2 and 3. The model also captures the early high flux of uranium, followed by a lower flux once the more stable uranium phases come to dominate the solution chemistry (Figure 3).

## Publications

Steefel, C.I., J.A.Apps, and N. Spycher, A kinetic model for the Ostwald Rule of Stages with application to the oxidative dissolution of uraninite (in preparation).

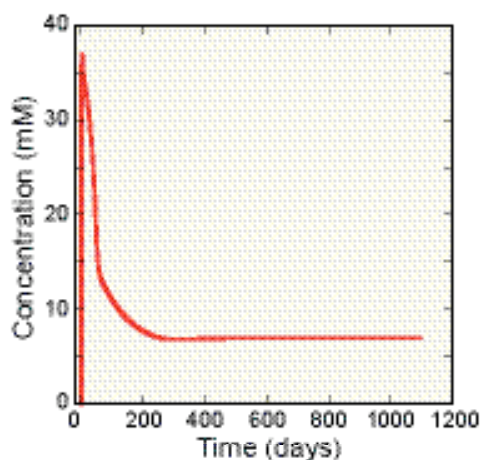


Figure 2. Ostwald Rule of Stages model for the formation of the more stable becquerelite using schoepite as a precursor. With generation of sufficient becquerelite surface area, crystal growth dominates and the solution chemistry is controlled by this phase.

## References

- Steefel, C.I., and P. Van Cappellen, A new kinetic approach to modeling water-rock interaction: The role of nucleation, precursors, and Ostwald ripening. *Geochimica et Cosmochimica Acta*, 54, 2657-2677, 1990.
- Wronkiewicz, D.J., J.K. Bates, T.J. Gerding, E. Veleckis, and B.S. Tani, Uranium release and secondary phase formation during unsaturated testing of  $\text{UO}_2$  at  $90^\circ\text{C}$ . *Journal of Nuclear Materials*, 190, 107-112, 1992.

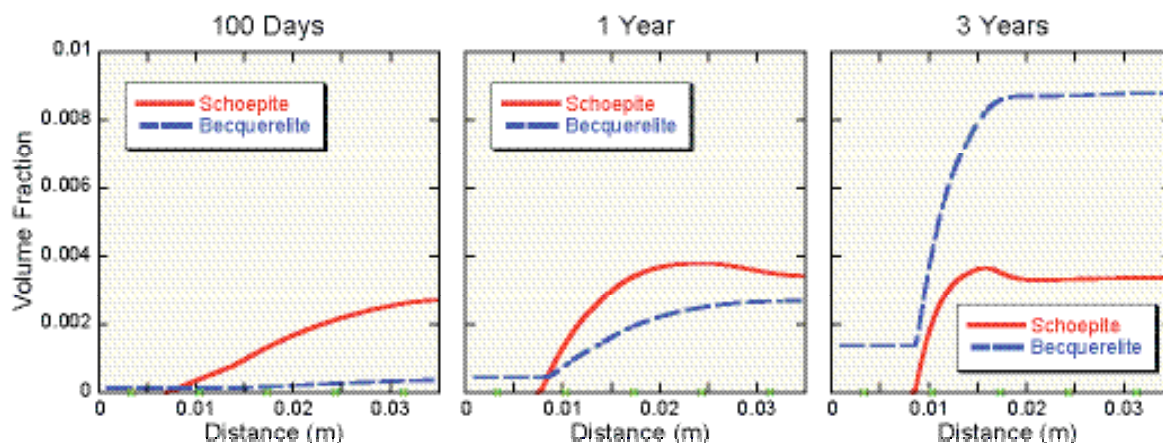
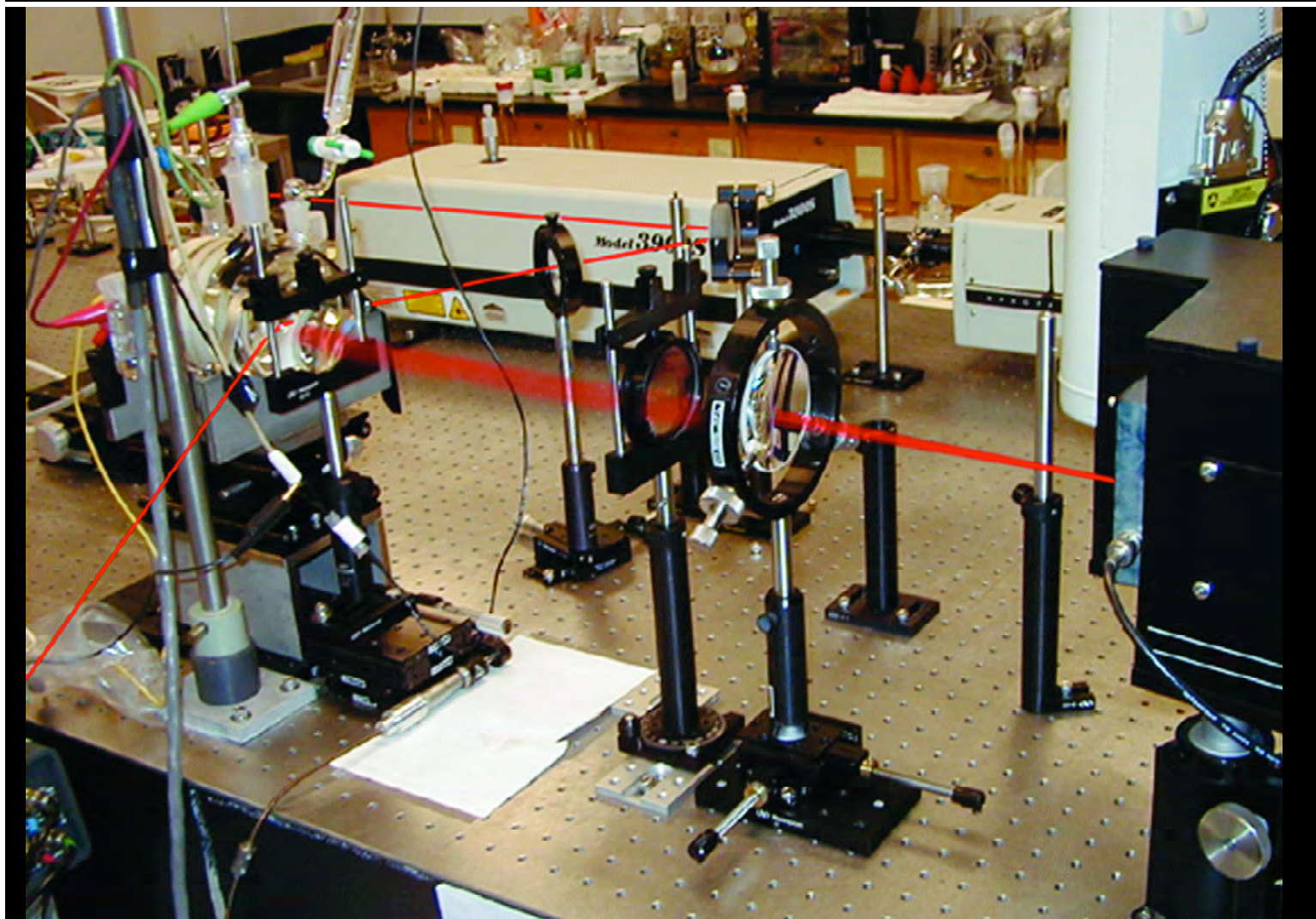


Figure 3. Simulated early release of uranium while schoepite dominates the solution chemistry, followed by a lower uranium flux once the more stable becquerelite develops enough reactive surface area that it can dominate kinetically.

---

This page intentionally left blank.



Surface Enhanced Raman Spectroscopy (SERS) for *insitu*  
analysis of the corrosion protection (passive) film on Ni-Cr-Mo alloys



# MATERIALS PERFORMANCE THRUST

Joe H. Payer, Materials Performance Thrust  
Case Western Reserve University  
Contact: 216.368.4218 | joe.payer@case.edu

## Background

The Yucca Mountain site was recommended by the President to be a geological repository for commercial spent nuclear fuel and high-level radioactive waste. The site was then selected by Congress and signed into law by the President. The multi-barrier approach was adopted for assessing and predicting system behavior, including both natural barriers and engineered barriers. A major component of the long-term strategy for safe disposal of nuclear waste is to completely isolate the radionuclides in waste packages for long times. A further benefit is to greatly retard the egress and transport of radionuclides from penetrated packages. The goal of the Materials Performance Thrust program is to further enhance the understanding of the role of engineered barriers in waste isolation. In addition, the thrust will explore technical enhancements and seek to offer improvements in materials cost and reliability.

## Opportunities for Performance and Technical Advances

The materials used for isolating waste in the proposed repository are an important component of the overall approach to the design of the repository system. The proposed emplacement drift is shown in Figure 1. Opportunities exist to enhance the understanding of material performance and to probe technical enhancements. These enhancements may include optimizing the performance of waste packages and drip shields for increased reliability and cost effectiveness.

Corrosion is a primary determinant of waste package performance at the proposed Yucca Mountain repository and will control the delay time for radionuclide transport from the waste package. Intact waste packages fully contain and isolate radionuclides at the proposed repository. Corrosion is the most likely degradation process that will determine when packages will be penetrated and also the shape, size, and distribution of those penetrations. Thus, corrosion resistance is important to the long-term performance of waste packages. This thrust program strives for increased scientific understanding, enhanced process models, and advanced technologies for long-term corrosion performance. The waste packages are manufactured from highly corrosion-resistant metals, and the surface of these metals is protected by the formation of a self-healing, passive layer. The metals for waste packages and drip shields have excellent corrosion resistance over a wide range of aqueous solution compositions and temperatures. Based upon measurements of corrosion rates of passive metals, if the passive film remains stable, the waste packages can remain

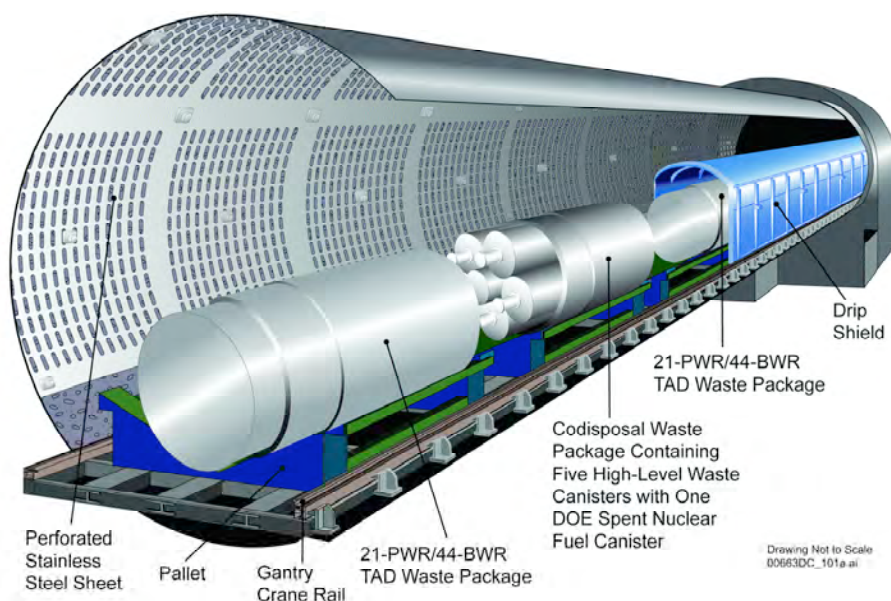


Figure 1. Proposed emplacement drift.



intact with no penetrations resulting from corrosion for durations of tens of thousands and even hundreds of thousands of years.

## Materials Performance Thrust Program Team

A team of experts from universities was formed by the DOE Science and Technology program under a Corrosion Cooperative (CorrCoOp). This team works closely with scientists and engineers at several national laboratories and other participants. The CorrCoOp is based at Case Western Reserve University and includes investigators at Arizona State University, Case Western Reserve University, Ohio State University, Pennsylvania State University, University of California-Berkeley, University of Minnesota, University of Toronto, University of Western Ontario, and University of Virginia. National laboratories that have participated include Argonne National Laboratory (ANL), Lawrence Livermore National Laboratory (LLNL), Lawrence Berkeley National Laboratory (LBNL), Oak Ridge National Laboratory (ORNL) and Pacific Northwest National Laboratory (PNNL). Other participants include Atomic Energy of Canada Limited (AECL) and OLI

Systems Inc. A sampling of the specialized capabilities and facilities is shown in Figure 2.

## Targeted Technical Thrusts

There are three multi-investigator projects within the Materials Performance Thrust. Each of these is a coordinated set of collaborative efforts.

### Corrosion of Metal Surfaces Covered with Particulate and Deposits

The waste packages are supported in air, and they will never be fully immersed in water. Rather, the metal surfaces may be covered with dust, particulate, and moisture from the surrounding rock and humidity. The analysis of corrosion cells under these conditions is a primary objective.

### Evolution of Corrosion Damage by Localized Corrosion

Understanding of localized corrosion processes, and particularly crevice corrosion, is a high priority. The examination of the rate of penetration and extent of corrosion damage by factors that determine localized corrosion over extremely long times is important.

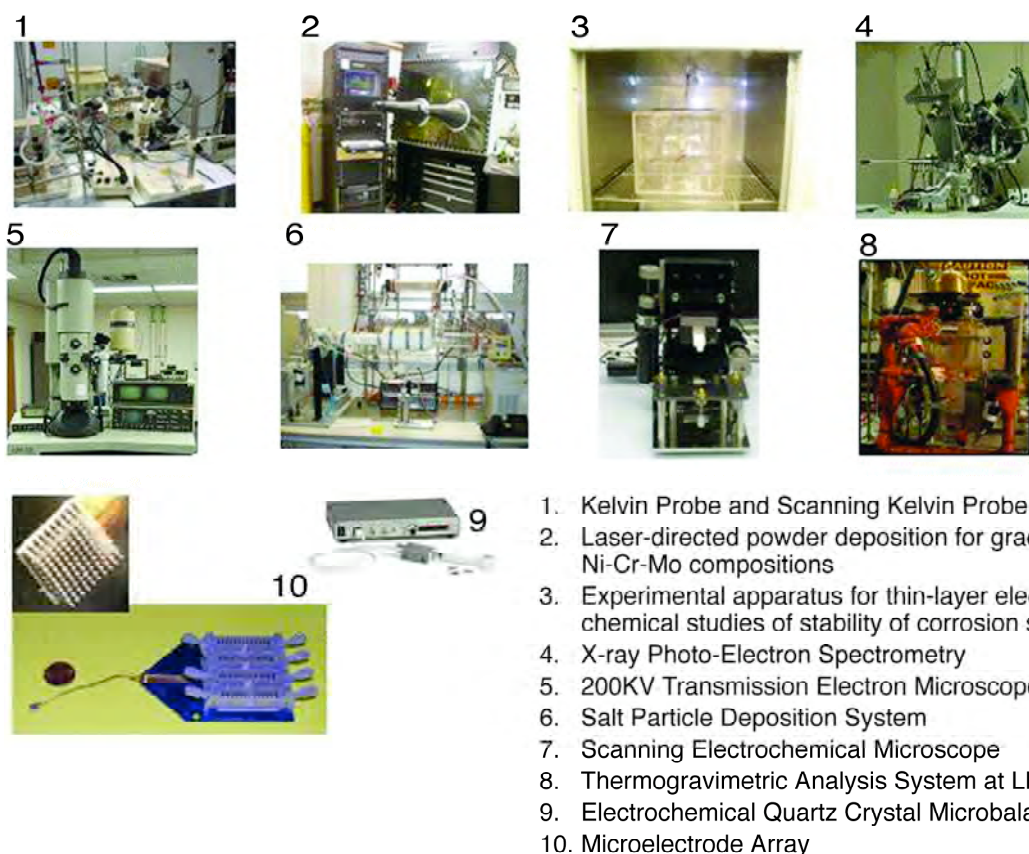


Figure 2. Sampling of the specialized capabilities and facilities of the Corrosion Cooperative.

## Evolution of Moisture Environment on Metal Surfaces

The corrosion performance of a metal is determined by the inherent corrosion resistance of the metal and the corrosivity of the environment to which the metal is exposed. The amount, distribution, and chemical composition of the moisture on waste packages are primary determinants of corrosion performance.

In addition to the multi-investigator projects, there are bridging projects that coordinate and integrate process-modeling activities in the Materials Performance Thrust to those in the Natural Barriers Thrust and the Source Term Thrust. The Materials Performance Thrust has been an incubator for work that transitioned to full development projects under the Advanced Technologies Thrust, e.g., advanced welding techniques and high-performance amorphous metal coatings.

## Corrosion of Metal Surfaces Covered with Particulate and Deposits

The objective of this multi-investigator effort is to determine the corrosion behavior of corrosion-resistant metal surfaces that are covered by thin layers of moisture and moist particulate and deposits. Advanced analytical and computational methods for corrosion processes in thin films, particulates, and deposits are developed. Inputs are generated for advanced, next-generation models and alternate conceptual models, based on less conservative assumptions. Enhanced scientific understanding of chemical, electrochemical, and corrosion processes is provided.

**Targeted thrust objective:** *Develop technical basis for and demonstrate the reduction in passive corrosion rate with time. There is a potential to extend predicted waste package life by 100 to 1,000 times compared to that predicted using a time-invariant rate.*

Highly corrosion-resistant materials are selected for the waste packages and drip shields for the proposed Yucca Mountain repository, i.e., Alloy 22, a nickel-chromium-molybdenum (Ni-Cr-Mo) alloy, and titanium (Ti), respectively. In oxidizing environments that are of interest for the proposed repository, these alloys depend upon the formation and the tenacity of a passive film, i.e., a thin oxide on the metal surface, for their corrosion resistance. Measured corrosion rates for passive metals decrease with time to (on the order of) 0.1 to 0.01 micrometer per year. At these rates, it takes 10,000 to 100,000 years to penetrate 1 mm of metal, and the Alloy 22 outer layer of the waste packages is on the order of 20 mm thick. Thus, accounting for the reduction in passive corrosion rates is important to life prediction.

**Targeted thrust objective:** *Identify corrosion processes for*

*metal covered with particulate and deposits. Where corrosion is based on fully immersed solutions and not corrosion in moist layers of dust/particulate, the fully immersed treatment is conservative in many cases.*

In the proposed repository, metal surfaces will be dry (no corrosion) or exposed to thin layers of moisture and significant moist particulates or deposits. The waste packages are placed on support pallets and sit in air at atmospheric pressure. There is no feasible scenario that will lead to waste packages being fully immersed in water. There is a limited amount of water moving through the rock, and there is a limited amount of salts and minerals available to deposit on the packages. The ambient waters in the mountain are dilute; however, those ambient waters can be modified and become concentrated by thermal-hydrological-chemical processes. The sources of water that can contact metal surfaces in the proposed repository are deliquescence, condensation and drips or seepage. Deliquescence (to dissolve and become liquid by absorbing moisture from the air) is determined by the composition of soluble salts in the particulate layers, the relative humidity, and temperature. Drips and seepage of water from the drift walls onto the metal surfaces are possible after the thermal barrier period, i.e., when the drift wall has cooled to below the boiling point of water. Metals will be exposed to thin layers of moisture and moist particles in deposits of dust and particulate.

A schematic diagram of corrosion in thin layers of particulate and a list of important parameters that affect corrosion are presented in Figure 3.

Significant progress has been made in the following tasks:

- Analysis of passive film properties and changes in corrosion rate with time
- Analysis of the role of oxygen reduction rates on corrosion and passivity
- Coordination of computational modeling and experimental projects
- Development and implementation of specialized experimental methods for corrosion and electrochemistry in thin layers of particulate and moisture
- Determination of relationships between the structure and composition of their passive film and the corrosion resistance of Ni-Cr-Mo alloys
- Elucidation of the corrosion processes in thin films, particulate, and deposits

The S&T Materials Performance funded projects related to Corrosion of Metal Surfaces Covered with Particulate and Deposits (pp. 63-76) are:

- “Kinetics of the Cathodic Reduction of Oxygen on

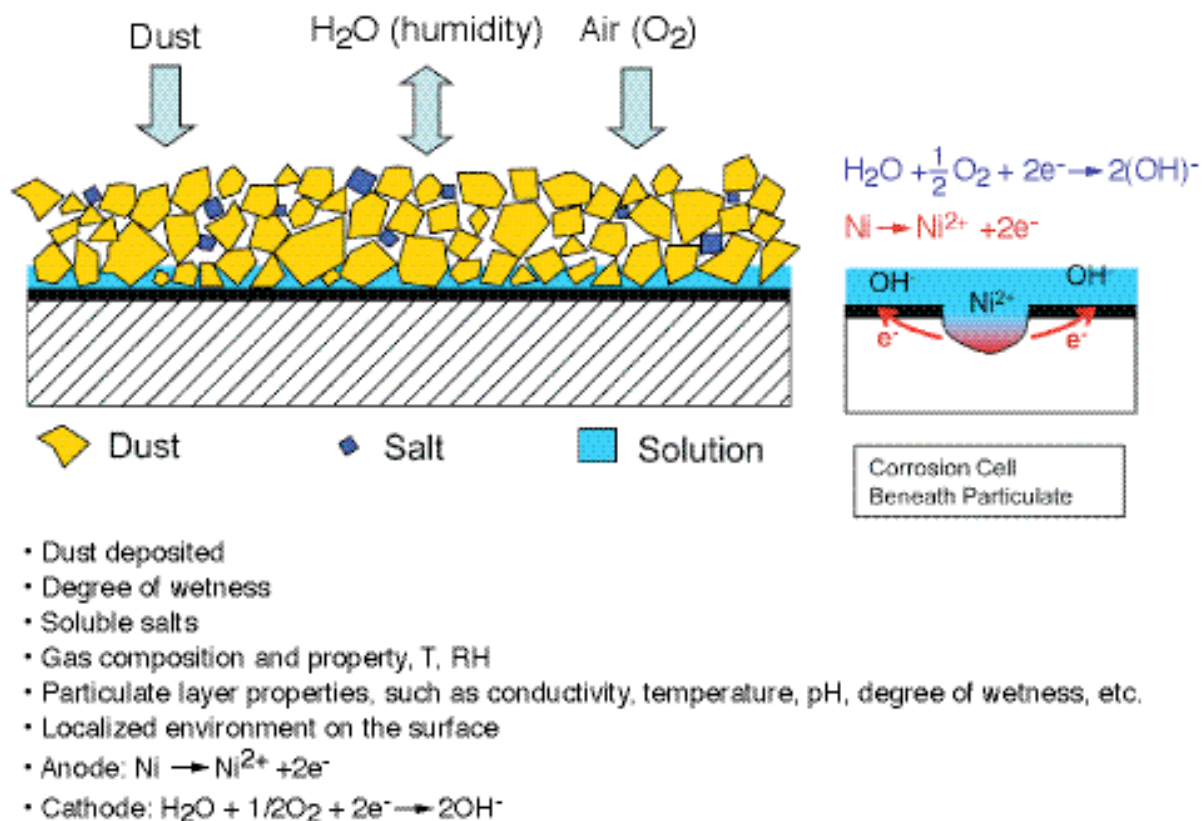


Figure 3. Schematic diagrams of corrosion of a metal covered by a thin layer of particulate and a corrosion cell beneath the particulate.

- "Passive Metals" by Shoesmith et al.
- "Oxygen Electro-Reduction on Passive Metals" by Gervasio et al.
- "Corrosion Cells beneath Thin Films, Particulate and Deposited Layers" by Payer et al.
- "Electrochemical Measurements of Corrosion under Thin Brine Layers" by Frankel et al.
- "Mechanism of Mixed-Ion Effects on Corrosion in Thin Films" by Newman et al.
- "Effect of Environmental Variables on the Structure and Composition of Passive Films" by Devine et al.

## Evolution of Corrosion Damage by Localized Corrosion

Localized corrosion processes and particularly crevice corrosion are high priorities. This technical thrust examines the rate of penetration and extent of corrosion damage by localized corrosion over extremely long times. Advanced analytical and computational methods for the time evolution of crevice-corrosion damage are developed. The requirements for the initiation and propagation of localized corrosion are determined. In addition, a focus is on the phenomena and processes that can result in the reduction in the rate, or complete arrest, of crevice corrosion.

**Targeted thrust objective:** Develop and analyze a logic-tree approach for the damage to waste packages by localized corrosion. In contrast to a simple go/no-go initiation criterion, the logic-tree approach provides a clear and transparent treatment to account for contributing factors.

**Targeted thrust objective:** Develop the technical basis for and demonstrate processes that slow penetration rates by localized corrosion in contrast to a treatment where a constant rate is presumed once damage (crevice corrosion) is started and there is no slowing or stopping of penetration rate. Where processes of stifling (slower rates) and arrest (corrosion stops) pertain, the amount of damage over long periods of time would be greatly reduced.

**Targeted thrust objective:** Demonstrate factors that may limit the initiation and propagation of localized corrosion. In contrast to a treatment that presumes crevices and supporting processes are always available, examine localized corrosion processes simulating coverage by rock and particulate.

The evolution of crevice-corrosion damage is determined by the initiation, propagation, stifling, and arrest stages of this form of localized corrosion. Crevice corrosion is affected by the crevice geometry and properties of the crevice former. For waste packages, metal surfaces can be covered with dust and particulate. The particulate, scale, and



deposits can form from dust, minerals from waters, and corrosion products. An important issue is how effective particulate layers and deposits are as crevice formers compared to metal/metal crevices on waste packages and polymer/metal crevices used in laboratory tests. Chemical, electrochemical, and metallurgical factors control the formation and evolution of the crevice solution chemistry. For crevice corrosion to persist, a critical crevice solution chemistry must be formed and maintained within the occluded region. These and other crucial issues are addressed by the projects in this technical thrust area.

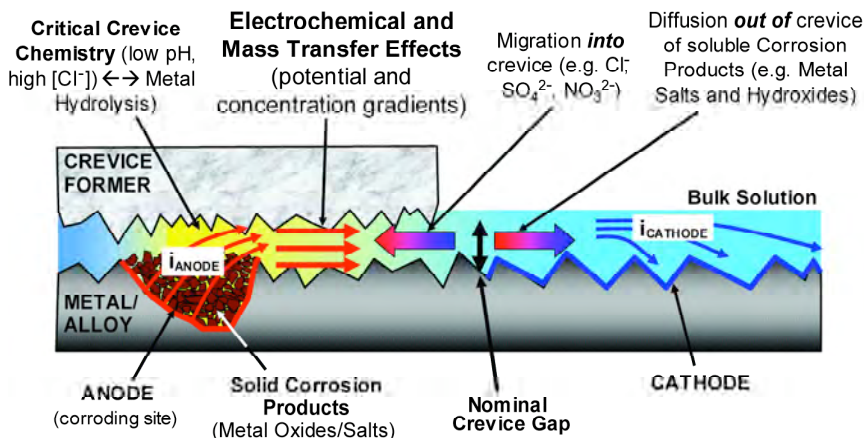


Figure 4. Schematic diagram of processes during crevice corrosion.

The approach has been to meet the objectives through a coordinated set of projects. Examples of the experimental methods and analytical modeling in this area are shown in Figures 4 and 5.

Significant progress has been made in the following tasks:

- Development and analysis of a logic-tree approach for the damage by localized corrosion
- Identification of the role of the interrelationship among anodic, cathodic, and coupled processes in the determination of crevice-corrosion behavior
- Coordination of computational modeling and experimental projects
- Development and implementation of specialized experimental methods for crevice-corrosion initiation, propagation and arrest
- Determination of the relationships between metallurgy (corrosion resistance of metals) and water chemistry (corrosivity of the environment) for Ni-Cr-Mo alloys and less corrosion-resistant metals in high-temperature, multi-species waters
- Establishment of a framework and process for the incorporation of findings into advanced methods for the "Prediction of Time Evolution of Localized Corrosion Damage"

The S&T Materials Performance funded projects related to Evolution of Corrosion Damage by Localized Corrosion (pp. 77-94) are:

- "Crevice-Corrosion Electrochemistry of Ni-Cr-Mo Alloys" by Scully et al.
- "Modeling of Critical Chemistry for Crevice

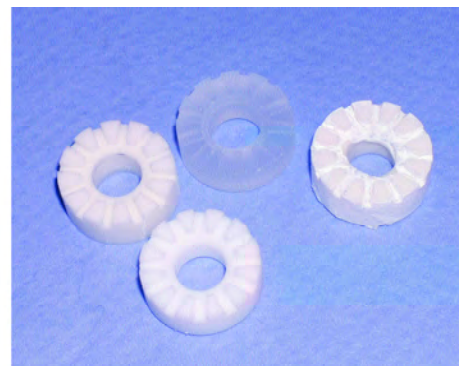


Figure 5. A multicrevice test assembly and crevice formers made from polymers and ceramics.

Corrosion" by Kelly et al.

- "Crevice-Corrosion Damage Function on Alloy-22" by Shoesmith et al.
- "Localized Corrosion Stability in the Presence of Non-Chloride Anions" by Newman et al.
- "Metallurgical Effects on Localized Corrosion of Ni-Cr-Mo Alloys" by Frankel et al.
- "Processes in Crevice-Corrosion Propagation, Stifling, and Arrest" by Payer et al.
- "Combinatorial Chemistry Approaches for Alloy Composition and Corrosion Behavior" by Buchheit et al.
- "Prediction of the Time Evolution of Localized Corrosion Damage" by Macdonald et al.

## Evolution of the Moist Environment on Metal Surfaces

The corrosion performance of a metal is determined by the inherent corrosion resistance of the metal and the corrosivity of the environment. The amount, distribution, and chemical composition of the moisture on waste packages are controlling parameters of corrosion performance. The

objective is to determine the properties of thin layers of moisture, moist particulates, and deposits that will affect the corrosion performance of metals. Advanced analytical and computational methods for the evolution of the environment on metal surfaces are developed. Scientific understanding is enhanced for moisture formation, chemistry, and evolution with time and for the properties of thin layers of particulates and deposits on metal surfaces.

**Targeted thrust objective:** *Develop and demonstrate evolution of environment (moisture) on metal surfaces in layers of moisture, particulate, and deposits.*

Key issues for corrosion behavior and long-term performance are determination of the presence of moisture on metal surfaces, the corrosive properties of the moisture, and the corrosion resistance of materials in these environments. Thin layers of electrolyte, particulates, and deposits are the conditions of interest for the analysis of corrosion of waste packages. A special feature of the proposed Yucca Mountain repository is the extremely long time frame of interest. Thus, the time evolution of the environment in contact with waste package surfaces and the time evolution of corrosion damage that may result are of primary interest in the determination of expected performance.

In the proposed repository, moisture can form on the metal surfaces by deliquescence and condensation processes as the waste packages cool from high temperatures after the heat-up period. A thermal barrier prevents drips and seepage into the drifts as long as the drift wall is hotter than the boiling point of water. After the thermal barrier period, a source of moisture on the metal surfaces is drips or seepage from the rock formation onto waste packages.

It is well accepted that dry metals, without the presence of an aqueous phase, do not corrode at an appreciable rate. Furthermore, full immersion in waters will not occur at the proposed repository under any realistic scenario. Therefore, corrosion in thin layers of electrolyte, particulate, and deposits are the conditions of interest. These thin layers of moisture can be a sufficient aqueous environment to support electrochemical dissolution. Anodes, cathodes, and an electrochemical corrosion cell can operate in a thin moisture layer. However, the factors that determine the onset of corrosion and the subsequent degree of damage can vary significantly in thin layers compared to fully immersed conditions.

The approach has been to meet the objective through a coordinated set of projects. Figure 6 shows several scenarios for the distribution of moisture within a layer of particulates.

Significant progress has been made in the following tasks:

- Coordination of experimental and computational

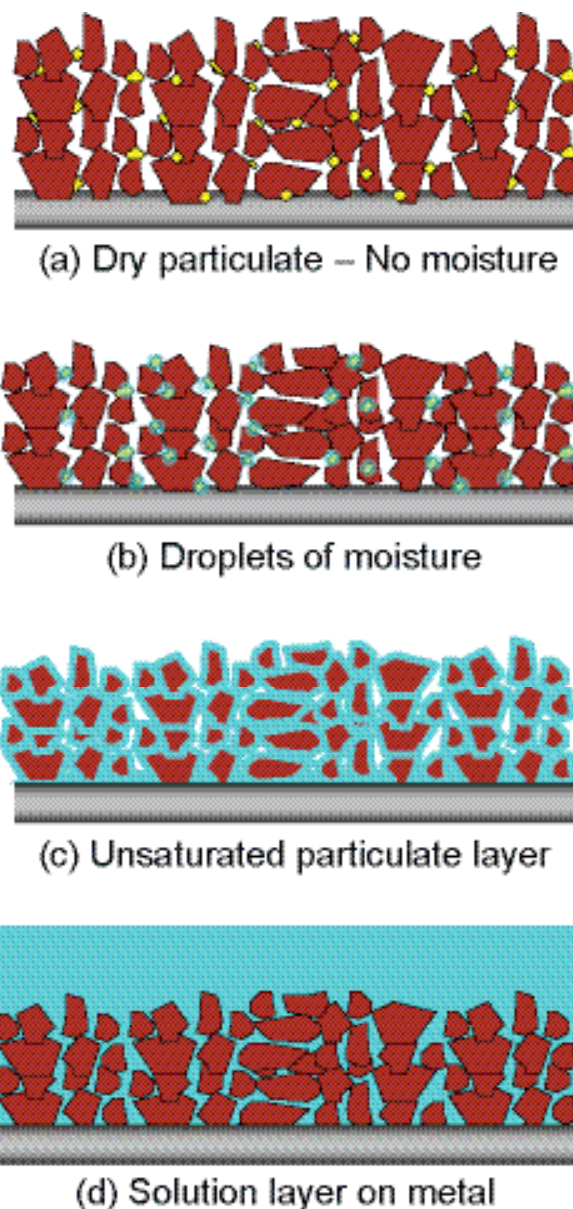


Figure 6. Scenarios for the distribution of moisture in a particulate layer.

projects to examine corrosion current distributions in moist particulate layers on metal surfaces.

- Determination of the properties and behavior of high-temperature multispecies solutions.
- Combination of the expertise and specialized facilities in geochemistry, corrosion, electrochemistry, and materials science.
- Establishment of a framework and process for incorporation of findings into advanced methods for the "Prediction of Time Evolution of Localized Corrosion Damage."
- Development and application of advanced analytical methods and sensors to determine the



---

properties of layers of moisture and particulate on metal surfaces.

The S&T Materials Performance funded projects related to Evolution of Environment on Metal Surfaces (pp. 95-108) are:

- “Modeling Chemical Environments within Corroding Crevices for Ni-Cr-Mo Alloys” by Wang et al.
- “Evolution of Solution Layer Chemistry during Localized Corrosion” by Kelly et al.
- “Modeling and Measurement of Current

Distribution on Particulate and Deposited Layers” by Landau et al.

- “Microelectronic and MEMS Devices for Solution Properties and Corrosion Evaluations” by Liu et al.
- “Optical Probes and Sensors to Determine Concentration Distributions in Thin Films on Reactive Surfaces” by Smyrl et al.
- “High-Temperature, Multi-Species Solution Properties and Behavior” by Cole et al.

Descriptions of projects in the Materials Performance Thrust area are provided in the following pages.

---

This page intentionally left blank.

# CORROSION OF METAL SURFACES COVERED WITH PARTICULATE AND DEPOSITS

## **Kinetics of the Cathodic Reduction of Oxygen on Passive Metals**

David W. Shoesmith, Dmitrij Zagidulin, Xueyuan Zhang, and James J. Noël,  
University of Western Ontario

## **Oxygen Electro-Reduction on Passive Metals**

Dominic Gervasio and Stephen P. Rogers, Arizona State University

## **Corrosion Cells Beneath Thin Films, Particulate, and Deposited Layers**

Joe H. Payer, Pallavi Pharkya, Xi Shan, Arun S. Agarwal, and Hongyi Yuan  
Case Western Reserve University

## **Electrochemical Measurements of Corrosion under Thin Brine Layers**

Gerald S. Frankel, Rudolph G. Buchheit, Bastian Meier, and Shoichiro Taira,  
Ohio State University

## **Mechanism of Mixed-Ion Effects on Corrosion in Thin Films**

Roger C. Newman and Christopher Healey, University of Toronto

## **Effect of Environmental Variables on the Structure and Composition of Passive Films**

Thomas M. Devine, Tzipi Cohen-Hyams, Marcela Miyagusuku, and Scott Harrington,  
University of California, Berkeley

---

This page intentionally left blank.

# Kinetics of the Cathodic Reduction of Oxygen on Passive Metals

David W. Shoesmith, Dmitrij Zagidulin, Xueyuan Zhang, and James J. Noël  
University of Western Ontario

## Research Objectives

The primary goal of this project is an elucidation of the mechanism and kinetics of the cathodic reduction of oxygen on Alloy 22, a nickel-chromium-molybdenum (tungsten) alloy. The accumulation of damage can be controlled either anodically (i.e., by the oxidative dissolution of the alloy components) or cathodically (i.e., by oxygen reduction). A clear definition of which of these two possible reactions is rate controlling, and a quantitative specification of the reaction kinetics, is important to the conceptual and numerical development of a corrosion model.

## Approach

To characterize the electrical properties of the thin passive oxide formed on the alloy surface, EIS (Electrochemical Impedance Spectroscopy) experiments have been conducted on Alloy 22 in deaerated 5 mol/L NaCl solutions at different temperatures. The data obtained have been analyzed using different electrical equivalent circuits.

Note: all potentials are indicated with respect to the saturated Ag/AgCl electrode,  $E=199$  mV vs. SHE.

Cyclic voltammetry (CV) experiments have been run in order to determine the electrochemical activity of the alloy surface preoxidized at different potentials and temperatures.

The electrochemical data have been correlated with the oxide composition and structure determined from XPS (X-ray Photoelectron Spectroscopy) and ToF SIMS (Time of Flight Secondary Ions Mass Spectrometry) experiments on Alloy 22 at different conditions in a deaerated 5 mol/L NaCl solution.

## Accomplishments

From XPS and ToF SIMS data, it is clear that the protective film has a layered structure (Figure 1). Cr(III) and Ni(II) hydroxides, Mo(VI) and W(VI) oxides form the outer layer. Ni(II) and Cr(III) oxides, Mo(II), Mo(IV), and non-stoichiometric Mo

oxides constitute the inner layer. Also, XPS data show that the relative concentration of  $\text{Cr}_2\text{O}_3$  is at a maximum for preoxidation potentials ( $E_{\text{pox}}$ ) in the range 0 to 0.2 V. At more positive  $E_{\text{pox}}$ , this Cr(III) oxide is partially converted to  $\text{CrO}_4^{2-}$  (soluble) and  $\text{Cr}(\text{OH})_3$ . At the same potentials conversion of  $\text{Mo}^{2+}$  and  $\text{Mo}^{4+}$  to  $\text{Mo}^{6+}$  takes place, and

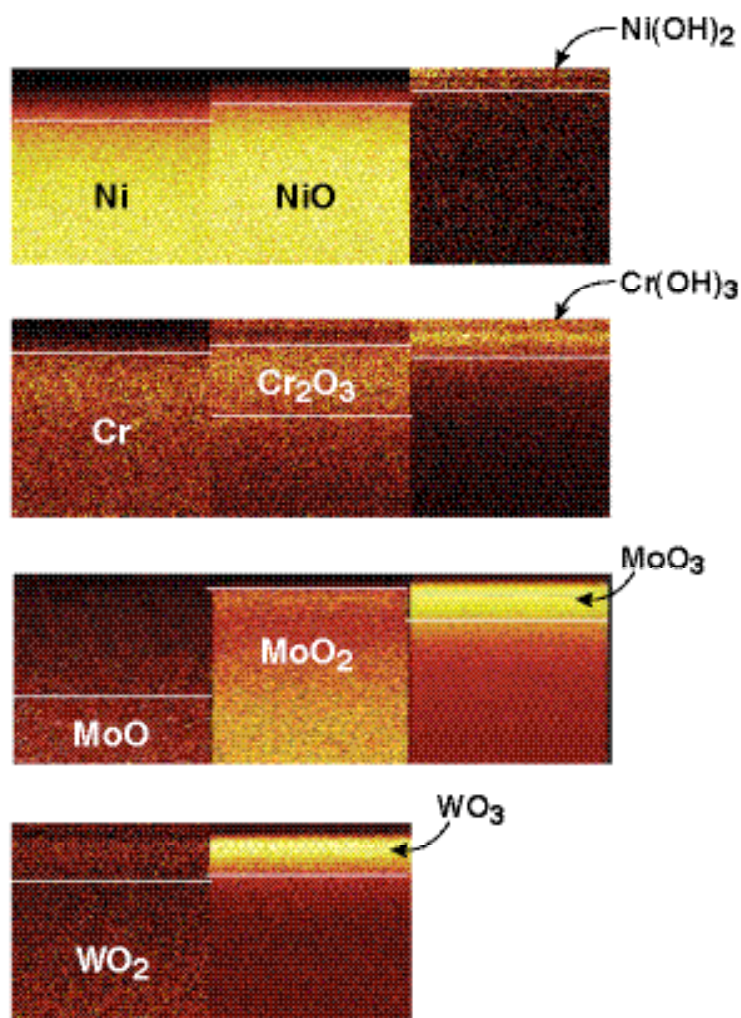


Figure 1. ToF SIMS depth profile obtained on Alloy 22. The oxide film was formed at 30°C and  $E_{\text{pox}} = 0$  V. First row—Ni, NiO,  $\text{Ni}(\text{OH})_2$ ; second row—Cr,  $\text{Cr}_2\text{O}_3$ ,  $\text{Cr}(\text{OH})_3$ ; third row—MoO,  $\text{MoO}_2$ ,  $\text{MoO}_3$ ; fourth row— $\text{WO}_2$ ,  $\text{WO}_3$ . The film/solution interface is on the top of each profile.



MoO<sub>3</sub> becomes the dominant Mo compound. Those changes coincide with a decrease in the film resistance (established by EIS) and create conditions where the surface can support oxygen reduction.

EIS data can be modeled taking into account three main processes, charge transfer through alloy/film interface; charge migration and diffusion in the oxide; and charge transfer at the oxide/solution interface. Charge transfer resistance at the alloy/oxide interface shows a very minor dependence on the temperature, but a strong dependence on  $E_{\text{pox}}$  with a maximum at 0.2V, the same potential at which capacitance has a minimum. As the temperature increases to 70°C, the capacitance decreases.

Charge migration in the oxide shows a maximum value for  $E_{\text{pox}}$  in the range 0 – 0.2 V (depending on temperature). Oxide capacitance values show similar behavior and values at all temperatures for  $E_{\text{pox}} < 0$  V. At more positive potentials at 70°C the film capacitance increases. By contrast at lower temperatures it decreases. This behavior suggests different film properties at 70°C compared to lower temperatures when  $E_{\text{pox}} > 0$  V. This is supported by XPS data, which shows that at 70°C and  $E_{\text{pox}} > 0.2$  V the concentration of non-stoichiometric Mo oxide increases while the Mo(VI) oxide decreased. At lower temperatures, the behavior is the opposite.

The need for a Warburg impedance to accurately fit the data indicates that defect diffusion occurs in the defective oxide. Values of  $L^2/D$  (where  $L$  is the effective diffusion thickness and  $D$  is the effective diffusion coefficient of the particle) calculated from the Warburg impedance show a minor dependence on  $E_{\text{pox}}$  at 30 and 50°C, but increase ~100 times at 70°C for  $E_{\text{pox}}$  in the range 0.4–0 V. Since ToF SIMS data show that the film thickness is increased at 70°C compared to lower temperatures, the decrease in  $L^2/D$  must be associated with an increase in mobility of electronic defects. This may be attributable to an increase in concentration of non-stoichiometric Mo oxide, a Mo(VI) oxide with a deficit of oxygen atoms, which would be expected to have high charge mobility.

For  $E_{\text{pox}} < -0.4$  V and  $> 0.4$  V a third component of the electrical equivalent circuit indicates a reaction impedance at the oxide/solution interface. The resistance for this surface reaction shows similar behavior at 50°C and 70°C, but the reaction capacitance values are different (at 50°C the capacitance increases over the potential range 0.4 V to 0.6 V, whereas at 70°C it decreases). This difference reinforces our argument that the oxide is different at 70°C. Experiments with alloys of different compositions would help elucidate these differences.



# Oxygen Electro-Reduction on Passive Metals

Dominic Gervasio and Stephen P. Rogers  
Arizona State University

## Research Objectives

The objective is to examine the corrosion behavior of Ni-Cr-Mo alloys, using electrochemical and spectroscopic techniques, to estimate rate constants for oxygen reduction and passivation behavior on the alloys at different temperatures and alkaline water environments. This work is intended to provide inputs to models relating environmental factors to the corrosion processes of the alloys for the development of advanced analytical methods and next-generation conceptual models of the Ni-Cr-Mo alloys corrosion with significantly reduced uncertainty.

## Approach

Cathodic redox reactions, such as oxygen ( $O_2$ ) electro-reduction on the Ni-Cr-Mo alloys in alkaline water solutions, with and without salt additives (brines), are being studied to simulate the cathodic processes in thin layers of moisture and layers of moist particulates and deposits on metal surfaces. The  $O_2$  reduction is of particular interest (although other redox reactions, such as nitrate reduction, may also contribute) as the source of cathodic current on the alloy surface that can sustain pitting, crevice corrosion, stress corrosion cracking, and galvanic action. A series of experiments were conducted to investigate  $O_2$  reduction on fresh and/or aged alloy surfaces as a function of: electrical potential, temperature, and solution chemical composition. Results are important inputs to the determination of the onset and extent of cathodic stifling of corrosion processes. These experiments will provide input to modeling of corrosion of the Ni-Cr-Mo alloy, and the results provide a basis for model validation.

Two experimental apparatuses have been constructed and used for this project: (1) a rotating (gold) ring (Ni-alloy) disk electrode (RRDE) utilizing thermostatic control and a cycling potential ring method (CPRM) and (2) an electrochemical Fourier transform infrared (Echem-FTIR) cell using a photoelastic modulator for polarization modulated infrared reflection-absorption spectroscopic (PM-IRRAS) inspection of water layers near and surface monolayers on reflective Ni-Cr-Mo alloy surfaces. Results for the former are summarized here. The experimental apparatuses and techniques measure  $O_2$  reduction, oxide growth, adsorbate-surface interactions, and other potential redox reac-

tions on passive metal as a function of potential and current. Research efforts have focused on:

- Measuring  $O_2$  reduction on freshly polished Ni-Cr-Mo alloy surfaces in alkaline water solutions at different temperatures
- Characterizing the Ni-Cr-Mo alloy surface at different potentials and in different alkaline solutions
- Examining the effects of mechanical damage (scratch) to the passive film on Ni-Cr-Mo alloys.

## Accomplishments

The voltammetry of Alloy 22 and C276 alloy was performed in argon (Ar) de-aerated and  $O_2$  saturated 1M KOH water solution at 30°C cycling between -0.6 V and 0.4 V versus saturated calomel electrode (SCE). The increasing capacitance of a Ni-Cr-Mo alloy electrode with each cycle suggests the accumulation of oxide on the alloy surface with each cycle. The voltammetry of the Alloy 22 and C276 is similar. These Ni-Cr-Mo alloys have similar compositions, with Alloy 22 having higher Cr (22% versus 16%) and lower Mo (13% versus 16%). Alloy C276 showed slightly lower capacitance (surface oxidation and reduction currents) at 30°C compared to Alloy 22 in Ar de-aerated alkaline water solution. That  $O_2$  reduction was occurring on the alloy surfaces could be seen by the smaller semicircles in Nyquist plots obtained using Electrochemical Impedance Spectroscopy (EIS) of the alloys in  $O_2$  saturated compared to Ar de-aerated alkaline water solution. Oxygen reduction is the most likely cathodic process for sustaining oxidative corrosion of a metal in air. Therefore, the rate of  $O_2$  reduction current was quantified by the RRDE method as inputs to models of the rate of metal corrosion.

We were able to validate the CPRM RRDE methodology by repeating Vilambi and Taylor's work of  $O_2$  reduction on a Au-ring and a Au-disk rotating electrode. The onset potential for  $O_2$  reduction on Alloy 22 and Alloy C276, in alkaline water at pH 14, was approximately -0.6V, and it continued to -1.5V (vs. SCE). The CPRM study with a Ni-Cr-Mo alloy disk and Au ring showed strong evidence for  $O_2$  reduction on nickel alloy surfaces by a series of two 2-electron steps. The rate constants,  $k_2$  and  $k_3$ , for these two steps were estimated, even though the limiting current for

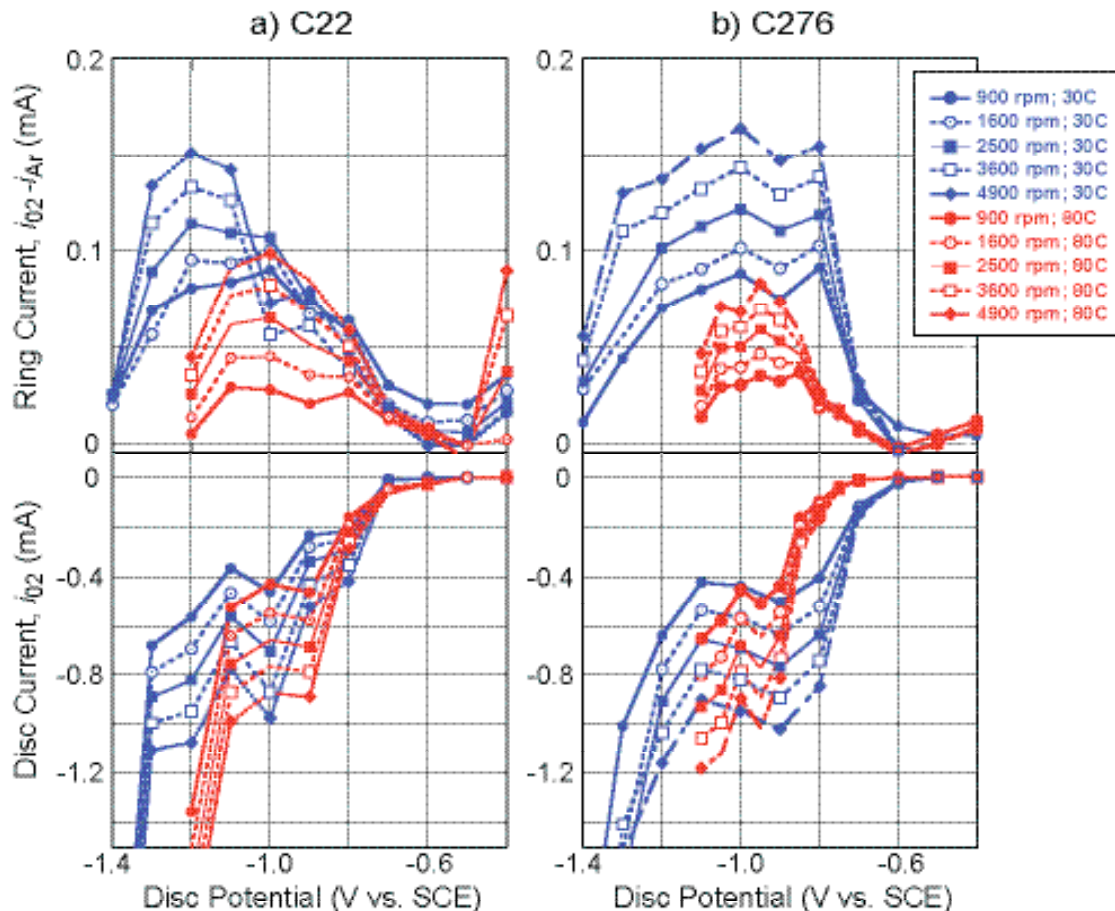


Figure 1. CPRM method (Au ring) to determine O<sub>2</sub> reduction on Ni-Cr-Mo alloy discs (a) Alloy 22 and (b) C276 in IM KOH (pH 14) at 30°C (in blue) and 80°C (in red).

the second step, peroxide reduction to water, was ill-defined because of its overlap with hydrogen generation due to the reduction of proton from water. At 30°C, the rate constants,  $k_2$  (@ -0.7V for O<sub>2</sub> to H<sub>2</sub>O<sub>2</sub>) and  $k_3$  (@ -1.2V for H<sub>2</sub>O<sub>2</sub> to H<sub>2</sub>O), were estimated to be 0.001 and 0.013 cm/s, respectively, for Alloy 22; and 0.193 and 0.232 cm/s, respectively, for Alloy C276. At 80°C,  $k_2$  and  $k_3$  were estimated to be 0.003 and 0.818 cm/s, respectively, for Alloy 22. The determinations of rate constants for O<sub>2</sub> reduction on nickel alloys at 80°C were more difficult owing to the poor seals of the Au ring and Ni-Cr-Mo alloy disc electrodes, and the enhanced H<sub>2</sub>O reduction to H<sub>2</sub> at 80°C from the data in Figure 1.

In an additional task, infrared spectroscopy is being used to investigate the Ni-Cr-Mo alloy surface in an alkaline electrolyte under potential control. The alloy is behind an optical window housed in glass, PEEK, and Teflon. The cell is fixed to an optical bench with x-y, tilt, and rotation, and

both are in a nitrogen-filled box with feed-throughs to a potentiostat and cell-purge gases. This work is in a preliminary stage, and results will be reported in the next period.

## References

- Vilambi, N. R. K. and E. J. Taylor, *Journal of Electroanalytical Chemistry*, 270, 61-77, 1989.
- Gervasio, D. and J. H. Payer, *Proceedings of the Electrochemical Society*, Orlando, FL, 58-70, 2003.
- Payer, J.H., B. Trautman, and D. Gervasio, *Methods Polymeric Materials Science and Engineering*, 68, 109-110, 1993.
- Pons, S, *Journal of Electroanalytical Chemistry*, 150, 495-504, 1983.
- Jiang, E, Y. and M. S. Bradley, A new approach to quantitative spectral conversion of PM-IRRAS: theory, experiments and performance comparisons with conventional IRRAS. ThermoFisher Scientific Application Note 01151.

# Corrosion Cells Beneath Thin Films, Particulate, and Deposited Layers

Joe H. Payer, Pallavi Pharkya, Xi Shan, Arun S. Agarwal, and Hongyi Yuan  
Case Western Reserve University

## Research Objectives

The objective is to examine the behavior of macro- and micro-corrosion cells in experiments on passive metals covered by thin layers of moisture, particulate, and deposits. The operation of corrosion cells under these conditions can vary significantly from the behavior observed in fully immersed conditions. The corrosion of active metals, e.g., iron and zinc, in thin layers of moisture that pertain to atmospheric corrosion has been studied extensively; however, the behavior of passive metals in thin layers of moisture has received little attention. The results of this project will provide input to the modeling efforts to describe passive metal behavior. The foci are (a) the post-initiation stages of the corrosion cells to gain insight concerning the propagation, stifling, and arrest processes for localized corrosion; and (b) the durability of passive films beneath moist particulate and deposits.

## Approach

A number of simulation cell configurations are used to investigate geometric effects, saturated and unsaturated particulate, chemical composition of moisture and particulate, temperature, and relative humidity. The current distribution and changes in chemical composition in thin layers of moisture and layers of moist particulate and deposits on metal surfaces are measured experimentally. The experiments are closely coupled to numerical modeling of corrosion cells. For passive film durability studies, the passive film properties are measured as a function of aging and the re-formation/repair behavior of the passive film after mechanical and/or chemical damage.

## Accomplishments

### Multiplate Cells for Simulation of Corrosion Cells

Of particular interest is the flow of current representative of corrosion scenarios to simulate the metal surface during pitting, crevice corrosion, stress corrosion cracking, and galvanic action. A range of layer thicknesses on metal surfaces is examined, i.e., from thin layers of absorbed moisture, to single particulate layers, to multi-particulate layers of 1 cm thickness and greater. A multiplate cell shown in Figure 1 was used to measure

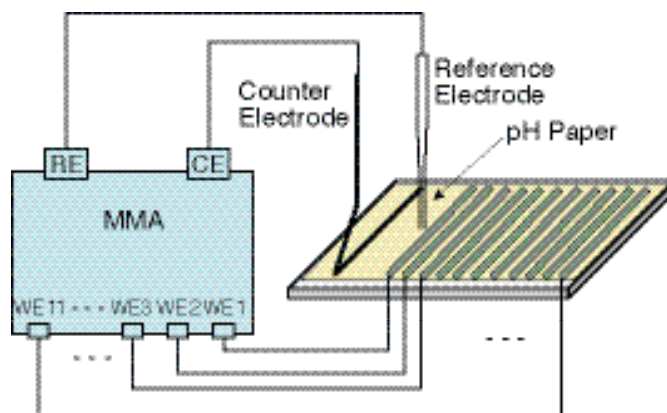


Figure 1. Schematic of multiplate cell to simulate crevice corrosion.

current distribution along the surface and chemical changes within the electrolyte for a simulated crevice-corrosion cell.

Cathodic current density was greatest on metal surfaces near the anode and fell off with distance away from the anode. As shown in Figure 2, the electrolyte became more alkaline on the cathode and more acidic on the

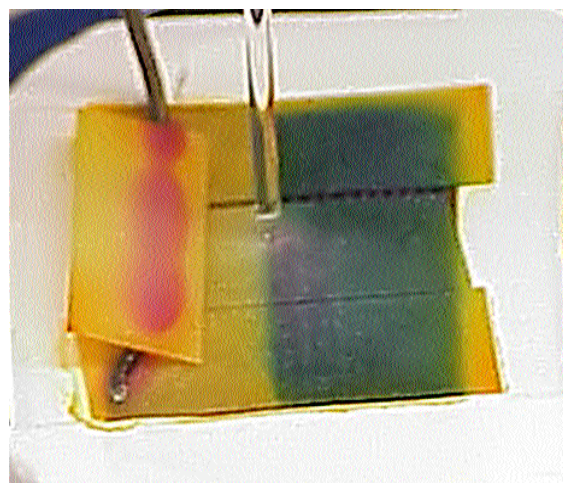


Figure 2. Chemical changes occur in the electrolyte layer due to hydroxyl generation on the cathodic surface (blue) and acid generation at the anodic surface (red).



anode. These chemical changes are more pronounced as electrolyte thickness decreases.

### Durability of the Passive Film

The methods used are cyclic potentiodynamic polarization, constant potential scratch-repassivation, electrochemical impedance spectroscopy, and auger electron spectroscopy. The cyclic potentiodynamic polarization method determines corrosion properties such as corrosion potential, breakdown potential, repassivation potential, and passive range of the alloy. A scratch-repassivation apparatus, shown schematically in Figure 3, is used to examine the durability of the passive film after severe mechanical damage. The passive film that protects the metal is removed by scratching with a diamond-pointed scribe at rotation speeds to 100 rpm. The amount of damage and repassivation behavior is examined by monitoring the anodic current from the specimen and by post-test surface examination. For controlled potentials within the passive range, the corrosion current from Alloy 22 decreased rapidly after the metal was scratched, indicating rapid repassivation (Figures 4 and 5). Preliminary surface analysis and electrochemical impedance spectroscopy found no significant change in the passive film properties before and after mechanical damage.

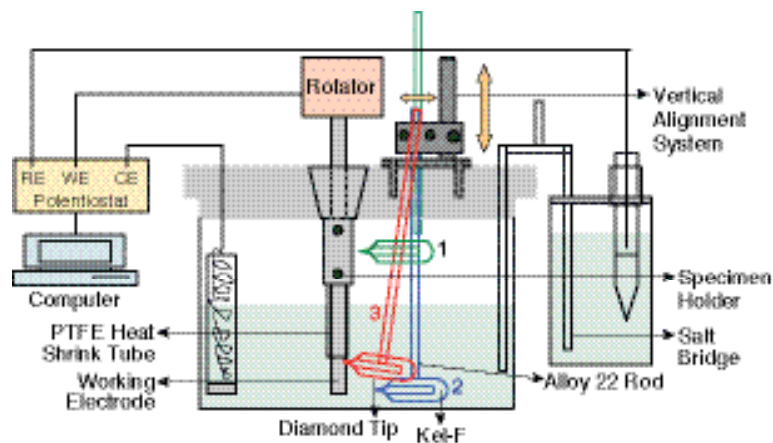


Figure 3. Schematic of scratch-repassivation apparatus with controlled rotation speed.

This project examines corrosion and passive film durability in thin moisture films and layers of particulate and deposits. Results are important inputs to determine the durability of the passive films that are responsible for the high corrosion resistance of Ni-Cr-Mo alloys and to determine the evolution of corrosion damage over long periods of time. The findings are beneficial to development of advanced, next-generation models and alternative conceptual models. A better scientific understanding of the chemical, electrochemical, and corrosion processes is provided.

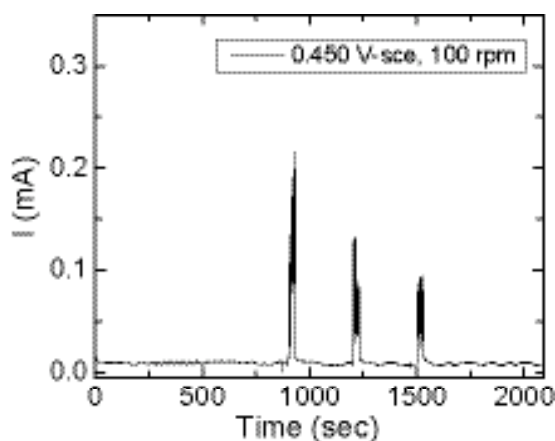


Figure 4. Scratch-repassivation behavior of Alloy 22 after scribing with a diamond tip at 15th, 20th, and 25th minute at  $+0.450 V_{SCE}$  in 0.6M NaCl (open to air),  $80^{\circ}\text{C}$  at rotation speed of 100 rpm. The passive film reformed after each scribing event.

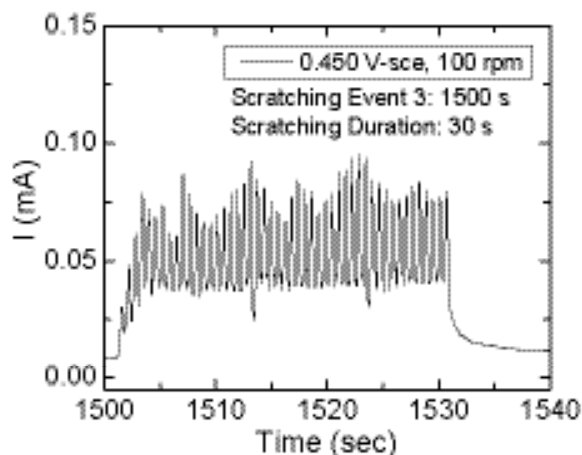


Figure 5. Current-time transients of Alloy 22 at 25th minute under the same experimental condition as in Figure 4.



# Electrochemical Measurements of Corrosion under Thin Brine Layers

Gerald S. Frankel, Rudolph G. Buchheit, Bastian Meier, and Shoichiro Taira  
Ohio State University

## Research Objectives

The objective is to make electrochemical measurements on corrosion-resistant alloys under thin electrolyte layers representative of dust, particulate, and adsorbed moisture (from monolayers to millimeters in thickness); and characterize the relationship between the physical characteristics of the layers and the electrochemical behavior of the alloys.

## Approach

A major challenge in making electrochemical measurements in thin electrolyte layers is the incorporation of a viable reference electrode with the ability to provide spatial resolution of the potential. In this task, Kelvin Probe (KP) and Scanning Kelvin Probe (SKP) techniques are utilized to make electrochemical measurements in the thin layers. The KP provides a noncontact measurement of potential. Since the KP is limited to room temperature operation, high-temperature measurements are made with an in-plane Ag/AlCl electrode. This approach is being used on Alloys 276 and 22 at temperatures up to 120°C. A schematic drawing of the glass chamber used is shown in Figure 1. The RH was controlled by the saturated salt solution in the bottom of the chamber. The whole chamber was placed in a furnace to fix the temperature. The open circuit potential (OCP) is monitored; a sudden drop in OCP is an indication of localized corrosion initiation.

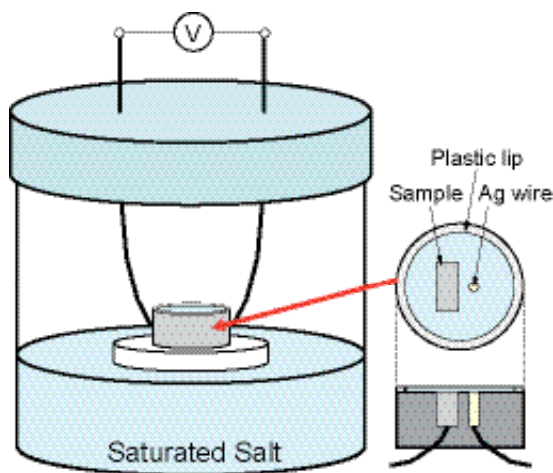


Figure 1. Schematic diagram of the cell for corrosion potential measurement.

In another approach, mineral deposition on Alloy 22 was simulated by cathodic reactions. The scenario being explored is precipitation of  $\text{Ca}^{2+}$  ions from thin layer solutions that become alkaline due to oxygen reduction occurring on the alloy surface. Mineral deposition was induced by cathodically polarizing Alloy 22 electrodes in saturated boiling  $\text{CaCO}_3$  or  $\text{Ca}(\text{NO}_3)_2$  at a potential of  $-0.2V_{\text{sce}}$  for two hours. To determine if the resulting deposits retarded or aggravated corrosion during subsequent exposure to a hot chloride solution, the modified electrodes were potentiodynamically polarized in a 5M NaCl solution or a 4M NaCl + 2M  $\text{KNO}_3$  solution.

## Accomplishments

### OCP Measurements with a Kelvin Probe during Electrolyte Drying

Drying experiments were performed with layers of chloride solutions on SS304 to investigate the influence of the initial electrolyte volume or the final electrolyte thickness on the pitting initiation time. As an electrolyte dries, the concentration increases. A volume of 0.5 M  $\text{MgCl}_2$  solution was spread over the SS304 sample, and then air with low (33%) humidity was flowed through the KP chamber. This results in a slow drying of the  $\text{MgCl}_2$  solution and an increase in the  $\text{Cl}^-$  concentration until pitting occurs. No dependence of the pitting initiation time on the electrolyte volume or the final electrolyte thickness was found.

Similar experiments were carried out with silica-covered SS304 to simulate rock dust on the surface. The silica layer was applied by cathodic electrophoretic deposition, and varying deposition time was used to simulate different dust layer thickness. A volume of 0.5 M  $\text{MgCl}_2$  again was spread over the coated SS304 sample, which was put in the KP chamber with a constant relative humidity of around 33%. The initiation of pitting as indicated by a drop in OCP was monitored. Silica layer thickness had no effect on pitting initiation time.

To determine the critical chloride concentration for pitting corrosion on 304 stainless steel, the corrosion potential and the solution layer thickness were monitored simultaneously with the Kelvin Probe. A volume of 0.44 M  $\text{MgCl}_2$  solu-

tion was put on the SS304 surface, and the chamber was purged continuously with air of constant 33% relative humidity. The critical chloride concentration was calculated from the electrolyte thickness at the point of pitting initiation and the exposed area. This concentration was found to lie between 5.1 M and 9.8 M.

### Measurements at High Temperature

The cell shown in Figure 1 was used in this work. The alloy sample was mounted with an Ag wire in epoxy resin, and polished with SiC paper up through 1200 grit. The Ag wire was chloridized prior to the experiment. A volume of 1M LiCl was spread on the surface, and saturated LiCl solution was placed at the bottom to keep the relative humidity constant. The glass container was then placed in a furnace and the potential between the sample and the Ag/AgCl electrode was monitored. With time, the LiCl solution layer thinned and approached saturation, which is known to be about 30 M in hot water. Figure 2 shows the change of OCP with time for Alloys 276 and 22 at 90°C and 120°C. In the case of Alloy 22, the OCP became constant after a few hours for both temperatures; the value for 120°C was higher than that for 90°C. For Alloy 276, the OCP was similar to that of Alloy 22 at 90°C. However, at 120°C the OCP decreased steadily for the first 5 hours and then precipitously dropped by about 200 mV.

The samples were analyzed with an optical microscope after the experiment, and pits were observed only for Alloy 276 at 120°C. Figure 3 shows an optical microscopy image and atomic force microscopy (AFM) characterization of the pits, which were found to have a diameter of about 6  $\mu\text{m}$  and depth of 300 to 500 nm. These results show that Alloy 22 is resistant to pitting at OCP even in 30M  $\text{Cl}^-$  at 120°C, whereas Alloy 276 is not.

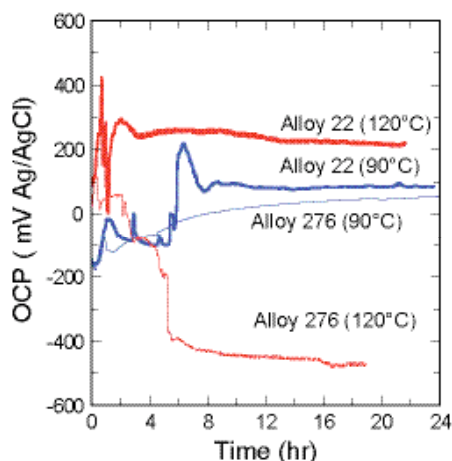


Figure 2. Variation of open circuit potential with time for Alloys 22 and 276 at 90°C and 120°C.

### Mineral Deposits

Results of this study show that cathodic polarization can contribute to the deposition of an adherent mineral layer from  $\text{Ca}^{2+}$ -bearing solutions. The effects of this layer on subsequent corrosion behavior in chloride and chloride-nitrate solutions are mixed. In general, Ca mineral layers formed in these experiments partially block the surface. After mineral deposition, the passive current density is reduced by one to two

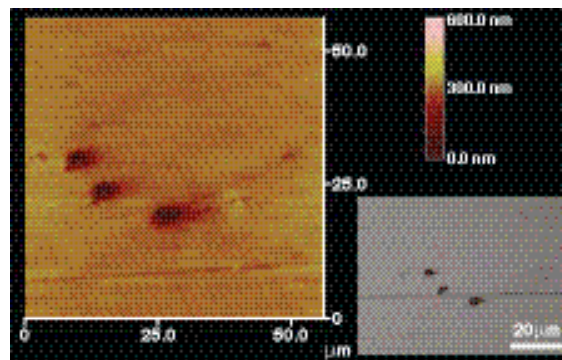


Figure 3. Morphology of pits formed on Alloy 276 at 120°C characterized by AFM and optical microscope picture of same area.

orders of magnitude. Part of this reduction is due to blocking of the surface by the mineral layer, but as suggested by increases of up to 200 mV in the corrosion potential, there may be a decrease in the true passive current density that contributes to the observed reduction. In both chloride and mixed chloride-nitrate environments, the presence of the mineral layer appears to lower the pitting potential or the onset of transpassive dissolution. Repassivation potentials are also lowered in the majority of cases. In post-test scanning electron micrographs there is clear evidence that localized corrosion occurs under and at the periphery of these deposits (Figure 4).

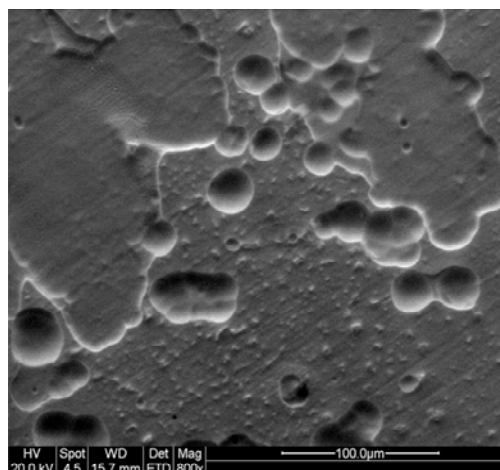


Figure 4. Localized corrosion under Ca mineral deposits after cyclic polarization in a mixed chloride-nitrate solution.

# Mechanism of Mixed-Ion Effects on Corrosion in Thin Films

Roger C. Newman and Christopher Healey  
University of Toronto

## Research Objectives

This project is designed to extend the artificial pit technique to thin particulate layers, applying similar rigorous mass transport analysis to that used in bulk solutions. We are applying the extended technique to investigate mixed ion effects on corrosion in thin films. A major focus is on nitrate inhibition of localized corrosion in chloride solutions.

## Approach

The artificial pit, or pencil electrode, technique involves embedding a metal wire in resin and dissolving it from one end in a salt solution, so that the entire exposed surface acquires the condition of a localized corrosion surface (pit or crevice). This creates a one-dimensional mass transport condition while simulating the metal dissolution and solution alteration (pH, [Cl<sup>-</sup>]) that occur within natural localized corrosion sites. The simplified mass-transport condition enables us to determine unambiguous kinetic parameters and to study the effect of inhibiting substances such as nitrate ions. It is important to note that with modern instrumentation, the currents that can be measured from such electrodes cover the whole range from penetration rates of microns per second, to those that are of concern for the long-term propagation of tight crevices or underdeposit events in equipment, e.g., microns per year.

The conditions chosen for the study were dilute chloride and chloride/nitrate solutions, at a temperature range of 75–95°C. A series of Ni-22Cr-xMo alloys were fabricated into thin wires and used as artificial pit electrodes.

We have shown, for the first time, that it is relatively straightforward to grow one-dimensional artificial corrosion cavities in thin, moist particulate layers—by mounting the electrode in resin within concentric Ag and Pt rings acting as reference and counter electrodes, respectively. A moist particulate layer is applied, and initiation and propagation of corrosion are easily monitored. Differences have been detected between thin layer and bulk-solution behavior. These are not always

in the direction expected. Impedance measurements between concentric chloridized Ag ring electrodes are used to monitor the properties of the moist layer and to examine reproducibility.

## Accomplishments

In this period, we made major improvements in the humidity chamber used to expose the corrosion sensors with thin particulate layers while making electrochemical measurements. Two samples can now be exposed under different conditions, and a drawer arrangement has been added to facilitate rapid changes of the salt solution that controls the humidity. An improved humidity sensor rated to 100°C has been installed.

We have compared kinetics in bulk and thin-film conditions for pure chloride solutions, assuming in the first instance that equilibrium prevails so that the aqueous phase within the particulate layer is the same as that in the bottom of the chamber. It is recognized that there may be detailed differences, due (for example) to capillary effects or the impact of hygroscopic corrosion products. Most experiments have been done in near-saturated NaCl conditions. Then, we developed methods to inoculate nitrate into the particulate layer while the pit was growing under electrochemical control. Initially this was done by spraying, but now a spotting technique is used. This aspect is under further development.

Figure 1 shows a typical repassivation transient for a relatively resistant alloy upon inoculation of nitrate to a relatively high level. In all such experiments performed to date, ingress of the newly added ion into the pit was more rapid than expected, and even more rapid than in a bulk solution. This highlights that we still have much to learn about the details of mass transport in such systems where capillary effects coexist with diffusion.

A peculiar phenomenon was observed when monitoring the impedance between concentric silver electrodes in thin particulate layers. Despite a fairly low solution resistance between the silver electrodes, the

corrosion process would not stabilize, possibly because the pit solution itself dries out the nearby particulate layer.

Next steps will involve the greater occlusion of the cor-

rosion cavity, to simulate in a short time the low limiting anodic current density under a dense membranous deposit that might take many years to form in practice, followed by further evaluation of the effect of nitrate inoculation.

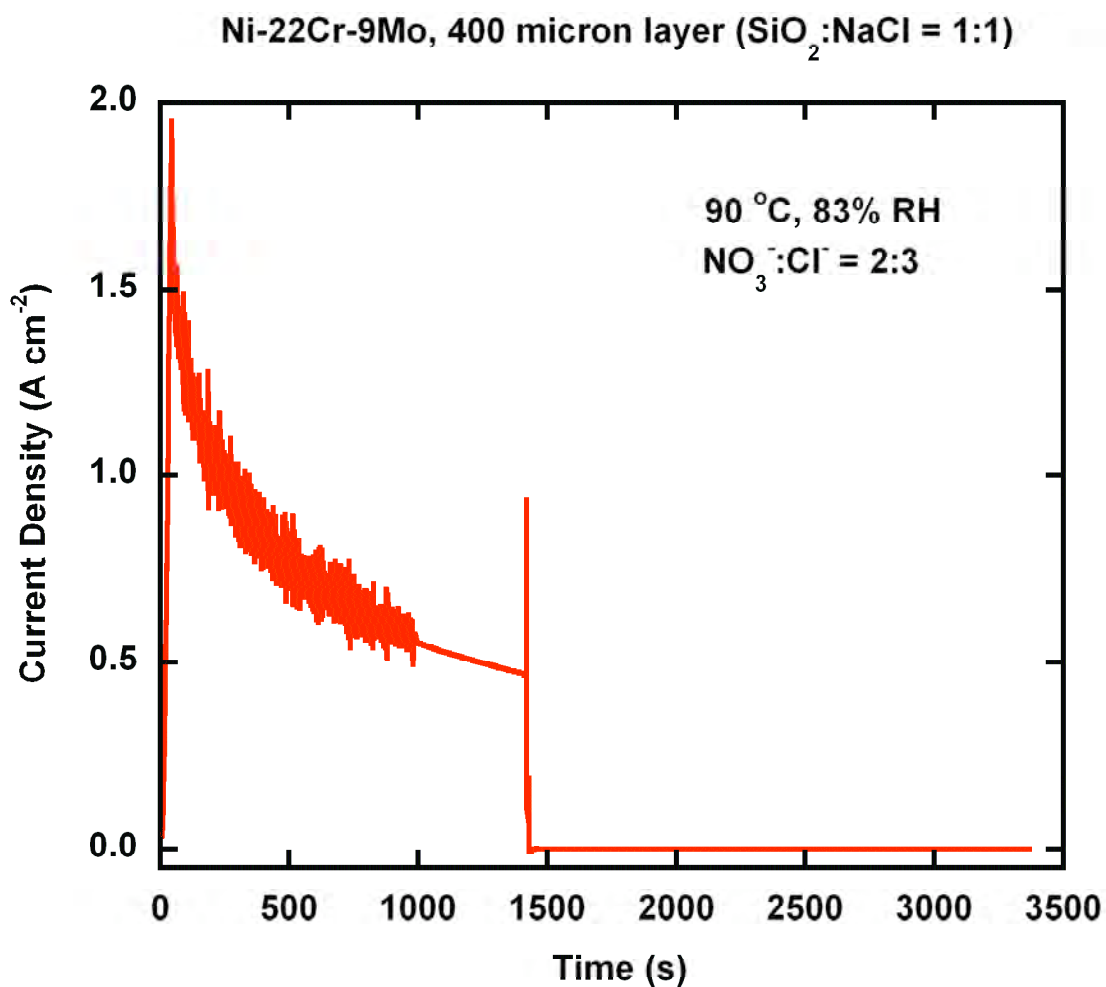


Figure 1. Repassivation of a corrosion cavity in a thin particulate layer due to the inoculation of nitrate (reduction in the noise after 900 s is due to dropping the potential from 900 mV to 325 mV (Ag/AgCl)). Nitrate inoculation at 1420 s.

# Effect of Environmental Variables on the Structure and Composition of Passive Films

Tzipi Cohen-Hyams, Marcela Miyagusuku, Scott Harrington, and Thomas M. Devine  
University of California, Berkeley

## Research Objectives

The focus of our research is the identification of the passive films that are responsible for the corrosion resistance of Alloy 22 and the determination of the film's fundamental properties that affect its protective nature.

## Approach

When passive films are removed from aqueous solutions, structure and properties can change. To avoid this, the present study uses five *in situ* techniques to examine passive films in a series of aqueous electrolytes: (1) chloride-free and chloride-containing solutions of near-neutral pH, typical of many engineering applications of passive alloys; (2) acidic solutions (0.001M–12M HCl) that mimic the electrolytes inside pits and crevices and that can severely damage the passive metals; and (3) neutral and acidic solutions with nitrate and sulfate ions, which may inhibit localized corrosion by chloride.

Identical experiments are conducted on Alloy 22 and its major alloying elements: Cr, Ni, Mo, and Fe. Results of tests conducted on the metallic elements help to interpret the results of tests performed on Alloy 22. Tests are also conducted on several alloys that, like Alloy 22, are protected by chromium-rich passive films: Alloy 600 (Ni-Cr-Fe) and 304 stainless steel (Fe-Cr-Ni). Comparing and contrasting the results of tests conducted on Alloy 22, Alloy 600 and 304 SS indicate the influence of alloy composition on the structure, composition, and properties of Cr-rich passive films.

## Accomplishments

Although the corrosion resistance of the alloys investigated is largely determined by the alloy's chromium concentration and the passive films of each alloy are mainly Cr-rich oxides/hydroxides/oxyhydroxides, our results have revealed that the chromium-rich films formed on Alloy 22, Alloy 600, 304 SS, and pure chromium are all different. The *in situ* Surface Enhanced Raman (SER) spectra of the passive films formed on chromium and Alloy 22 at -0.2V vs. Ag/AgCl in 1M HCl are presented in Figure 1 and illustrate the point. The spectra are clearly different. The combination of peaks present in the SER spectra of chromium's

passive film approximately match the set of peaks associated with Cr(III)-O bonds, but do not match the spectra of known oxides and hydroxides of chromium. Accordingly, chromium's passive film in 1M HCl is best characterized as an amorphous Cr(III) oxide.

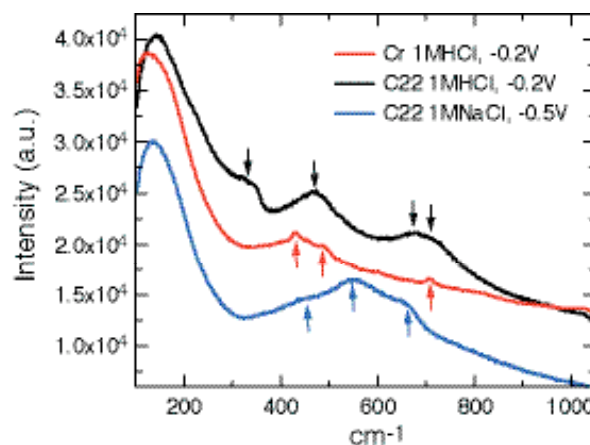


Figure 1. SERS of passive films of Cr and Alloy 22.

The peaks present in the SER spectrum of the passive film formed on Alloy 22 have not yet been assigned. Suffice to say, the spectrum does not match the spectrum of any known oxide/hydroxide of chromium. It is possible that molybdenum is present in the Alloy 22 passive film, but it is unlikely that nickel or iron contribute significantly to the Alloy 22 passive film in 1M HCl, since films were not formed on unalloyed nickel or iron in 1M HCl. At this time, it is safe to say that the passive films of Alloy 22 and Cr in 1M HCl are quite different.

In addition to the alloy's composition, the passive film depends on the pH of the electrolyte. Comparison of the SER spectra of Alloy 22 in 1M NaCl (-0.5V) and in 1M HCl (-0.2V) illustrates the strong influence of the electrolyte pH on the identities of Alloy 22 passive films (0.5V in 1M NaCl and -0.2V in 1M HCl have approximately the same hydrogen overpotential). The three, broad, overlapping peaks in the SERS of Alloy 22 film in 1M NaCl are tentatively assigned to a mixture of  $\text{Ni}(\text{OH})_2$ , which is most likely an outer layer, and  $\text{NiCr}_2\text{O}_4$ . Thus, lowering the pH from approximately 5.5 (1M NaCl) to 0 (1M HCl) converts the passive film from a mixture of  $\text{Ni}(\text{OH})_2$  and  $\text{NiCr}_2\text{O}_4$  to an amorphous Cr(III) oxide.



Our SERS results indicate that anions present in the electrolyte can absorb into the outer layer of the passive films. In chloride-free borate buffer (pH8.4) there is a critical potential above which borate ions absorb into the passive films. The ions are thought to absorb into the outer layer of the film rather than adsorb on the film's surface, because the anions remain part of the SER spectra until the potential is lowered considerably below the critical potential. A similar result was obtained for chloride ions in tests conducted in 1M NaCl and 1M HCl.

Electrochemical Quartz Crystal Microbalance (EQCM) measurements, Cyclic Polarization (CyP), Electrochemical Impedance Spectroscopy (EIS) and Mott-Schottky analysis (M-S) provide valuable information about various properties that strongly influence the protectiveness of the passive films. For example, EQCM measurements of chromium in borate buffer indicate that the formation of the passive film is not 100% efficient. That is, only a portion of the overall oxidation current goes into film growth. The remainder is attributed to alloy dissolution. Given that SERS indicates each of the Cr-rich passive films formed on Alloy 22, Alloy 600, Alloy 304SS, and unalloyed Cr, are different, it will be instructive to use EQCM to determine how protective each passive film is by measuring how much alloy dissolution accompanies film growth.

The combination of CyP, SERS, and EQCM tests have been especially valuable in investigating the oxidation of Cr0 to CrVI, a reaction that occurs at relatively high potentials and is thought to have an important negative influence on the alloy's resistance to pitting corrosion. Our results have found that Cr0 is oxidized to CrVI by a two-step process consisting of Cr0  $\rightarrow$  CrIII, followed by CrIII  $\rightarrow$  CrVI. At least some (if not all) of the CrVI is formed within the CrIII film, rather than at the film/electrolyte interface. The rate of the electrochemical reduction of CrVI formed during anodic polarization was unaffected by stirring of the electrolyte.

The EIS measurements indicate the films have very narrow space charge regions, <1 nm, which is consistent with the high values of immobile charge density ( $\sim 10^{21}/\text{cc}$ ) measured by M-S plots. The M-S plots also indicate the values of the flat band potentials of the passive films. The flat band potentials measured for Cr and Alloy 22 passive films in 1M HCl, 0.1M HCl, 0.1M  $\text{H}_2\text{SO}_4$  + 1M NaCl, 1M NaCl, and 0.1M borate buffer (pH8.4) are presented in Figure 2, along with the calculated values of the hydrogen equilibrium potential. In all electrolytes tested, the flat band potentials of Alloy 22,  $V_{fb}(\text{Alloy 22})$ , are approximately equal to the

hydrogen equilibrium potential,  $\Delta\phi_e(\text{H})$ , which indicates equilibrium between electrons in Alloy 22 passive film and electrons in the  $\text{H}/\text{H}^+$  redox couple. An alternative interpretation is that Alloy 22 passive film is so thin that electrons in Alloy 22 are in equilibrium with electrons in the  $\text{H}/\text{H}^+$  redox couple – i.e., electrons can tunnel through the film from (to) states in the alloy to (from) states in the  $\text{H}/\text{H}^+$  redox couple.

The low value of  $V_{fb}(\text{Cr})$  relative to the hydrogen equilibrium potential suggests that the flat band potential of Cr passive film is determined by ion adsorption rather than by electron transfer, which, as discussed above, is the case for the Alloy 22 passive film. That is, the flat band potential of Cr passive film is that potential at which the rates of ion

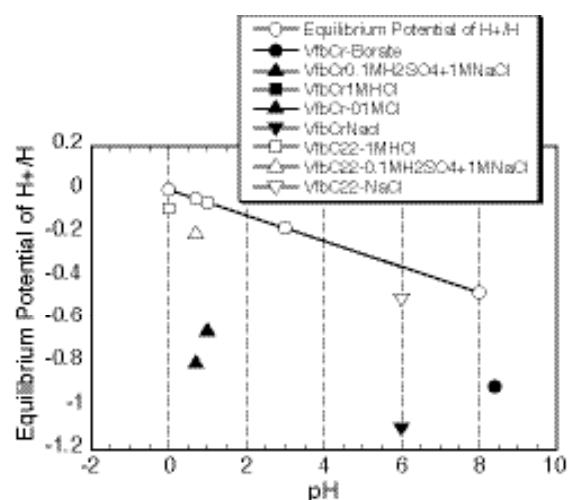


Figure 2.  $V_{fb}(\text{Alloy 22})$  – open points, and  $V_{fb}(\text{Cr})$  – solid points as a function of electrolyte's pH.

adsorption and desorption are equal. The largely different values of  $V_{fb}(\text{Alloy 22})$  and  $V_{fb}(\text{Cr})$  are consistent with the different SER spectra of Alloy 22's and Cr's passive films. The low value of  $V_{fb}(\text{Cr})$  compared to the value of  $V_{fb}(\text{Alloy 22})$  is also consistent with the higher rate of  $\text{H}^+$  reduction on the surface of Alloy 22 than on the surface of Cr.

In summary, our comprehensive *in situ* investigation of the passive films of Alloy 22, using five different experimental techniques, indicate the films are chromium-rich, but are distinct from the chromium-rich passive films that form on unalloyed chromium and on other nickel-chromium and iron-chromium alloys. The identities of the films are strong functions of the electrolyte's pH and the potential of film-formation.

# EVOLUTION OF CORROSION DAMAGE BY LOCALIZED CORROSION

## **Crevice-Corrosion Electrochemistry of Ni-Cr-Mo Alloys**

John R. Scully, Florent Bocher, and Francisco Presuel-Moreno, University of Virginia

## **Modeling of Critical Chemistry for Crevice Corrosion**

Robert G. Kelly, Andrew J. Hodges, and Francisco Presuel-Moreno, University of Virginia

## **Crevice-Corrosion Damage Function on Alloy 22**

David W. Shoesmith, Dmitrij Zagidulin, P. Jakupi, and James J. Noël, University of Western Ontario

## **Localized Corrosion Stability in the Presence of Non-Chloride Anions**

Roger C. Newman and David X. He, University of Toronto

## **Metallurgical Effects on Localized Corrosion of Ni-Cr-Mo Alloys**

Gerald S. Frankel, Rudolph G. Buchheit, Ajit Mishra, and Federico Gambina, Ohio State University

## **Processes in Crevice-Corrosion Propagation, Stifling, and Arrest**

Joe H. Payer, Xi Shan, Arun S. Agarwal, and Uziel Landau, Case Western Reserve University

## **Combinatorial Chemistry Approaches for Alloy Composition and Corrosion Behavior**

Rudolph G. Buchheit, Gerald S. Frankel and Fariaty Wang, Ohio State University

## **Prediction of the Time Evolution of Localized Corrosion Damage**

Digby D. Macdonald, Igor Nicic and George R. Engelhardt, Pennsylvania State University

---

This page intentionally left blank.



# Crevice-Corrosion Electrochemistry of Ni-Cr-Mo Alloys

John R. Scully, Florent Bocher, and Francisco Presuel-Moreno  
University of Virginia

## Research Objectives

The objective of this project is to understand the impact of electrochemical driving force (e.g., applied potential), physical and geometric conditions (e.g., temperature and crevice gap/depth), and unconventional crevice-former properties (e.g., semi-permeability and reactivity) on the crevice-corrosion susceptibility of Ni-Cr-Mo alloys. The test conditions and materials were selected to provide insight into the crevice corrosion of Alloy 22 (UNS N06022) in high-temperature multispecies brines. Additionally, crevice formers will simulate dust, debris, and other deposits. Lesser corrosion-resistant materials such as stainless steel AISI 316 (UNS S31600), Alloy 625 (UNS N06625), and a family of Ni-Cr-Mo alloys were introduced for comparison to Alloy 22.

## Approach

The focus is on the combination of anodic material properties, and physical and electrochemical conditions, that govern crevice corrosion of Ni-Cr-Mo alloys. Consequently, various test conditions are being implemented, including: proximate cathodes, limited and infinite cathodes, and porous crevice formers. Proximate and limited cathodes are linked to crevice corrosion occurring within a limited volume of solution (e.g., droplets such as might exist on a metal surface) where the cathode will be next to the crevice mouth and its current capacity will be limited by the wetted area outside the crevice. The porous crevice-former experiments are associated with the characteristics of the real life crevice formers, e.g., pieces of rock and dust particles. Some of these unconventional crevice-former characteristics have been reproduced in a controlled fashion, for instance by using O<sub>2</sub>-permeable crevice-former materials. The crevice-corrosion behavior of stainless steel AISI 316 and Alloys 625 and 22 under these conditions is being compared. This is accomplished by studying crevice corrosion initiation, propagation, and repassivation and/or stifling using coupled multi-electrode arrays in rescaled crevices, as well as with conventional multi-crevice assemblies (MCA), to verify trends seen in rescaled crevices. Scaling laws are used to rescale the crevice geometry to a larger length scale while keeping the electrochemical corrosion properties similar to those of a smaller natu-

ral crevice. Coupled multi-electrode arrays (CMEA) consisting of close-packed coupled electrodes are capable of obtaining local electrochemical information as a function of spatial location within crevices. CMEAs can provide combined spatial and temporal resolution of electrochemical properties within the rescaled crevice. The rescaled crevice provides unprecedented information on how a crevice anode initiates, propagates, and reorganizes under realistic conditions.

A related objective is to characterize Ni-Cr-Mo alloys' corrosion electrochemistry focusing on active dissolution properties relevant to isolated anodes, as a function of well-controlled artificial, acid-chloride crevice solutions. The solution chemistries for crevice corrosion range from solutions saturated in metal salts to dilute bulk solutions. The effects of metal alloy composition on conditions for depassivation and activation as well as active corrosion rates are determined. Critical crevice chemistries for active dissolution are defined. The anodic polarization behaviors of model Ni-22Cr-XMo alloys, Alloy 22 and Alloy 625, were previously studied in hydrochloric acid of various concentrations to crudely simulate critical crevice solutions at various percentages of dilution. In order to more accurately simulate crevice solution and crevice anode electrochemistry, HCl has been replaced by LiCl+HCl solution in this project to enable the independent control of the total chloride content and the pH and to provide more realistic simulants of crevice anolytes. The anodic polarization behaviors of alloys 625 and 22 as well as Ni-22Cr-XMo model alloys (X = 0, 3, 6, 9 and 13) are under study, using single microelectrodes in LiCl + HCl solutions. This E-i polarization behavior complements crevice studies and is used to help understand crevice behavior in CMEA. Subsequent modeling studies examine whether these electrochemical conditions can be met in realistic crevices. Data from isolated anode microelectrodes are free of artifacts and geometric effects, and thus can serve as valid E-i boundary conditions for input to modeling studies.

## Accomplishments

A database of E-i polarization behavior of model Ni-22Cr-XMo (X=0, 3, 6, 9 and 13) in HCl solutions of different concentrations (0.1 M, 1 M and 10 M HCl) and at different

temperatures (22°C, 50°C, and 85°C) was established and extended to alloys 625 and 22. Anodic polarization of those two alloys was also investigated in LiCl + HCl based solutions. These solutions' compositions are derived from the alloys' Ni, Cr, Mo, and Fe content, assuming congruent dissolution of the alloys and hydrolysis of  $\text{Cr}^{3+}$  as the main source of hydronium ions. The effect of the chloride concentration on the hydronium's activity is also taken into account.

The anodic polarization data provide E-i boundary conditions that are used to derive scaling laws. Scaling laws provide information concerning the crevice  $G/x_{\text{crit}}^2$  ratio ( $G$ : crevice gap,  $x_{\text{crit}}$ : critical crevice length where crevice corrosion initiates). The relationship between  $G$  and  $x_{\text{crit}}^2$  is linear up to a crevice gap of approximately 30 microns, depending on the materials, conditions, and model crevice-corrosion solutions used. For a given gap and equivalent environment, i.e., temperature and model crevice solution, it is found that the distance  $x_{\text{crit}}$  increases with the pitting resistance equivalent number (PREN) of the Ni-Cr-Mo alloys.

The array design provides the flexibility of arranging a number of electrodes both inside and outside of the crevice, so that the effect of highly aggressive crevice solution leaking outside the crevice can be studied. In a bulk environment of 0.6M NaCl, crevice corrosion initiates at higher potentials and temperatures as the PREN of the material increases. The initiation and propagation of crevice corrosion on a CMEA for Stainless Steel 316 and for Alloy 625 are shown in Figure 1 (a) and (b), respectively. It is notable that no crevice corrosion was observed for Alloy 22 at 50°C. Alloy 22 only suffered crevice corrosion at 90°C. This is consistent with the fact that its critical crevice temperature is reported to be approximately 85°C.

The impact of a proximate cathode on crevice corrosion of AISI 316, and Alloys 22 and 625 was also determined. It was found that, in the presence of a proximate cathode, crevice-corrosion initiation required a much higher applied potential and only occurred at deeper depths from the crevice mouth. The value of  $x_{\text{crit}}$  may increase beyond the physical depth of the debris when the cathode is close.

Crevice corrosion of a multi-crevice assembly (MCA) was initiated at high potentials using an infinite cathode

(potentiostat) and switched to galvanic coupling with decreasing finite cathode area. The effect of limited cathodic current on propagation and stifling of crevice corrosion is also studied for Alloys 22 and 625. These studies will be repeated using CMEAs.

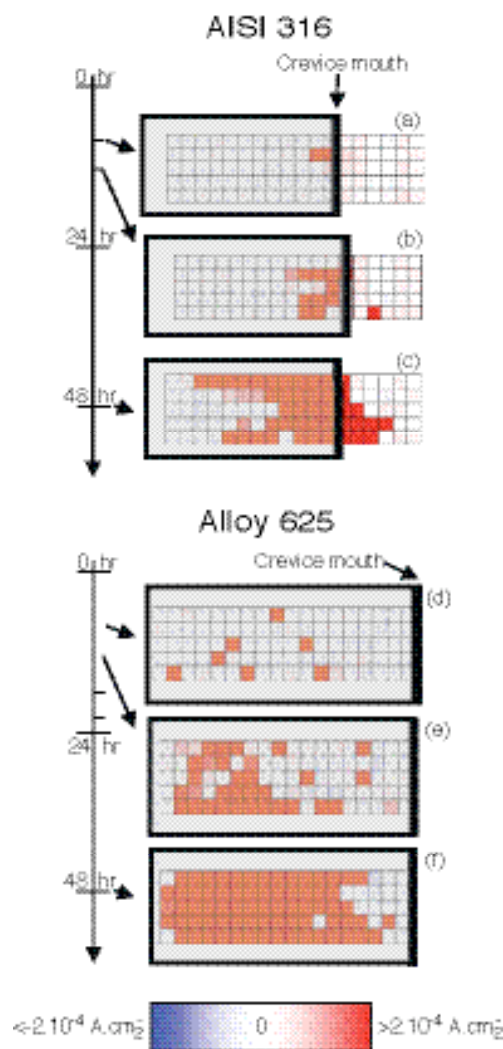


Figure 1. Comparison of crevice-corrosion initiation and propagation between stainless steel AISI 316 and Alloy 625 in 0.6 M NaCl at 50°C. The crevice mouth is indicated by the bold black line and the covered area within the shaded rectangle (not up to scale with the real life crevice former). (a) 7 hrs at 0  $V_{\text{SCE}}$ , (b) 11 hrs at 0  $V_{\text{SCE}}$ , and (c) 24 hrs at 0  $V_{\text{SCE}}$  + 24 hrs at 25  $mV_{\text{SCE}}$ ; (d) 18 hrs at 50  $mV_{\text{SCE}}$ , (e) 22 hrs at 50  $mV_{\text{SCE}}$ , and (f) 24 hrs at 50  $mV_{\text{SCE}}$  + 24 hrs at 75  $mV_{\text{SCE}}$ . "SCE" is saturated calomel electrode.



# Modeling of Critical Chemistry for Crevice Corrosion

R.G. Kelly, Andrew J. Hodges and Francisco Presuel-Moreno  
University of Virginia

## Research Objectives

A primary goal of this work is to establish a stronger scientific basis for the calculation of the stability of crevice-corrosion propagation for corrosion-resistant alloys (i.e., stainless steels, Ni-Cr-Mo-Fe alloys) under atmospheric exposure conditions. Of particular interest is the current demanded by a localized corrosion site as a function of crevice geometry, temperature, alloy composition, RH, and external solution layer composition. Augmenting this work has been the experimental study of crevice-corrosion stability using crevices with rigorously defined geometries.

## Approach

A previously developed crevice-corrosion computational code has been used to probe the ability of a crevice to maintain a region of active corrosion. The crevice has a set gap and length. The electrochemical kinetics for the Type 316L stainless steel and Ni-22Cr-6Mo were abstracted from literature data or from other projects in the DOE Corrosion Cooperative in order to quantify the effects of pH and chloride concentration on the dissolution kinetics. A series of crevice gap/length combinations were studied in which the initial solution within the occluded region was set to be sufficiently aggressive as to activate crevice corrosion. A transient analysis of the mass transport allowed a determination of whether that crevice corrosion could remain active—whether the dissolution within the crevice was sufficient to create additional low pH, high chloride solution faster than it could diffuse out of the crevice. In addition, the effects of high chloride concentrations on the activity of the hydrogen ion (leading to lower effective pH values) and on the conductivity were considered, as were the effects of the presence of cathodic reactions within the crevice.

The experimental work used microfabrication methods to produce crevice samples with gaps between 3 and 11 microns, and lengths between 1 and 8 mm. Experiments were conducted on Type 316 stainless steel in which the crevice was filled with an aggressive solution ( $\text{pH} < 1.5$ ,  $[\text{Cl}^-] > 1 \text{ M}$ ) before immersion in an electrolyte and the application of an applied potential. The ability of the crevice to maintain active corrosion was monitored by

measurement of the current. The initial solution composition was sufficiently aggressive to depassivate the surface. If the crevice geometry was not sufficiently occluded to maintain the critical chemistry, the crevice repassivated. Conversely, if the geometry restricts mass transport out of the crevice sufficiently, the dissolution rate can maintain the critical chemistry despite diffusion out of the crevice. Afterwards, crevice attack was verified and its location and depth quantified with a confocal laser scanning microscope.

## Accomplishments

The results of the modeling work show that the effects of the high chloride ion concentration on the activity coefficient for the hydrogen ion and conductivity are important in crevice stabilization. Figure 1 shows an example for Type 316L stainless steel. For a 1.2 micron gap, crevice corrosion is predicted to be stabilized only if these effects are taken into account. If they are not considered in the model, the crevice repassivates, i.e., the current rapidly falls to low values and decreases with longer times. It was also found that inclusion of cathodic reactions within the

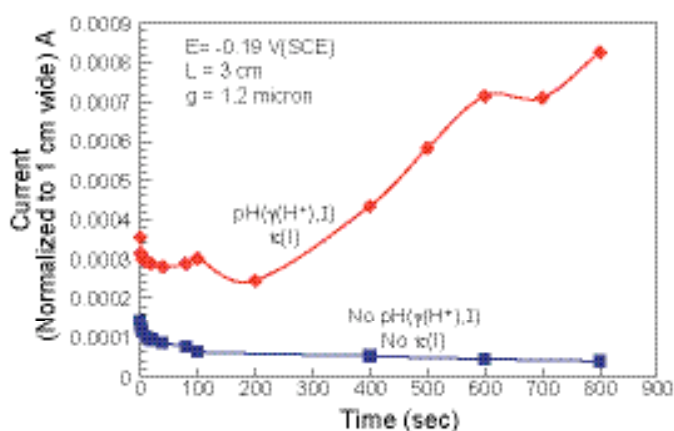


Figure 1. The effect of high chloride concentration (in terms of ionic strength,  $I$ ) on the stabilization of crevice corrosion in Type 316L stainless steel.

crevice hindered stabilization. The hindering of stabilization is due to the creation of hydroxyl ions within the crevice. These ions act to neutralize the acidity that is produced by the hydrolysis of the chromium formed by dissolution. As crevice corrosion can only be stabilized if the

crevice solution becomes highly acidic, the formation of hydroxyl within the crevice makes attainment and maintenance of the critical chemistry more difficult, and thus a tighter gap or more rapid dissolution kinetics are required.

Work on the Ni-22Cr-6Mo alloy showed that an initial crevice solution pH lower than -0.2 is required for a 1.2 micron gap to stabilize.

The modeling work has developed a tool that allows the effects of crevice geometry and material behavior (i.e., the electrochemical kinetics of the material in the range of crevice solutions) to be predicted. The experimental work had two major aspects: (1) growth laws for crevice-corrosion damage, and (2) crevice geometry effects on crevice stability. Alloy 22 crevice-corrosion samples from the work of Kehler et al. (2001) were analyzed using the confocal microscope to quantitatively assess the extent of damage. A wide range of damage extents was included. The slope of the graph for the volume of material removed versus the maximum depth allows an assessment of the type of crevice-corrosion growth that occurred. A slope of unity indicates growth as a cylinder, a slope of two indicates trench formation, and a slope of three is consistent with growth as a hemisphere. The best fit to the data was found when a slope of one was used at small amounts of damage (<50 microns), and a slope of two was used for depths of

attack between 50 and 500 microns. Thus, it appears that the crevice corrosion in these samples started as cylinders and then evolved into trenches.

By varying the crevice gap and crevice length independently, a critical ratio of crevice gap to length was found to be required to achieve critical crevice geometry and get a sufficiently large potential drop for crevice corrosion to remain active. Thus, the solid points in Figure 2 are gap/length combinations that supported stable crevice corrosion, whereas the samples represented by the open symbols repassivated. In addition, the standard Oldfield-Sutton model (Oldfield and Sutton, 1978) predicts that a tighter crevice gap is needed to support stable crevice corrosion than that determined in the present work. The experimental work has developed methods that can be applied to produce rigorously defined crevice geometries that allow controlled experiments to be conducted and compared to model predictions.

## References

- Kehler, B.A., G.O. Ilevbare, J.R. Scully, *Corrosion*, 57 (12) (2001), 1,042, 2001.
- Oldfield, J. W., and W.H. Sutton, *British Corrosion Journal*, 13, 104, 1978.

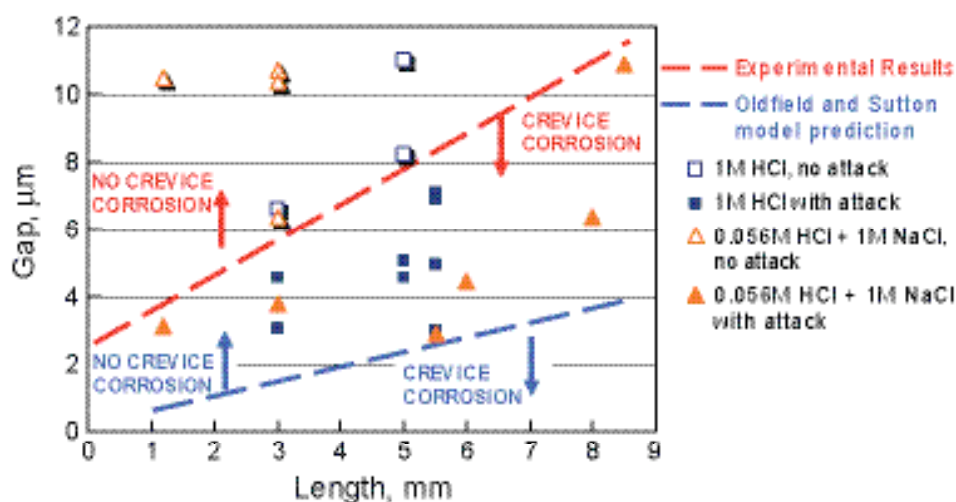


Figure 2. Crevice gap/length combinations that supported stable crevice corrosion (solid symbols), and samples for which the sample repassivated (open symbols). Also included is the line resulting from the classical model for crevice corrosion (Oldfield and Sutton, 1978). Material: SS316L, room temperature.

# Crevice-Corrosion Damage Function on Alloy-22

David W. Shoesmith, Dmitrij Zagidulin, Pellumb Jakupi, and Jamie Noël  
University of Western Ontario

## Research Objectives

This report presents the progress and status of the above project as part of the Materials Performance Thrust. Within the Materials Performance Thrust, leading faculty and researchers at universities and national laboratories are organized to address important issues for the long-term performance of waste package materials and other engineered materials. The primary goals of this research project are to develop a crevice-corrosion damage function that can be used to assess material penetration rates and to determine how the different alloying elements affect the crevice-corrosion resistance of Alloy 22.

## Approach

Current and potential thresholds have been established to delineate the conditions required to initiate and sustain active crevice propagation in 5 M NaCl solution at 120°C. Experimental results suggest that stifling and repassivation of crevice corrosion on Alloy 22 are caused by external cathode limitations and cathodic reaction starvation.

The chemical compositions of corrosion products and corroded regions have been characterized using a variety of surface analytical techniques such as: Energy Dispersive X-ray analysis (EDX), X-ray Photoelectron Spectroscopy (XPS), and Raman spectroscopy.

## Preliminary Technical Results

Initiation and subsequent crevice-corrosion propagation have been shown to be difficult on Alloy 22 under natural corrosion conditions, i.e., no applied electrochemical perturbations. Therefore the crevice corrosion of Alloy 22 was artificially initiated by a series of galvanostatic polarizations in 5M NaCl solutions at 120°C. This series of experiments showed that, independent of applied current (as long as it is large enough to initiate and maintain active crevice propagation), the measured potentials in these experiments were all shown to exceed +200 mV (in all experiments a saturated Ag/AgCl reference electrode was used) before they significantly decreased to a near-steady-state value of approximately -160 mV. This decrease in measured potential indicates the onset of

active propagation. For crevice initiation to be possible, two mandatory conditions must be satisfied—the creation of a critical chemistry, and the presence of a sufficient IR drop inside the crevice. Then, for crevices with the same tightness, higher currents will lead to shorter crevice initiation times, and for initiation and active propagation to occur, an applied current higher than 5  $\mu\text{A}$  is necessary. A series of these experiments have allowed us to establish current and potential thresholds for the establishment of the necessary combination of critical chemistry and IR drop for crevice corrosion on Alloy 22 under our experimental conditions. It should be noted that this threshold current depends on a number of parameters, including solution composition, temperature, crevice tightness, etc. The potential threshold is consistent with the results from Electrochemical Impedance Spectroscopy (EIS) and XPS experiments (described in a separate technical report) which show that the threshold of  $\sim 200$  mV vs. Ag/AgCl coincides with defect injection into the passive film, leading to a significant decrease in resistance.

Optical micrographs of the crevice-corroded regions of the Alloy 22 samples reveal the grain structure of the alloy. The grain boundaries were shown to be decorated with pits, and the grains to be partially covered with a corrosion product deposit. Closer inspection of the grain surfaces shows this deposit to be cracked and flaky. It is most likely that the grain surface was totally covered by this deposit, and that part of it was lost when it dried and fractured following emersion from solution. EDX analyses of the deposit-covered areas are dominated by Mo and W signals, whereas the composition of the uncovered areas is dominated by Ni and Cr, as expected for the alloy covered by a thin passive oxide formed on air exposure after the experiment. Under the very acidic conditions prevailing in an actively propagating crevice, Mo(VI) can create soluble compounds which become amorphous at higher pH. The surface analyses suggest that, during propagation, the surface of the grains becomes covered with such an amorphous Mo/W containing gel (which dries and cracks on emersion). It is possible that this deposited gel inhibits metal dissolution on the grain surface. Subsequent attempts to propagate corrosion in the grain boundaries may be inhibited for the same reason, leaving propagation across freshly

exposed grains as the only available route for ongoing corrosion. This could explain the observed limited propagation into the material and the much more extensive propagation across the surface.

Raman Spectroscopy analyses also showed an enrichment of Mo and W within the grain boundaries of the crevice-corroded area (Figure 1). Raman Spectroscopy data analysis (in progress) will reveal the exact Mo and

W chemistry involved (i.e., chemical bonding and oxidation states).

Therefore, the crevice-corrosion behavior in this alloy can be rationalized by considering the microchemistry imposed by the alloying elements. Moreover, additional work will be done to elucidate how the damage (penetration depth) evolves within the crevice-corroded regions with different applied propagation currents.

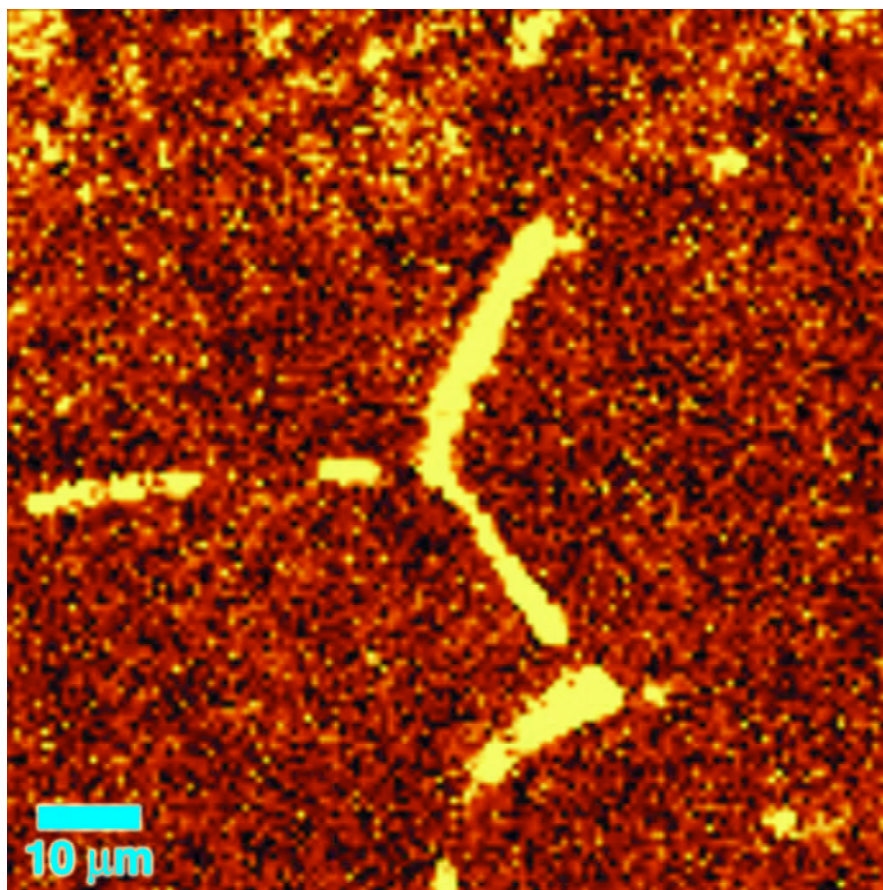


Figure 1. Raman map obtained from a crevice-corroded area. The signal intensity at each point is the integrated sum intensity for all Raman-active bands from 0 to 5,000  $\text{cm}^{-1}$ .



# Localized Corrosion Stability in the Presence of Non-Chloride Anions

Roger C. Newman and David X. He  
University of Toronto

## Research Objectives

This project is designed to generate rigorous electrochemical kinetic data for NiCrMo alloys in localized corrosion environments using the artificial pit technique, and then to measure and understand the effect of nitrate or other anions as inhibitors.

## Approach

The artificial pit, or pencil electrode, technique involves embedding a metal wire in resin and dissolving it from one end in a salt solution, so that the entire exposed surface acquires the condition of a localized corrosion surface (pit or crevice). This creates a one-dimensional mass-transport condition while simulating the metal dissolution and solution alteration (pH,  $[\text{Cl}^-]$ ) that occur within natural localized corrosion sites. The simplified mass-transport condition enables us to determine unambiguous kinetic parameters and to study the effect of inhibiting substances such as nitrate ions.

It is important to note that with modern instrumentation, the currents that can be measured from such electrodes cover the whole range, from penetration rates of microns per second to those that are of concern for the long-term propagation of tight crevices or underdeposit events in equipment, e.g., microns per year.

The conditions chosen for the study were dilute chloride and chloride/nitrate solutions, temperature 75–95°C. A series of Ni-22Cr-xMo alloys were fabricated into thin wires and used as artificial pit electrodes.

In addition to the dc measurements, it has been valuable to use electrochemical impedance spectroscopy to measure the solution resistance within the cavity. Depending on the conditions, the ionic resistance of an anodic salt film can be measured, and the conditions for salt film formation and dissolution can be examined.

## Accomplishments

There were two main aspects of the project that had to be completed. The first is the exhaustive measurement of kinetics in localized corrosion cavities; the second is the

elucidation of the effect of nitrate or other inhibitors. The nature of the first part is that not much can be published until the data are fully gathered and modeled using a finite difference procedure. We are still improving the input data (such as concentration-dependent diffusivity) that are required for this. The second aspect has shown unexpected departures from deterministic behavior that are very interesting but a little frustrating—since the *raison d'être* of the artificial pit technique is to obtain as nearly as possible deterministic behavior.

By relatively rapid back-scanning of the potential from the high-potential (diffusion controlled) condition, anodic kinetics of the alloys in the nearly saturated cavity solution were determined. These showed detailed differences from stainless steels, but nothing too surprising. Slower potential backscans allowed us to determine the response to dilution of the cavity solution. The blocking effect of alloyed Mo showed two sharp onsets: between 0 and 3% Mo, and between 9 and 13% Mo. The latter holds some interest in terms of practical considerations—the impedance study showed evidence for a resistive layer that only forms at high Mo content.

Progress has been made on the finite difference modeling of experiments where the cavity solution is allowed to dilute and the metal dissolution kinetics are measured at potentials similar to those prevailing in practice. Data have been obtained on concentration-dependent diffusivity that are essential for a properly modeled result. Surprisingly, in terms of critical concentration of pit solution, at 90°C there is not much effect of Mo content up to 9% on the repassivation condition.

In Figure 1, preliminary results for NiCr alloy show more immediate but less complete repassivation (indicated by rapid decrease of current) than 316SS on nitrate addition. This result, which has not been completely reproducible to date, is being examined. Even the 316SS shows a random element in the time to repassivation in extremely well-controlled, identical experiments. We are now working intensively on this aspect. Our hypothesis was that a 125  $\mu\text{m}$  wide artificial pit electrode, apparently dissolving uniformly, still has areas of active and passive state that move around with time. Impedance data have confirmed this suggestion, even for 316SS at room temperature. So



with nitrate present, there is a stochastic aspect in the repassivation event depending on these local sites and how they are impacted, individually, by nitrate ingress. There is a feedback process such that once repassivation

starts at one site, it tends to kill dissolution on the whole electrode. This may occur by runaway nitrate reduction accompanied by solution dilution.

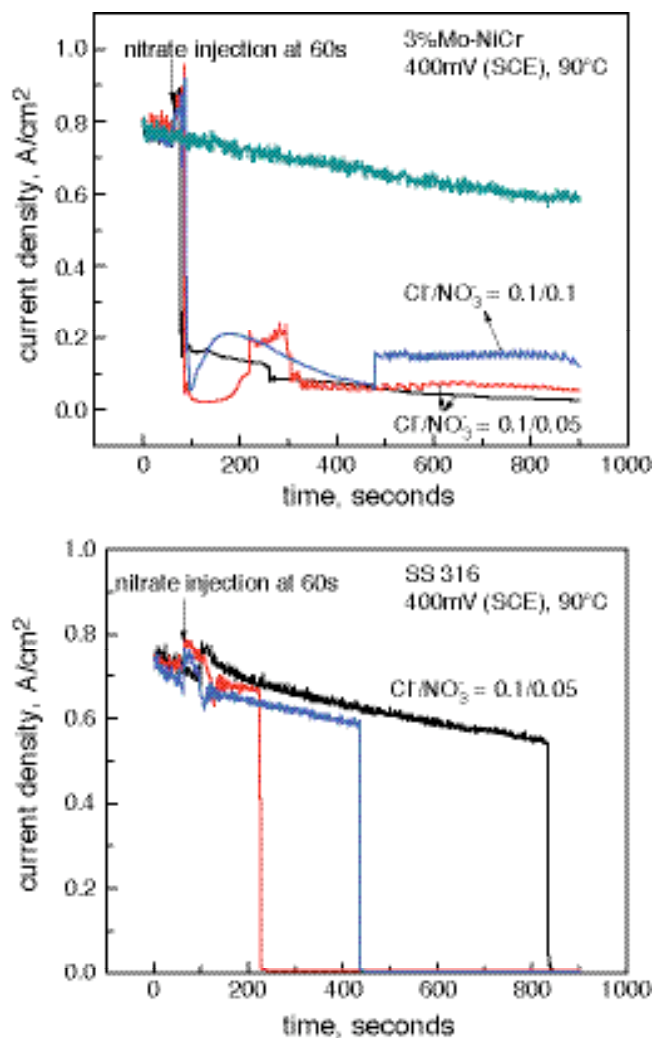


Figure 1. Current transients for Ni-22Cr-3Mo and SS316 upon injection of nitrate to the indicated molar levels after growth of an artificial pit cavity in pure 0.1M NaCl solution to ca. 400 microns depth at 90°C.

# Metallurgical Effects on Localized Corrosion of Ni-Cr-Mo Alloys

Gerald S. Frankel, Rudolph G. Buchheit, Ajit Mishra, and Federico Gambina  
Ohio State University

## Research Objectives

The objectives of this project are to study several metallurgical aspects of localized corrosion. These could include changes produced by welding and long-term aging on the corrosion resistance of Alloy 22.

## Approach

Alloy 22 is highly resistant to general and localized corrosion. However, in aggressive conditions of high chloride concentration, applied potentials, and temperature, it may suffer crevice corrosion, a form of localized corrosion. The effects of a variety of factors, including metallurgical factors, on localized corrosion are being studied. Cyclic potentiodynamic polarization (CPP) is a common technique for the assessment of localized corrosion in metallic alloys. However, the standard CPP methodology does not determine a conservative value of repassivation potential ( $E_{R,CREV}$ ) because the pit or crevice does not grow deep. A novel approach named the Tsujikawa-Hisamatsu Electrochemical (THE) technique is being used to assess crevice corrosion in Alloy 22, because it provides a more conservative value of  $E_{R,CREV}$ . One aspect of the current study is to assess the procedures used in the THE technique. The revised procedure has been used to study welded and nonwelded Alloy 22 and to evaluate the influence of various oxyanion species in solution. Oxyanions like nitrates can act as inhibitors of Alloy 22 corrosion in the presence of chloride.

## Accomplishments

The standard definition of Crevice Repassivation Potential ( $E_{R,CREV}$ ) in the THE technique is “the potential in step 3 where the current density does not increase with time and also not afterward,” shown as  $E_{R,CREV}(I)$  in Figure 1. In many cases, the assignment of this value is unclear because the current can increase again at lower potentials, indicating that crevice corrosion had not repassivated. This suggests that the first definition does not provide a conservative estimate of repassivation potential. In this work, a new definition of  $E_{R,CREV}$  has been evaluated.

$E_{R,CREV}(II)$  in Figure 1 is the potential at which the cur-

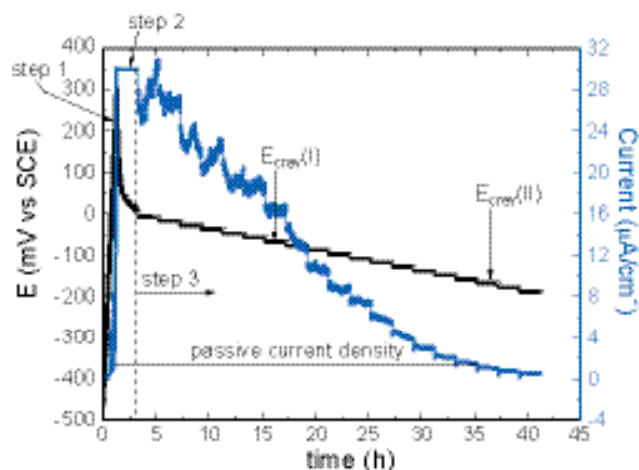


Figure 1. Schematic of THE technique showing different steps.

rent density reached the passive current density measured on the upward scan.

The difference between  $E_{R,CREV}(I)$  and  $E_{R,CREV}(II)$  is small (about 10 mV) when the hold current density in Step 2 is small,  $2.1 \mu\text{A}/\text{cm}^2$ . However, for a hold current density of  $30 \mu\text{A}/\text{cm}^2$ ,  $E_{R,CREV}(II)$  is 75–100 mV lower and much more reproducible. Thus, the newer definition of crevice repassivation potential in the THE technique is better because it is more conservative and reproducible. Further,  $E_{R,CREV}(II)$  for bulk and welded Alloy 22 specimens at  $90^\circ\text{C}$  is within 5–10 mV, indicating that the weld has similar susceptibility to crevice corrosion as the base metal. It should be noted that the passive current density measured on the upward scan might not be an accurate reflection of the true passive current density on the backwards scan, which is expected to be somewhat lower as a result of the excursion to higher potential. Nonetheless, the potential at that current density measured during the backscan is a figure of merit that provides a reproducible value.

The change in the definition of  $E_{R,CREV}$  enabled a change to the procedure for the THE technique that makes the test easier and faster. The potentiostatic steps in Step 3 were replaced by a potentiodynamic sweep at a scan rate of 0.167 or 0.0167 mV/s. The values of  $E_{R,CREV}(II)$  were found to be relatively independent of scan rate at 75 and

90°C and in 0.1 and 1.0M NaCl, and were similar to the values determined by the standard potential stepping approach.

The modified THE procedure was used to investigate the inhibitive effects of various oxyanions such as nitrate, sulfate, carbonate, and bicarbonate. A critical value of the ratio  $\text{NO}_3^-/\text{Cl}^-$  was found for complete inhibition of crevice corrosion. When  $\text{NO}_3^-/\text{Cl}^- > 0.2$  at 90°C, the apparent repassivation potential jumped by hundreds of mV, and no crevice corrosion was observed (Figure 2).

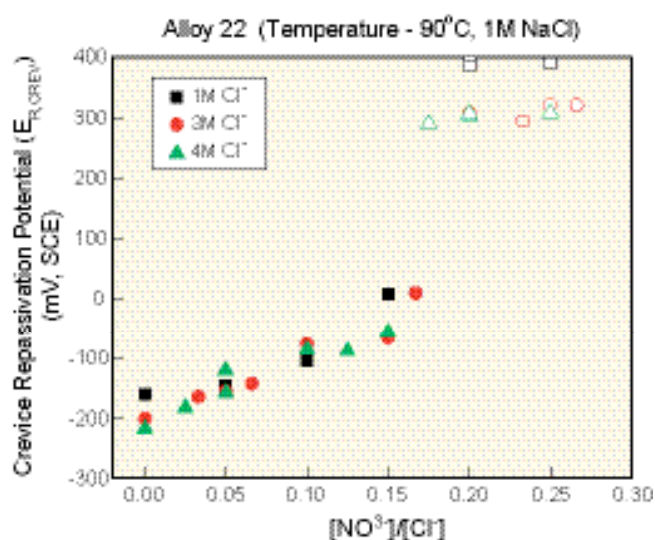


Figure 2. Effect of nitrate ions on inhibition of crevice corrosion of Alloy 22 in aggressive solution (open symbol indicates no crevice attack).

Addition of sulfate in a chloride environment also resulted in inhibition of crevice corrosion of Alloy 22, but a much higher concentration was needed. At 90°C, the critical

$\text{SO}_4^{2-}/\text{Cl}^-$  ratio for complete inhibition was 1.5 at 1.0 M  $\text{Cl}^-$  and 0.6 at 0.1 M  $\text{Cl}^-$ .

Interestingly, the amount of nitrate required for complete inhibition of crevice corrosion of Alloy 22 decreased slightly when sulfate was added to the chloride solution. Further, there was no negative effect of sulfate addition (both at high and low sulfate concentration) to nitrate inhibition in a chloride environment at high temperature.

Thus, it can be concluded that the concentration of strong inhibitor needed for complete inhibition of crevice corrosion of Alloy 22 in an aggressive environment decreased slightly when mixed with a weak inhibitor. Current work is investigating the effect of other inhibitive anions like carbonate and bicarbonate (individually and mixed) on the inhibition of crevice corrosion for Alloy 22 in an aggressive environment.

The THE technique was modified further to determine crevice repassivation temperature,  $T_{R, CREV}$ . In this new approach, the first two steps were identical to the standard THE technique, as shown in Figure 1. However, the third step consisted of holding the potential constant and decreasing the temperature stepwise, 2°C every 20 min. The current was monitored with time, and the temperature at which the current density in Step 3 reached the passive current density that was measured on the upward scan is defined as  $T_{R, CREV}$ . This experiment was performed in 1M NaCl solution at a hold current density of 3 or 7  $\mu\text{A}/\text{cm}^2$ , and the initial temperature in Step 3 was 90°C, for both bulk and as-welded Alloy 22 specimens.  $T_{R, CREV}$  was around 69 and 65°C for unwelded and welded Alloy 22, respectively.  $T_{R, CREV}$  was not strongly influenced by the hold current density for both bulk and as-welded Alloy 22 specimens. The lower  $T_{R, CREV}$  for the welded alloy indicates a slightly increased susceptibility to crevice corrosion.

# Processes in Crevice-Corrosion Propagation, Stifling, and Arrest

Joe H. Payer, Xi Shan, Arun S. Agarwal, and Uziel Landau  
Case Western Reserve University

## Research Objectives

The objective is to analyze crevice-corrosion-damage evolution for passive metals covered by layers of moisture, particulate, and deposits. A focus is the determination of the effect of the crevice former on localized corrosion damage propagation. In accelerated tests, crevice corrosion is forced to initiate by aggressive environments and applied potentials. Then, the post-initiation stages of propagation, stifling, and arrest are examined. Computational analysis of the creviced area is conducted for evolution of corrosion damage by modeling of the current flow and potential gradients coupled to process chemistry and electrochemistry.

## Approach

Our approach consists of a combination of experimental measurements of localized corrosion with various crevice formers, and analytical computations of the crevice damage profile as a function of crevice geometry, environment, and corrosion resistance of the metal. Standard crevice corrosion test methods are modified by (a) the use of metal, polymer, and ceramic materials as crevice formers and (b) the variation in size and shape of the crevices. The metal surface, deposits, and corrosion products are analyzed. Further post-test analysis includes 3-D reconstruction of corrosion damage profiles. Figure 1 shows the crevice test assembly, a crevice former, and post-test crevice-corrosion damage.

## Accomplishments

### Stages of Crevice Corrosion Damage Evolution

During constant potential tests, measurements of the current indicate the initiation and rate of crevice corrosion through the stages of propagation and any stifling or arrest. Four stages of crevice corrosion have been observed: initiation, propagation, stifling, and arrest. Typical results are shown in Figure 2. In many cases, after an incubation period the corrosion current increased, and then a number of stifling steps (decreased current) were observed followed by arrest (repassivation). The onset of crevice corrosion, the amount of damage observed, and the occurrence of sti-

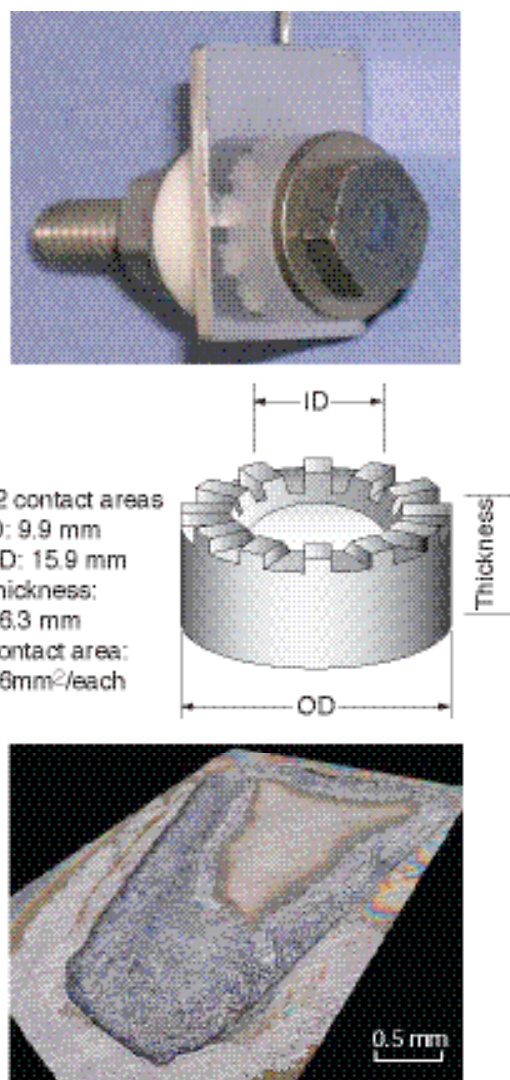


Figure 1. (a) A multi-crevice test assembly, (b) a schematic of the crevice former (12 contact areas) and (c) post-test micrograph of corrosion damage beneath one crevice contact area after an accelerated test.

fling or arrest depend upon the severity of the test conditions. Tests were interrupted after different levels of damage in order to examine damage evolution. Surface profiles after different amounts of damage (coulombs of corrosion) are shown in Figure 3.

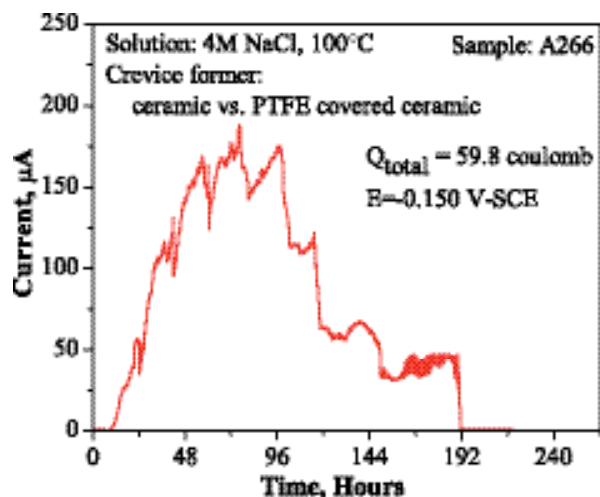


Figure 2. The current in constant potential tests indicates the initiation (current rise) and rate of corrosion throughout the test. Drops in current indicate stages of stifling and arrest of corrosion.

#### Effect of Crevice Former on Localized Corrosion

A necessary condition for crevice corrosion is that a crevice former must create a restricted geometry on the metal surface. Crevice corrosion is affected by the crevice geometry and properties of the crevice former. An important issue is how effective particulate layers and deposits are as crevice formers compared to metal/metal crevices and polymer/metal crevices used in laboratory tests. In head-to-head comparisons, the polymer-covered ceramic crevice former (an accelerated laboratory technique) was significantly more severe than a ceramic or a polymer alone.

#### Analysis of Corrosion Products and the Alloy Surface after Corrosion

For Alloy 22 (Ni-Cr-Mo-W alloy), the metal surface

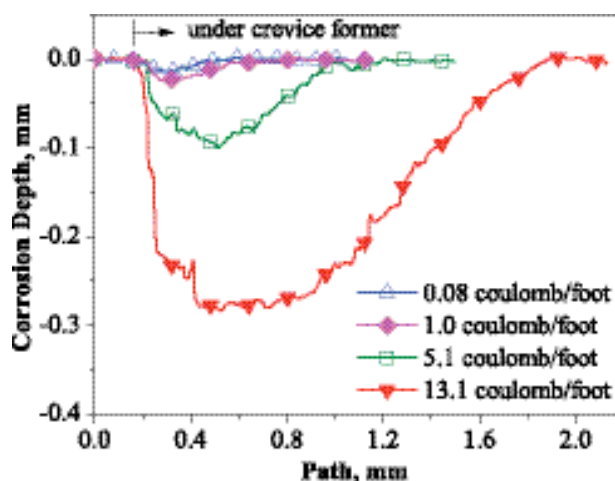


Figure 3. Corrosion damage profiles after different amounts of damage (coulombs of corrosion). The damage profiles indicate deepest penetration toward the outer edge of the contact area (foot) and propagation across the contact area.

beneath corrosion products had essentially the same composition as the bulk alloys, indicating congruent dissolution. The passive film under the corrosion products was a chromium oxide-type as is found on the bulk alloy. Corrosion products within the crevice area were enriched in Mo and W, two elements that increase the corrosion resistance of the alloy. The Ni was found to transport as a soluble ion from the crevice to the solution outside of the crevice.

This project addresses factors that affect the initiation, propagation, stifling, and arrest of localized corrosion. The findings are an important contribution to the determination of the penetration rate and extent of corrosion damage by localized corrosion over extremely long times.



# Combinatorial Chemistry Approaches for Alloy Composition and Corrosion Behavior

Rudolph G. Buchheit, Gerald S. Frankel, and Fariaty Wang  
Ohio State University

## Research Objectives

The objective of this project is to study the effect of alloy composition on the corrosion behavior of Ni-Cr-Mo alloys. The role of each alloying element was examined by analyzing the electrochemical response for different temperatures and solution chemistries. Correlation of alloy composition to localized corrosion behavior was constructed using multiple linear regression analysis on the electrochemical data collected.

## Approach

Ni-based solid solution alloys with variations in Cr (8 to 30% by weight) and Mo (3 to 25% by weight) content were fabricated using vacuum arc melting. The fabricated alloys were heat treated to develop more homogenized microstructure.

Electrochemical characterization was performed using a Multichannel Microelectrode Analyzer (MMA) (Scribner Associates, Inc., Southern Pines, NC). The MMA allows simultaneous measurement of multi-element working electrode arrays. Arrays used in this study were comprised of the different alloy compositions fabricated. Anodic and cathodic polarization curves were collected using this approach. Little variation in cathodic polarization behavior as a function of alloy chemistry was detected, and experiments have focused on composition dependence in the anodic polarization response. Anodic polarization measurements were carried out using dilute and acidified chloride solutions with temperatures ranging from 45 to 90°C.

Characteristic potentials (corrosion potential  $E_{\text{corr}}$ , critical pitting potential  $E_{\text{pit}}$ , transpassive potential  $E_{\text{tr}}$ , and repassivation potential  $E_{\text{repass}}$ ) extracted from the anodic responses of the Ni-Cr-Mo alloys in dilute sodium chloride solutions at various temperatures were used in multiple linear regression analysis, in order to relate their variation to alloy composition. The validity of these expressions was tested by comparing to characteristic potentials of the same Ni-Cr-Mo alloys measured in acidified chloride, sul-

fate, and nitrate solutions at various elevated temperatures.

## Accomplishments

Anodic polarization response of the alloys in a warm to hot dilute sodium chloride solution shows that alloys with low Cr and Mo experienced pitting. Alloys with very low Cr content (about 10 wt.%) suffer severe corrosion that looks more like uniform rather than localized corrosion,

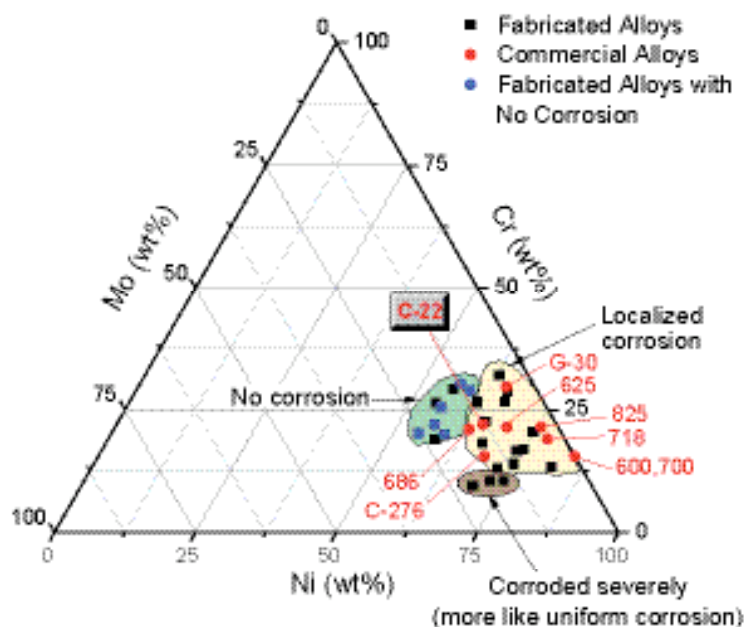


Figure 1. A Ni-Cr-Mo ternary diagram showing composition regions of alloys that experience severe uniform corrosion, localized corrosion, or are corrosion resistant.

while some alloys with moderate to high amount of Cr and Mo demonstrated high resistance to localized corrosion. The most corrosion resistant alloys have Cr content between 20 to 30 wt. % and Mo content between 12 to 25 wt. %. Figure 1 is a Ni-Cr-Mo ternary diagram showing regions of alloying composition that exhibited localized corrosion, susceptibility to severe (more uniform) corrosion, and corrosion resistance. Alloy 22 is close to the no-corrosion region. However, it should be noted that the effects of tungsten, iron, and other alloying elements in

Alloy 22 are not accounted for in this study.

Multiple linear regression analysis is performed on these anodic polarization data sets. The correlations between the breakdown potential ( $E_b$ ) and repassivation potential ( $E_{rp}$ ) with Cr and Mo content at different temperatures are shown in Table 1. It is observed that the role of Mo has become more significant as the temperature increases, as seen by the increasing Mo/Cr ratio in Table 1, particularly on the repassivation potential. The correlation factor for the breakdown potential at 45°C is low, because most alloys did not experience breakdown in that mild environment. Synergistic effects between elements have not been evaluated.

Anodic polarization measurements were also performed on the same Ni-Cr-Mo alloys in pH 2.75 mixed chloride-sulfate and nitrate solutions at 60, 80, and 95°C. Similar to the dilute sodium chloride experiments, the alloys

that show high resistance to breakdown are alloys with 20 to 30 wt.% Cr and 12 to 25 wt.% Mo. It is noted that there is a regular dependence between the breakdown potential estimated from the correlation equations from Table 1 and the experimental data. There is some dependency on the repassivation potential from the correlation equation to the experimental data, although it is less regular than the breakdown potential.

In stainless steels, Pitting Resistance Equivalency Number (PREN) is often used to rank pitting susceptibility based on the content of the alloying elements. Table I suggests that the correlation between alloy composition and localized corrosion behavior of Ni-Cr-Mo alloys is considerably different than that of stainless steels. As such, the PREN expression developed for stainless steels should be used with caution when assessing tendencies for localized corrosion of Ni-Cr-Mo alloys.

**Table 1. Equations that correlate breakdown ( $E_b$ ) and repassivation potentials ( $E_{rp}$ ) to Cr and Mo content obtained from multiple linear regression analysis on experimental data**

Temp (°C)	Fitting Results	R <sup>2</sup>	Mo/Cr
45	$E_b = 0.77(\text{wt\%Cr}) + 1.16(\text{wt\%Mo}) + 558.44$	0.57	1.5
60	$E_b = 7.95(\text{wt\%Cr}) + 12.99(\text{wt\%Mo}) + 133.82$	0.92	1.6
75	$E_b = 10.09(\text{wt\%Cr}) + 15.24(\text{wt\%Mo}) + 37.49$	0.85	1.5
90	$E_b = 7.79(\text{wt\%Cr}) + 18.69(\text{wt\%Mo}) - 26.5$	0.83	2.4

# Prediction of the Time Evolution of Localized Corrosion Damage

Digby D. Macdonald, Igor Nicic, and George R. Engelhardt (Consultant)  
Pennsylvania State University

## Research Objectives

The purpose of this project is to further identify the important electrochemical processes and parameters involved in long-term corrosion. More specifically, the project purpose involves development of theoretical models, use of electrochemical measurements, and calculating long-term evolution of corrosion damage.

## Approach

Both theoretical and experimental studies are under way to address the understanding of long-term corrosion prediction.

Chronoamperometry experiments have been performed on Type 316L stainless steel, and the transition from metastable pitting to stable pitting was observed, showing that 316L SS does exhibit typical pitting characteristics that have been observed for many other stainless steels. The purpose of this work was to experimentally determine the survival probability, which is the ratio of number of metastable pits that occur before a transition to a stable pit is observed, divided by the total number of metastable events. It is expected to be a function of  $[Cl^-]$ , potential, pH, temperature, etc.

An artificial pit has been developed and used to study the effect of pit depth on the “observed” critical breakdown potential. The artificial pit can also be used to study the separation of anodic and cathodic reactions and to understand how the length of the diffusion path affects the pit growth and repassivation.

Passivity breakdown is the initial event that occurs in the nucleation of localized corrosion damage. Accordingly, a viable mechanistic description of this phenomenon is important for the development of deterministic models for predicting the evolution of localized corrosion damage on metal and alloy surfaces. (Macdonald, 1999; Macdonald and Urquidi-Macdonald, 1992). One interesting observation is that most if not all metals and alloys display susceptibilities towards passivity breakdown that depend on anion size. Thus, for the stainless steels, iron, and nickel, the ability of halide ions to induce passivity breakdown lies in the order  $F^- < Cl^- > Br^- > I^-$ , whereas in the case of

titanium, the greatest susceptibility is induced by bromide ion. These observations suggest that ion size is an important, but not the sole, factor in determining the ability of an anion to induce passivity breakdown. This is because, while ion size changes monotonically along the halide series, the ability of the halide to induce passivity breakdown passes through a maximum.

The anion size effects on passivity breakdown are explored theoretically within the framework of the Point Defect Model (PDM). It is shown that the observed dependence of the breakdown potential on anion size can be accounted for at a semi-quantitative level by the PDM in terms of three factors that affect the absorption of the halide into surface oxygen vacancies: (1) the work of expansion of the vacancy to accommodate the adsorbing halide ion, (2) the accompanying entropy change, and (3) dehydration of the anion and possibly also of the surface oxygen vacancy. All three of these factors control the thermodynamics of anion absorption into a surface oxygen vacancy, but the impact that each has on the Gibbs energy of absorption occurs in opposite directions as the anion radius is changed. Thus, increasing ion size requires greater work to be performed in expanding the vacancy to accommodate the ion and hence gives rise to an increasingly positive contribution to  $\Delta G$ . Contrariwise, increasing anion size gives rise to a smaller positive contribution to  $\Delta G$  from the change in entropy and to a less positive Gibbs’ energy change for anion dehydration. These factors cause the Gibbs energy of adsorption to pass through a positive minimum as a function of ion size. For the passive films on iron, nickel, and stainless steels, the extremum in  $\Delta G$  occurs roughly at the ionic radius of  $Cl^-$ . Increasing the size of the oxygen vacancy results in a shift in the contribution to  $\Delta G$  from vacancy expansion to larger ionic radius, so that the minimum in  $\Delta G$  shifts in like manner. This effect is offered as the explanation as to why bromide ion is most aggressive in the case of passivity breakdown on titanium, whereas chloride is most aggressive in the case of iron, nickel, and the stainless steels, assuming that an oxygen vacancy in the surface of the passive film on titanium is larger than in the surface of the barrier layer on iron (or nickel). However, complete theoretical resolution of these effects will require careful definition of the sizes of surface oxygen vacancies in the barrier passive films on various metals and alloys.

Two problems regarding theoretical treatment of the accumulation of corrosion damage inside the crevice have been considered. First, we considered the accumulation of chloride or other aggressive anions inside the crevice, due to the establishment of a differential aeration cell. Second, we considered the development of a preliminary version of a code for deterministic Monte Carlo simulation of corrosion damage. Relative to the first problem, our main aim was to develop a relatively simple method for predicting the chloride concentration, pH, and potential distribution inside an active crevice. The current density inside pits,  $i_{pit}$  (i.e., the rate of pitting corrosion) can be described in general terms by the equation:

$$i_{pit} = k_A C_A^\lambda$$

where  $C_A$  is the concentration of the aggressive anions,  $k_A$  is the rate constant for the reaction proceeding in the anodic direction (which depends on potential and, in the general case, on pH), and  $\lambda$  is the effective kinetic order of the metal dissolution reaction with respect to the anion concentration. In many cases, the value of  $\lambda$  is between 0.5 and 1, which indicates that this dependence can be important. In addition, information about  $[Cl^-]$  is critical for predicting breakdown with the PDM, as this is the value that determines the passivity breakdown voltage and the rate of pit nucleation (MacDonald and Urquidi-Macdonald, 1987; 1989; 1992).

Experimental electrochemical impedance studies (EIS) and Mott-Schottky analysis of 316L SS have been performed to further validate the PDM. 316L SS was chosen because its passive film is primarily defective chromic oxide, which is the same as in Alloy 22, and because it is much more prone to corrosion than Alloy 22. The solution used was 0.2M borate buffer with the pH of 8.35. As a part of extracting kinetic parameters from impedance data, a code was developed.

## Accomplishments

1. We evaluated the impact of  $[Cl^-]$  and potential on the survival probability and reported the preliminary results.
2. We showed that the observed dependence of the breakdown potential on anion size can be accounted for at a semi-quantitative level by the PDM in terms of three factors that affect the absorption of the halide into surface oxygen vacancies.
3. We developed a simplified and very accurate analytical method for estimating chloride concentrations and potentials inside the crevice. It has been shown that the amplification factor for the chloride concentration is proportional to the passive corrosion current density and to the square of the crevice depth, and it is inversely proportional to the width of the crevice and to the chloride ion bulk concentration. Also, it has been shown that the influence of the external environment must be taken into account to quantitatively describe the transport processes inside the crevice.
4. We developed a preliminary model for Monte Carlo simulation of pitting corrosion damage inside the crevice has been developed.
5. We developed a code enabling us to perform non-linear regression while imposing constraints on the parameters to be optimized, as well as applying the most appropriate weighting functions to the EIS data.

## References

- Macdonald, D.D., Pure Appl. Chem., 71, 951, 1999.  
 Macdonald, D.D., and M. Urquidi-Macdonald, J. Electrochem. Soc., 134, 41, 1987.  
 Macdonald, D.D., and M. Urquidi-Macdonald, J. Electrochem. Soc., 136, 961, 1989.  
 Macdonald, D.D., and M. Urquidi-Macdonald, J. Electrochem. Soc., 139, 3434, 1992.

# EVOLUTION OF MOISTURE ENVIRONMENT ON METAL SURFACES

## **Modeling Chemical Environments within Corroding Crevices for Ni-Cr-Mo Alloys**

Peiming Wang, Ronald D. Springer, and Andre Anderko, OLI Inc.

## **Evolution of Solution Layer Chemistry during Localized Corrosion**

Robert G. Kelly and Z. Chen, University of Virginia

## **Modeling and Measurement of Current Distribution on Particulate and Deposited Layers**

Uziel Landau, Arun S. Agarwal, Xi Shan, and Joe H. Payer  
Case Western Reserve University

## **Microelectronic and MEMS Devices for Solution Properties and Corrosion Evaluations**

Chung-Chiun Liu, Meijun Shao, and Laurie Dudik, Case Western Reserve University

## **Optical Probes and Sensors to Determine Concentration Distributions in Thin Films on Reactive Surfaces**

William H. Smyrl and Francis Guillaume, University of Minnesota

## **High-Temperature Multi-Species Solution Properties and Behavior**

David R Cole, Lawrence M. Anovitz, Mirosław S. Gruszkiewicz, Donald A. Palmer, Jorgen Rosenqvist, David J. Wesolowski, and Leslie L. Wilson, Oak Ridge National Laboratory; Lawrence M. Anovitz, University of Tennessee; Andre Anderko, George Engelhardt, and Peiming Wang, OLI Systems; Digby D. Macdonald, Pennsylvania State University



---

This page intentionally left blank.

# Modeling Chemical Environments within Corroding Crevices for Ni-Cr-Mo-W-Fe Alloys

Peiming Wang, Ronald D. Springer, and Andre Anderko  
OLI Systems Inc.

## Research Objectives

The objective of this project is to develop a comprehensive model for the thermophysical properties of the environments that are likely to occur within corroding crevices in Ni-Cr-Mo-W-Fe alloys. Such a model is an important component for understanding the propagation, stifling, and inhibition of crevice corrosion.

The environments within actively growing crevices contain chloride solutions of dissolved metal species whose concentrations may reach or approach saturation. Further, the solutions are usually strongly acidic because of hydrolysis of metal cations, which drives the pH below the depassivation pH of the alloy. Thus, quantitative modeling of environments within growing crevices necessitates a comprehensive treatment of dissolution products of Ni, Cr, Mo, W, and Fe in acidic chloride solutions. Further, it is necessary to account for the effects of other common anions that may coexist with chlorides, especially sulfates and nitrates. The main properties of interest here are (1) the solubilities of various solid corrosion products, which provide the limits of concentrations in the anodic environment; (2) speciation of the solution, i.e., the chemical identity and distribution of species including products of hydrolysis and complexation; (3) activities of dissolved species, including the effective solution pH; (4) diffusivities and ionic conductivities of individual species, and (5) overall properties of the anodic solution, including ionic conductivity and density.

## Approach

Previously developed models have been shown to be capable of reproducing thermodynamic and transport properties of mixed-solvent electrolyte (MSE) systems in wide ranges of concentration and temperature. The MSE thermodynamic model has been shown in previous studies to be very accurate for representing the properties of complex, multicomponent salt solutions in wide concentration ranges (i.e., up to the fused salt or solid saturation limit). Therefore, it has been selected for modeling the properties of chemical environments that exist within the crevice as well as those outside of the crevice. Recently, it has been successfully applied to model deliquescence in Na-K-Mg-Ca-Cl-NO<sub>3</sub> systems.

In this work, we developed a self-consistent set of parameters for the Ni-Cr-Mo-W-Fe-H-Cl-SO<sub>4</sub>-NO<sub>3</sub> systems. The work was focused on the following tasks:

- (1) Literature search and critical evaluation of thermodynamic and transport property data for aqueous Ni-Cr-Mo-W-Fe-H-Cl-SO<sub>4</sub>-NO<sub>3</sub> mixtures. The data include phase equilibria, speciation data from spectroscopic and other measurements, pH data, heats of dilution and mixing, densities, diffusion coefficients, viscosity, and electrical conductivity. These data allow us to constrain thermodynamic and transport parameters to obtain a self-consistent model of crevice chemistry.
- (2) Development of thermodynamic parameters of the MSE model for systems containing Ni(II), Fe(II), Fe(III), Cr(III), Mo(III), Mo(IV), Mo(VI), and W(VI) in neutral and acidic solutions containing chlorides, nitrates, and sulfates.
- (3) Development of parameters for associated transport-property models. Specifically, electrical conductivity and self-diffusivity model parameters have been developed for aqueous chloride, nitrate, and sulfate solutions of Ni(II), Fe(II), Fe(III), and Cr(III), and for neutral and acidic solutions of Mo(VI) and W(VI). Transport property model parameters have been developed based on the speciation obtained from thermodynamic equilibrium calculations.

Attention was focused on the properties of relevant salt subsystems and mixtures containing both salts and corresponding acids. This treatment ensured that the model realistically reproduces the crevice environments, which are acidic during the propagation of localized corrosion.

## Accomplishments

Thermodynamic and transport property data have been successfully reproduced for the following classes of systems:

- (1) Chlorides, sulfates, and nitrates of chromium (III),

nickel (II), and iron (II and III)

- (2) Systems combining the metal chlorides, sulfates, and nitrates with hydrochloric, sulfuric, and nitric acids
- (3) Molybdenum (III, IV, and VI) and tungsten (VI) oxides and their mixtures with hydrochloric, sulfuric, and nitric acids.

Because of the predictive nature of the model, accurate reproduction of the properties of the above systems ensures the correct representation of the properties of mixed Ni-Cr-Mo-W-Fe systems. This has been demonstrated using available data for the dissolution of alloys including both pH values and solubility limits.

Figure 1 illustrates the representation of pH data in systems containing Cr(III) ions. The agreement with experimental data indicates that the hydrolysis of ions is accurately reproduced. Figure 2 shows the calculated and experimental solubilities of  $\text{WO}_3$  in HCl and  $\text{HNO}_3$ . As shown in the figure, the  $\text{Cl}^-$  and  $\text{NO}_3^-$  ions have a markedly different effect on the solubility of  $\text{WO}_3$  at higher acid concentrations, which can be expected to correlate with the behavior of passive films.

The MSE models for thermodynamic and transport properties have been implemented in a general software system.

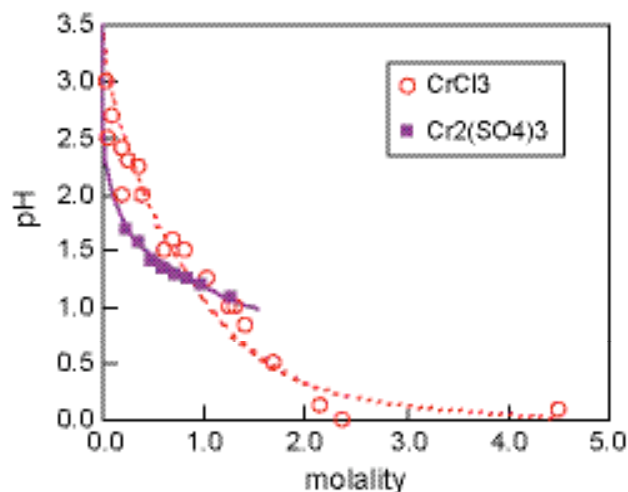


Figure 1. Comparison of calculated and experimental pH values for  $\text{CrCl}_3$  and  $\text{Cr}_2(\text{SO}_4)_3$  solutions. The data are from Mankowski and Szklarska-Smialowska (*CorrSci* . 1975, 15, 493) and Vinokurov et al. (*RussJCoordChem* . 2004, 30, 496).

Coupled with a graphical user interface, the software can be used to calculate all the necessary thermodynamic and transport properties. Alternatively, a callable module can be used to provide thermophysical properties to other higher-level programs. The callable version can be used as a phase equilibrium and thermophysical property generator for programs that model the evolution of crevice corrosion.

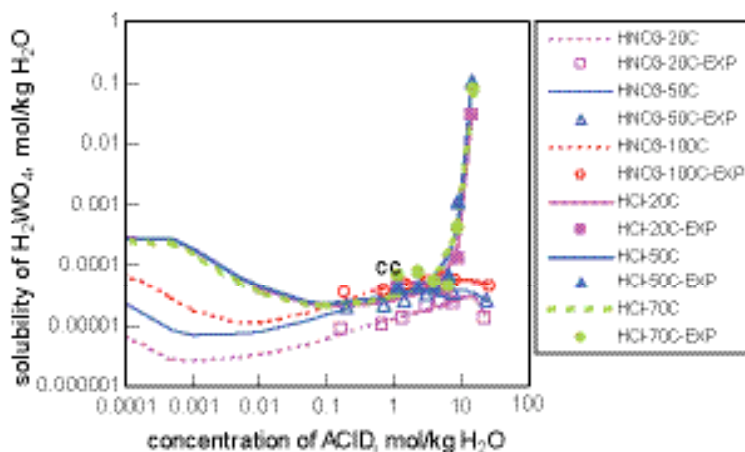


Figure 2. Comparison of the effects of chloride and nitrate ions on the solubility of W(VI) oxide in acidic solutions. The thick lines indicate a steep increase in solubility as a function of  $\text{Cl}^-$  concentration, whereas a weak decrease is observed for  $\text{NO}_3^-$  ions. The data are from Meerson and Mikhailova (*RussJInorgChem* . 1967, 12, 849) and Wood (*Geochim Cosmochim. Acta* 1992, 56, 1827).

# Evolution of Solution Layer Chemistry in the Presence of Dust

R. G. Kelly and Zhuoyuan Chen  
University of Virginia

## Research Objectives

The goal of this study is to investigate the ability of a wetted metal surface of limited area to support an active localized corrosion site via the production of cathodic current. Studies of cathodic control of localized corrosion of corrosion-resistant alloys are sparse, and studies considering thin electrolyte layers are essentially nonexistent. Quantification of the total current that a wetted surface could deliver under a given set of conditions provides a scientific basis for analyses of both the maximum rate and the stability of localized corrosion. These results will be coupled with complementary calculations of the requirements of localized corrosion sites for current to remain stable.

## Approach

An analytical method for evaluating the stability of pitting corrosion of corrosion-resistant alloys under thin-layer conditions was sought. The method utilizes the concept of an equivalent cathode (Chen et al., 2007; Chen and Kelly, 2007) to calculate the maximum cathodic current, termed the cathode capacity, that can be provided by a surface exposed to a given set of atmospheric conditions, i.e., temperature, relative humidity (RH), and deposition density of salt. Knowledge of the geometry of the cathode and its electrochemical kinetics are needed as input, as is deliquescence data for the salt of interest.

The anode demand (the minimum current required to maintain stability in a localized corrosion site) can be calculated via the Galvele pit stability criterion, and depends on the localized corrosion site geometry and the pit stability product, which is a material property. By coupling these two approaches, the stability of a pit or other localized corrosion site can be determined for a given environmental scenario. The method has been applied to the atmospheric pitting corrosion of Type 316L stainless steel, leading to a quantitative description of limiting stable pit sizes.

## Accomplishments

The analytical equations developed for both one- and two-dimensional geometries have been validated against finite element calculations. The equations have then been exer-

cised for a variety of atmospheric scenarios to develop quantitative descriptions of the total cathode current available. Figure 1 shows an example for Type 316L stainless steel. For a circular cathode surrounding a circular pit, a linear dependence of the total cathode current on the deposition density was found. In addition, the total cathode current increases with increasing pit size due to the decrease in the approach resistance for a larger pit. This effect allows a larger cathode area to participate.

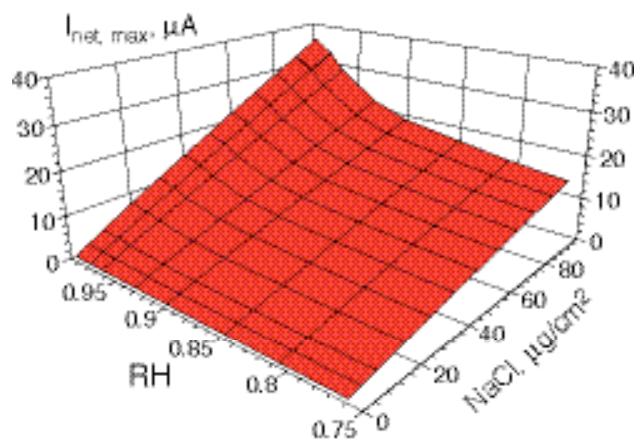


Figure 1. The effect of relative humidity and amount of deposited NaCl particles on the cathode capacity of SS 316L under atmospheric exposure. The cathode is circular around a pit with radius of 10  $\mu\text{m}$ . Temperature is 25°C.

The coupling of the cathode capacity equations to a localized corrosion site stability criterion is shown in Figure 2 for several scenarios. At high RH and deposition density, the cathode capacity curve ( $I_{\text{net}}$ ) exceeds the anode demand ( $I_{\text{LC}}$ ) for pit sizes below 39 microns. Thus, pits below this size can grow stably. However, once a pit reaches 39 microns, it can no longer grow with the cathode being considered. It must either fully repassivate or stifle in such a way that only a portion of its surface remains active.

If the RH is lowered to 85%, the maximum stable pit size decreases to less than 20 microns; similarly, if much of the salt were washed off, the maximum stable pit size falls to below 10 microns. Under these conditions, previously

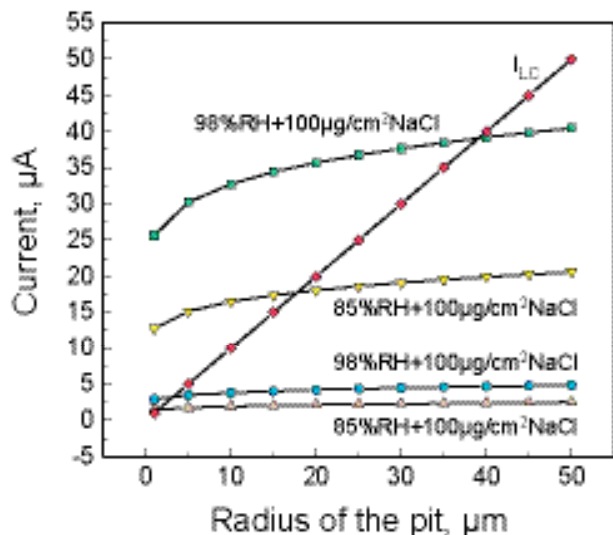


Figure 2. The effect of the radius of the pit on the circular cathode capacity,  $I_{\text{net, max}}$ , and anodic current demand,  $I_{\text{LC}}$ . Material: 316L, room temperature.

grown pits would be unable to continue to grow, and the driving force for repassivation would be very high.

One strength of the analytical modeling is its dependence on data that are straightforward to obtain for a given exposure scenario. A great deal of salt deliquescence data exists, and generation of new data is straightforward. The cathodic kinetics can be measured in the solutions expected under full immersion conditions, with the increased oxygen reduction current experienced under thin-film conditions taken into account. Finally, the pit stability product has been determined for some materials, and the methods to do so for others are established.

A second strength of the approach is the fact that it provides a bounding estimate of total cathodic current, in the sense that a given cathode cannot produce more current than that calculated. The assumptions inherent in the calculation are that (1) the chemistry and kinetics are fixed, (2) the thin film solution has no particulate in it, and (3) the cathode surface is perfectly wetted. In reality, the pH at cathode sites rises with time from a near-neutral starting solution, and the cathodic kinetics then slow. In most engineering applications, there is dust and other particulate that would tend to increase resistivity, thereby reducing the  $I_{\text{net}}$  because more voltage is lost to ohmic drop. Finally, any contact angle less than  $180^\circ$  would lead to less cathode area available to supply current.

Thus, this work provides a framework for evaluating the effects of both material and environmental parameters on the bounding conditions for localized corrosion stability.

## Related Publication

- Chen, Z.Y. F. Cui, and R.G. Kelly, Computational modeling of the stability of crevice corrosion of wetted SS316L. ECS Transactions (in press), 3, 2007.
- Chen, Z.Y., and R.G. Kelly, An analytical modeling method for calculating the maximum cathode current deliverable by a circular cathode under atmospheric exposure. In: Simulation of Electrochemical Processes II., V.G. DeGiorgi, C.A. Brebbia, and R.A. Adey, eds., WIT Press, Boston, pp. 33-42, 2007.
- Payer, J. H., and R.G. Kelly, Processes contributing to the stifling and arrest of localized corrosion. In: Scientific Basis for Nuclear Waste Management XXX, D.S. Dunn, C. Poinssot, and B. Begg, eds., Mater. Res. Soc. Symp. Proc. 985, Paper 0985-NN08-01, Warrendale, PA, 2007.



# Modeling and Measurement of Current Distribution for Localized Corrosion in Thin Layers of Particulates and Electrolyte Films

Uziel Landau, Arun Agarwal, Xi Shan, and Joe H. Payer  
Case Western Reserve University

## Research Objectives

The objective is to model the current patterns and distribution in thin layers of moisture and layers of moist particulates and deposits on metal surfaces. Of particular interest is the flow of current representative of corrosion scenarios at the metal surface: pitting, crevice corrosion, stress corrosion cracking, and galvanic action. Layer thicknesses range from monolayer coverage to thicker particulate layers. Results provide important insights for cathodic stifling processes, effects of surface roughness and particulates within a crevice, and the evolution of surface profiles from crevice-corrosion damage.

## Approach

The project examines geometric effects, saturated and unsaturated particulate layers, chemical composition of moisture and particulates, temperature, and relative humidity. A less complex representation that is amenable to straightforward treatment was developed for the crevice-corrosion system depicted in Figure 1(a). The heterogeneous, particulate-containing film was represented in terms of a simplified equivalent system with smooth surfaces and homogeneous electrolytes, as shown in Figure 1(b). The ohmic effects due to surface irregularities and the presence of particles were accounted for by specific treatments based on system properties.

## Accomplishments

### External Cathode

The presence of particulates in thin electrolyte films covering the freely exposed external metal surface could significantly reduce the ability of the cathode to support metal dissolution under the crevice former, by increasing the ohmic potential drop between the cathode and the internal anode. This effect was quantified by representing the heterogeneous electrolyte in terms of a homogeneous electrolyte, accounting for the particles' effects through two corrections; (1) an effective conductivity ( $K_{eff}$ ) of an equivalent homogenous electrolyte was defined based on the volume fraction occupied by particles ( $\phi_p$ ) using Bruggeman's equation:

$$K_{eff} = K(1 - \phi_p)^{3/2}$$

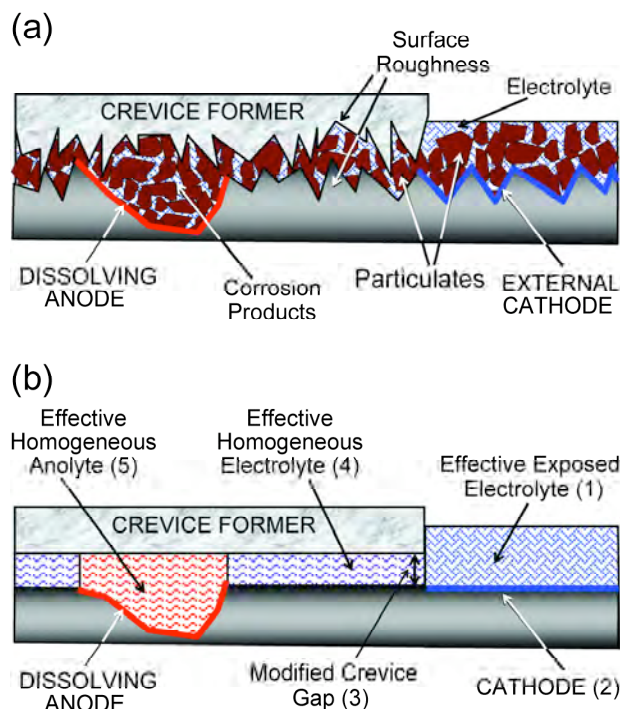


Figure 1. (a) Schematic diagram of a crevice-corrosion system indicating the various elements (particulates and surface roughness) contributing to ohmic limitations; (b) equivalent "simplified" crevice-corrosion system with (1) exposed electrolyte conductivity modified to account for the particulates on the cathode, (2) cathode kinetics adjusted for area coverage by particles; (3) equivalent smooth crevice gap obtained by constriction factor analysis for surface roughness; (4) equivalent conductivity for particles under crevice former, and (5) effective conductivity of the anolyte at the dissolution site for solid corrosion products.

and (2) the effect of the surface area coverage by the inert particles was accounted for by applying a modified kinetics parameter (exchange current density,  $i_0'$ ) based on total ( $A_T$ ) and exposed ( $A_E$ ) electrode area:

$$i_0' = i_0 \times A_E/A_T$$

Cathode current capacities (maximum current the cathode can produce) for the heterogeneous systems where current and potential fields are numerically simulated in particle-containing electrolyte were found to be in good agreement (less than 5% variation) with those obtained for homogeneous electrolytes, with corrections for the particles effects, as depicted in Figure 2. Particles with varying shapes and

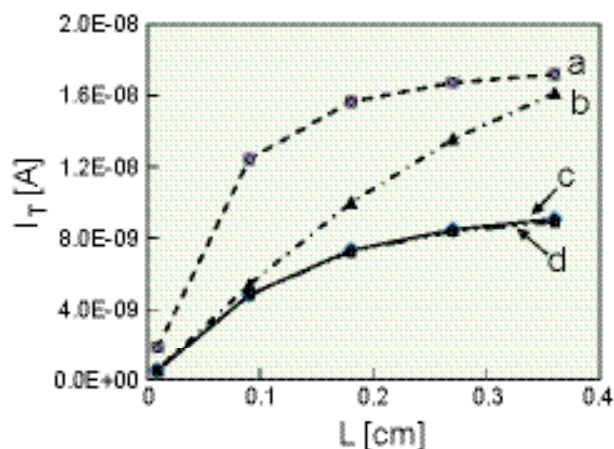


Figure 2. Effect of the cathode length ( $L$ ) on the total current capacities ( $I_T$ ) for the various particle effect models: (a) homogenous electrolyte corrected only for the solution conductivity, (b) homogenous electrolyte corrected only for the area coverage effect, (c) complete 3-D simulations of particulate layer (dashed line), (d) simulation of an equivalent homogenous electrolyte applying corrections for the solution conductivity and area coverage effects (solid line). Clearly, the equivalent presentation with both corrections provides excellent agreement with the detailed 3-D simulation.

arrangement, including multilayers, were analyzed, and the results corroborated the above findings. Effects of particles on cathode capacity and saturation length (no appreciable increase in capacity beyond this length) were also modeled.

### Within the Crevice

The volume blockage effect of particles under the crevice former could be due to dust deposition, precipitation of deposits, and solid corrosion products. This effect was modeled by applying an effective conductivity using Bruggeman's equation (Equation 1). The resulting potential drop was found to be in agreement with the heterogeneous electrolyte (particulate-containing) model.

The surface roughness associated with the crevice former and the metal substrate is expected to form constrictions along the narrow passages, leading to high localized ohmic drop. In order to model this effect, the crevice was represented in terms of an equivalent "idealized" smooth crevice by calculating a constriction factor based on the cross-sectional gap profile. A comparison of the constriction factor correction to a full 3-D numerical simulation indicated the validity of the approach over a broad range of parameters. The effect of solid corrosion product accumulation on corrosion propagation at the dissolution site under the crevice former was modeled by decreasing the

local conductivity, based on the volume fraction occupied by the particles. As damage evolves, the volume of accumulated solid oxides resulting from metal dissolution increases and the local conductivity,  $K_{eff}$ , decreases. The subsequent corrosion profiles were observed to propagate the damage evolution preferentially towards the crevice mouth (Figure 3). This effect was not seen in the system modeled without particulate accumulation. In the latter, a symmetrical cylinder-like propagation was observed at the corroding site.

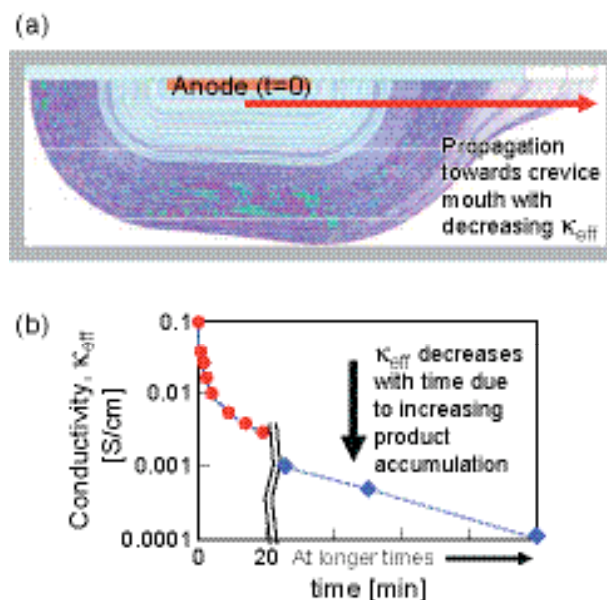


Figure 3. (a) Corrosion profile evolution in the presence of solid oxide accumulation. (b) Effective conductivity ( $K_{eff}$ ) at corrosion site based on accumulated particle volume as a function of time.

### Analytical Modeling

One-dimensional analytical models were developed for determining the current distribution along the cathode and for the cathode capacity in the thin electrolyte films. These models were found to be in excellent agreement with numerical results for cathodic polarization kinetics. The analysis provides scaling parameters, such as the Wagner number, for predicting the current distribution non-uniformity as a function of process parameters.

This work quantifies the ohmic effects imposed by geometrical features associated with crevices formed in thin electrolyte films, including particulates. It also determines the conditions where corrosion is limited or completely stifled due to constraints on the cathodic currents necessary to support localized corrosion.

# Microelectronic and MEMS Devices for Solution Properties and Corrosion Evaluations

Chung-Chiun Liu, Meijun Shao, and Laurie Dudik  
Case Western Reserve University

## Research Objectives

This research focuses on the design and fabrication of microsensors to assess critical environmental parameters that can affect the corrosion of metal covered by a thin layer of particulates. The important parameters include temperature, pH, solution conductivity, oxidizing potential, and oxygen concentration. The results of this research will provide a better understanding of how these environmental parameters affect the corrosion of metal covered by a thin layer of particulates.

One of the important objectives is to experimentally obtain the needed information for establishing the diffusion coefficient of dissolved oxygen in the presence of a thin sand or other particulate layer. Knowing the diffusion coefficient of dissolved oxygen in the presence of a thin particulate layer will be useful for assessing the potential corrosion in thin layers of electrolytes and in electrolyte with particulates.

## Approach

Microfabrication processing is used for the production of these sensors. Both thick film and thin film metallization techniques are used in the fabrication of the sensor prototypes. All of these sensors are operated in the electrochemical mode, even though the reaction mechanisms are different in each. For example, the solid state Pd/PdO pH sensor is operated in a potentiometric mode, whereas the oxygen sensor is operated in an amperometric mode. For conductivity measurement, high frequency (1000 Hz) alternating current is used, avoiding any potential effect on the solution.

## Accomplishments

Microfabrication processing was successfully conducted to produce the microsensors. A thin film metallization technique was used to fabricate the conductivity microsensors; thick film technique was used to produce the other environmental sensors. A silicon substrate was employed for the thin film microsensors, whereas an alumina substrate was employed for the thick film microsensors. For the conductivity sensor, various dimensions of electrode width,

electrode length, tip width, and gap width were used. A general statement can be made about the results of the conductivity study: At a fixed electrode distance, the resistance decreased as the depth of the testing solution increased at a lower frequency range. At a high frequency (i.e., 10,000 Hz or higher), the solution depth showed no appreciable effect on the resistance. Thus, in our study, a frequency of 1,000 Hz was used successfully.

The present work focused on the modifications of the thick film pH and oxygen sensor. Experimental measurements of pH and dissolved oxygen concentrations in the testing solution in the presence of a sand layer were carried out.

Palladium/palladium oxide pH sensors have two versions, one a three-electrode configuration and the other a two-electrode configuration. We found the potentiometric mode of operation to perform reasonably well. Figure 1 shows one version of different sizes of the pH sensor prototypes. The electrode elements and the insulation layer are all printed by thick film processing using appropriate metallic and insulation inks, a highly cost-effective process. A very good linear relationship exists between the output of the micro-pH sensor and the pH value of the testing medium. It is important to recognize that the increase or decrease in thickness of the sand layer in the

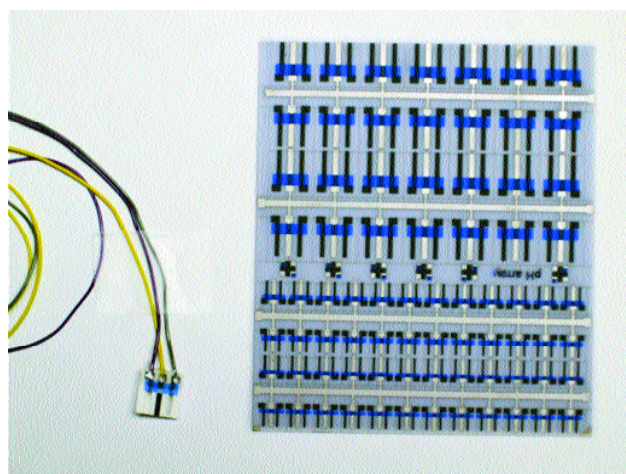


Figure 1. Thick film screen pH sensor prototypes.

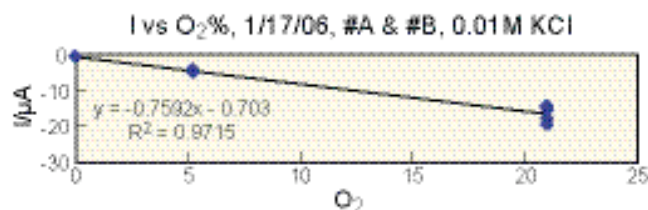


Figure 2. Performance of the oxygen sensor over a concentration range of 0 to 21% V/V.

testing solution does not affect the pH value of the testing medium. The results obtained in the pH measurements, and the approach of using thick film screen-printing technology for manufacturing this micro-pH sensor, indicate that this micro-pH sensor can be used effectively for environmental or corrosion-of-metal assessment in the presence of various sand (or similar material) layer thicknesses.

The fabricated oxygen sensor had a three-electrode configuration. Both the working and the counter electrodes are gold with the reference electrode Ag/AgCl. Thick film screen-printing processes were used to produce the sensor prototype, on an alumina substrate. The sensor was operated in the amperometric mode, and a reduction potential of -0.6 V versus the Ag/AgCl electrode was applied. The reduction current of oxygen was then used to quantify the oxygen concentration. In the experimental measurements, a 0.01M KCl was used as the testing medium, with an oxygen concentration range of 0 to 21% V/V. The sand layer thickness varied from 3 to 10 mm. Four oxygen sensors were tested each time. Figure 2 shows the relationship between the typical reduction current and the oxygen concentration.

To evaluate the diffusion coefficient of the dissolved oxygen in the sand layer, the established Cottrell equation is used:

$$I = nFAC_0\sqrt{\frac{D}{\pi t}}$$

in which  $n$  is the number of electron transfer (4 in this case),  $F$  is the Faraday constant,  $A$  is the surface area of the working electrode, which is  $0.015 \text{ cm}^2$ , and  $C_0$  used is  $.281 \times 10^{-6} \text{ mol/cm}^3$  at  $21^\circ\text{C}$ . The current  $I$  was then measured as a function of time. The diffusion coefficient is calculated.

The oxygen diffusion coefficient in an aqueous solution is reported in the literature as  $20 \times 10^{-6} \text{ cm}^2/\text{sec}$ . In our studies, the experimental results showed that the oxygen diffusion coefficient at  $21^\circ\text{C}$  was  $9.5 \times 10^{-6} \text{ cm}^2/\text{sec}$  and  $3.1 \times 10^{-6} \text{ cm}^2/\text{sec}$  for a thickness of sand or similar particulate layer of 3 mm and 10 mm, respectively. These results are reasonable and are useful for this study.

Microsensor development and measurement of dissolved oxygen within the testing medium, in the presence of various sand-layer thicknesses, is important. As stated previously, evaluating the diffusion coefficient of dissolved oxygen in the presence of a sand or particulate layer is a major objective of this research endeavor. The result of this study will add to our knowledge about the role of dissolved oxygen in the corrosion of metal covered with a thin layer of particulates.





# Optical Probes and Sensors to Determine Concentration Distributions in Thin Films on Reactive Surfaces

William H. Smyrl and Francis Guillaume  
University of Minnesota

## Research Objectives

The objective was to reveal the reaction distributions on heterogeneous, reactive metal surfaces. Previous work has revealed the current/potential distributions at individual reactive sites and at arrays of sites that may be galvanically coupled on metal surfaces, including those under thin films of electrolytes. Fluorescence techniques are powerful tools to measure physico-chemical conditions (pH, gas concentration) and anolyte species *in situ*. These have been adapted in previous work in our laboratory to monitor localized corrosion on aluminum alloys with a submicrometric spatial resolution. The goal in the present study has been to design fluorescent multiprobe sensors capable of monitoring oxygen partial pressure, pH, and specific metal ions at and near reactive (corroding) surfaces. In addition, there has been interest in extending the studies to reaction and concentration distributions at metal surfaces under particulate layers.

## Approach

The fluorescent sensor probes were based on isolating the probes in matrix hosts to prevent dissolution of the dyes in the aqueous electrolytes. The matrix host must fulfill several criteria that include: (1) optical transparency to facilitate measurements without interference due to inherent fluorescence from the matrix; (2) solubility of the dye(s) in the matrix; (3) matrix must not quench the dye fluorescence; (4) matrix must be permeable to oxygen, to H<sup>+</sup> ions, or to metal cations; (5) sensor must not consume the species to be sensed; (6) sensor must be reversible, and; (7) the immobilized dye must not leach out from the matrix. It was discovered that these criteria were difficult to satisfy.

## Accomplishments

### Oxygen Sensor Results

A miniature optical sensor was developed and has been shown to measure oxygen in the gas and liquid phases.

It utilizes the fluorescence of a ruthenium dye immobilized in a poly(dimethylsiloxane)(PDMS) matrix for sensing. The fluorescence is quenched in the presence of oxygen, but oxygen is not consumed in the process. The techniques for assembly and for operation of the sensor were developed. Future developments may include oxygen depletion in crevice corrosion and other localized corrosion processes. Further miniaturization may enable one to use the sensor on a scanning fiber to image the concentration field of oxygen around reactive sites on a metal immersed in solution.

### pH Sensor Results

The fluorescence intensity versus pH was measured for a derivatized optical fiber (DOF) immersed in solution. A 470 nm Panasonic blue light emitting diode (LED) was used as the excitation source. The sensor response time was not measured, but appeared to be extremely fast (<1 second). The fluorescence characteristics were similar to those found for the dye dissolved in aqueous solution. It was discovered that the intensity at the end points of pH 2 and pH 10 are too high. This was due to dye leakage from the polymerized acrylamide gel matrix. Results were obtained with an improved dual fiber configuration consisting of a single-mode fiber coupled to an Ar ion laser as illumination and a DOF multimode fiber for sensing. The two fibers were assembled side-by-side in a glass capillary, embedded in epoxy, polished at the end, and treated as above to form the photo-polymerized acrylamide host plus dye on the multimode fiber. The dual fiber configuration gave useful spectra with virtually no distortion of the fluorescein spectrum. This new configuration was adopted for experiments for pH sensing. Then the photo-polymerization of acrylamide gels was adopted to formation of thin films for pH sensing/monitoring. Dye leakage from the polymerized matrix was not solved by modifying the photo-polymerization solution. The leakage caused hysteresis and the termination of the approach. Several approaches for pH sensor development were studied. None was completely successful.



---

This page intentionally left blank.

# High-Temperature Multi-Species Solution Properties and Behavior

David R. Cole<sup>1</sup>, Lawrence N. Anovitz<sup>1,2</sup>, Mirosław S. Gruszkiewicz<sup>1</sup>, Donald A. Palmer<sup>1</sup>, Jorgen Rosenqvist<sup>1</sup>, David J. Wesolowski<sup>1</sup>, Leslie L. Wilson<sup>1</sup>, Andre Anderko<sup>3</sup>, George Engelhardt<sup>3</sup>, Peming Wang<sup>3</sup>, and Digby D. Macdonald<sup>4</sup>

<sup>1</sup>Oak Ridge National Laboratory (ORNL) | <sup>2</sup>University of Tennessee | <sup>3</sup>OLI Systems Inc. | <sup>4</sup>Pennsylvania State University

## Project Objectives

This project is aimed at developing an enhanced scientific understanding of the behavior of high-temperature, multi-species solutions. Earlier in the reporting period, the goals were to complete the study of the partitioning of mineral acids from liquid water to steam as a function of temperature, and the scoping study of the effect of tuff particles on brine chemistry. Some of these earlier results were transmitted to OLI Systems for use in their chemical modeling subtask in order to enhance our understanding of the corrosion evolutionary path of a metal alloy–aqueous system. More recently, we have initiated an effort to determine the solution chemistry associated with actively corroding crevices, in particular, the speciation of W, Mo, and Cr in concentrated brines relevant to the localized crevice environment.

## Approach

The approach in this phase of the project was to take advantage of unique experimental techniques developed at ORNL: (1) to use a high temperature volatility apparatus to quantify liquid/vapor interactions as a function of temperature, solution composition, prevailing humidity, and time; (2) to use high temperature *in situ* pH cells to determine the pH of brines interacting with volcanic tuff as a function of temperature, solution composition, and time; and (3) to incorporate the experimental results into a Mixed-Solvent Electrolyte (MSE) computer model database to enhance our understanding of the corrosion evolutionary path of the system. A new subtask focuses on using spectroscopic and *in situ* pH methods to determine the speciation and thermodynamic stability of metal ions found in active crevices on alloy surfaces as a function of temperature, solution composition, and acidity.

## Accomplishments

### Partitioning of Anions from the Liquid Film to the Vapor Phase

Experiments were completed utilizing the ORNL volatility apparatus to determine the partitioning constants of the inorganic acids of fluoride, nitrate, chloride, and bisulfate over the temperature range of 60 to 200°C. The liquid

phase was composed of sodium salts of acids, with the pH of the solution being controlled by the acid dissociation constant of bisulfate that is known from published results from our laboratory (Dickson et al., 1990). Knowledge of pH is critical, as it dictates the concentrations of these acids in the liquid phase that are known to be many orders of magnitude more volatile than their corresponding sodium salts. The results have been obtained using a crude activity coefficient model at this time until OLI Systems can process the data to derive accurate coefficients. The approximate order of volatility for these acids is  $\text{HF} \gg \text{HNO}_3 > \text{HCl} > \text{H}_2\text{SO}_4$ . Indeed, this initial treatment of the data did not include the association of the relatively weak acid, HF, and this correction will only enhance the partitioning constant further.

The implications of these results are that in an open system, fluoride will readily be lost to the air from solution, and this effect will also tend to raise the pH of the remaining solution as HF is lost. Secondly, nitrate is more volatile than chloride by about a factor of two over the range of temperatures investigated here, noting that the partitioning constants of all electrolytes increase dramatically as the critical temperature of water is approached. Finally, sulfate will only partition significantly from a liquid film to the surroundings at low pH and may be considered to be less volatile at all conditions than the other three mineral acids.

### Solution Chemistry Associated with the Interaction of Tuff Particles with Brine

Batches of well-characterized volcanic tuff powders were reacted with NaCl brines at 0.1 and 1.0 molal ionic strength and a starting  $\text{pH}_m \{ \equiv -\log(\text{mH}^+) \}$  ranging from 1 to 3 at 80–120°C for periods up to two weeks. Figure 1 is a representative plot, showing that the powdered tuff (surface area 3.5 m<sup>2</sup>/g) is able to increase the pH of the solution significantly over relatively short time periods (days). Comparison of the X-ray diffraction patterns of the starting material and run products indicates the formation of the clay mineral montmorillonite during the reaction with abundant alkali feldspar in the tuff with the acidic brine. These preliminary experiments demonstrate that the tuff itself has a significant capacity to rapidly neutralize acidic solutions that might be encountered on a tuff-dust-covered metal surface at elevated temperatures.

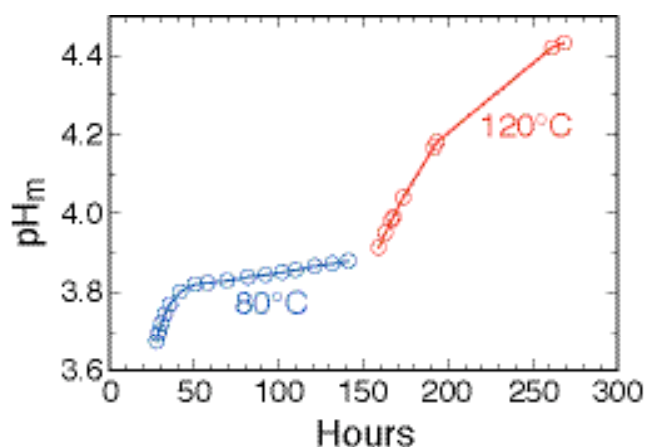


Figure 1. Plot of measured  $\text{pH}_m$  for a 41.5 grams of a starting aqueous solution of  $\text{pH}_m = 3.0$  and ionic strength 1.0 molal (NaCl) reacted with 1.07 grams of tuff sample as a function of time in the stirred hydrogen-electrode cell.

### Solution Chemistry Associated with an Actively Corroding Crevice

This new task was initiated to obtain thermodynamic data on the interaction of specific metal ions (i.e., Cr(III), Ni(II), Fe(II), Mo(V,VI) and W(VI)) with highly acidic chloride and nitrate brines to 120°C. We currently have been investigating the speciation of W(VI) at elevated temperatures. A number of potentiometric titrations of  $\text{Na}_2\text{WO}_4$  solutions at 50°C in 5.0 molal  $\text{NaNO}_3$  ionic medium have been performed using an automatic titrator (Figure 2). The value “ $n$ ” in the figure is defined as the total number of ‘missing’ protons (i.e., the difference between the concentration of  $\text{H}^+$  calculated from the input solution compositions and the measured  $\text{H}^+$  concentration) divided by the total metal concentration in solution at each titration point. The steep slopes of the curves in the pH-range 5.5–6.5

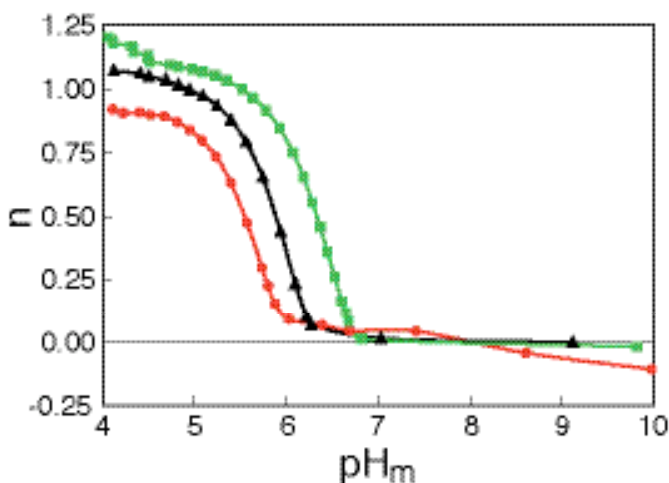


Figure 2. Proton uptake by  $\text{WO}_4$  versus  $\text{pH}_m$   $n$  is defined as the average number of protons per  $\text{WO}_4$  unit. Green squares = 0.003 molal total  $\text{WO}_4$ . Black triangles = 0.001 molal total  $\text{WO}_4$ . Red circles = 0.0003 molal total  $\text{WO}_4$ .

indicate formation of polynuclear species. The relatively large shift of the curves to lower pH with decreasing total  $\text{WO}_4$  concentration and the noninteger values of the plateaus below pH 5 also suggest that the solution speciation is dominated by larger polynuclear species. The identity of these polynuclear species is being assessed by a combination of an ultraviolet/visible information system (UV/VIS) and Raman spectroscopy.

### Related Publications

Dickson, A.G., D.J. Wesolowski, D.A. Palmer, and R.E. Mesmer, Dissociation constant of bisulfate ion in aqueous sodium chloride solutions to 250°C. *J. Phys. Chem.*, 94, 7978–7985, 1990.

---

This page intentionally left blank.



Parallel overlying drifts in the Hazel-Atlas Mine



# NATURAL BARRIERS THRUST

Yvonne Tsang, Natural Barriers Thrust

Lawrence Berkeley National Laboratory (LBNL)

Contact: 510.486.7047 | Yvonne\_Tsang@ymp.gov

## Introduction

For the Office of the Chief Scientist (an office within the Office of Civilian Radioactive Waste Management, U.S. Department of Energy), the Natural Barriers Thrust supports scientific studies of the natural system at the proposed repository site of Yucca Mountain. This natural system is composed of the unsaturated zone and the saturated zones at that site, and the hydrothermal-chemical environment within the emplacement drifts. The Natural Barriers Thrust stresses the realistic representation of the natural system with respect to processes and parameters, by means of laboratory, field, and modeling studies.

During the last 20 years, a substantial amount of research has been devoted to Yucca Mountain by the Office of Civilian Radioactive Waste Management (OCRWM). Site characterization of Yucca Mountain has been successfully carried out through experiments in tens of deep surface-based boreholes (reaching the water table), and in an underground facility. Extensive computational models have also been developed to simulate and understand the relevant processes at the site. However, in spite of the quantity of data collected and the knowledge acquired, the complexity of processes in the fractured rock, as well as the general scarcity of studies in the unsaturated zone fractured rock prior to the recent research on Yucca Mountain, make it necessary for the project to adopt significant conservatism in the Total System Performance Assessment (TSPA). This conservatism has been noted by many review committees. In an International Peer Review of the Yucca Mountain Project (YMP) TSPA for Site Recommendation, the Nuclear Energy Agency (NEA) of the Organization for Economic Cooperation and Development (OECD), and the International Atomic Energy Agency (IAEA), wrote that (*Total System Performance Assessment for the Site Recommendation (TSPA-SR)/OECD, Paris, 2002, page 12*):

...demonstrating understanding should be complementary to demonstrating compliance and of at least equal importance. Two approaches are needed. The first is to present what is considered to be a realistic (i.e., nonconservative) analysis of the

likely performance of the repository using realistic assumptions and data....The second approach is an analysis for compliance purposes where conservative assumptions and parameter values are used to make the case more defensible.

More recently, NEA wrote (*Post-closure Safety Case for Geological Repositories, Nature and Purpose (OECD, Paris, 2004), pp. 43–44*), regarding a TSPA analysis related to showing compliance:

Due to the use of pessimistic parameter values and conservative assumptions, the performance of the repository is likely to be more favourable than that indicated by the analyses. Conservatism of the analyses constitutes an additional qualitative argument for safety, although conservatism in and of itself may also be interpreted as a lack of knowledge, and may thus detract from confidence. Conservatism is inevitable, and greatly to be preferred to optimism, but should be used and managed judiciously.

The Natural Barriers Thrust recognizes that conservatism may be interpreted as a lack of knowledge, and aims to reduce conservatism through increasing knowledge. We believe that if certain key conservatisms can be successfully addressed, it may be that it can then be shown that Yucca Mountain provides sufficient public health protection—even in the unlikely event that engineered systems have lost their integrity earlier than expected.

The proposed 2005 Environmental Protection Agency (EPA) two-tier standard with requirements beyond the original period of 10,000 years emphasizes the significance of the natural system's contribution to repository performance over geological time scales. Human civilization with recorded history has existed for approximately 10,000 years. On the other hand, geologic records over tens of thousands to millions of years are well established for natural attributes.

## Basic Elements of the Natural Barriers Thrust

From the repository drifts to the accessible environment, the basic elements of the Natural Barriers Thrust are:

1. Drift Seepage
2. In-drift Environment
3. Drift Shadow
4. Unsaturated Zone (UZ) Flow and Transport
5. Saturated Zone (SZ) Flow and Transport.

As illustrated in Figure 1, the natural system components are interrelated and coupled to waste form and waste packages within the drifts, encompassing the unsaturated zone (UZ), through the saturated zone (SZ), to the compliance boundary, 20 km from the repository (where a well is schematically shown).

## Drift Seepage

Representation of drift seepage and the amount and chemistry of water contacting waste packages and waste in the current Yucca Mountain approach is believed to be conservative. The Natural Barriers Thrust is investigating various ways of obtaining an improved understanding of the seepage process under different repository conditions. This effort includes enhanced data collection to reduce uncertainty, investigation of coupled processes during the thermal period, and the use of natural ventilation to greatly reduce or eliminate seepage.

- *Suppression of seepage by natural ventilation.* Ventilation and heat-induced circulation, caused by air-density variations resulting from temperature differences within drifts, can lead to evaporation and removal of moisture, preventing moisture from contacting waste packages. It is likely that these processes prevent drip formation and

thus seepage into the drifts, thus alleviating the need for costly in-drift engineered components.

- *Self-sealing due to chemical precipitation around the drift.* This results from coupled thermal, hydrological, chemical, and mechanical processes; it could change the flow pattern around the drift, greatly reducing seepage into drifts.

## In-Drift Environment

The in-drift chemical environment plays a key role in determining the potential extent of waste package corrosion and the subsequent possibility of radionuclide release into the near-field rock. In the current Yucca Mountain Project approach, the coupled thermal, hydrological, and chemical processes within the drift are described by several zero- or one-dimensional models, which leads to multiple accounting of water available for waste dissolution and thus to a conservative representation of the drift barrier function in prevent-

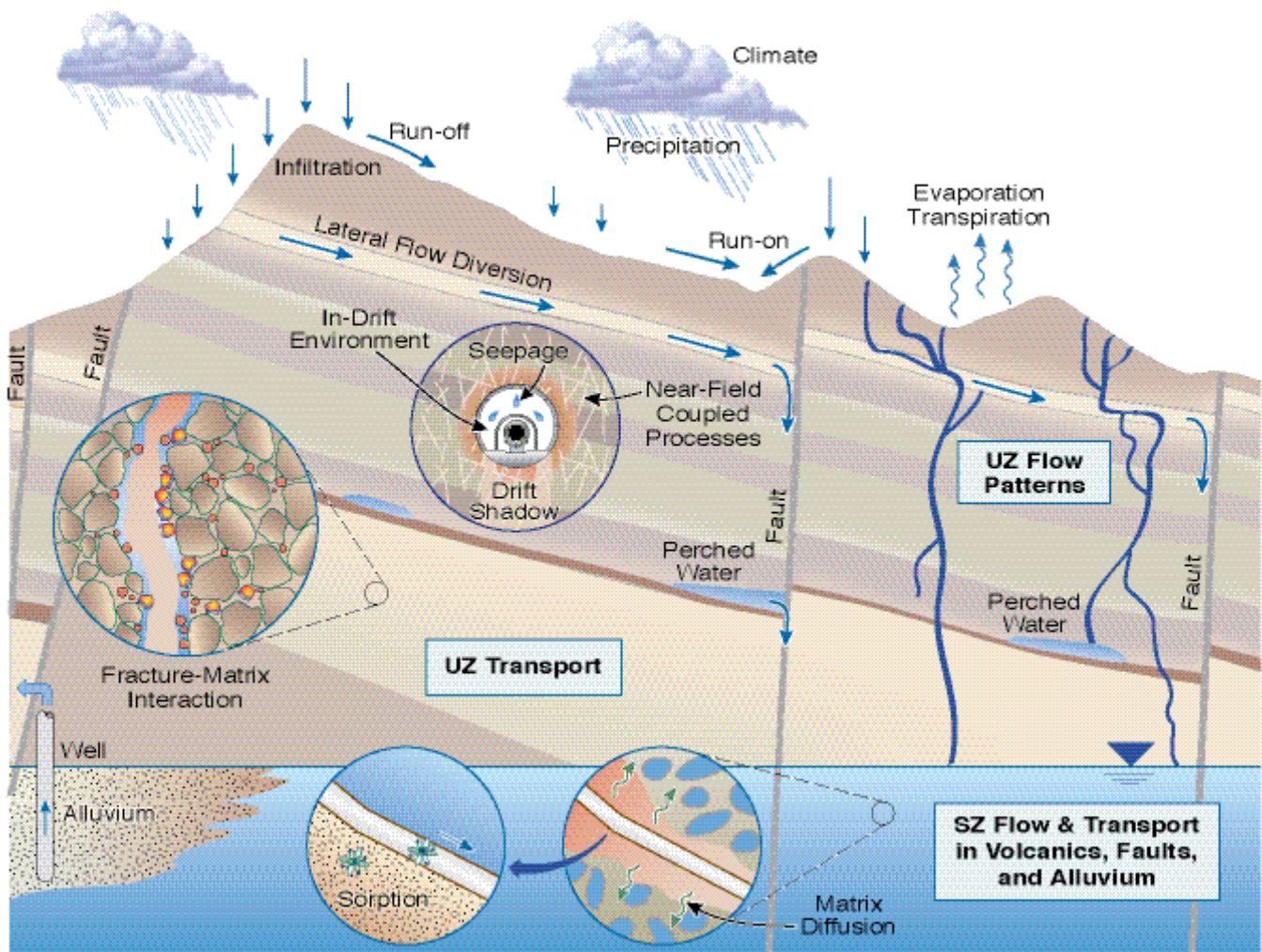


Figure 1. The Natural Barriers Thrust area.

ing release of radionuclides to the near-field rocks. The three science thrust areas described in this volume—Source Term, Materials Performance, and Natural Barriers—take an integrated approach toward investigating ways to remove the conservatism in the current project approach, thus achieving an improved representation of the drift barrier performance:

- *Integrated model to replace disjointed models:* The current approach of employing several disparate models, each describing an individual process—contributing discretely to (for example) the water composition of the end members, or salts on the waste package surfaces, or interactions with dust within the drift—limits the YMP’s ability to address key questions concerning the in-drift chemical environment. A fully coupled approach that rigorously accounts for mass balance will improve the representation of the drift barrier function.
- *Coupling of in-drift transport with UZ processes in surrounding rocks.* There is currently no integrated treatment of transport of gas, vapor, or water between the near-field rocks and the waste emplacement drifts, nor within the drift. Capture of in-drift moisture transport along the drift into an enhanced model would enable realistic representation of evaporation and condensate movement.

### Drift Shadow

The drift shadow is a region below a void in an unsaturated environment that is partially sheltered from downward-percolating water. It forms when the capillary forces are too weak to fully draw percolating water into the region. The drift shadow concept is not incorporated into the current Yucca Mountain approach, which assumes release of radionuclides into, and fast transport through, the fractures whenever seepage at the top of the drift occurs. The drift shadow concept, once demonstrated and validated, could greatly enhance repository performance by:

- *Delaying radionuclide release by thousands or tens of thousands of years.* Drift shadow is the natural consequence of water diversion around an underground opening (resulting from the negative capillary pressure in the rock), giving rise to greatly reduced water flux immediately below the opening—thus significantly limiting the mobility of radionuclides immediately below the drift.
- *Reducing peak dose potentially by orders of magnitude.*

Significantly reduced transport velocity in the shadow zone leads to delayed radionuclide breakthrough and reduced peak dose.

### Unsaturated Zone (UZ) Flow and Transport

The UZ is the main natural-barrier component: it delays, retards, and sorbs radionuclides, and if represented realistically, can contribute to orders-of-magnitude dose reduction. The current Yucca Mountain representation of UZ transport is conservative. The Natural Barriers Thrust is investigating the different UZ retardation processes, with the aim of greatly reducing the uncertainty and conservatism of the present model:

- Effectiveness of matrix diffusion in retarding radionuclide transport
- Conservatism of the  $K_d$  approach and measurements based on crushed rock samples
- Other processes such as lateral diversion, permeability barriers below perched water bodies, and flow in faults.

### Saturated Zone (SZ) Flow and Transport

Many processes that contribute to the SZ barrier function are represented conservatively in the current Yucca Mountain approach. Improved understanding of the SZ can greatly improve the description of the SZ barrier function, thus removing the overconservatism in the present project model description. The Natural Barriers Thrust addresses the following topics related to the SZ:

- *Determining if reducing conditions exist in the SZ for enhanced retardation.* One possible natural barrier to radionuclide migration in the SZ is the presence of nonoxidizing or reducing environments; the mobility of some radionuclides is known to greatly diminish in reducing groundwater.
- *Removing conservatisms in description of the retardation mechanisms.* Processes leading to retarded radionuclide transport include dilution, matrix diffusion, and sorption in the SZ.

The Natural Barriers Thrust places significant focus on the SZ to explore whether orders-of-magnitude dose reduction by dilution, diffusion, retardation, and other mechanisms can be demonstrated.

Progress in the Natural Barriers Thrust program of work through the first half of FY07 is reported in the pages that follow, addressing the above-listed scientific issues.

---

This page intentionally left blank.

## DRIFT SEEPAGE

### **Thermal-Hydrological Near-Field Model Studies and Impact of Natural Convection on Seepage**

George Danko, University of Nevada, Reno; Jens T. Birkholzer, Lawrence Berkeley National Laboratory (LBNL)

### **Integrated Assessment of Critical Chemical and Mechanical Processes Affecting Drift Performance: Laboratory and Modeling Studies**

Derek Elsworth, Abraham S. Grader, Chris J. Marone, and Ki-Bok Min, Pennsylvania State University; Jonny Rutqvist and Eric Sonnenthal, Lawrence Berkeley National Laboratory (LBNL)



---

This page intentionally left blank.

# Thermal-Hydrological Near-Field Model Studies and Impact of Natural Convection on Seepage

George Danko<sup>1</sup> and Jens T. Birkholzer<sup>2</sup>

<sup>1</sup>University of Nevada, Reno | <sup>2</sup>Lawrence Berkeley National Laboratory (LBNL)

## Research Objectives

The heat output of the nuclear waste to be emplaced at Yucca Mountain will strongly affect the thermal-hydrological (TH) conditions in and near the geologic repository. While the rock mass heats up, the open drifts will act as important conduits for natural convection and ventilation processes. For example, as a result of natural convection driven by axial temperature gradients, water will evaporate from the drift walls in elevated-temperature sections of the drifts, migrate along the drifts, and condense in cooler sections (i.e., the end sections with no waste emplaced). Evaporation driven by natural convection may significantly reduce the moisture content in the near-drift fractured rock, which in turn can significantly reduce the potential for seepage of formation water into the drift. The research project described in this report aims at developing a multiscale, coupled seepage modeling approach that accounts for natural convection and ventilation. The potential of in-drift gas flows to remove moisture from emplacement drifts is examined, and the impact of axial moisture movement on seepage is determined.

## Approach

A new seepage modeling approach is developed that accounts for the impact of evaporation caused by natural convection and ventilation processes. A simulation tool that aims to predict seepage rates affected by evaporation must address water, vapor, air, and heat transport in both the fractured rock mass and the open drift, and must handle the significant property differences between the two domains. In our approach, the flow and transport processes in the rock mass are simulated with the multiphase, multicomponent simulator TOUGH2 (Pruess et al., 1999), and the in-drift heat and moisture flows are simulated with the MULTIFLUX (MF) code (Danko et al., 2006). MF provides an efficient iterative coupling technique for matching the mass and heat transfer between the rock mass and the drift. To improve on the efficiency of the iterative coupling technique, MF applies a surrogate numerical transport code functionalization (NTCF) model (Danko, 2006) that periodically substitutes for TOUGH2 in the iterative solution process using surrogate response functions.

MF describes the relevant heat, moisture and air transport modes in the in-drift domain with a lumped-parameter CFD (Computational Fluid Dynamics) modeling approach. Various options are offered when configuring the coupled thermal-hydrologic air flow model. The lumped-parameter CFD model may be configured either for an open-volume drift air space that is connected to the ambient atmosphere, or for a closed-volume, pressure holding cavity. The transport of heat and moisture by laminar or turbulent air flow in the drift may be approximated as a dispersion process, with effective dispersion coefficients for heat and moisture, estimated via supporting CFD analyses from literature. Alternatively, the velocity distribution in the drift air space, and the transport of heat and moisture by laminar or turbulent convection, may be explicitly modeled in the lumped-parameter CFD model. The latter is a recent project development that significantly increases the applicability of the new model.

## Accomplishments

Several research tasks have been accomplished to date. The coupled iterative solution procedure comprised of TOUGH2, MF, and NTCF elements has been developed and tested, and software qualification of the MF and NTCF elements is nearly completed. The new solution procedure has been applied to evaluate the heat-driven flow and transport processes in and near a representative waste emplacement drift at Yucca Mountain. One full emplacement drift was studied embedded in a monolithic, three-dimensional rock mass modeled in TOUGH2. The in-drift domain was initially modeled using a lumped-parameter CFD model in MF that describes the coupled laminar or turbulent air flow in the drift as a dispersion process, both above and below the drip shields (Danko et al., 2006). Several iterations were completed, refreshing the NTCF model against TOUGH2 runs. Figure 1 shows the 10th and 11th iteration results, confirming excellent convergence. Also shown for comparison are the results from an alternative model that uses a simplified in-drift model within TOUGH2.

The above application example was then simulated using a CFD configuration that solves explicitly for natural air flows in the drift air space. This model configuration offers two strategic advantages. First, because the in-drift air flows

are simulated as temporally and spatially varying processes, no prior knowledge of equivalent dispersion coefficients is necessary. Second, as the velocity distribution in the drift is explicitly modeled, the complex flow patterns in the drift are better represented. The second iteration results of the new model are shown in Figure 1, together with the previous “dispersion model” results. The differences—higher temperature and more moisture in the coldest drift segments where no waste is emplaced—can be attributed to the stronger air-flow circulation in the axial drift direction. The results suggest that the new model, because it includes physical processes not heretofore considered, predicts more favorable conditions in the emplacement drift.

Another research task was initiated recently to explicitly determine the impact of the in-drift moisture transport on drift seepage. Because seepage is driven by small-scale heterogeneities in the rock mass, seepage simulations were conducted at high resolution, with rock-mass (sub)domains similar to previous seepage models (e.g., Birkholzer et al., 2004). The in-drift conditions for the small-scale seepage model—most importantly the temperature and relative humidity conditions in the drift—were provided by the full-scale in-drift results shown in Figure 1. Average percolation fluxes were increased by a factor of ten to represent a high-percolation domain, where seepage is more likely. Example results are presented in Figure 2, in the form of the saturation history

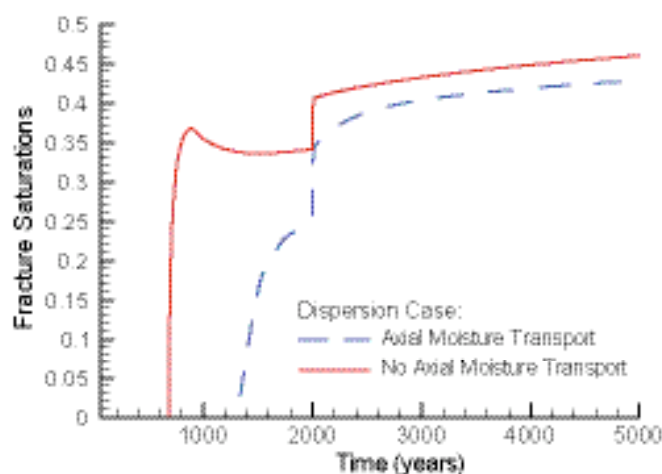


Figure 2. Saturation history at a potential seepage location in fractured rock near drift crown, at hottest drift segment. Two simulation cases are considered: with and without axial moisture transport. Percolation flux is increased by a factor of ten.

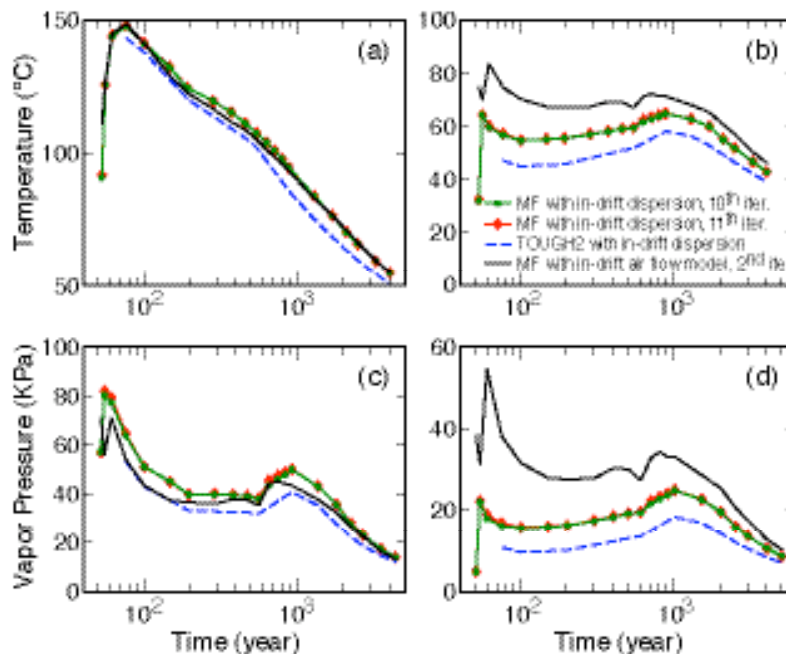


Figure 1. Drift wall temperature evolution at the hottest (a) and coldest (b) drift segments; and vapor-pressure evolution at the hottest (c) and coldest (d) drift segments.

at a potential seepage location in the rock mass near the crown of the hottest drift segment. Earlier rewetting and higher fracture saturations are predicted for the case in which moisture transport along the drift axis is neglected, which indicates a higher potential for seepage. Ongoing work evaluates the seepage differences between models with and without natural convection. Direct coupling of the small-scale seepage model to MF, rather than using predefined boundary conditions, is under way.

## Related Publications

- Birkholzer, J.T., S. Mukhopadhyay, and Y. Tsang, Modeling seepage into heated waste emplacement tunnels in Unsaturated Fractured Rock. *Vadose Zone Journal*, 3, 819–836, 2004.
- Danko, G., Functional or operator representation of numerical heat and mass transport models, *Journal of Heat Transfer*, 128, 162–175, February 2006.
- Danko, G., D. Bahrami, and J.T. Birkholzer, The effect of unheated sections on moisture transport in the emplacement drift. *Proceedings, Int. High-Level Radioactive Waste Management Conference*, Las Vegas, 2006.
- Pruess, K., C. Oldenburg, and G. Moridis, *TOUGH2 User's Guide, Version 2.0*. Report LBNL-43134, Lawrence Berkeley National Laboratory, Berkeley, California, 1999.

# Integrated Assessment of Critical Chemical and Mechanical Processes Affecting Drift Performance: Laboratory and Modeling Studies

Derek Elsworth<sup>1</sup>, Jonny Rutqvist<sup>2</sup>, Ki-Bok Min<sup>1</sup>, Abraham S. Grader<sup>1</sup>, Chris J. Marone<sup>1</sup>, and Eric Sonnenthal<sup>2</sup>

<sup>1</sup>Pennsylvania State University | <sup>2</sup>Lawrence Berkeley National Laboratory (LBNL)

## Research Objectives

This work involves recovering unusually well-constrained laboratory data to define changes in the mechanical and transport properties of fractures as a result of hydrothermal conditions anticipated in the drift-local environment. These data will be incorporated into novel thermal-hydrological-mechanical-chemical (THMC) process simulators to evaluate the influence of strong couplings between stress and chemistry on drift performance.

## Approach

We are examining the implication of critical coupled chemical-mechanical processes on drift performance at Yucca Mountain, through a coordinated suite of experimental and modeling studies.

## Accomplishments

Activities have been divided between laboratory experiments to determine mechanical-chemical constitutive behavior, and modeling to upscale these results and to examine the resulting processes on drift performance.

Single direct shear experiments have been conducted on roughened planar surfaces of tuff to measure the evolution of permeability with shear loading. These experiments have returned peak friction coefficients on the order of  $\mu \sim 0.6$  and exhibit a slight reduction at maximum shear offset ( $\sim 10$  mm). Initial bulk permeabilities of the smooth fracture sample begin at  $k_b \sim 10^{-14}$ – $10^{-15}$  m<sup>2</sup> and decrease with an increase in initial normal stress, and with an increase in shear stress or shear offset. The decrease in permeability with shear offset results from the generation of wear products at the interface. These products are observed on the fracture surfaces at the completion of the test.

Constitutive modeling has focused on defining the mechanical and transport response of fractures to increasing stress and temperature,

and on implementing these preliminary representations in distributed parameter models (Elsworth and Yasuhara, 2006; Min et al., 2007). Few data are available to constrain such models. However, existing laboratory data and an understanding of critical processes have been used to develop preliminary constitutive models, supported by data from prior laboratory studies and from the results of a prior large-scale *in situ* block experiment (the TerraTek experiment at the Idaho Springs Mine, c. 1982).

The constitutive models incorporate the separate influences of stress and temperature in controlling changes in permeability, and are informed by laboratory data on novaculite. Importantly, these behaviors are capable of representing field observations in which fracture apertures are observed to decrease from 30  $\mu$ m to 10  $\mu$ m under constant stress, for an increase in temperature from 20° to 100°C—corresponding to a thirty-fold reduction in permeability under constant stress.

These behaviors have been incorporated into finite element models, to represent the thermo-mechanical response of the drift environment to combined thermal and stress effects. These include projections in permeabilities and the feedback on anticipated reductions in stresses over the case where these behaviors are not accommodated.

For typical drift-local conditions, permeabilities are shown to evolve as in Figure 1, representing a two-order-of-mag-

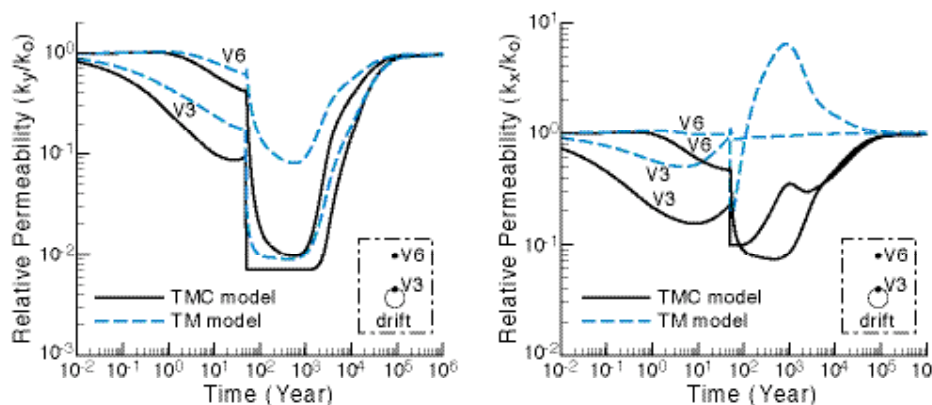


Figure 1. Comparisons of relative permeability evolution with (TMC) and without (TM) considering chemical strains at selected points. Relative changes in vertical (left) and horizontal (right) permeabilities. V3 is located at the top of the drift and V6 is located 10.75 m vertically above.

nitude change in permeability. Comparison of thermo-mechanical (TM) and thermo-mechanical-chemical (TMC) modeling shows that there can be up to a one-order-of-magnitude difference between the cases in which chemical effects are and in which they are not considered. The permeability is reduced more where chemical effects are considered together with mechanical effects, versus when they are not. The time to maximum reduction in permeability is concurrent with peak stress and temperature for the case of vertical permeability, which is most strongly influenced by changes in horizontal stress. Conversely, the evolution of vertical thermal stress is not straightforwardly related to temperature and makes the change in horizontal permeability dependent on relative local displacement constraints. Although changes caused by chemical strains will be irreversible, these current evaluations are merely reversible.

These interactions also change stress distribution. The thermal stress generated is smaller than where chemical effects are absent, because the reduction in aperture caused by temperature increase partially cancels the expansion of the intact rock. The overshoot in the reduction of stress upon cooling is explained by the irreversible change of aperture. What this behavior implies is important, since excess thermal stresses are reduced over anticipated magnitudes, and the ultimate reduction in stress may result in the loss of keying around underground excavations, where local failure may be more likely, owing to loss of confinement.

We are examining data from the Yucca Mountain Drift Scale Test (Rutqvist et al., 2007) for evidence of such effects. These include mismatches between anticipated and measured permeabilities, strains, and stresses. Such analyses are complicated by the concurrent influences of changing thermal-stress (TM) and water-saturation (TH) fields. Permeability data for the cooling phase have recently been evaluated, and we now have data for the entire 4 years of heating and subsequent 4 years of cooling.

Preliminary evaluations from the 46 measurement points, which are located at distances of between ~ 5 to 20 m away from the heated drift, are available. These evaluations indicate that permeabilities are depressed in the heating phase close to the heat source and recover slowly in the cooling phase, but suffer some irreversible changes. The maximum reduction in permeability is about one-

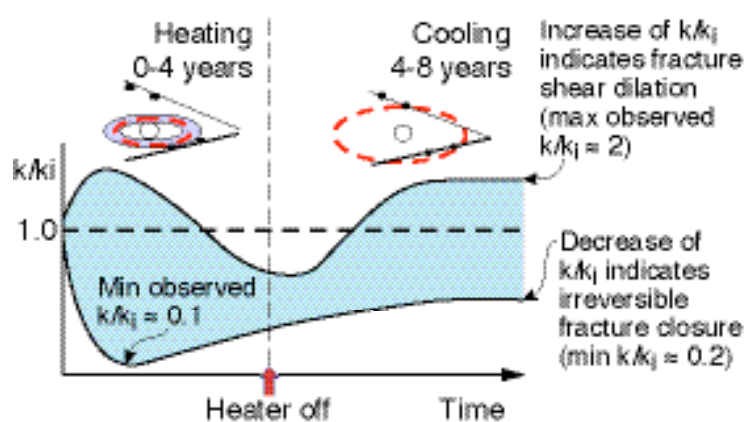


Figure 2. Schematic of observed changes in air-permeability at the Drift Scale Test during the 4-year heating period followed by a 4-year cooling period.

order-of-magnitude, and occurs during heating. At the end of cooling, the maximum permeability increase is a factor of 2, and the strongest permeability reduction is a factor of 0.2 of the original permeability. Thus, changes in permeability at the Drift Scale Test are limited to within one order of magnitude, as illustrated in Figure 2.

Importantly, the observed changes in permeability can only be explained by considering both TH and TM effects. The induced changes in permeability are within one order of magnitude (increase or decrease). Moreover, the permeability changes measured at the end of the cooling period likely reflect mechanically induced changes in permeability that might be mediated by chemo-mechanical effects. Displacement data are being examined to examine the causality of these observed permanent changes in permeability.

## Related Publications

- Elsworth, D., and H. Yasuhara, Mechanical and transport constitutive models for fractures subject to dissolution and precipitation. 2006 (submitted).
- Min, K.-B., J. Rutqvist, and D. Elsworth, Chemically and mechanically mediated influences on the transport and mechanical characteristics of rock fractures. 2007 (submitted).
- Rutqvist, J., et al. (2007) Analysis of coupled THM effects on permeability at the Yucca Mountain Drift Scale Test—Evidence of irreversible changes after heating and cooling in fractured rock. 2007 (in preparation).



## IN-DRIFT ENVIRONMENT

### **Coupling Thermal-Hydrological-Chemical (THC) Models to Process Models for Waste Packages**

Guoxiang Zhang, Nicolas Spycher, Eric Sonnenthal, and Carl Steefel, Lawrence Berkeley National Laboratory (LBNL)

---

This page intentionally left blank.

# Coupling Thermal-Hydrological-Chemical (THC) Models to Process Models for Waste Packages

Guoxiang Zhang, Nicolas Spycher, Eric Sonnenthal, and Carl Steefel  
Lawrence Berkeley National Laboratory (LBNL)

## Research Objectives

The main objective of this project is to develop an integrated, coupled thermal, hydrological, and chemical (THC) model of the near-field rock and in-drift environment at Yucca Mountain, to provide a link between the THC processes in the near field (evaluated under the Natural Barrier Targeted Thrust) and those taking place in waste-emplacement drifts, affecting waste package corrosion and fuel degradation (evaluated under the Materials Performance Targeted Thrust and Source Term Targeted Thrust). Specifically, this project aims to:

- Develop a quantitative model of coupled THC processes potentially leading to brine formation on top of waste packages and/or a drip shield.
- Dynamically integrate the model into the larger-scale process models within and around waste-emplacement tunnels, and into the smaller-scale waste-package corrosion models.

## Approach

Process models were implemented into TOUGHREACT to allow modeling of evaporative concentration to very high ionic strength, boiling point elevation caused by dissolved salts, boiling/evaporation to dryness, and salt deliquescence (Zhang et al., 2006a, 2006b).

Using TOUGHREACT, we ran an integrated near-field/in-drift THC simulation using a vertical 2-D grid extending from near the ground surface to the groundwater table and covering a width equal to half the designed drift spacing of 81 m (a symmetrical model consistent with other ongoing near-field THC modeling investigations). A heterogeneous permeability field and high infiltration rates (10 times mean infiltration) were assumed, to ensure seepage into the drift. Starting water composition was taken from analyses of pore waters in Alcove-5 of the Exploratory Studies Facility (ESF). The geologic time period simulated was 600 years, with the boiling front collapsing at ~250 years, followed by in-drift seepage.

The integrated model was then used to simulate a discrete dripping event within the drift. At first, interactions with the waste source were not considered. The model was then

refined to consider the release of radionuclides (representatively,  $\text{UO}_2^{+2}$  and  $\text{NpO}_2^{+2}$ ) into seepage water as this water contacts the waste package and flows through the invert. (The oxidation of the waste form to  $\text{UO}_2^{+2}$  and  $\text{NpO}_2^{+2}$  was not explicitly modeled.) The precipitation of uranophane ( $\text{Ca}(\text{UO}_2\text{SiO}_3\text{OH})_2 \cdot 5\text{H}_2\text{O}$ ) and Np-uranophane was also considered. These minerals form in the invert from the neutralization of mildly acidic seepage water by clay minerals.

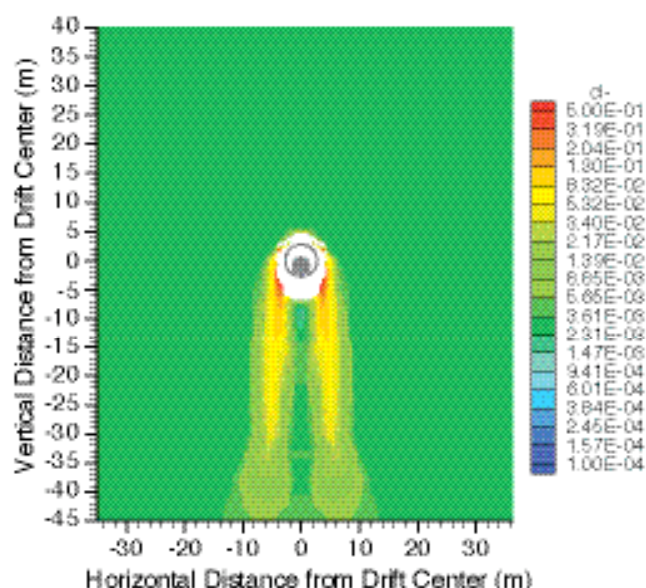


Figure 1. Simulated distribution of chloride concentrations during the collapse of the boiling front (at ~300 years) showing “shedding” of mildly concentrated waters resulting from the dissolution of previously precipitated salts in the dry-out zone.

## Accomplishments

Model results provide information of direct interest to the Natural Barrier, Materials Performance, and Source Term Thrusts. Preliminary integrated simulations indicate:

- The near-field and in-drift brine chemical evolution is dominated by the precipitation of  $\text{NaCl}$ ,  $\text{CaSO}_4$ , and  $\text{CaCO}_3$ .
- Rewetting of salts during collapse of the boiling front yields chloride concentrations  $< 20 \times$  ambi-

ent values in waters percolating back towards the drift (Figure 1).

- The generation of acid gases at high evaporative concentration yields  $\text{PHCl} \sim 10^{-7}$  bar at boiling temperatures, with pH staying  $>5$  in condensation areas.
- Salt separation on the drip shield is not predicted, because the volume of brine that remains once the first salt precipitates ( $\text{NaCl}$ ) is too small to allow further brine movement.
- The clay minerals in the invert neutralize the pH of seepage water, although this result is sensitive to assumptions regarding the kinetics of reactions with clays.
- The drift invert may act as a pH buffer promoting uranophane precipitation and impeding downward migration of radionuclides at elevated concentrations (Figures 2 and 3).

These results are preliminary and specific to the conditions considered. The buffer effects could be different (stronger or weaker) depending on the initial pore water composition and other in-drift physical and chemical conditions.

## Related Publications

Zhang, G., N. Spycher, E. Sonnenthal, and C. Steefel, Implementation of a Pitzer activity model into TOUGHREACT for modeling concentrated solutions. Proceedings, TOUGH2 Symposium, Lawrence Berkeley National Laboratory, Berkeley, CA, May 15–17, 2006a.

Zhang, G., N. Spycher, T. Xu, E. Sonnenthal, and C. Steefel, Reactive geochemical transport modeling of concentrated aqueous solutions: Supplement to the TOUGHREACT Users's Guide for the Pitzer ion-interaction model. Report LBNL-62718, Lawrence Berkeley National Laboratory, Berkeley, CA, 2006b.

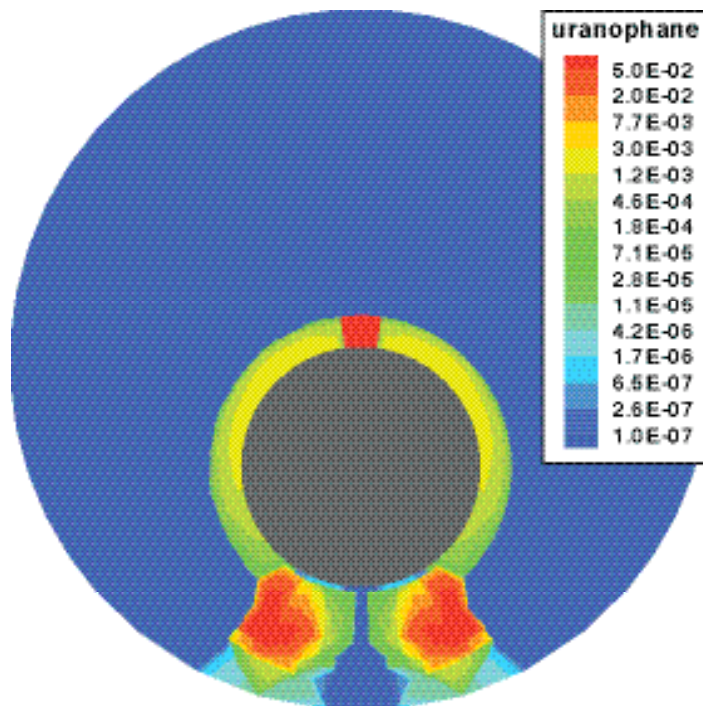


Figure 2. Simulated distribution of uranophane ( $\text{mol/m}^3$  of medium) precipitated after 25 years of continuous dripping. Precipitation of this mineral in the drift invert removes most of the  $\text{UO}_2^{+2}$  mass from the seepage water and substantially decreases the  $\text{UO}_2^{+2}$  concentration in water percolating out of the drift.

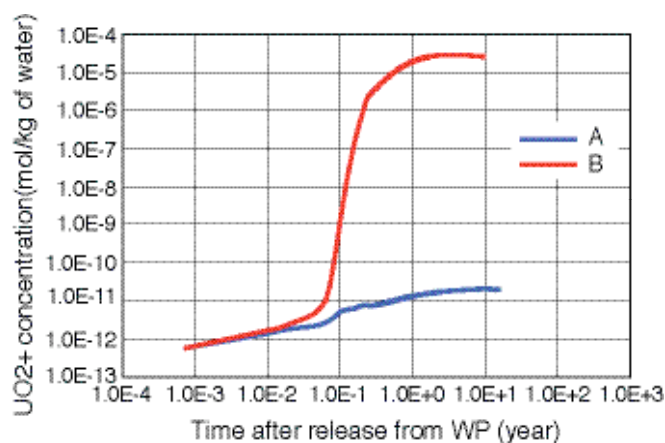


Figure 3. Simulated time evolution of  $\text{UO}_2^{+2}$  concentration at the base of the drift, with (A) and without (B) consideration of uranophane precipitation, showing the clear effect of precipitation of this mineral in the drift invert.

## DRIFT SHADOW

### **Nature of Drift Shadows at Analogue Sites**

Tim Kneafsey, Teamrat A. Ghezzehei, Grace Su, and Paul Cook, Lawrence Berkeley National Laboratory (LBNL), and Brian Marshall, United States Geological Survey (USGS)

### **Testing the Concept of Drift Shadow**

James Paces and Leonid A. Neymark, United States Geological Survey (USGS); Teamrat A. Ghezzehei and Patrick Dobson, Lawrence Berkeley National Laboratory (LBNL)

### **Testing the Concept of Drift Shadow with X-Ray Absorption Imaging Experiments**

Susan J. Altman, Clifford K. Ho, Aleeca Forsberg, and William Peplinski, Sandia National Laboratories (SNL)



---

This page intentionally left blank.

# Nature of Drift Shadows at Analogue Sites

Tim Kneafsey<sup>1</sup>, Teamrat A. Ghezzehei<sup>1</sup>, Grace Su<sup>1</sup>, Paul Cook<sup>1</sup>, and Brian Marshall<sup>2</sup>

<sup>1</sup>Lawrence Berkeley National Laboratory (LBNL) | <sup>2</sup>United States Geological Survey (USGS)

## Research Objectives

The drift shadow is a region below an underground void (such as a drift) in an unsaturated environment that is sheltered from downward-percolating water. Such a region forms when capillary forces are too weak to immediately draw percolating water into this region. Thus, radionuclide transport directly below a drift would take place primarily by the slow process of diffusion. The presence of a drift shadow below the drifts at the Yucca Mountain repository would significantly enhance the performance of the repository, and could be engineered by mining tunnels above waste emplacement drifts to shadow these drifts. The drift shadow concept has been demonstrated theoretically (Philip et al., 1989) and by numerical simulation (Houseworth et al., 2003); our objective is to collect the field and laboratory data needed to verify the concept.

## Approach

Our approach to investigating the drift shadow is to find a field site containing a natural or mined cavity in the unsaturated zone, measure flow-affecting parameters, predict the drift shadow numerically, and use geophysical, hydrologic, and geochemical tools to assess its presence and extent. In our first year of work, we were able to locate a suitable site, the Atlas Mine at the Black Diamond Mines Regional Preserve in Antioch, California. We are now proceeding with the aforementioned measurements, predictions, and assessments.

## Accomplishments

In FY2006 and the first two quarters of FY2007, we:

- Formalized an agreement with the site owner allowing our investigation.
- Prepared seven Technical Implementing Procedures (TIPs) to facilitate our investigation.
- Made initial field and laboratory measurements to gain an understanding of site-relevant parameters.
- Designed, constructed, and surveyed a test bed including an active and passive test. Test bed

design used site-specific information and numerical simulation. The resulting test bed is composed of 20 boreholes having lengths ranging from 1.5 m to 4 m.

- Collected and preserved core from the 60 m (200 ft) of boreholes.
- Performed gravimetric moisture analyses of 166 core samples and x-ray scanning of all core retrieved.
- Performed two ground-penetrating-radar investigations of water content between boreholes.
- Initiated deployment of water potential sensors in the boreholes.

Additional information on a number of these accomplishments is presented below.

### Initial Field and Lab Tests

We conducted two falling-head ring-infiltrometer tests near our test bed and simulated the water level in the ring and responses of the subsurface electrical resistance probes using a 3-D model.

### Field Test Design, Construction, Survey, and Preparation

We developed a three-dimensional iTOUGH2 model (5 m wide, 2.5 m deep, and 10 m high) to aid in test design. In the model, with  $k=100$  mD, a distinct drift shadow began to form in about 100 days, and a fully developed steady-state drift shadow zone required approximately 300 days. Our test bed (Figure 1) encompasses regions surrounding the upper (machinery) and lower (haulage) drifts.

We surveyed borehole locations and directions, drift geometry and orientation, and relation to ground surface, and have begun installation of monitoring equipment, including 92 calibrated gypsum blocks, 20 custom tensiometers (for water potential), and 26 calibrated thermistors.

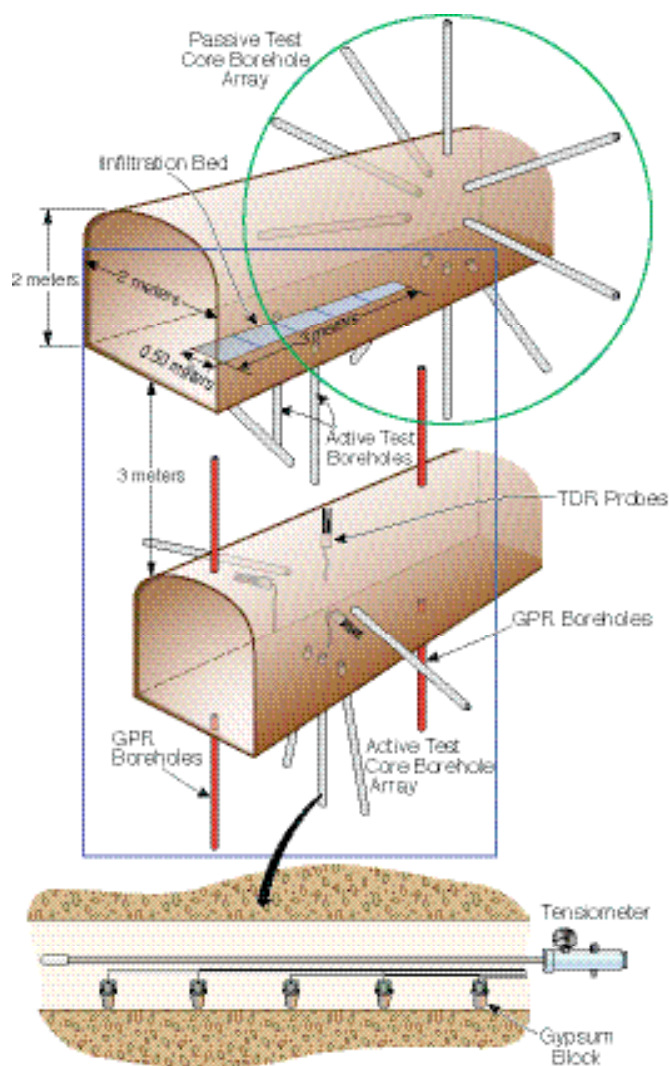


Figure 1. Borehole schematic. Passive test boreholes are identified by the green circle, active test boreholes by the blue box, and ground-penetrating-radar holes by the red boreholes.

### Ground Penetrating Radar

We performed two sets of ground-penetrating-radar measurements between adjacent borehole pairs to provide a measure of water content between the boreholes. The region between the two drifts is relatively dry, and water content increases with depth below the lower drift.

### Core Collection and Gravimetric Moisture Analysis

We carried out gravimetric moisture analyses of core from each borehole, as well as x-ray scanning of core to identify high-density regions resulting from the deposition of

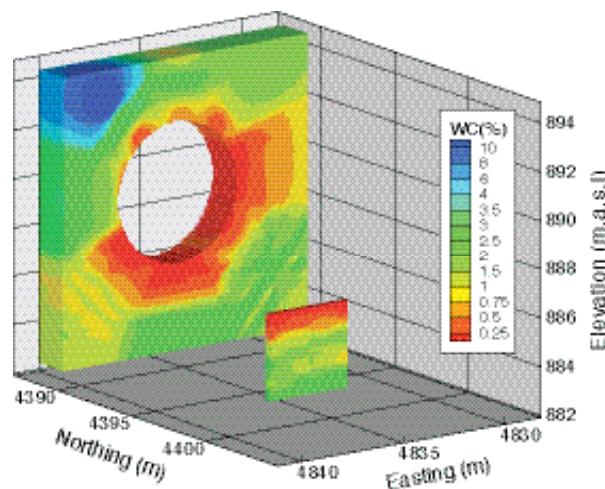


Figure 2. Gravimetric water content (percent) around the upper drift.

evaporite minerals. X-ray scanning provided no indication of a drift shadow. Results of gravimetric moisture analyses of 166 samples from 11 boreholes were interpolated using an inverse-distance approach. The resulting water content distribution around the upper drift is shown in Figure 2.

Dipping, resembling the visible dip of the strata at the site, is clear. The region below the drift is generally drier than the region above; however, water potential (rather than water content) is the preferred parameter to test the presence of drift shadow.

### References

- Houseworth, J.E., S.A. Finsterle, and G.S. Bodvarsson, Flow and transport in the drift shadow in a dual-continuum model. *Journal of Contaminant Hydrology*, 62-63, 133-156, 2003.
- Philip, J.R., J.H. Knight, and R.T. Waechter, Unsaturated seepage and subterranean holes: Conspectus, and exclusion problem for circular cylindrical cavities. *Water Resources Research*, 25(1), 16-28, 1989.

#### *Journal Papers Accepted and Conference Papers Given:*

- Ghezzehei, T.A., T.J. Kneafsey, and G.W. Su, Correspondence of the Gardner and van Genuchten relative permeability functions. *Water Resources Research*, 2007 (in press).
- Su, G.W., T.J. Kneafsey, T.A. Ghezzehei, P.J. Cook, and B.D. Marshall, Field investigation of the drift shadow. Berkeley Lab Report LBNL-59455. Proceedings of the 11th International High-Level Radioactive Waste Management Conference, Las Vegas, NV, April 30-May 4, 2006

# Testing the Concept of Drift Shadow

James Paces<sup>1</sup>, Leonid Neymark<sup>1</sup>, Teamrat Ghezzehei<sup>2</sup>, and Patrick Dobson<sup>2</sup>

<sup>1</sup>United States Geological Survey (USGS) | <sup>2</sup>Lawrence Berkeley National Laboratory (LBNL)

## Research Objectives

Water percolating through fractured tuff at Yucca Mountain, Nevada, may be diverted around voids in the unsaturated zone (UZ) by capillary forces rather than seeping into openings. Drift shadows, defined as zones of decreased water saturation and flow velocity, may be present for some distance beneath UZ openings until capillary forces reestablish uniform flow. Drift shadows present beneath proposed emplacement drifts may contribute to the performance of the natural-system barrier at the proposed high-level radioactive waste repository, by increasing UZ groundwater travel times. The objective of this project is to study drift shadows beneath natural lithophysal cavities (voids formed during emplacement of tuffs) in the Yucca Mountain UZ that should result in variable degrees of water saturation and differences in chemical and isotopic compositions of whole-rock and pore-water samples.

## Approach

To test for the presence of naturally formed drift shadows, uranium (U) concentrations and  $^{234}\text{U}/^{238}\text{U}$  activity ratios (AR) in rock samples were used to evaluate long-term differences in water fluxes. Zones of greater water flux should develop lower U concentrations, because of the high solubility of U in oxidizing, carbonate-rich solutions, and greater depletion of  $^{234}\text{U}$  relative to  $^{238}\text{U}$ , because of alpha-recoil processes. Therefore, rock samples from drift-shadow zones should have systematic differences in U-series data relative to rock at cavity margins. In addition, drift shadow zones should have pore water with higher concentrations of conservative ions (such as Cl) due to longer residence times and the possibility of greater *in situ* liquid-gas exchange.

Rock samples were collected from lithophysal cavities in the Exploratory Studies Facility (ESF) at 2,979 and 3,018 m from the tunnel portal and in the Enhanced Characterization of the Repository Block (ECRB) Cross Drift at 1,615 and 1,617 m from the ESF. Samples obtained with a ~15 mm diameter percussion drill formed irregular grids beneath each cavity. Hand samples also were collected from the sides and top of two cavities.

Pore-water samples were obtained from five 6 m long dry-cored horizontal boreholes between 1,610 and 1,618 m in the ECRB. Video logs were used to identify lithophysal cavities intersected by these boreholes. Subjacent boreholes angled 3° downward were cored at two of these sites to obtain core 0.3 to 0.5 m beneath cavities intersected in the horizontal holes. Pore water from one of the horizontal boreholes was extracted by ultracentrifugation of 200-gram core samples at ~15,000 revolutions per minute for 6 hours.

## Accomplishments

### Whole-Rock Analyses:

U-series isotope analyses were completed on 77 whole-rock samples from around lithophysal cavities exposed in tunnel walls. Results show a general covariance between

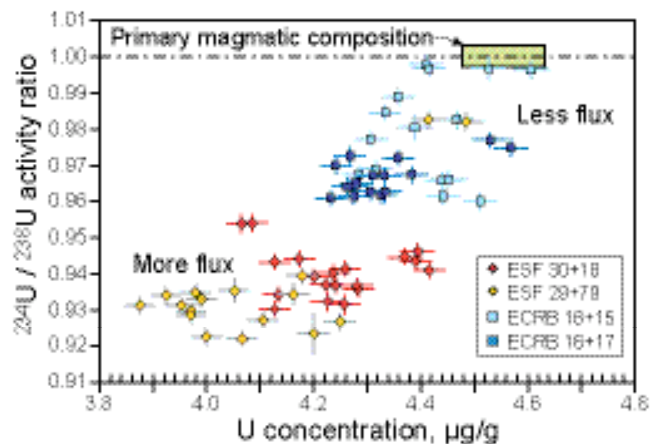


Figure 1. Relations between uranium (U) concentration and  $^{234}\text{U}/^{238}\text{U}$  activity ratio (AR) for whole-rock samples associated with four lithophysal cavities. Error bars represent 2 sigma analytical uncertainties.

rock U concentration and  $^{234}\text{U}/^{238}\text{U}$  AR (Figure 1). Concentrations of other minor and trace elements indicate that the observed trend in U concentrations does not reflect primary magmatic variations. Instead, U-series data are interpreted to reflect greater postdepositional U loss and  $^{234}\text{U}$  depletion in samples from the ESF than samples from the ECRB. These results, along with the larger thick-

ness of secondary mineral coatings in the ESF cavities, are interpreted as evidence for greater UZ percolation flux in this area.

Spatial patterns of  $^{234}\text{U}$  depletion are present in samples beneath lithophysal cavities. Three of the four cavities have less  $^{234}\text{U}$  depletion beneath cavities relative to samples from cavity margins, consistent with the concept of drift shadow. In contrast, results from samples associated with the largest cavity (~130-cm wide) at ESF 3,018 m indicate that more  $^{234}\text{U}$  depletion is present beneath the cavity than near its margins. A 3 cm thick secondary mineral coating floors this cavity, which is substantially thicker than coatings in the other cavities, and indicates that it received more water seepage than the other cavities. This finding implies that fluxes exceeded the seepage threshold at this location.

*Pore-water Analyses:* Gravimetric moisture contents for 22 samples from a 2 m long interval in borehole ECRB DS3 1616 appear correlated with the presence of lithophysal cavities intersected in the borehole, although the geometries of voids intersected by the borehole are difficult to quantify. Pore-water extraction was successful only where moisture contents exceeded 2.5 to 3.0 weight percent. Solute concentration varied with moisture content (highest Cl<sup>-</sup> concentrations are from samples with the lowest moisture contents), implying that evaporation, either in situ or during core drilling, may be an important process controlling pore-water compositions.

Compared to other Yucca Mountain pore-water samples, the samples from borehole ECRB DS3 1616 are more dilute with Cl<sup>-</sup> concentrations between 5.0 and 20.4 mg/L. Weight ratios of  $\text{NO}_3^-/\text{Cl}^-$  between 1.2 and 2.2 are higher than values in other pore-water samples and would have less impact on waste-package corrosion. Concentrations of Cl<sup>-</sup>,  $\text{NO}_3^-$ , and  $\text{SO}_4^{2-}$  are strongly correlated and are consistent with evaporative concentration by as much as a factor of 4. However,  $\text{Na}^+$  and  $\text{Ca}^{2+}$  concentrations in the same samples vary by less than a factor of 2 and do not regress through zero, indicating that additional processes besides evaporation are involved. Chemical tracers (LiBr) added to the water used for tunnel construction were not detected. These chemical data indicate that (1) both evaporation and water/rock reaction affected pore-water samples, (2) pore-water heterogeneities are maintained at the same spatial scales observed for lithophysae, and (3) moisture contents and concentrations are likely related to the presence of

drift shadows.

Unlike elemental concentrations measured in pore-water samples, uranium and strontium isotope ratios are not affected by evaporative processes. Pore water had  $^{234}\text{U}/^{238}\text{U}$  AR ranging between 1.79 and 2.60, substantially lower than other samples of repository-level pore water and fracture water (calculated from initial  $^{234}\text{U}/^{238}\text{U}$  AR values in fracture minerals).  $^{234}\text{U}/^{238}\text{U}$  AR values do not show clear spatial relations to the large cavity in borehole ECRB DS3 1616, although samples from within the cavity tend to have lower values than samples outside the cavity zone.  $^{87}\text{Sr}/^{86}\text{Sr}$  values determined for five of the pore-water samples ranged from 0.71235 to 0.71259, with no apparent trend with depth in the borehole. These values are within the range observed for other pore-water data from the repository horizon.

Pore water also was extracted from two core samples within the same 2 m long interval by vacuum distillation and analyzed for stable H and O isotopes. Resulting values of -89.5‰  $\delta^2\text{H}$  and -11.9‰  $\delta^{18}\text{O}$  in one sample and -93.2‰ and -13.1‰ in the other are consistent with infiltration during warmer (Holocene) rather than cooler (Pleistocene) climates. Both samples plot near the global meteoric line, showing no obvious effects of evaporation during drilling.

*Modeling:* Numerical simulations of drift-shadow dimensions for theoretical matrix- and fracture-flow systems used a two-dimensional dual permeability flow model scaled to dimensions appropriate for the meter-scale lithophysal cavities. Under the gravity-dominated advective fracture-flow conditions present within the proposed repository horizon, preliminary simulations indicate that drift shadows would develop beneath cavities ~1 m in diameter or larger. These simulations only addressed conditions where percolation fluxes do not exceed the seepage threshold into the cavity.

## Summary

U-series whole-rock isotope analyses show patterns of disequilibrium that are consistent with conceptual and numerical models of drift shadow associated with cavities in this study. Existing pore-water data associated with lithophysal cavities also support the presence of drift shadows. However, patterns of  $^{234}\text{U}/^{238}\text{U}$  disequilibrium are complicated beneath cavities where percolation fluxes may have exceeded seepage thresholds.



# Testing the Concept of Drift Shadow with X-Ray Absorption Imaging Experiments

Susan J. Altman, Clifford K. Ho, Aleeca Forsberg, and William Peplinski  
Sandia National Laboratories (SNL)

## Research Objectives

X-ray absorption imaging is used to test the concept of the drift shadow in geological samples. The drift shadow model predicts that water travels around underground tunnels, or drifts, leaving areas of high saturation along the sides of the drift (roof-drip lobe) and an area of low saturation beneath the drift (drift shadow). The drift shadow model could impact nuclear waste repositories designed with open tunnels, such as Yucca Mountain, by impacting the flux available to transport waste beneath the repository. However, without strong evidence for the drift shadow effect, it is difficult to justify its inclusion in performance assessment calculations.

## Approach

Our study uses x-ray absorption imaging to test the concept of the drift shadow. X-ray absorption imaging techniques have been shown to be a powerful tool to visualize and quantify flow and transport in opaque systems (Altman et al., 2004; Tidwell et al., 2000). Laboratory-scale volcanic tuff samples are imaged to directly visualize pathways of infiltrating water in the vicinity of the drift. In addition, outflow samples are collected in and beneath the model drift to further confirm the visualization results. Through the use of geological samples, we not only test the drift-shadow concept, but also provide data in heterogeneous materials to assist in future numerical modeling.

Samples of Topopah Spring welded tuff (Tsw), collected from Busted Butte, Nevada Test Site, were used for this study. Test cells were prepared with different fracture apertures (Figure 1). Prior to starting an experiment, test cells were saturated with water. At the start of the experiment, a tracer was dripped at a controlled flow rate through four ports at the top of the test cells. Transport through the cell was measured by collecting and weighing sponges both in the drift and at collection ports at the bottom of the flow cell. X-ray images were collected prior to the start of the experiment and at different times during the experiment. By subtracting the image taken prior to the start of the experiment from the images taken during the experiment, the x-ray absorption due to the geological

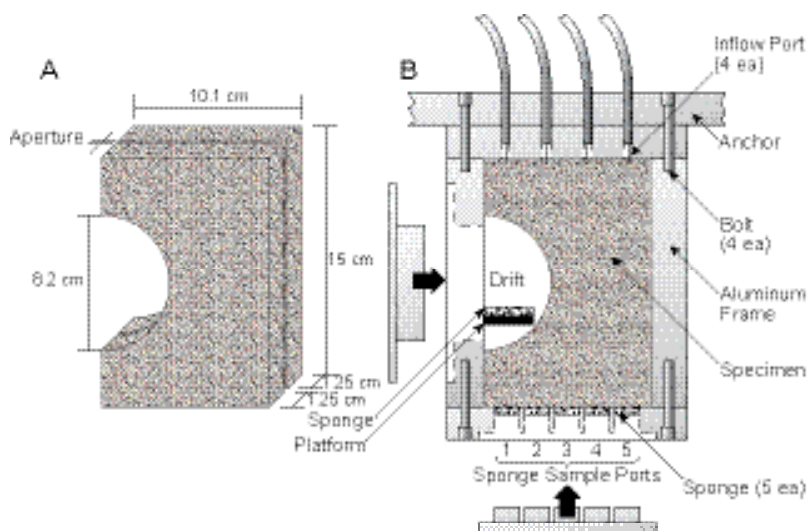


Figure 1. Schematic of specimen after sample preparation (A) and in the test cell (B).

media was removed, and the tracer pathways in the geological samples become visible.

## Accomplishments

Experiments were completed by the summer of 2006. Since this time, our focus has been on presenting and publishing our interpretations of the experimental results. Presentations have been made at the Geological Society of America Annual Meeting (October 2005) and the International High-Level Radioactive Waste Management Conference (May 2006). Publications include one in the *Proceedings for the International High-Level Radioactive Waste Management Conference* (Altman et al., 2006) and a manuscript submitted to the *Journal of Hydrology* (Altman et al., in review). A modified version of the conclusions from the *Journal of Hydrology* manuscript is presented below:

X-ray absorption experiments provide clear images of a roof-drip lobe and drift shadow forming in real time on geological samples (Figure 2). The imaging shows a tracer-solution flow path above the drift being diverted around the drift and shedding beyond the drift. In all but two of the tests, less than 1% of the inflow mass was discharged into the drift. The evidence for a drift shadow is generally

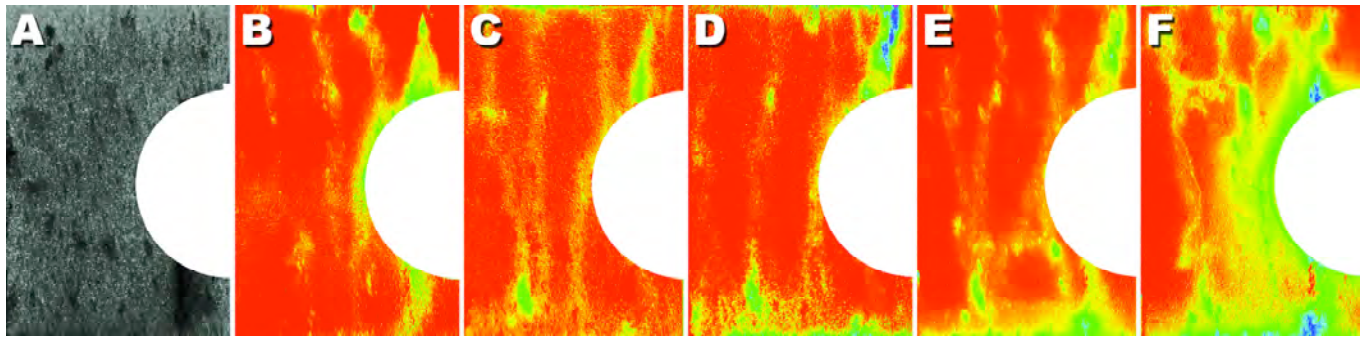


Figure 2. X-ray absorption images of the 250  $\mu\text{m}$  aperture test cell taken before (A) and 5 hours (B-F) after the start of experiments. Flow rates are 0.01, 0.05, 0.09, 0.13, and 0.24 mL/min for tests B, C, D, E, and F, respectively. Red going to yellow, green, blue, and purple indicates increasing tracer concentration. Image of cell without tracer (A) shows more porous pumice fragments as darker areas.

demonstrated through the observation of less discharge under the drift and greater discharge just beyond the drift than if flow was uniformly vertical (Figure 3). However, there is also evidence that under the right conditions (low flow rates and small-fracture apertures), water might be transported back under the drift. In addition, natural heterogeneities can influence the extent of the drift shadow effect.

While these studies provide quantitative and visual evidence that only a fraction of the total percolation flux is available for transporting radionuclides immediately beneath the repository, further work is needed to quantify the effect of the drift shadow on radionuclide transport.

The experiments presented here can feed into a numerical modeling exercise that can more fully capture the impact of heterogeneities and the range of hydrogeological parameters (e.g., infiltration rates, fracture apertures). This modeling exercise can also account for the impact of the smaller scale of our experiments relative to field-scale drifts on the experimental results. Thus, these experiments, coupled with future modeling, can provide the data needed for performance assessment calculations to account for the impact of the drift shadow on radionuclide transport. If implemented, such studies could lead to improved natural barrier performance in future calculations.

## References

- Altman, S. J., A. Forsberg, W. Peplinski, and C. K. Ho, Testing the concept of drift shadow with x-ray absorption imaging. In 2006 International High-Level Radioactive Waste Management, conference held in Las Vegas, NV, April 30–May 4, 2006.
- Altman, S.J., A.A. Forsberg, W.J. Peplinski, and C.K. Ho, Experimental observation of the drift-shadow effect using x-ray absorption imaging. *J. Hydrol.*, in review (submitted April 2007).
- Altman, S.J., M. Uchida, V.C. Tidwell, C.M. Boney, and B.P. Chambers, Use of x-ray absorption imaging to examine heterogeneous diffusion in fractured crystalline rocks. *J. Contam. Hydrol.*, 69(1-2), 1-26, 2004.
- Tidwell, V.C., L.C. Meigs, T. Christian-Frear, and C.M. Boney, Effects of spatially heterogeneous porosity on matrix diffusion as investigated by X-ray absorption imaging. *J. Contam. Hydrol.*, 42(2-4), 285-302, 2000.

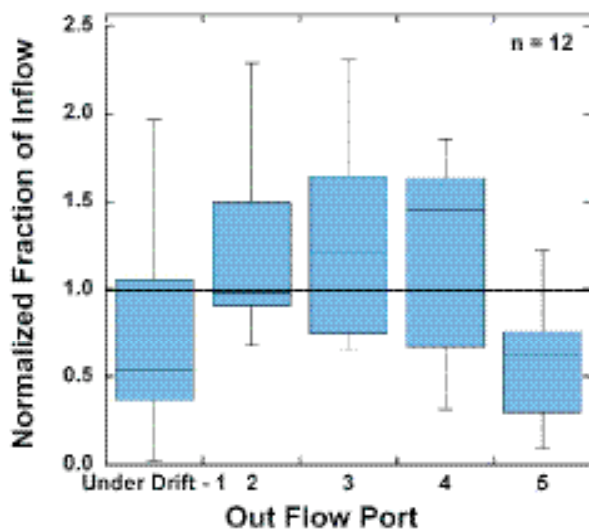


Figure 2. Normalized fraction of inflow discharging through outflow ports for 12 tests presented in Altman et al. (in review). Each box encloses 50% of the values with the central line representing the median value. The bars show the minimum and maximum values. Fractions are normalized such that if the inflow were discharged uniformly, the normalized discharge would be 1.

# UNSATURATED ZONE FLOW AND TRANSPORT

## **Enhanced Retardation of Radionuclide Transport in Fractured Rock**

Hui-Hai Liu, Yinqi Zhang, and Keni Zhang, Lawrence Berkeley National Laboratory (LBNL); Fred J. Molz, Clemson University

## **Peña Blanca Natural Analogue**

Schön S. Levy, Amr Abdel-Fattah, John Dinsmoor, Steve Goldstein, and Michael T. Murrell, Los Alamos National Laboratory (LANL); Paul Cook, Patrick F. Dobson, and Teamrat Ghezzehei, Lawrence Berkeley National Laboratory (LBNL); Mostafa Fayek, University of Tennessee-Knoxville; Philip Goodell and Katrina Pekar, University of Texas-El Paso (UTEP); Richard Ku and Shangde Luo, University of Southern California (USC)

## **Matrix/Fracture Flow in Subrepository Units**

Leonid Neymark and James Paces, US Geological Survey; David Vaniman and Steve Chipera, Los Alamos National Laboratory (LANL)

## **Pore Connectivity, Episodic Flow, and Unsaturated Diffusion in Fractured Tuff**

Qinhong Hu, Lawrence Livermore National Laboratory (LLNL); Robert P. Ewing, Iowa State University; Liviu Tomutsa, Lawrence Berkeley National Laboratory (LBNL)

---

This page intentionally left blank.

# Enhanced Retardation of Radionuclide Transport in Fractured Rock

Hui-Hai Liu<sup>1</sup>, Yinqi Zhang<sup>1</sup>, Keni Zhang<sup>1</sup>, and Fred J. Molz<sup>2</sup>

<sup>1</sup>Lawrence Berkeley National Laboratory (LBNL) | <sup>2</sup>Clemson University

## Research Objectives

The matrix diffusion process is crucial for the retardation of contaminant transport in fractured rocks. It has been previously shown that the key parameter controlling the matrix diffusion process, the effective matrix diffusion coefficient, is scale dependent (Liu et al., 2004, Zhou et al., 2006). During FY06/FY07, the focus of our research is on investigating the physical mechanisms behind this scale-dependent behavior.

## Approach

Analyses and numerical experiments have been systematically performed to investigate the possible mechanisms behind matrix-diffusion-coefficient scale dependence for some relatively simple fracture-matrix systems. We have identified two possible mechanisms: the flow geometry effect and subsurface heterogeneity effect.

## Accomplishments

We have previously investigated how the flow geometry affects the effective matrix diffusion coefficient. According to percolation theory, a flow path consists of both globally connected fractures and relatively small fractures that form local flow loops. A simplified system was constructed that contains a single flow path with different levels of flow loops. This geometry results in a general increase in the effective matrix diffusion coefficient with observation scale. Our conclusion is that a combination of local flow loops and scaling properties in flow-path geometry contributes to the scale dependence of the matrix diffusion coefficient.

During FY06/FY07, we focused on examining how subsurface heterogeneity affects the effective matrix diffusion coefficient. For this purpose, we have developed analytical expressions for the effective matrix diffusion coefficient in two fracture-matrix systems: (1) a single fracture system with a heterogeneous matrix-porosity distribution, and (2) a multiple fracture system with a heterogeneous matrix diffusion coefficient among different fractures.

In the single-fracture system (Figure 1), we assume matrix

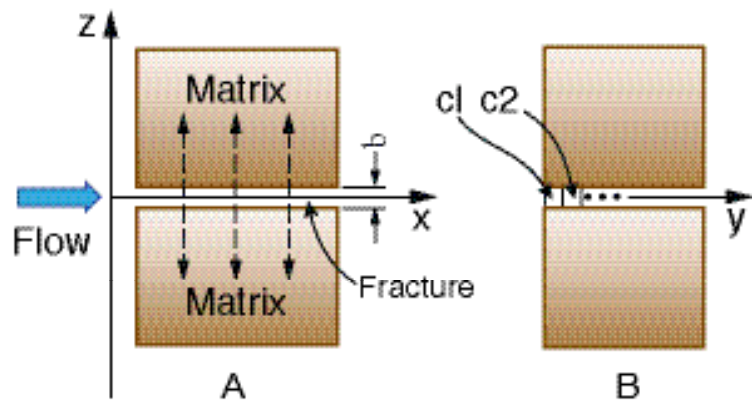


Figure 1. Schematic of a single fracture system.

porosity to be log-normally distributed. Given the intrinsic relation between matrix porosity and matrix permeability (Costa, 2006), the matrix permeability is also log-normally distributed. We derived an analytical formulation (Equation 1) for this system (Liu et al., 2007a):

$$\frac{D_e}{D_m} = \left[ \frac{K_e}{K_g} \right]^{\frac{9}{2m^2}} \quad (1)$$

where  $D_e$  is the effective matrix diffusion coefficient,  $K_e$  is the effective matrix permeability,  $D_m$  is the local-scale matrix diffusion coefficient, and  $K_g$  is the geometric mean of matrix permeability. For a typical value of  $m = 3$  (Costa, 2006):

$$\frac{D_e}{D_m} = \left[ \frac{K_e}{K_g} \right]^{\frac{1}{2}} \quad (2)$$

Equation (2) provides an intrinsic relationship between the effective matrix diffusion and the effective matrix permeability. While it has been widely recognized that the effective permeability generally increases with test scale, Equation (2) indicates that the effective matrix diffusion coefficient should follow the same trend as the permeability.

In addition to the single fracture system, we also investi-



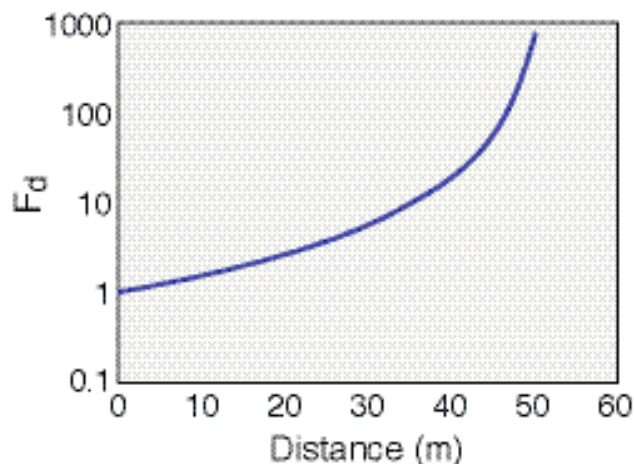


Figure 2. Effective matrix diffusion coefficient as a function of travel distance.

gated matrix diffusion in a more realistic multiple-fracture system. Flow and transport processes in such a system are generally characterized by flow channels (e.g., Tsang and Neretnieks, 1998). Different flow channels may have different flow and transport properties. In this study, we use a simplified conceptual flow model to investigate the effects of interchannel heterogeneity on diffusive properties. Specifically, we consider a simplified multichannel system in which each flow channel has uniform properties and does not mix with any other channels, except at influent and effluent points. Similar conceptual models have been used by other researchers to analyze flow and transport processes in fractured rock (e.g., Neretnieks, 2002). These channels have the same length, width, fracture aperture, and water velocity, but different matrix diffusion coefficients. This treatment allows us to exclude the effects of dispersion processes and focus on the effects of variability in diffusive properties among different flow channels.

Based on the above conceptual model and simplifications, an analytical solution was derived for the ratio of effective matrix diffusion coefficient to the averaged local-scale diffusion coefficient,  $F_d$ , for a multiple fracture system. Figure 2 shows  $F_d$  as a function of test scale for some typical rock

property values. Obviously,  $F_d$  is scale dependent and increases with solute travel distance.

In summary, we have theoretically demonstrated that in addition to effects of flow-path geometry (Liu et al., 2007b), the heterogeneities of rock matrix properties within a single fracture and among different flow channels also contribute to the scale dependence of the effective matrix diffusion coefficient.

## References and Journal Articles

- Costa, A., 2006, Permeability-porosity relationship: A reexamination of the Kozeny-Carman equation based on a fractal pore-space geometry assumption. *Geophy. Res. Lett.*, 33, L02318, doi:10.1029/2005GL025134, 2006.
- Liu, H.H., G.S. Bodvarsson, and G. Zhang, The scale-dependency of the effective matrix diffusion coefficient. *Vadose Zone Journal*, 3, 312–315, 2004.
- Liu, H.H., Y. Zhang, and F.J. Molz, Scale dependence of the effective matrix diffusion coefficient: Some analytical results. *Vadose Zone Journal* (in press), 2007a.
- Liu, H.H., Y. Zhang, Q. Zhou and F.J. Molz, An interpretation of the potential scale dependence of effective matrix diffusion coefficient. *Journal of Contaminant Hydrology*, 90(1-2), 41–57, 2007b.
- Neretnieks, I., A stochastic multi-channel model for solute transport—Analysis of tracer tests in fractured rock. *J. Contam. Hydrol.*, 55, 175–211, 2002.
- Tsang, C.F., and I. Neretnieks, 1998. Flow channeling in heterogeneous fractured rock. *Review of Geophysics*, 36(2), 1998.
- Zhou, Q., H.H. Liu, F.J. Molz, Y. Zhang and G.S. Bodvarsson, Effective matrix diffusion coefficient for fractured rock: Results from literature survey. *Journal of Contaminant Hydrology* (in press), 2006.

# Peña Blanca Natural Analogue

Schön S. Levy<sup>1</sup>, Amr Abdel-Fattah<sup>1</sup>, Paul Cook<sup>2</sup>, John Dinsmoor<sup>1</sup>, Patrick F. Dobson<sup>2</sup>, Mostafa Fayek<sup>3</sup>, Teamrat Ghezzehei<sup>2</sup>, Steve Goldstein<sup>1</sup>, Philip Goodell<sup>4</sup>, Richard Ku<sup>5</sup>, Shangde Luo<sup>5</sup>, Michael T. Murrell<sup>1</sup>, and Katrina Pekar<sup>4</sup>

<sup>1</sup>Los Alamos National Laboratory (LANL) | <sup>2</sup>Lawrence Berkeley National Laboratory (LBNL)

<sup>3</sup>University of Tennessee-Knoxville | <sup>4</sup>University of Texas-El Paso (UTEP) | <sup>5</sup>University of Southern California (USC)

## Research Objectives

The objective is to study radionuclide transport at a site with characteristics analogous to a nuclear-waste repository at Yucca Mountain, and to use the results to test an entire process model and total system performance assessment. This will be accomplished by using field and laboratory measurements and process-model results from the Peña Blanca, Chihuahua, México, site. A three-dimensional conceptual and numerical model of radionuclide transport in the unsaturated and saturated zones will be developed.

Specific objectives for improved understanding include (1) identifying active fractures and the extent of fracture-matrix geochemical interaction, (2) investigating aqueous transport behavior in the unsaturated and saturated zones, (3) studying the role of colloid transport and colloid-facilitated transport of radionuclides; and (4) studying surficial and shallow subsurface transport processes.

## Approach

The Peña Blanca Nopal I site, in Chihuahua, México, is a former mine in a uranium ore body within fractured, welded tuff similar to the repository host rock at Yucca Mountain. The site is in the southern Basin and Range province in an arid environment with a thick (>200 m) unsaturated zone. Three wells were drilled within and adjacent to the ore body, providing access to saturated-zone waters. A seepage-collection system in an old mine adit provides information about percolating water in the unsaturated zone. Field work also includes core sampling, sampling of fractured rock at various distances from the ore body, and mapping, sampling, and *in situ* gamma surveying of surficial materials related to previous surface storage of high-grade ore. Structural and stratigraphic studies provide a basis for the assembly and analysis of geochemical data. Field data, plus chemical and isotopic analysis of rock and water samples, provide the input for process models and a total-system performance assessment.

## Accomplishments

Research results were presented at the 2005 Geological Society of America Annual Meeting, the 2006 International High-Level Radioactive Waste Management Conference, and the 2007 American Geophysical Union Joint Assembly.

Site visits conducted throughout 2006 concluded in December 2006. Saturated-zone waters were collected by bailing or pumping on-site wells and by sampling near-site wells being pumped for agricultural use. In August 2006, downhole instruments to monitor water level, pH, and dissolved oxygen were installed in the three onsite wells. The recorded data were downloaded periodically by Autonomous University of Chihuahua faculty and students, who will analyze the data. Large-volume pumped-water samples were run through manganese cartridge filters to collect short-lived radionuclides. Samples were also collected for colloid and radon analysis.

Water samples were collected from a seepage-collection array in an adit. Seepage water collection involved using fixed bottles with collector funnels and automated columns that recorded volume and time of seepage water arrival. A weather station installed in March 2006 recorded continuous measurements of basic meteorological data. Figure 1 shows rainfall and seepage volumes at the automated collectors between May 2006 and December 2006.

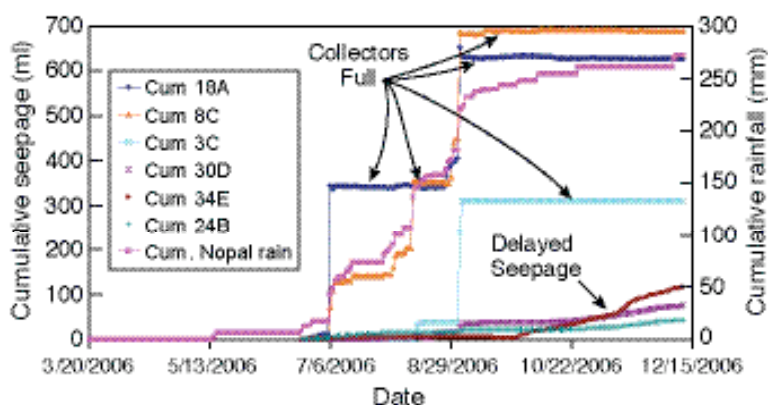


Figure 1. Rainfall and seepage water collected using automated columns at Nopal I (arrows indicate the maximum volume of water in the automated seepage collectors).

The first big storm of the summer rainy season was in July. Data show that in two of the collection sites, seepage water traveled through 8 m of fractured tuff within two hours (the measurement interval) or less. Seepage arrival at the other collectors was much more gradual. These results clearly demonstrate the existence of fast and slow flow pathways.

Seepage waters are enriched in deuterium (D) and  $^{18}\text{O}$  relative to saturated-zone waters. A subset of the oxygen isotope data, representing seepage waters from automated columns at 18A and 27C, is shown in Figure 2 as a function of time. There is a marked temporal variation in composition related to the timing of the seasonal rainy period. Both  $\delta\text{D}$  and  $\delta^{18}\text{O}$  values increase as the dry season progresses, and then a sharp decrease in values occurs right after the onset of the summer monsoon season (first week of July). The increase in  $\delta\text{D}$  and  $\delta^{18}\text{O}$  values during the dry season is likely a result of evaporation occurring as water slowly infiltrates through the rock mass.

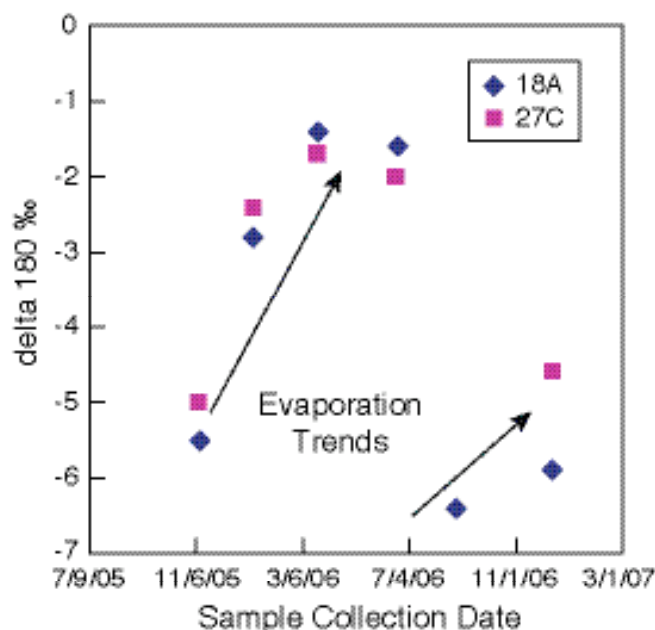


Figure 2. Oxygen isotopic data for seepage waters from two automated collectors at Nopal I.

In general, there are high U concentrations and low  $^{234}\text{U}/^{238}\text{U}$  ratios (close to secular equilibrium) in waters from the front of the adit and low U concentrations with high  $^{234}\text{U}/^{238}\text{U}$  values in samples from the rear of the adit. These results confirm the concept that water from the front of the adit has experienced a longer rock-water interaction time and/or greater U dissolution rate relative to waters

from the rear of the adit. The larger data set shows no seasonal variation of uranium isotopic systematics.

Analyses of ultra-filtered well waters collected in 2006 indicate that ~93–97% of the uranium present is truly dissolved and not in colloidal form. Particle counts for local and regional well samples collected in 2004–2006 indicate colloid contents ranging from  $1.0\text{E}8$  to  $1.4\text{E}6$  particles/mL (~0.2 to 0.003 mg/L). Particle counts for the Nopal I wells have decreased from 2004 to 2006; the earlier, higher counts may have been related to drilling operations. There is a bimodal distribution of colloid surface charge (one population negatively charged and one population neutral or slightly positive) that may reflect the presence of both natural and anthropogenic (e.g., bacteria) colloids.

Uranium concentrations for well waters collected in August 2006 are approaching “steady-state” or “equilibrium” concentrations (23 ppb in PB-1 and 398 ppb in PB-3; Figure 3), down from values as high as 18,000 ppb soon after the wells were drilled. The rates of decrease in aqueous uranium concentration since the wells were drilled (in 2003) suggest that groundwater flow rates are <10 m/yr.

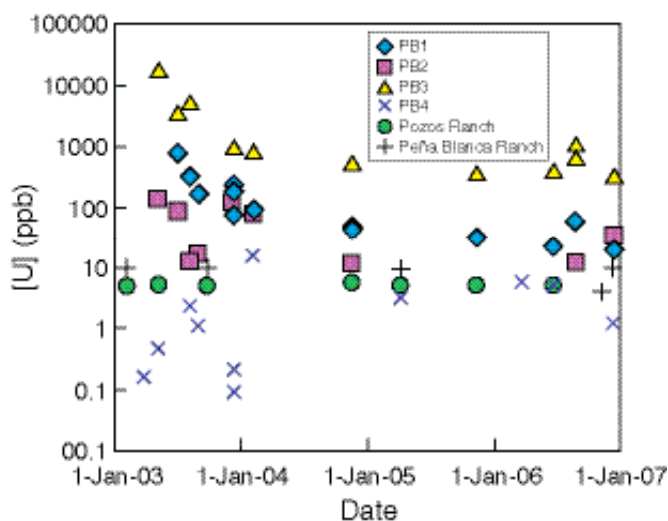


Figure 3. Time series for uranium concentrations in saturated-zone waters of the Peña Blanca region.

A study of  $^{238}\text{U}$ - $^{239}\text{Pu}$  disequilibrium in four saturated zone water samples (PB1, PB2, PB3, and PB4) collected in December 2003 was completed. All samples had  $^{239}\text{Pu} < 50$  atoms/g, and sample PB3 had the highest U concentration of 966 ppb. These values were used to calculate an upper limit Pu/U ratio of  $2\text{E}-14$ , based on the assumption that any Pu in the sample is derived from neutron reactions

with  $^{238}\text{U}$ . Comparison of this value with the lower-limit secular equilibrium ratio of  $2\text{E-}12$  allows us to estimate that  $\text{R(Pu)}/\text{R(U)}$  is at least  $\sim 100$ , where  $\text{R}$  is the retardation factor (transport rate of groundwater/transport rate of radionuclide). This means that Pu is at least two orders of magnitude less mobile than U in the saturated zone at Nopal I.

Prior studies of  $^{238}\text{U}$ - $^{234}\text{U}$ - $^{230}\text{Th}$ - $^{226}\text{Ra}$  disequilibria showed that  $\text{R(Ra)}/\text{R(U)}$  ranges from 0.01 to 100, and  $\text{R(Th)}/\text{R(U)}$  ranges from 1 to 200. Efforts to determine  $\text{R(U)}$  from short-lived nuclide data are under way, but it typically is on the order of  $\sim 1,000$  elsewhere. The short-lived nuclide data were used to calculate retardation factors on the order of 1,000 for radium and 10,000 to 10,000,000 for lead and polonium. Radium has enhanced mobility in adit water and fractures near the uranium deposit. Mean fracture width in the area is estimated to vary from  $\sim 0.2$  to  $\sim 4.0\ \mu\text{m}$ . Also, well-water samples were sent to the DOE Idaho Falls laboratory for analysis of technetium-99, but all samples were below the detection limit of about E-6 ppb for concentrated samples.

Preliminary mineral isotopic ages from Nopal I suggest the following: (1) a uraninite mineralizing event at  $32\pm 8$  Ma, possibly related to Basin and Range tectonism; (2) an oxidizing event at  $\sim 3.1$  Ma that formed uranophane; (3) a second uraninite mineralizing event at  $\sim 1.6$  Ma; and (4) subsequent oxidizing events that precipitated schoepite ( $\sim 85$  ka) and weeksite/boltwoodite ( $\sim 41$  ka). The relation between  $<1$  Ma uraninite from the Pozos conglomerate 100 m below the main ore body and the  $\sim 1.6$  Ma uraninite is unclear. However, the conglomerate may have scavenged uranium moving downward through the unsaturated zone.

Forty-element chemical analyses were obtained for 20 Peña Blanca samples, including high-grade ore and host rock. These analyses will provide source-term information for numerical modeling of radionuclide transport. Gamma-ray spectroscopy of soils beneath and downslope of a block of high-grade uranium ore, emplaced on the ground surface during active mining, indicates that dispersion of particulates from the ore into the soil has reached a depth of 20 cm over 25 years. A preliminary effort has

been made to calculate effective dispersion coefficients for  $^{234}\text{Th}$ ,  $^{230}\text{Th}$ ,  $^{234}\text{U}$ ,  $^{226}\text{Ra}$ , and  $^{210}\text{Pb}$  in the soil.

## Related Publications

- Presentations made at the GSA annual meeting in October 2005 were listed in the *OSTI Annual Report 2005*.
- Fayek, M., M. Ren, P. Goodell, P. Dobson, A. Saucedo, A. Kelts, S. Utsunomiya, R. Ewing, L. Riciputi, and I. Reyes, Paragenesis and geochronology of the Nopal I uranium deposit, Mexico. Proceedings of the 11th International High-Level Radioactive Waste Management Conference, pp. 55–62, Las Vegas, Nevada, April 30–May 4, 2006.
- French, D., E. Anthony, and P. Goodell, U-Series disequilibria in soils, Peña Blanca Natural Analogue, Chihuahua, Mexico. Proceedings of the 11th International High-Level Radioactive Waste Management Conference, pp. 63–69, Las Vegas, Nevada, April 30–May 4, 2006.
- Ghezzehei, T., P. Dobson, J. Rodriguez and P. Cook, Infiltration and seepage through fractured welded tuff. Proceedings of the 11th International High-Level Radioactive Waste Management Conference, pp. 105–110, Las Vegas, Nevada, April 30–May 4, 2006.
- Goldstein, S.J., S. Luo, T. Ku, and M. Murrell, Uranium-series constraints on radionuclide transport and groundwater flow at the Nopal I uranium deposit, Sierra Peña Blanca, Mexico. Proceedings of the 11th International High-Level Radioactive Waste Management Conference, pp. 215–222, Las Vegas, Nevada, April 30–May 4, 2006..
- Luo, S., T. Ku, V. Todd, M. Murrell, and J. Dinsmoor, Increased concentrations of short-lived decay-series radionuclides in groundwaters underneath the Nopal I uranium deposit at Peña Blanca, México. Eos Transactions, American Geophysical Union, 88 (23), Joint Assembly Supplement, Abstract GS22A-03, 2007.
- Pekar, K., P. Goodell, J. Walton, E. Anthony, M. Ren, Modeling of U-series radionuclide transport through soil at Peña Blanca, Chihuahua, México. Eos Transactions, American Geophysical Union, 88 (23), Joint Assembly Supplement, Abstract GS22A-02.
- Saulnier, G., The Peña Blanca Natural Analogue performance assessment model. Proceedings of the 11th International High-Level Radioactive Waste Management Conference, April 30–May 4, 2006, Las Vegas, Nevada, 228–235, 2006.

---

This page intentionally left blank.



# Matrix/Fracture Flow in Subrepository Units

Leonid Neymark<sup>1</sup>, James Paces<sup>1</sup>, David Vaniman<sup>2</sup>, and Steve Chipera<sup>2</sup>

<sup>1</sup>US Geological Survey | <sup>2</sup>Los Alamos National Laboratory (LANL)

## Research Objectives

The objective of this study is to investigate the time-integrated fracture-matrix interaction and transport of natural uranium (U) in zeolitized tuffs below the proposed repository at Yucca Mountain, Nevada, by comparing the mineralogical, chemical, and U-series isotopic compositions of samples from fracture surfaces and from variably fractured rocks.

## Approach

Retardation of radionuclides by sorption on minerals in the rocks along downgradient groundwater flow paths is a positive attribute of the natural barrier at Yucca Mountain, Nevada, the site of a proposed high-level nuclear waste repository. Alteration of volcanic glass in nonwelded tuffs beneath the proposed repository horizon produced thick, widespread zones of zeolite- and clay-rich rocks with high sorptive capacities. The high sorptive capacity of these rocks is enhanced by the large surface area of tabular to fibrous mineral forms, which is about 10 times larger in zeolitic tuffs than in devitrified tuffs, and about 30 times larger than in vitric tuffs. The alteration of glass to zeolites, however, was accompanied by expansion that reduced the matrix porosity and permeability. Because water would then flow mainly through fractures, the overall effectiveness of radionuclide retardation in the zeolitized matrix actually may be decreased relative to unaltered vitric tuff.

Isotope ratios in the decay chain of  $^{238}\text{U}$  are sensitive indicators of long-term water-rock interaction. In systems older than about 1 m.y. that remain closed to mass transfer, decay products of  $^{238}\text{U}$  are in secular radioactive equilibrium where  $^{234}\text{U}/^{238}\text{U}$  activity ratios (AR) are unity. However, water-rock interaction along flow paths may result in radioactive disequilibrium in both the water and the rock, the degree of which depends on water flux, rock dissolution rates,  $\alpha$  recoil processes, adsorption and desorption, and the precipitation of secondary minerals.

The effects of long-term water-rock interaction that may cause radionuclide retardation were measured in samples of Miocene-age subrepository zeolitized tuffs of the Calico Hills Formation (Tac) and the Prow Pass Tuff (Tcp), from borehole USW SD-9 (Engstrom and Rautman, 1996) near

the northern part of the proposed repository area. Mineral abundances and whole rock chemical and U-series isotopic compositions were measured in unfractured core samples (depth interval 451.1 to 633.7 m) representing rock matrix, in rubble (about 1 cm) rock fragments representing zones of higher permeability (assuming that the rubble core indicates a broken zone in the rock mass rather than an artifact of drilling), and in samples from surfaces of natural fractures representing potential fracture pathways. U concentrations and isotopic compositions also were measured in samples of pore water obtained by ultracentrifugation or by leaching rock samples with deionized  $\text{H}_2\text{O}$ . The concentrations and isotopic compositions of loosely bound U adsorbed on reactive mineral surfaces were obtained by analyzing 1 M sodium acetate (NaOAc) leachates of whole-rock samples.

Mineral abundances were measured at Los Alamos National Laboratory by x-ray powder diffraction methods using the full-pattern quantitative analysis program FULLPAT. Chemical compositions of major and trace elements were determined at the U.S. Geological Survey (USGS) laboratory in Denver by several techniques, including standard x-ray fluorescence spectroscopy (XRF) and inductively coupled plasma-mass spectrometry (ICP MS) techniques. Uranium concentrations and isotopic compositions were measured at USGS using a thermal ionization mass spectrometer (TIMS). Reproducibility of TIMS analyses was about 1% ( $2\sigma$ ) for elemental concentrations and 0.2% for U isotope ratios. Atomic isotope ratios were converted to activity ratios using known decay constants.

## Accomplishments

The most common secondary minerals in 35 samples of the zeolitized tuff are clinoptilolite (0.5 to 76.3 %), opal-CT (6.5 to 21.8 %), mordenite (1.2 to 22.4 %), and smectite (0.1 to 44 %). Fracture surfaces have more smectite (median value of 6.1%) than unfractured and rubble core (median value of 3.2%).

Concentration trends with depth for whole-rock samples from the upper 50 m of the Tac indicate accumulation of Ca accommodated by loss of Na as a result of downward water movement and cation exchange within the zeolitized rock sequence, consistent with published results

(Vaniman et al., 2001). However, systematic variations with depth and zeolite abundance are not observed for U concentrations over this same depth interval.

Uranium contents in NaOAc leachates (0.012 to 0.071  $\mu\text{g/g}$  rock) represent a mobile U component adsorbed on mineral surfaces or in readily acid-soluble secondary minerals. Compared with whole-rock analyses, these data indicate that the adsorbed U comprises 0.3 to 1.7 percent of total rock  $^{238}\text{U}$ . These data allow estimates of the time-integrated *in situ* U partition coefficient ( $K_d = C_s/C_w$ , where  $C_s$  and  $C_w$  are concentrations in the solid and water, respectively) under natural flow conditions. Use of median U concentrations in pore water (5 ng/mL) and NaOAc leachates (0.035  $\mu\text{g/g}$  rock) yields an estimate of the  $^{238}\text{U}$   $K_d$  value of about 7 mL/g. This value is larger than the value of 0.5 mL/g obtained for crushed tuffs from laboratory batch experiments that currently is used for zeolitized units at Yucca Mountain (BSC, 2004, Table 5-1).

Whole-rock samples of unfractured core, rubble core, and fracture surfaces have similar  $^{234}\text{U}/^{238}\text{U}$  AR, ranging from 0.92 to 1.16 indicating both enrichments ( $^{234}\text{U}/^{238}\text{U}$  AR > 1) and depletions ( $^{234}\text{U}/^{238}\text{U}$  AR < 1) in the daughter  $^{234}\text{U}$  relative to the parent  $^{238}\text{U}$ . In contrast to the rock samples, all pore water and rock leachate samples have elevated  $^{234}\text{U}/^{238}\text{U}$  AR ranging from 1.1 to 5.2. Whole-rock  $^{234}\text{U}/^{238}\text{U}$  AR greater than 1 for these zeolitized rocks contrast with data from samples of the welded part of the Topopah Spring Tuff (Tpt), the proposed repository horizon, that invariably have  $^{234}\text{U}/^{238}\text{U}$  AR < 1. The depletion in  $^{234}\text{U}$  in Tpt rocks is caused by preferential removal of  $^{234}\text{U}$  by the percolating water as a result of  $\alpha$  recoil processes. Therefore, the large  $^{234}\text{U}/^{238}\text{U}$  AR in pore water and in U sorbed on mineral surfaces indicate that  $^{234}\text{U}$  removed from overlying units is transported in percolating water and retained in underlying zeolitized units. U-series isotope data for whole-rock samples from subrepository units having  $^{234}\text{U}/^{238}\text{U}$  AR > 1 also strongly support the potential for retention of U from percolating water by zeolitized rocks and indicate that amounts of retardation of radionuclides may be greater than currently credited to zeolitized rocks at Yucca Mountain.

Evolution of  $^{234}\text{U}/^{238}\text{U}$  AR in zeolitized rocks continuously adsorbing U from percolating water is described by a simple box model. The model assumes that U in zeolitized rock is derived from three components: (1) U in the rock matrix; (2) U adsorbed onto mineral surfaces from percolating water; and (3)  $^{234}\text{U}$  produced from decay of adsorbed  $^{238}\text{U}$  and implanted into the rock matrix by alpha-recoil processes. The model does not consider U loss or gain from the relatively slower processes of bulk rock dissolution and secondary mineral precipitation. According to simulations from this model, the observed similarity of ARs in samples of pore water and NaOAc rock leachates indicates that U adsorption in zeolitized tuffs from percolating water is a reversible process occurring at rates much faster than radioactive decay of  $^{234}\text{U}$ . Values of time-integrated *in situ* distribution coefficients  $K_d \gg 1$  for U adsorption indicate that zeolitized rocks may be important in retardation of U and other actinides with similar geochemical properties in the subrepository zeolitized units in the Yucca Mountain UZ. The *in situ* retardation factor for U in samples of zeolitized rocks is as much as 290, which means that U moves through zeolitized rocks much more slowly than the percolating water.

## References

- BSC, Technical Basis Document No. 10: Unsaturated zone transport, Revision 1. Bechtel SAIC Company, LLC, Las Vegas, Nevada. Accessed March 6, 2006, at <http://www.lsnnet.gov> (LSN# NRC000024904), 2004.
- Engstrom, D.A. and C.A. Rautman, Geology of the USW SD 9 Drill Hole, Yucca Mountain, Nevada," SAND96-2030, 128 p., Sandia National Laboratories, Albuquerque, New Mexico. Accessed March 6, 2006, at <http://www.lsnnet.gov> (LSN# DEN000707221), 1996.
- Vaniman, D.T., S.J. Chipera, D.L. Bish, J.W. Carey, and S.S. Levy, Quantification of unsaturated-zone alteration and cation exchange in zeolitized tuffs at Yucca Mountain, Nevada, USA. *Geochimica et Cosmochimica Acta*, 65, 3409–3433, 2001.

# Pore Connectivity, Episodic Flow, and Unsaturated Diffusion in Fractured Tuff

Qinzhong Hu<sup>1</sup>, Robert P. Ewing<sup>2</sup>, and Liviu Tomutsa<sup>3</sup>

<sup>1</sup>Lawrence Livermore National Laboratory (LLNL) | <sup>2</sup>Iowa State University | <sup>3</sup>Lawrence Berkeley National Laboratory (LBNL)

## Research Objectives

In low-permeability, unsaturated fractured rock, water flows predominantly through the interconnected fracture network, with some water moving into or out from the neighboring matrix rock. During flow episodes, wetting advectively transports radionuclides from fractures into the matrix; between flow episodes, drying at the fracture face advectively moves radionuclides back toward the fracture. Diffusion transports radionuclides from the fracture into the matrix (matrix diffusion), or from the matrix back into flowing fractures (back diffusion). Finally, some radionuclides in the matrix sorb onto matrix rock. These fracture-matrix interactions—with interacting wetting and drying, diffusion, and sorption—tend to retard breakthrough of a radionuclide pulse released to the fracture network. Factors such as matrix pore connectivity, and the timing and magnitude of fracture flow events, influence these interacting processes. These factors are investigated in our work.

## Approach

We have developed and used innovative approaches (e.g., application of imbibition tests to probe pore connectivity) and techniques (e.g., the unsaturated transport-sorption method, laser ablation coupled with inductively coupled plasma-mass spectrometry [LA/ICP-MS] for microscale solid sampling). Coupled with pore-scale network modeling, these approaches and techniques are used to further understand and quantify the interacting imbibition-diffusion-sorption processes influencing radionuclide transport in unsaturated fractured rock at Yucca Mountain.

## Accomplishments

### Preparation of Initially Moist Samples

Partially saturated cores were obtained by equilibrating initially fully saturated cores within relative humidity (RH) chambers controlled by different oversaturated brines until they reached constant weights. Two RH chambers, with respective RH values of 44% (mimicking the low RH during the heat-dissipation phase after nuclear waste package emplacement) and 98% (mimicking the in situ condition of the vadose zone at Yucca Mountain),

were used in this project. Equilibrated core samples were then used in the tests for tracer imbibition and unsaturated diffusion.

### Unsaturated Transport-Sorption Tests

Unsaturated transport-sorption tests were performed on TSw, CHv, and CHz samples, imbibing a tracer solution into samples at different antecedent water saturations (oven-dried, equilibrated at 44% or 98% RH). The tracer solution contained a suite of nonsorbing and sorbing tracers (including  $\text{ReO}_4^-$  and the radionuclides  $^{237}\text{Np}$  and  $^{242}\text{Pu}$ ). We then used LA/ICP-MS to measure the fine-scale distribution of tracers as a function of distance from the imbibing rock face. Figure 1 shows the nonretarded transport of  $\text{ReO}_4^-$  and transport delayed by sorption for  $^{237}\text{Np}$  and  $^{242}\text{Pu}$  tracers in TSw34 samples at different antecedent water saturations. For imbibition into an initially dry core, the  $\text{ReO}_4^-$  front is steep, because a strong capillary force drives advective flow and tracer transport (Figure 1a). During imbibition into a moist medium, solutes disperse by mixing with “old” water, and thus a less sharp  $\text{ReO}_4^-$  profile is observed (Figure 1c).

### Saturated and Unsaturated Tracer Diffusion

Saturated diffusion tests were conducted to investigate tracer diffusion into fully water-saturated cylindrical rock samples (TSw34, CHv, and CHz). We directly mapped the tracer concentration distribution in the rock sample after a certain diffusion time, which ranged from minutes to one day, depending upon rock properties.

Following our published two-element (source-sink) approach (Hu et al., 2004), we conducted unsaturated diffusion tests for three tuff samples under two initial water saturations (44 and 98% RH equilibrated). Tracer distributions on the surface, as well as in the interior, of both elements were immediately mapped using LA/ICP-MS. Analysis to obtain the diffusion coefficient is under way. Preliminary results show the expected diffusion at high water saturation, while diffusion at lower (initially equilibrated at 44% RH) is significantly hindered.

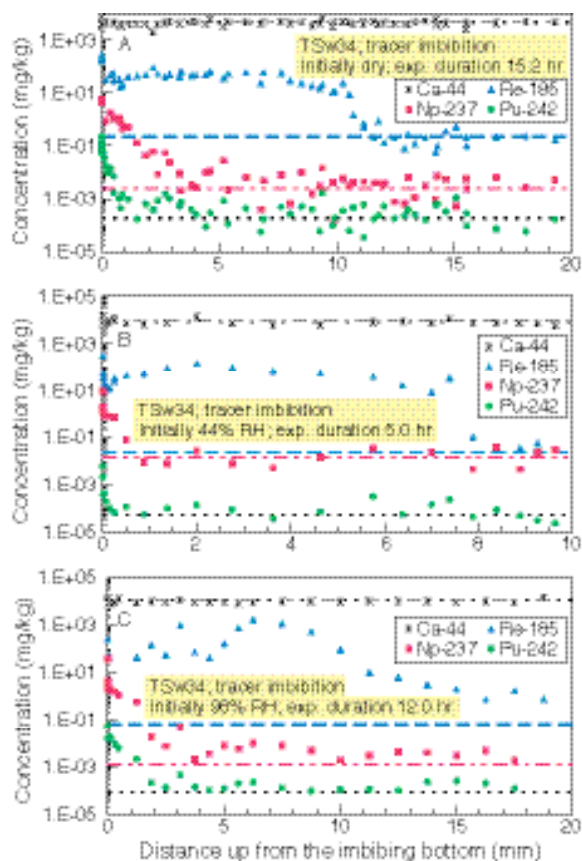


Figure 1. Distribution of imbibed tracers in initially (A) dry, (B) moist at 44% RH, and (C) moist at 98% RH TSw34 cores. Ca concentration intrinsic to the rocks is distributed uniformly. Dashed lines are background levels for each tracer.

### Episodic Fracture Flow and Tracer Transport

We have conducted the fracture flow test with the TSw34 devitrified rock under episodic flow events. We prepared a saw-cut fracture core (length 10.2 cm, diameter 4.4 cm, and fracture aperture 100  $\mu\text{m}$ ) for TSw34 initially equilibrated at >97% relative humidity. Episodic flow involved four cycles of tracer solution flow within the fracture, followed by flushing with high humidity air. Each flow episode contained at least one nonsorbing tracer ( $^3\text{H}$ , Se, Br, Mo,  $^{99}\text{Tc}$ , I, and Re) and one sorbing tracer (Sr, Cs,  $^{235}\text{U}$ ,  $^{237}\text{Np}$ , and  $^{241}\text{Pu}$ ). The nonsorbing  $^3\text{H}$  and  $\text{ReO}_4^-$  serve as diffusivity tracers with different aqueous diffusion coefficients.

Liquid effluent from the flow reactor was analyzed to obtain the breakthrough curves of non- or less-retarded tracers. After the flow tests were complete, the flow reactor was opened and the distribution of strongly retarded tracers within the fractured core characterized by LA/ICP-MS.

Results indicate interacting imbibition, diffusion, and sorption, which will contribute to radionuclide retardation under fracture-dominated preferential flow.

### Pore-Scale Network Modeling

Some of the laboratory imbibition tests showed two distinct regimes, having slopes of one-half and one-quarter in log-log (cumulative mass imbibed over time) space. "Normal" imbibition gives the slope of one-half (the imbibition front moves with the square root of time), but the lower-slope regime appears in rock with poorly interconnected pore space. In some cases, imbibition transitioned from low-slope to normal-slope behavior; the opposite was never observed. This behavior was produced in the pore-scale simulations as well, with bonds in the cubic lattice pruned almost to the percolation threshold. It is known from percolation theory that processes operating at scales smaller than the correlation length will exhibit anomalous behavior, while above that scale they will behave normally. The distance from the inlet face at which the slopes cross from anomalous to normal is the correlation length of percolation theory and is related to the connectedness of the medium.

The measured crossover distance is a function of both pore connectivity and sample size and shape. This past year, we ran multiple simulations of different-shaped lattices, with length:diameter ratios ranging from 1/8 to 8. These were run at several connectivity values above the percolation threshold. To cope with the high variance of samples near the percolation threshold, we ran several hundred additional simulations at and just above the threshold itself. Simulations were slower the closer they were to the percolation threshold, so significant computer time was involved in these studies.

The statistics of the imbibition curves, whether measured or simulated, pose some challenges. How should the breakpoint (where a curve changes slope) be determined, especially when the data are noisy or the break appears gradual? How should we decide whether a given curve is "really" one line, or two? One new method—the Weighted Hidden Markov Method—and the classical 3-parameter minimum sum of squares method both appear fairly robust with respect to finding the breakpoint. We also compared several test statistics for deciding whether the data represent one line or two. A manuscript detailing this statistical subinvestigation will soon be submitted to a peer-reviewed journal.

### References

- Hu Q., T.J. Kneassey, J.S.Y. Wang, L. Tomutsa, and J.J. Roberts, Characterizing unsaturated diffusion in porous tuff gravels. *Vadose Zone Journal*, 3 (4), 1425-1438, 2004.

## SATURATED ZONE FLOW AND TRANSPORT

### **Determining the Redox Properties of Yucca Mountain-Related Groundwater Using Trace-Element Speciation for Predicting the Mobility of Nuclear Waste**

James Cizdziel and Vernon Hodge, University of Nevada, Las Vegas; Karen H. Johannesson, University of Texas at Arlington

### **Field Studies for the Determination of Transport Properties of Radioactive Solutes and Colloids Using Chemical Analogues**

Barry Freifeld, Lawrence Berkeley National Laboratory (LBNL)

### **Improved Characterization of Radionuclide Retardation in Volcanics and Alluvium**

Cynthia A. Dean, Mei Ding, Paul W. Reimus, Cheryl Sedlacek, Schon Levy, and Steve Chipera, Los Alamos National Laboratory (LANL)

### **Carbon-14 Groundwater Analysis**

Gary L. Patterson, United States Geological Survey (USGS); James Thomas, Desert Research Institute



---

This page intentionally left blank.

# Determining the Redox Properties of Yucca Mountain-Related Groundwater Using Trace-Element Speciation for Predicting the Mobility of Nuclear Waste

James Cizdziel<sup>1</sup>, Vernon Hodge<sup>1</sup>, and Karen H. Johannesson<sup>2</sup>

<sup>1</sup>University of Nevada, Las Vegas | <sup>2</sup>University of Texas at Arlington

## Research Objectives

The objective of this task is to determine the principal oxidation state (redox) species of select elements in samples of groundwater in the vicinity of Yucca Mountain, which is being evaluated as a site for geologic disposal of the nation's spent nuclear fuel and high-level nuclear waste. Samples to be analyzed include, but are not limited to, groundwater from wells of the Nye County Early Warning Drilling Program. Elements to be studied include arsenic (As), antimony (Sb), selenium (Se), chromium (Cr), manganese (Mn), copper (Cu), molybdenum (Mo), vanadium (V), tungsten (W) and uranium (U). Percentages of major redox species of these elements and total concentrations will be measured and tabulated.

The purpose is to develop a more accurate and complete description of the redox properties of Yucca Mountain-related groundwater, which influences the solubility and transport of radionuclides should they enter the groundwater system. A possible natural barrier to radionuclide migration in the saturated zone (SZ) is the presence of nonoxidizing or reducing environments. For example, the mobility of Tc-99 in oxic groundwater, ascribed to the pertechnetate ion, is greatly diminished in reducing groundwater. The containment of radionuclides away from the accessible environment is a key feature in the Yucca Mountain performance assessment.

## Approach

In the current study, we have attempted to expand on previous work using multiple redox couples to generate an empirically based scale of redox conditions in Nye County groundwater. Although traditionally used to predict redox species in groundwater,  $E_h$ -pH relationships are based on thermodynamic concepts, and natural water systems are rarely in equilibrium. Moreover, some redox couples do not react on Pt electrodes at or near neutral pH values or at low concentrations. Thus there is some question as to how well by  $E_h$ -pH diagrams predict actual groundwater species. Indeed, a tentative thesis title for a graduate student working on the project is "How Well Do  $E_h$ -pH Diagrams Predict the Redox Species Distribution in Groundwater: Test Case: Southern Nevada." However, there are also challenges to measuring elemental oxidation states in groundwater, including sampling in a manner

that preserves the native redox species, while employing suitable calibration standards and identifying interferences and artifacts in the analysis.

Our sampling approach has been to piggy-back sampling efforts to collect groundwater whenever other research or monitoring groups are pumping in the area. Samples are filtered, collected without headspace in a specially designed inert apparatus to minimize contact with the atmosphere, transported to the laboratory on ice, and analyzed as soon as possible to measure the native redox species. Field measurements, including  $E_h$  measurements from a Pt-electrode and other redox measures, are included for comparison purposes. Our analytical approach for the trace element redox analysis couples ion chromatography (to separate the ions) and inductively coupled plasma mass spectrometry (as an element selective detector). Multiple spikes and other QA measures are incorporated to assess data quality and to make sure on-column chemistry is not altering the redox species native to the groundwater.

## Accomplishments

- The scientific investigation plan (SIP-UNLV-048) was reviewed and accepted in February 2006. Task personnel completed QA indoctrination and training. The task participated in the OCRWM Natural Barriers Thrust Area Project Review Meeting, held in Berkeley on February 13, 2006.
- An ion chromatograph was successfully coupled to two different inductively coupled plasma mass spectrometers. Scoping studies were performed to test procedures and optimize experimental parameters. Procedures for ten elements were tested using water from well J-12 on the Nevada Test Site (NTS). The method is published on the Nevada System of Higher Education's Quality Assurance Programs website.
- Altering the redox conditions of a mixed element standard revealed that vanadium (V) is particularly sensitive to redox changes using our

---

methodology. Thus, V, and potentially other elements, may serve as early indicators of subtle changes in the redox conditions of groundwater. Changes for less sensitive elements may suggest more drastic modification of the groundwater redox environment.

- A sample collection scheme was devised to minimize groundwater contact with air and preserve oxidation states native to the sample. Groundwater was collected from wells from the Nye County Early Warning Drilling Program (NCEWDP). This network of wells is generally located downgradient of Yucca Mountain in the Death Valley regional groundwater flow system. Samples were collected and analyzed from the following NCEWDP wells: 191M1 Zone 1 and 5, 1S Zone 1 and 2, and 9SX Zone 1-4. Additional sampling is planned for the NTS and Ash Meadows National Wildlife Refuge.
- Data from the NCEWDP wells indicate that most of the groundwater from these locations is oxidizing with respect to the elements measured. However, there also appear to be pockets of groundwater with reducing conditions (e.g., well 7SC, measured earlier). There is a minor trend with greater percentages of reduced species by depth within the same well. Using the measured values of the redox couples, together with field

measurements of pH,  $E_h$  values were calculated for comparison to field-measured values obtained by a standard Pt-electrode.

- A field-speciation method for arsenic, described in *USGS Water-Resources Investigations Report 02-4144*, was employed with slight modification at select sampling sites: 191M1 Zone 1 (unfiltered), 1S Zone 2 (filtered), 9SX Zone 1 (filtered), 9SX-Zone 4 (filtered). The results were comparable with data obtained by IC-ICP-MS, giving us increased confidence in our technique.
- Availability of oxidation state standards from qualified suppliers is extremely limited. Procedures were developed for the IC-ICP-MS analysis and for the acceptance of unqualified inorganic oxidation state calibration standards for quality-affecting work.
- The presentation "Redox Properties of Groundwater near Yucca Mountain Using Trace Element Speciation Determined by IC-ICP-MS" was given at the American Chemical Society National Meeting (3/21/07) at a special symposium entitled "Understanding Radionuclide Transport in the Environment: Remediation, Nuclear Waste Disposal and Long-Term Stewardship." A poster was also presented at the Devil's Hole Conference.

# Field Studies for the Determination of Transport Properties of Radioactive Solutes and Colloids Using Chemical Analogues

Barry Freifeld<sup>1</sup>, Paul Reimus<sup>2</sup>, M. J. Umari<sup>3</sup>, and Kathy Gilmore<sup>4</sup>

<sup>1</sup>Lawrence Berkeley National Laboratory (LBNL) | <sup>2</sup>Los Alamos National Laboratory (LANL)

<sup>3</sup>United States Geological Survey (USGS) | <sup>4</sup>Nye County Nuclear Waste Repository Project Office, Nye County, NV

## Research Objectives

The objective of this program (hereafter referred to as the *in situ* Kd program) is to provide an enhanced understanding of saturated zone (SZ) radionuclide sorptive processes, resulting in refined estimates of transport rates along critical flow paths through volcanic tuffs south of the proposed Yucca Mountain repository. Based on relationships to be determined in the laboratory between sorptive behavior of radionuclides and appropriate chemical analogues, injection/pump back tests using analogues will be conducted in the field to observe *in situ* reactive transport processes. As a result of early observations performed at Borehole NC-EWDP-24PB (24PB) suggesting rapid SZ transport, the *in situ* Kd program shifted effort into the understanding of the fast flow paths encountered in 24PB. An emphasis was placed on the interpretation of data collected as a result of the logging and development of 24PB.

## Approach

To further pursue a greater understanding of SZ processes, we developed a test bed for reactive transport sorptive studies. Specifically, the Nye County Nuclear Waste Repository Project Office drilled and completed Borehole 24PB in February and March of 2006. The 24PB testing program includes participation by staff from the Nye County Nuclear Waste Repository Project Office, Lawrence Berkeley National Laboratory, Los Alamos National Laboratory, and the United States Geological Survey. Borehole 24PB is located approximately 15 km south of the proposed Yucca Mountain repository and 6 km north of Highway 95 (Figure 1).

As part of the 24PB drilling program, geophysical logs (including gamma, formation resistivity, self-potential, single-point resistivity, and optical televiewer) were acquired. In addition to the standard suite of logs, flowing fluid electrical conductivity logs (FEC) and distributed thermal perturbation sensor (DTPS) logs were also acquired. The initial goal for collecting flowing FEC logs was to identify

hydrologically significant intervals for the placement of the U-tube groundwater sampling systems for reactive transport tests. The FEC logging program was planned to occur over one to two days. However, observations of fluid fluxes that were greater than expected led to the acquisition (between February 24 and February 28, 2006) of an extensive data set, consisting of six distinct tests comprising 30,000 ft of FEC logs collected over 32 runs. The DTPS logs were acquired to confirm the interpretation of the FEC logs.

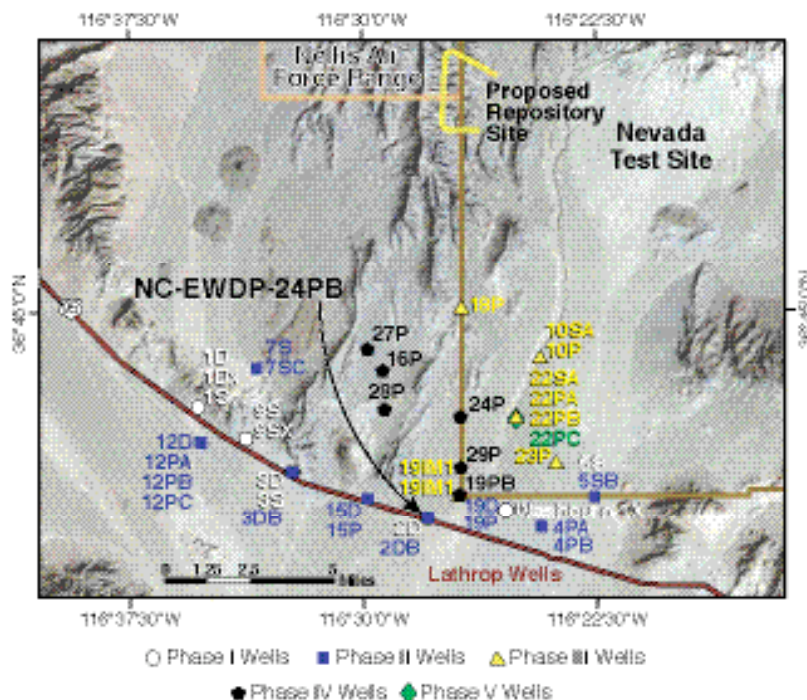


Figure 1. Location of Borehole NC-EWDP-24PB in the Amargosa Valley, approximately 15 km due south of the proposed repository site and 6 km north of Highway 95. Figure courtesy of Nye County NWRPO.

## Accomplishments

The analysis of the FEC and DTPS data provides information not previously obtained from prior Yucca Mountain SZ characterization efforts. Accurate delineation of the spatial distribution of flow within a wellbore, coupled with well-constrained estimates for specific discharge, pro-

vides a comprehensive picture of local advective transport processes. Figure 2 shows DTPS data. The increase in temperature surrounding 24PB is plotted between 24 hours and 48 hours of heating. The fluid flux estimates shown in Figure 2 were produced using a numerical heat and mass-transport simulation that included both advective and diffusive heat-transport mechanisms. What is most significant in the top 125 m is the occurrence of two relatively thin high-flow zones, one at the water table (131–143 meters below ground surface) and the other towards the bottom of the Bullfrog Tuff (221–240 mbgs). Given that the fracture porosity for the Bullfrog Tuff is generally considered to be less than 1%, estimates for groundwater velocities in these fast flow zones are significantly greater than 10 km/yr.

To disseminate the results of this research to the wider scientific community, we gave a poster presentation at the

2006 AGU Fall Meeting in San Francisco, CA, as well as an oral presentation at the 2007 Devil's Hole Workshop, Death Valley, CA. It was emphasized that further investigation of the lateral extent of the identified fast-flowing pathways was required. In light of 24PB being close to where groundwater transitions from volcanics into an alluvial system, we believed that heterogeneities associated with this transition may be responsible for channeling groundwater into narrow geologic conduits. Still, given the implications of rapid transit of released radionuclides, and the close proximity of 24PB to the compliance boundary, further characterization of groundwater transport beneath and south of the proposed Yucca Mountain repository would seem to be warranted. With additional measurements of specific discharge and flow distribution, the current SZ model, based on the measured potentiometric surface, can be better calibrated, and significant reduction in uncertainty will be possible.

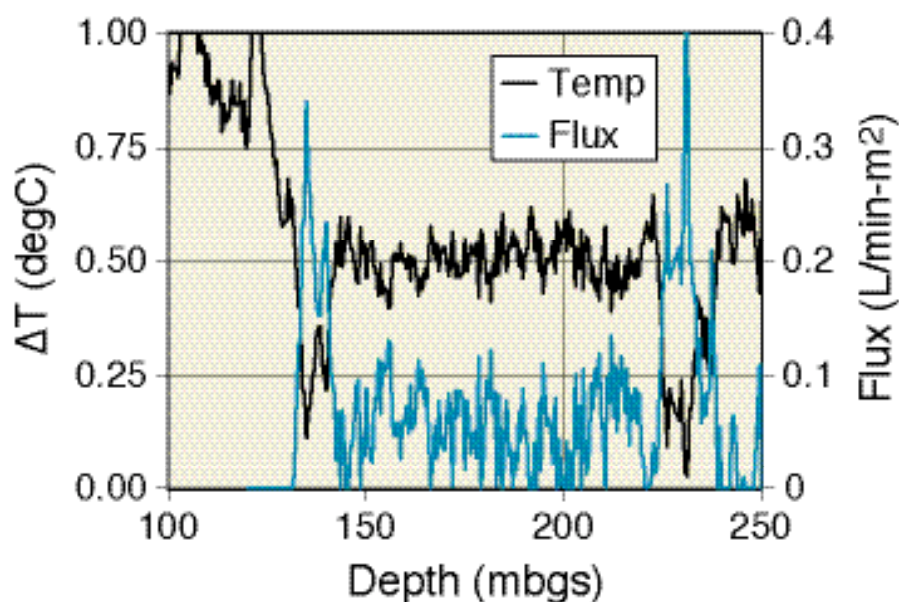


Figure 2. Acquired temperature data and estimated fluid flux for Borehole NC-EWDP-24PB. The groundwater table is located at 126 mbgs. Two distinct fast flow zones with large fluid fluxes are readily identifiable at the depth ranges between 131–143 mbgs and 221–240 mbgs.



# Improved Characterization of Radionuclide Retardation in Volcanics and Alluvium

Cynthia A. Dean, Mei Ding, Paul W. Reimus, Cheryl Sedlacek, Schon Levy, and Steve Chipera  
Los Alamos National Laboratory (LANL)

## Research Objectives

The objective of this project is to demonstrate that uranium (U) and neptunium (Np) retardation in the saturated zone (SZ) is likely to be significantly higher than is currently assumed in Yucca Mountain Project (YMP) process models when slow desorption kinetics are considered. Secondary objectives are to investigate a possible correlation between hydraulic conductivity and sorption, and to study the effects of water chemistry and secondary mineralogy on the ability of the host rock to retard and/or attenuate radionuclides.

## Approach

U and Np sorption to geologic media in current SZ models is based almost entirely on batch sorption and short-term desorption experiments that assume reversible, linear first-order kinetics. Only a single distribution coefficient ( $K_d$ ) can be derived from such experiments, and stronger sorption sites with slower desorption kinetics tend not to be appropriately weighted because they are not effectively interrogated. To investigate the long-term desorption behavior of U and Np from Yucca Mountain saturated alluvium, specially designed column experiments were performed after one to fourteen days of batch sorption of U or Np to alluvium. Several alluvium and groundwater combinations were used in the experiments to study the effects of water chemistry and secondary mineral phases on radionuclide desorption behavior. Desorption rate constants estimated from these experiments were used to calculate a range of effective  $K_d$  values that account for strong sorption sites with slow desorption kinetics, while also accounting for less favorable U and Np sorption sites in the alluvium. Strong sorption sites are believed to be associated with smectite clays and zeolites in the alluvium, and the strength of sorption increases as carbonate concentrations in the groundwater decrease. These observations are consistent with a surface complexation sorption process that is suppressed by carbonate complexation in solution. An explicit kinetic model was developed to model the long-term desorption behavior and to corroborate effective  $K_d$  values obtained from the experimental data.

To investigate the role of clay minerals and water chemistry in Np sorption, we carried out batch sorption of Np

to clays separated from Yucca Mountain alluvium in solutions of varying pH (6.5-10.2). To complement the batch sorption experiments, we conducted x-ray adsorption spectroscopic studies on the clay residue from the experiments to determine whether the Np had undergone any oxidation state changes during sorption.

To investigate a possible correlation between radionuclide sorption and saturated hydraulic conductivity, we also carried out U and Np batch sorption studies using alluvium from NC-EWDP-19PB, which was a sonic drill core hole. The saturated hydraulic conductivity of the material was measured by the Nye County Early Warning Drilling Program in large columns packed with alluvium from the same borehole intervals used in the batch experiments. Quantitative x-ray diffraction analysis and BET surface area measurements of the alluvium were also performed.

## Accomplishments

During FY06, we completed U and Np long-term desorption experiments in the saturated alluvium. During the first quarter of 2007, we also completed interpretative modeling of the U and Np long-term desorption data for alluvium from NC-EWDP-19IM1A, 22SA and 10SA and groundwater from NC-EWDP-19D Zone 1 (lower carbonate), Zone 4 (higher carbonate) and NC-EWDP-10S. Relatively simple spreadsheet calculations provided the estimated ranges of effective partition coefficients ( $K_{d,eff}$  values) in Table 1. These spreadsheet calculations were conducted in lieu of a more complex interpretive modeling approach, because there was insufficient time to qualify the software needed for a more complex model. Effective  $K_d$  values ( $K_{d,eff}$ ) were calculated by dividing an upper and a lower bound sorption rate constant ( $K_{fmax}$  and  $K_{fmin}$ ) by a desorption rate constant ( $K_r$ ) calculated in two ways: a discrete method that sums the  $K_r$  values for each desorption sample multiplied by the fraction of radionuclide desorbed in each sample, and a binned method in which the desorption data is split into four mass fraction bins, and a numerical average  $K_r$  for each bin is calculated and multiplied by the fraction of radionuclide desorbed in that bin.

To corroborate the  $K_{d,eff}$  values derived from the spread-

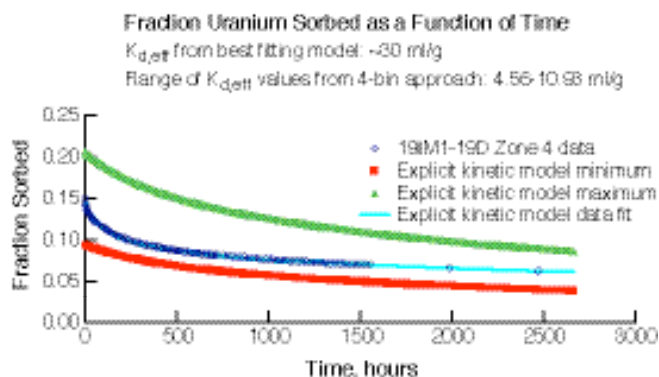


Figure 1. Fraction of uranium sorbed to 19IM1A alluvium in 19D Zone 4 groundwater as a function of time. The red and yellow curves were calculated with the explicit kinetic model using a single  $K_{f,min}$  or  $K_{f,max}$  value in conjunction with the average  $K_r$  values from each of the four mass fraction bins assumed in the binned approach. The blue model curve (fit) was generated using the explicit kinetic model and allowing  $K_f$  and  $K_r$  to vary for each of the four mass fraction bins to obtain a best fit to the experimental data.

sheet calculations, an explicit kinetic model was developed to simulate four simultaneous sorption/desorption reactions, and therefore to determine if the sorption and desorption rate constants estimated from the four-bin approach described above yielded reasonable approximations to the fraction sorbed versus time in the desorption experiments. The red and yellow curves in Figure 1 were generated using the explicit kinetic model with the lower and upper bound rate constants, respectively, and the corresponding desorption rate constants were calculated from the binned experimental data. The blue model curve (fit) was generated using the explicit kinetic model, allowing the sorption and desorption rates for each of four sorption sites to vary independently until a best fit of the data was achieved. Figure 1 reflects the general trends observed

**Table 1. Effective  $K_{d,eff}$  values from U and Np long-term desorption experiments**

NC-EWDP Well No.	Groundwater/ Radionuclide	14 Day Batch Sorp.	$K_{d,eff}$ (ml/g) Discrete		$K_{d,eff}$ (ml/g) Binned	
			Min	Max	Min	Max
19IM1A	19D-Zone 1/U	5.22	65.83	280.72	62.57	266.81
19IM1A	19D-Zone 4/U	1.36	4.70	11.26	4.56	10.93
22SA	19D-Zone 1/U	9.96	36.14	80.03	45.01	99.69
22SA	19D-Zone 4/U	3.25	10.30	55.75	9.74	52.72
10SA	10S/U	5.17	17.98	23.62	17.63	23.16
19IM1A	19D-Zone 1/Np	10.12	99.77	242.15	96.55	234.35
19IM1A	19D-Zone 4/Np	5.75	40.12	128.27	41.49	132.66
22SA	19D-Zone 1/Np	23.31	160.10	463.94	158.06	458.02
22SA	19D-Zone 4/Np	17.87	109.42	332.95	108.57	330.35

when going through this exercise for each of the data sets of Table 1. Batch sorption experiments of Np onto clays and subsequent x-ray absorbance near-edge (XANES) spectra of the Np-sorbed clay residue were completed in FY06. The results indicated that adsorption of Np onto clays increases as pH increases in solution. At pH 6.5 and 8.5, about 40% Np was adsorbed on clays. However, at pH 10.2, more than 90% of Np was removed from the solution. Note that the pH of the water was adjusted using  $HNO_3$  and NaOH with no carbonate species added. The ionic strength of the water was controlled with  $NaNO_3$ . XANES

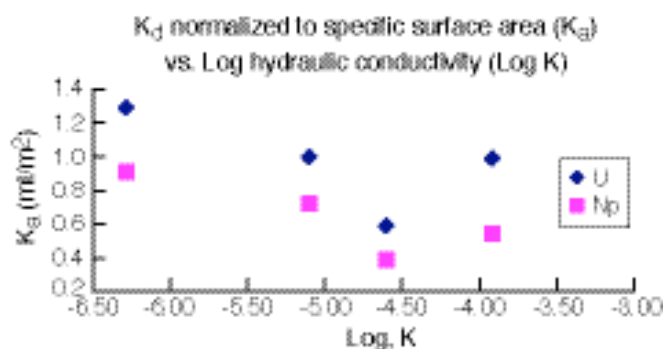


Figure 2.  $K_a$  (ml/m<sup>2</sup>) plotted against Log K. The data suggest a weak correlation between hydraulic conductivity and sorption for U and Np.

spectra, and fitting results indicated that the Np sorbed at a solution of pH 10.2 was almost completely Np(V) which was the starting Np oxidation state in solution in all the experiments.

We also completed U and Np batch sorption experiments using four separate sonic-drill core alluvium samples from different depth intervals of NC-EWDP-19PB and groundwater from NC-EWDP-19D lower carbonate (shallow) zone. The results in Figure 2 indicate that a weak negative correlation exists between hydraulic conductivity and sorption of U and Np. The weakness of the correlation can possibly be attributed to a more fundamental dependence of sorption on alluvium mineralogy, with much of the apparent trend being explained by a secondary correlation between mineralogy and hydraulic conductivity. This secondary correlation results from the tendency for stronger sorbing clays and zeolites to be smaller-sized particles that are generally associated with lower saturated hydraulic conductivities.

# Carbon-14 Groundwater Analysis

Gary L. Patterson<sup>1</sup> and James Thomas<sup>2</sup>

<sup>1</sup>United States Geological Survey (USGS) | <sup>2</sup>Desert Research Institute

## Research Objectives

The current range of groundwater travel times being used in performance assessment modeling of Yucca Mountain is overly conservative, because of the uncertain age estimates available using traditional dissolved-inorganic-carbon (DIC) groundwater dating techniques. The objective of this work is to provide improved estimates of groundwater ages along flow paths downgradient from Yucca Mountain. Improved ages can be used to provide more realistic estimates of the time required for any potential contaminants to reach the accessible environment.

## Approach

The approach to this problem involves the measurement of carbon-14 ( $^{14}\text{C}$ ) activities in both dissolved inorganic carbon (DIC) and dissolved organic carbon (DOC) in groundwater from wells located along flow paths emanating from Yucca Mountain. Traditional DIC radiocarbon dating assumes that the  $^{14}\text{C}$  percent modern carbon (pmc) acquired during recharge through the soil zone only changes along a flow path as a result of radioactive decay of  $^{14}\text{C}$ . This assumption is not completely valid when the aquifer material contains carbonates having 0 pmc  $^{14}\text{C}$  activity ("dead" carbon) that can be isotopically exchanged into the water. Radiocarbon dating of DOC has the advantage of not requiring corrections based on assumed models of water-rock interaction. Like DIC, DOC is acquired from the soil zone during recharge; however, little  $^{14}\text{C}$ -bearing DOC is expected to be present in aquifer materials along flowpaths. Thus, radiocarbon dating of DOC should give a direct measure of the amount of time elapsed since the groundwater entered the system.

Both sets of measurements, along with  $^{13}\text{C}$ -DIC,  $^{13}\text{C}$ -DOC, and hydrochemical modeling, are used to more accurately estimate the age of groundwater. The USGS computer program NETPATH was used to model the changes in groundwater chemistry along potential flowpaths and to assess mixing of different waters.

## Accomplishments

The chemical and isotopic content of groundwater in the

vicinity of Yucca Mountain was used to identify areas forming six relatively distinct hydrochemical facies: Western Yucca Mountain, Eastern Yucca Mountain, Fortymile Wash, Bare Mountain, Amargosa River, and Eastern Amargosa Valley (Figure 1). The general hydrochemical relations within these facies, along with generalized flow paths determined from hydrochemical and hydrologic information (Figure 2), were used to guide the NETPATH modeling.

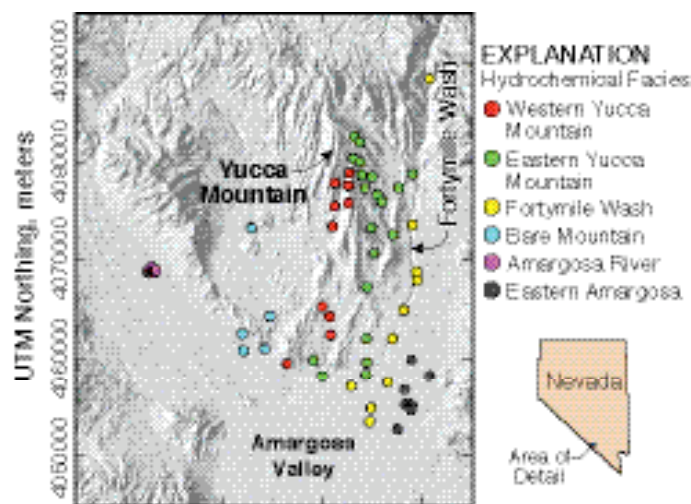


Figure 1. Hydrochemical facies in groundwater samples in the Yucca Mountain vicinity (wells in text will be labeled).

Wells located within the Fortymile Wash facies were used to assemble hypothetical end-member flowpaths and several mixing flowpaths. Water from the two wells at the north end of the wash, UE29a#1 and UE29a#2, have deuterium ( $\delta\text{D}$ ) values that are too heavy relative to any of the downgradient Fortymile Wash facies wells to be the sole source of these downgradient waters. Similarly, water from well NC-EWDP 02D at the south end of the facies is isotopically much lighter than the other Fortymile Wash facies wells in the vicinity, so it also must represent a mixture of waters. Furthermore, waters from UE29a#1 and a#2 have  $\delta^{13}\text{C}$  values that are isotopically light in comparison to water in wells along the Fortymile Wash flowpath. NETPATH modeling of these three wells did not produce satisfactory results as end-member waters with or without



mixing with other Fortymile Wash groundwaters. This indicates that upper Fortymile Wash groundwater mixes with groundwaters from other facies as it moves downgradient to the south.

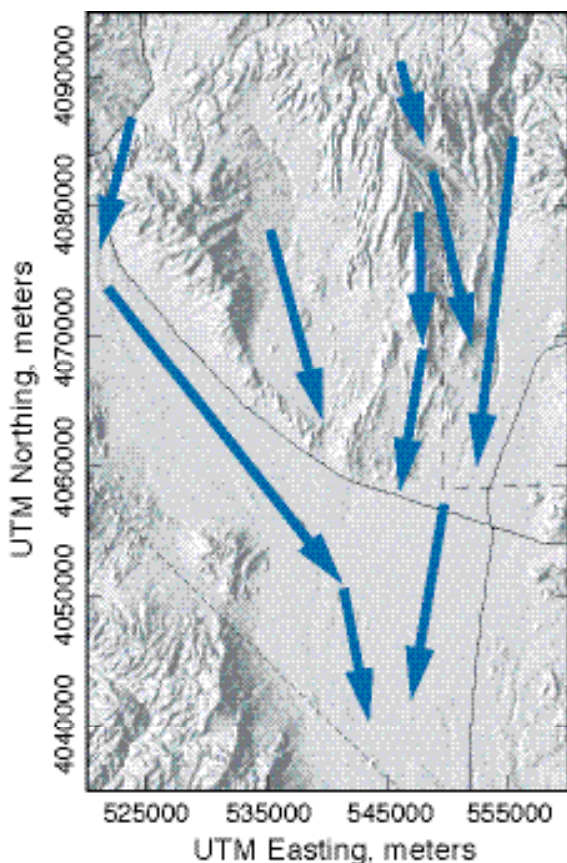


Figure 2. Generalized groundwater flow paths identified from hydrochemical and isotopic parameters.

Mixing Fortymile Wash facies water with water from the Eastern Yucca Mountain facies produced more satisfactory geochemical models. For example, mixing water from UE29a#2 with waters from WT-3 and NC-EWDP 10P-zone-1 successfully simulated the hydrochemical characteristics of water from NC-EWDP 02D. Models of mixtures of Fortymile Wash and Eastern Yucca Mountain groundwaters yield calculated travel times of 2,000 to 4,000 years.

Wells located within the Eastern Yucca Mountain hydrochemical facies were used to assemble hypothetical end-member flow-path groundwaters and several mixing flow-

paths. For the nonmixing simulations, well WT-24 served as the northernmost end-member of the Eastern Yucca Mountain facies. Models successfully simulated flow from WT-24 to H4, but models from H4 to WT-3, WT-12, WT-17 or NC-EWDP 18P were not successful, due to large differences between observed and modeled  $\delta D$ ,  $\delta^{13}C$ , and/or mineral mass-transfer values. These differences may indicate the need to add recharge as a mixing component along these potential flow paths.

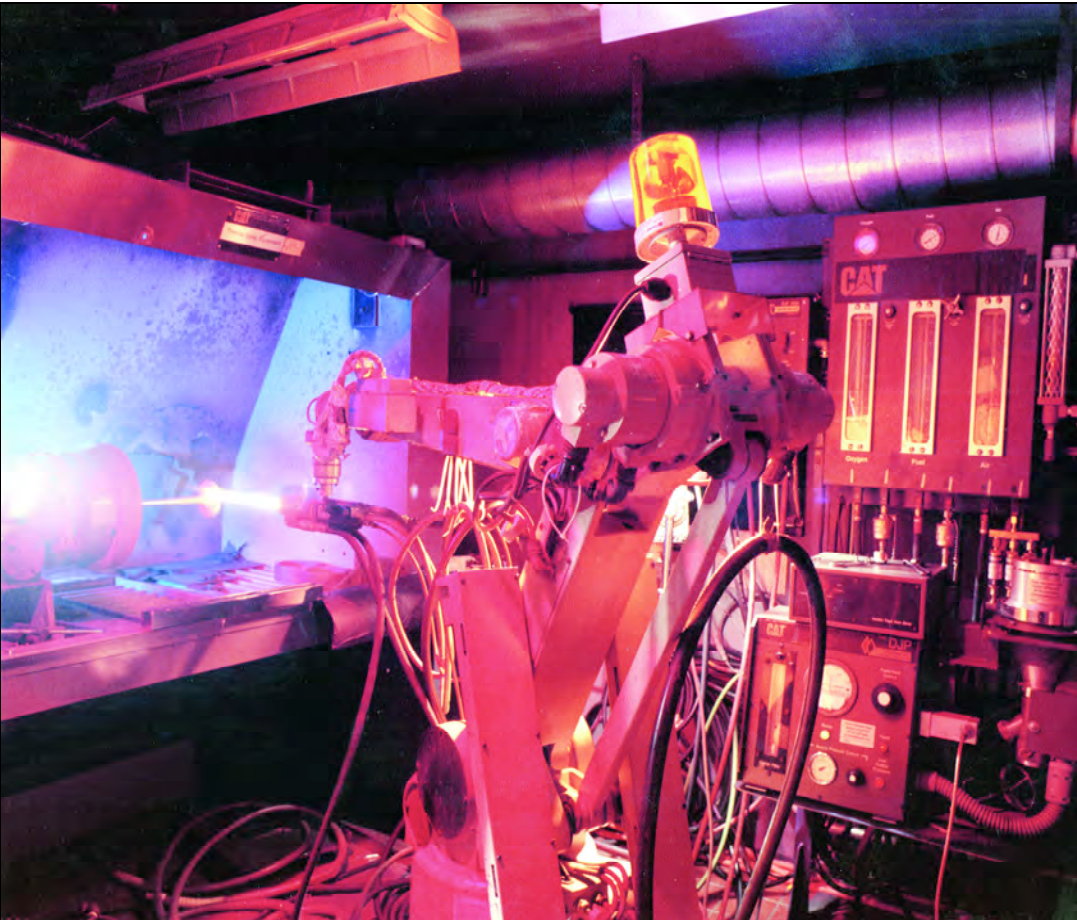
Several nonmixing flowpaths were simulated for wells in the Western Yucca Mountain facies. Flowpaths from H5 to SD-6 and H5 to WT-10 were successfully simulated and resulted in calculated travel times of approximately 2,500 and 3,500 years, respectively. Models that failed to simulate downgradient chemistry include WT-10 to NC-EWDP 28P, and WT-10 to NC-EWDP 16P. Additional models for the southern end of the facies include H6 to NC-EWDP 9SX, which had excessive mass transfer of silica, and H6 to NC-EWDP 12PA, which required excessive exchange to match measured and modeled  $\delta^{13}C$  values. The unsuccessful models may indicate the need to add recharge as a mixing component for these flow paths. Two mixing models successfully simulated downgradient chemistry. These models represent a mixture of groundwater from well H5 and well SD6, flowing to well WT-10; and a mixture of groundwater from wells H5, H6, and WT-10 flowing to well NC-EWDP 3D.

Although preliminary, the results of the hydrochemical modeling effort are important, in that flow paths from north to south within the Western Yucca Mountain facies and from the Eastern Yucca Mountain facies into Fortymile Wash were successfully simulated. Simulations that failed to adequately represent the groundwater chemistry also are valuable and in many cases may indicate that local recharge may be a substantial component of groundwaters, particularly in alluvial wells. Travel times of 2,500 to 3,500 years between particular wells in the Western Yucca Mountain facies, and 2,000 to 4,000 years for mixtures of Fortymile Wash facies and Yucca Mountain facies groundwaters, may allow more accurate estimates of travel time from Yucca Mountain to the accessible environment. Travel times for other more hypothetical flow paths and mixtures of waters produce a range of about 1,000 to 6,000 years using Nye County wells as the end points of flow paths. More detailed assessment of groundwater travel times from directly beneath the proposed repository is not currently possible, because little  $^{14}C$ -DOC data are available for groundwater beneath Yucca Mountain.

---

This page intentionally left blank.





Remote spray coating using the High Velocity Oxy-Fuel (HVOF) process. The HVOF spray coating process can be used with newly developed iron-based alloys to produce a low-cost, durable metal coating with a corrosion resistance equal to or greater than Alloy 22.

# ADVANCED TECHNOLOGIES THRUST

Jeffrey Walker

Office of Civilian Radioactive Waste Management (OCRWM),  
U.S. Department of Energy (DOE)

Contact: [jeffrey.walker@rw.doe.gov](mailto:jeffrey.walker@rw.doe.gov)

The purpose of the Advanced Technologies Thrust (ATT) is to:

- Identify and/or develop technologies and processes.
- Reduce the cost of proposed repository development, construction, and operation with the application of these new technologies and processes.
- Provide the data necessary to demonstrate feasibility of new technologies and processes.

This thrust area was a primary focus in the Science & Technology Office during fiscal years 2005 through 2007. Each of the five ATT projects is listed below; the descriptions appearing on the following pages (pp. 159-177) summarize the most current progress in each project.

- "Applications in the Nuclear Industry for Corrosion-Resistant Amorphous-Metal Thermal-Spray Coatings," by Joseph Collin Farmer and Jor-Shan Choi.
- "Criticality-Control Applications in the Nuclear Industry for Thermal Spray Amorphous Metal and Ceramic Coatings," by Joseph Collin Farmer and Jor-Shan Choi.
- "Evaluation of Structural Amorphous Materials to Improve Tunnel Boring Machine Disc Cutters," by Frank Wong and Craig Blue.
- "Extreme Ground Motions," by Lloyd Cluff.
- "Reduced Pressure Electron Beam Closure Welding of Nuclear Waste Containers," by T. James Dorsch and Christopher Punshon.

If shown successful, these technologies possess the potential to increase the efficiency, enhance the safety, improve

the design, or reduce the cost of constructing and operating the proposed repository.

Many of the ATT projects have produced results potentially very valuable to the baseline program. For example, thermally sprayed structurally amorphous metal coatings give the design team the option, for the first time, of an easily applied coating that resists corrosion and can be used in criticality-control applications as well.

Similarly, reduced-pressure electron-beam welding will produce a single-pass weld in thick metals that has the potential to significantly reduce the time and thereby the cost of manufacturing waste packages, and could possibly do the same for the final closure weld.

In approaching a project in the ATT area, a directed scoping study is initially used to investigate the potential of emerging technologies or approaches. Those that demonstrate promise for use at the proposed Yucca Mountain repository offer potential cost savings, operational or safety improvements, and a clear pathway to implementation. If selected, the projects are usually directed to the laboratories or to industry, with proposals solicited in a competitive manner. Principal investigators for the selected projects assemble teams of researchers, scientists, engineers, and technicians from universities, national laboratories, private industry, the proposed repository, and other federal offices to develop work plans and performance criteria for the technology. The ATT projects not only tailor the technology to the repository application, but must also include an analysis of the economic, technical, and regulatory feasibility of the new application of technology or knowledge prior to transfer to the repository baseline program.

Due to their exploratory nature, Office of Science & Technology (S&T) activities are not strictly part of the Yucca Mountain Project and as such do not require regulatory approval or oversight by the Nuclear Regulatory Commission. Activities within the projects are performed with a high level of quality expected to easily transfer to "Q" level quality assurance if accepted by the repository baseline. Each ATT project is able to provide robust data for safety analyses, certification, and licensing as necessary to fully integrate into the repository design.

While efforts on some of the ATT projects continue into fiscal year 2008, funding constraints and schedule demands pervasive throughout the Office of Civilian Radioactive Waste Management (OCRWM) require deferring future S&T activities in order to accommodate completion and submittal to the Nuclear Regulatory Commission of an application for a license to construct the repository.

---

This page intentionally left blank.

**Applications in the Nuclear Industry for Corrosion-Resistant Amorphous-Metal Thermal-Spray Coatings**

Joseph Collin Farmer and Jor-Shan Choi,  
Lawrence Livermore National Laboratory (LLNL)

**Criticality-Control Applications in the Nuclear Industry for Thermal Spray Amorphous Metal and Ceramic Coatings**

Joseph Collin Farmer and Jor-Shan Choi,  
Lawrence Livermore National Laboratory (LLNL)

**Evaluation of Structurally Amorphous Materials to Improve Tunnel Boring Machine Disc Cutters**

Frank Wong, Lawrence Livermore National Laboratory (LLNL); and Craig Blue, Oak Ridge National Laboratory (ORNL)

**Extreme Ground Motions**

Lloyd Cluff, Pacific Gas and Electric (PG&E)

**Reduced Pressure Electron Beam Closure Welding of Nuclear Waste Containers**

T. James Dorsch, BAE Systems; and Christopher Punshon, The Welding Institute—United Kingdom

---

This page intentionally left blank.



# Applications in the Nuclear Industry for Corrosion-Resistant Amorphous-Metal Thermal-Spray Coatings

Joseph Collin Farmer and Jor-Shan Choi  
Lawrence Livermore National Laboratory

## Research Objectives

Structurally amorphous metals (SAM), a family of Fe-based amorphous metals with very good corrosion resistance, have been developed that can be applied as a protective thermal spray coating. One of the most promising formulations within this family was found to be  $\text{Fe}_{49.7}\text{Cr}_{17.7}\text{Mn}_{1.9}\text{Mo}_{7.4}\text{W}_{1.6}\text{B}_{15.2}\text{C}_{3.8}\text{Si}_{2.4}$  (SAM2X5), which includes chromium (Cr), molybdenum (Mo), and tungsten (W) for enhanced corrosion resistance, and boron (B) to enable glass formation and neutron absorption (Farmer et al., 2007 [in press]; 2006a; 2006b; 2006c; 2005).

The parent alloy for this series of amorphous alloys, which is known as SAM40 and is represented by the formula  $\text{Fe}_{52.3}\text{Cr}_{19}\text{Mn}_2\text{Mo}_{2.5}\text{W}_{1.7}\text{B}_{16}\text{C}_4\text{Si}_{2.5}$ , has less molybdenum than SAM2X5 and was originally developed by Branagan [2004a; 2004b]. In addition to SAM2X5, yttrium-containing SAM1651 ( $\text{Fe}_{48}\text{Mo}_{14}\text{Cr}_{15}\text{Y}_2\text{C}_{15}\text{B}_6$ ) has also been explored.

The hardness and corrosion resistance of the SAM coatings, as well as their neutron absorption properties (see “Criticality-Control Applications in the Nuclear Industry for Thermal Spray Amorphous Metal and Ceramic Coatings,” included in this volume) and possible cost savings, make them potentially attractive for use in the long-term disposal of spent nuclear fuel (SNF). This paper discusses experimental investigations into corrosion resistance of the SAM coatings. The objectives of this study revolve around determining key characteristics of the SAM coatings, which may help determine the feasibility of using SAM coatings in SNF transportation and disposal.

## Approach

The coatings discussed here were made with the high-velocity oxy-fuel (HVOF) process, which involves a combustion flame and is characterized by gas and particle velocities that are three to four times the speed of sound. This process is ideal for depositing metal and cermet coatings, which have typical bond strengths of 5,000 to 10,000 lbs per square inch, porosities of less than 1%, and extreme hardness. The cooling rate that can be achieved in a typical thermal spray process such as HVOF are on the order of  $10^4$  Kelvin per second (K/s), and is high enough to enable many alloy compositions to be deposited above their

respective critical cooling rates, thereby maintaining the vitreous state.

A wide variety of standardized coating samples were made for corrosion testing. Included are samples of the powders used; crevice samples with a bolt hole in the center; Alloy 22 (UNS N06022) rods coated with SAM2X5 and SAM1651, used to monitor open-circuit corrosion potentials and corrosion rates, as determined with linear polarization; weight loss samples used for long-term immersion testing; and ultra-thick ( $\sim 0.75$  cm) coatings. These samples were subjected to a variety of standard corrosion-resistance testing, including cyclic polarization, salt-fog testing, and immersion testing. In addition to corrosion testing, x-ray diffraction tests were used to confirm the amorphous structure of the SAM materials.

## Accomplishments

X-ray diffraction (XRD) measurements of SAM2X5 powder (Lot # 06-015) and thermal spray coatings, made by depositing the powder on Type 316L stainless steel substrates, were conducted and are shown here in Figure 1 and Figure 2. Similar results were also achieved with Alloy 22 substrates. In regard to the thermal spray coating, the

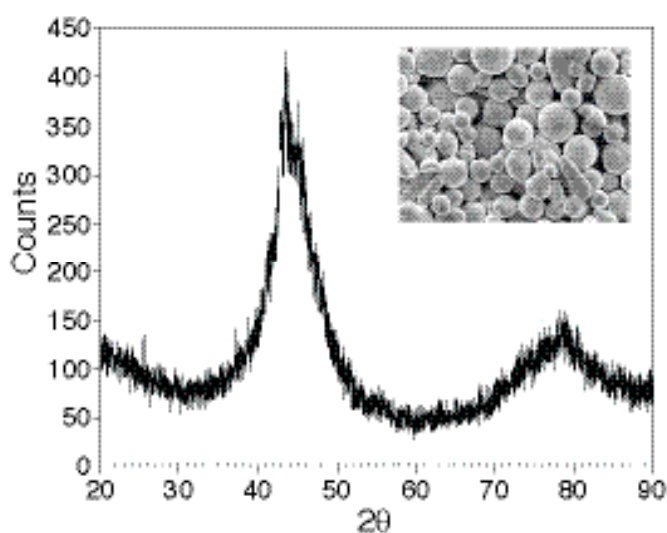


Figure 1. X-ray diffraction of SAM2X5 amorphous metal powder.

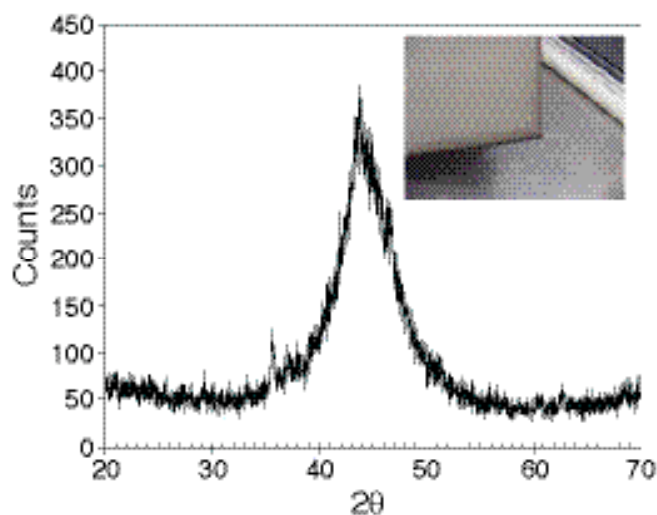


Figure 2. X-ray diffraction of SAM2X5 amorphous metal coating.

broad halo observed at  $2\theta$  to  $\sim 44^\circ$  indicated that the coating was predominately amorphous, and the small sharp peaks were attributed to the presence of minor crystalline phases.

These phases are believed to include  $\text{Cr}_2\text{B}$ ,  $\text{WC}$ ,  $\text{M}_{23}\text{C}_6$  and bcc ferrite, which are known to have a detrimental effect on corrosion performance. These potentially deleterious precipitates deplete the amorphous matrix of those alloying elements, such as chromium, responsible for enhanced passivity. Coatings with less residual crystalline phase have been observed.

### Cyclic Polarization Testing

The corrosion resistance of melt-spun ribbons and drop-cast ingots of Fe-based amorphous metals is exceptional. Cyclic polarization data for three drop-cast ingots of SAM1651 Fe-based amorphous metal with yttrium in three different environments (seawater at  $90^\circ\text{C}$ ; 3.5 molal  $\text{NaCl}$  at  $90^\circ\text{C}$ ; and 5M  $\text{CaCl}_2$  at  $105^\circ\text{C}$ ) is shown (Figure 3). All three cyclic polarization curves show outstanding passivity. Cyclic polarization data for a wrought prism of nickel-based Alloy 22, a drop-cast ingot of Fe-based SAM1651 amorphous metal, and a melt-spun ribbon of SAM8 (SAM1651 + 3 atomic percent tungsten), all obtained with 5M  $\text{CaCl}_2$  at  $105^\circ\text{C}$ , is shown in Figure 4. Both SAM1651 and SAM8 showed passive film stability comparable to or better than Alloy 22.

The addition of 3 atomic-percent tungsten to the SAM1651 enhanced the passive film stability, and also

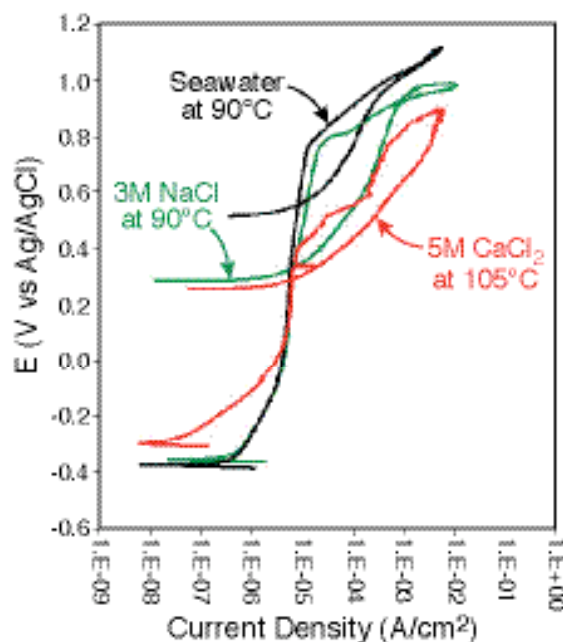


Figure 3. Cyclic polarization data for three drop-cast ingots of SAM1651 Fe-based amorphous metal with yttrium in three different environments: seawater at  $90^\circ\text{C}$ , 3.5 molal  $\text{NaCl}$  at  $90^\circ\text{C}$ , and 5M  $\text{CaCl}_2$  at  $105^\circ\text{C}$ .

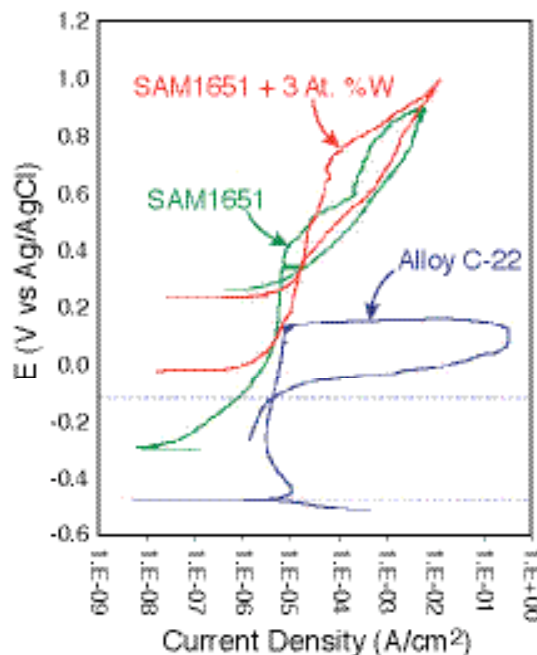


Figure 4. Cyclic polarization data for a wrought prism of nickel-based Alloy 22, a drop-cast ingot of Fe-based SAM1651 amorphous metal, and a melt-spun ribbon of SAM\* (SAM1651 + 3 atomic % W), all obtained with 5M  $\text{CaCl}_2$  at  $105^\circ\text{C}$ .

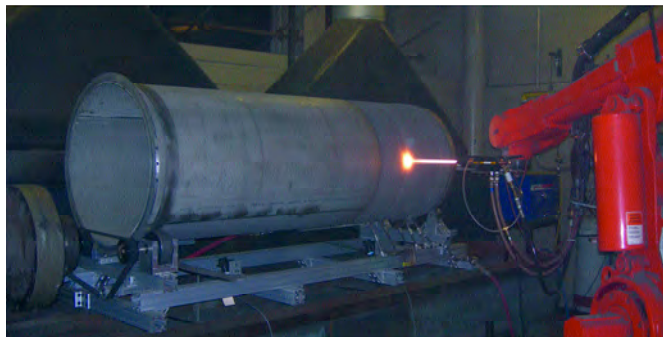


Figure 5. Coating of half-scale SNF container with HVOF process at Caterpillar.

yielded more ductile and damage-tolerant amorphous metal ribbons.

### Prototype Containers and Salt Fog Testing

Type 316L stainless-steel cylinders were coated with SAM2X5 and served as half-scale models of containers for the disposal of SNF. SAM2X5-coated cylinders and plates were subjected to eight (8) full cycles in the GM salt fog test (GM9540P). Cylinders have also been coated with the Y containing SAM1651 and tested.

Several reference samples and amorphous-metal coatings have been made and subjected to salt fog testing. Salt fog tests were conducted according to the standard General Motors (GM) salt fog test, identified as GM9540P. Figure 6 shows four samples, all after 8 full cycles in the GM salt fog test. Clearly, the thermal-spray coatings of SAM2X5 have good resistance to corrosive attack in such environments. Similar testing was done with a half-scale SNF container coated with SAM1651. Some running rust was observed on one bottom of the container, which may be attributable to surface preparation prior to coating.

### Linear Polarization

Initial corrosion-rate measurements of SAM2X5 coatings and wrought Alloy 22 in several environments were made with linear polarization. Table 1 shows corrosion rates for Alloy 22 and SAM2X5 in seawater at 30° and 90°C, and in 5M CaCl<sub>2</sub> at 105°C, after a few days immersion. The Alloy 22 and SAM2X5 rates were comparable in seawater; however, SAM2X5 appeared to

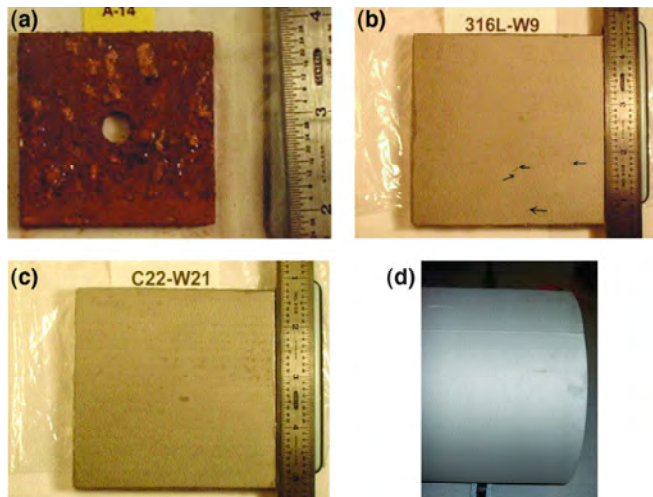


Figure 6. Photographs of (a) 1018 Steel, (b) SAM2X5 on 316L, (c) SAM2X5 on Alloy 22, and (d) SAM2X5 on 316L container.

have a lower corrosion rate in 5M CaCl<sub>2</sub> at 105°C.

### Weight-Loss and Dimensional-Change

Long-term weight-loss and dimensional-change data for SAM2X5 were also needed. After 135 days of immersion, weight-loss and dimensional measurements were used to determine the corrosion rates of SAM2X5 coatings on Alloy 22 weight-loss samples (Figure 7). Depending upon the assumed coating density, these rates were determined to be: (1) 14.3–15.9 µm/yr in natural seawater at 90°C; (2)

**Table 1. Corrosion rates of Alloy 22 and SAM2X5 HVOF coatings in seawater**

Environment	Sample	E <sub>Corr</sub> (mV vs. SSC)	Corrosion Rate (µm/year)
30° Seawater	HVOF SAM2X5	-87.4	0.18
30° Seawater	Wrought Alloy 22	-163.2	0.09
90° Seawater	HVOF SAM2X5	-241.0	1.58
90° Seawater	Wrought Alloy 22	-318.2	1.22
105°C 5M CaCl <sub>2</sub>	HVOF SAM2X5	-240.9	2.70
105°C 5M CaCl <sub>2</sub>	Wrought Alloy 22	-464.3	5.04
105°C 5M CaCl <sub>2</sub>	HVOF Alloy 22	-347.9	115.7



8.4–9.3  $\mu\text{m}/\text{yr}$  in 3.5-molal NaCl solution at 30°C; (3) 26.1–29.7  $\mu\text{m}/\text{yr}$  in 3.5-molal NaCl solution at 90°C; (4) 4.6–5.1  $\mu\text{m}/\text{yr}$  in 3.5-molal NaCl and 0.525-molal  $\text{KNO}_3$  solution at 90°C; (5) 8.3–9.4  $\mu\text{m}/\text{yr}$  in simulated diluted water (SDW) at 90°C; (6) 2.8–3.0  $\mu\text{m}/\text{yr}$  in simulated concentrated water (SCW) at 90°C; and (7) 16.5–18.1  $\mu\text{m}/\text{yr}$  in simulated acidic water (SAW) at 90°C.

As expected, greater corrosion rates were observed at higher temperature, and nitrate anion inhibited the corrosion of these Fe-based materials in concentrated chloride solutions. Corrosion rates in bicarbonate-type brines were less than those in concentrated chloride solutions. The range of corrosive attack of SAM2X5-coated rods from a 135-day exposure to various concentrated brines at 90°C is illustrated in Figure 8.

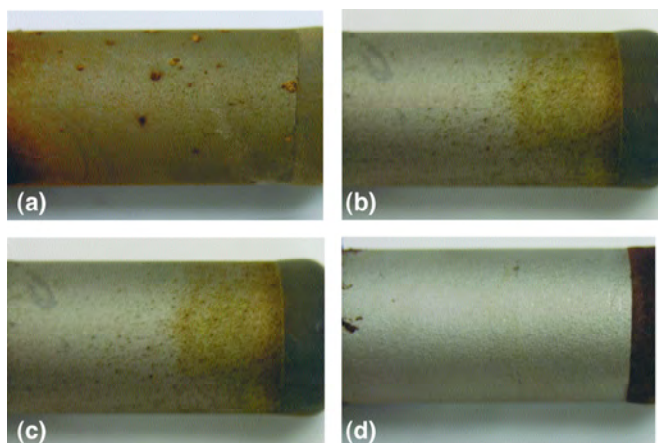


Figure 8. Corrosive attack of SAM2X5-coated rods in four environments.

Test solutions included (a) natural seawater; (b) an aqueous solution with 3.5-molal NaCl + 0.525-molal  $\text{KNO}_3$ ; (c) neutral simulated dilute water, aka SDW; and (d) simulated acidic water, also known as SAW. Both SDW and SAW are based upon Well J-13 water composition at Yucca Mountain. Similar data for SAM1651 coatings, based on preliminary measurements, are shown in Figure 9.

Early Fe-based amorphous metal coatings had very poor corrosion resistance and failed salt-fog tests. The HPCRM Program has developed new Fe-based amorphous-metal

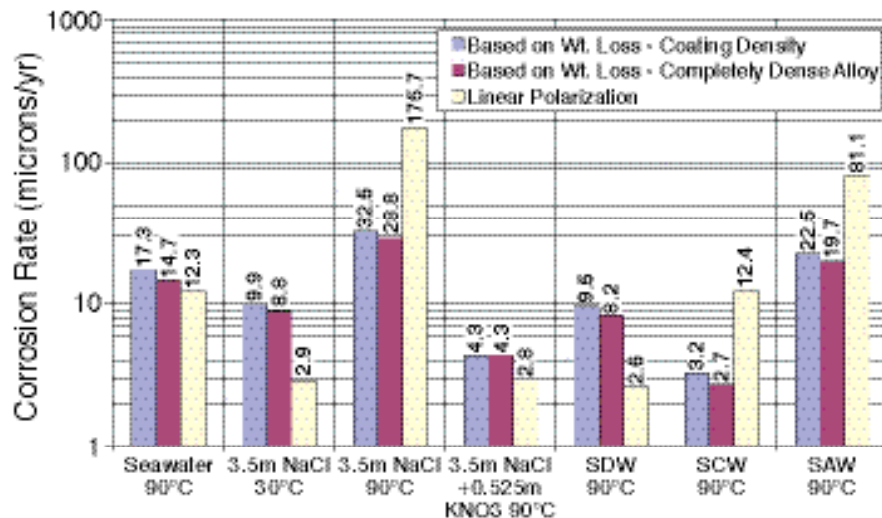


Figure 7. Corrosion rates of SAM2X5 coatings after 135 days.

alloys with good corrosion resistance, high hardness, and exceptional absorption cross sections for thermal neutrons. More than 40 high-performance Fe-based amorphous alloys were systematically designed and synthesized. Cr, Mo and W were added to enhance corrosion resistance; Y

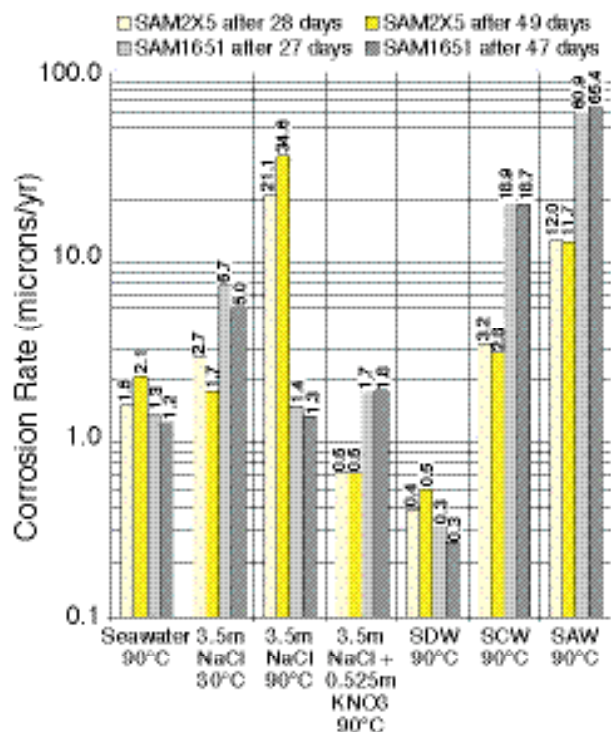


Figure 9. Comparison of corrosion rates for SAM2X5 and SAM1651 coatings.

was added to lower the critical cooling rate; and B was added to render the alloy amorphous and to enhance capture thermal neutrons. Phase stability has been demonstrated well above 500–600°C and at high neutron doses. With additional development, these materials could be used to achieve cost benefits for the fabrication of next-generation SNF containers.

Multi-ton quantities of gas-atomized SAM2X5 and SAM1651 powder have been produced and applied as protective coatings on numerous prototypes and parts. These new materials are now under evaluation for several applications of national importance.

## References

- Branagan, D., Method of modifying Fe-based glasses to increase crystallization temperature without changing melting temperature. U.S. Pat. Appl. No. 20040250929, Filed Dec. 16, 2004, 2004a.
- Branagan, D., Properties of amorphous/partially crystalline coatings. U.S. Pat. Appl. No. 20040253381, Filed Dec. 16, 2004, 2004b.
- Farmer, J., J. Haslam, S. Day, T. Lian, C. Saw, P. Hailey, J. Choi, R. Rebak, N. Yang, J. Payer, J. Perepezko, K. Hildal, E. Lavernia, L. Ajdelsztajn, D. Branagan, Corrosion resistance of thermally sprayed high-boron Fe-based amorphous-metal coatings: Fe<sub>49.7</sub>Cr<sub>17.7</sub>Mn<sub>1.9</sub>Mo<sub>7.4</sub>W<sub>1.6</sub>B<sub>15.2</sub>C<sub>3.8</sub>Si<sub>2.4</sub>. UCRL-TR-227111 Rev. 1, LLNL, Livermore, CA; 2007; JMR-2007-0058, MRS, 2007 (in press).
- Farmer, J., J. Haslam, S. Day, T. Lian, C. Saw, P. Hailey, J. Choi, N. Yang, C. Blue, W. Peter, J. Payer and D. Branagan, Corrosion resistances of Fe-based amorphous metals with yttrium and tungsten additions in hot calcium chloride brine and natural seawater, Fe<sub>48</sub>Mo<sub>14</sub>Cr<sub>15</sub>Y<sub>2</sub>C<sub>15</sub>B<sub>6</sub> and W-containing variants. Critical Factors in Localized Corrosion 5, A Symposium in Honor of Hugh Issacs, 210th ECS Meeting, N. Missert, ed., ECS Transactions, 3, ECS, 2006a.
- Farmer, J., J. Haslam, S. Day, T. Lian, C. Saw, P. Hailey, J. Choi, R. Rebak, N. Yang, R. Bayles, L. Aprigliano, J. Payer, J. Perepezko, K. Hildal, E. Lavernia, L. Ajdelsztajn, D. J. Branagan, and M. B. Beardsley, A high-performance corrosion-resistant Fe-based amorphous metal – The effects of composition, structure and environment on corrosion resistance. Scientific Basis for Nuclear Waste Management XXX, Symposium NN, MRS Symposium Series, 985, 2006b.
- Farmer, J., J. Haslam, S. Day, T. Lian, R. Rebak, N. Yang, and L. Aprigliano, Corrosion resistance of Fe-based amorphous metal coatings. PVP2006-ICPVT11-93835, ASME, New York, NY, 2006c.
- Farmer, J., J. Haslam, S. Day, D. Branagan, C. Blue, J. Rivard, L. Aprigliano, N. Yang, J. Perepezko, and M. Beardsley, Corrosion characterization of Fe-based high-performance amorphous-metal thermal-spray coatings, PVP2005-71664, ASME, New York, NY, 2005.



---

This page intentionally left blank.

# Criticality-Control Applications in the Nuclear Industry for Thermal Spray Amorphous Metal and Ceramic Coatings

Joseph Collin Farmer and Jor-Shan Choi  
Lawrence Livermore National Laboratory

## Research Objectives

The outstanding corrosion resistance that may be possible with amorphous metals was recognized several years ago (Telford, 2004; Sorensen and Diegle, 1987; Polk and Giessen, 1978). A family of iron-based amorphous metals with very good corrosion resistance has been developed that can be applied as a protective thermal spray coating. One of the most promising formulations within this family was found to be

$\text{Fe}_{49.7}\text{Cr}_{17.7}\text{Mn}_{1.9}\text{Mo}_{7.4}\text{W}_{1.6}\text{B}_{15.2}\text{C}_{3.8}\text{Si}_{2.4}$  (SAM2X5), which included chromium (Cr), molybdenum (Mo), and tungsten (W) for enhanced corrosion resistance, and boron (B) to enable glass formation and neutron absorption (Farmer et al., 2007 [in press]; 2006a; 2006b; 2006c; 2005).

SAM2X5 may benefit applications such as the long-term disposal of spent nuclear fuel (SNF). The conceptual standard container for the disposal of SNF assemblies in the proposed deep geological repository at Yucca Mountain holds the SNF assemblies in place with a basket made of interlocking alloy plates that run the length of the waste container. Through the use of computational modeling and experimental testing, the present study seeks to determine the feasibility of using boron-containing structurally amorphous metal (SAM) coatings to provide criticality control in waste containers that may be used in a proposed SNF and high-level radioactive waste repository at Yucca Mountain.

Specifically, the objectives of these criticality evaluations are:

- To evaluate the effectiveness of the boron-containing, iron-base SAM2X5 as neutron poison for support basket material inside the SNF disposal containers.
- To examine the potential use of SAM2X5 inside the SNF disposal and transportation containers, and hence, supporting the Department of Energy's Office of Civilian Radioactive Waste Management (OCRWM) for flexibility in its program planning.

## Approach

A combination of computational modeling, experimental investigations, and large-scale demonstration were used to examine the feasibility of using boron-containing SAM coatings in criticality control applications. A one-half scale basket assembly, based on the criticality control modules included in the conceptual waste-container designs, was produced and assembled. The one-half scale model was coated with SAM 2X5, demonstrating the logistical feasibility of manufacturing and applying coatings to these basket assemblies.

Computational criticality evaluations were performed for a disposal container designed to hold 21 spent pressurized water reactor (PWR) fuel assemblies. The computational model simulates each fuel pin within a  $17 \times 17$  assembly. Each of the 21 assemblies is surrounded with 0.635 cm (1/4") thick borated stainless steel with various concentrations of natural boron. One-millimeter-thick boron-containing SAM coatings are uniformly applied on the surface of the borated stainless steel, hence complementing the neutron-absorbing effectiveness of the borated stainless steel and reducing the overall keff of the disposal container. The spent PWR fuel assemblies are exposed to a burn-up of 35 GWd/MgHM with a 4-year decay. Results of the criticality evaluations are obtained based on this computational model.

Materials used in criticality control applications must be relatively stable during irradiation with thermal neutrons. To evaluate the stability of the SAM coatings, melt-spun ribbon samples of various iron-based amorphous metals were subjected to high neutron doses in the 1.5 MW TRIGA reactor at McClellan Nuclear Radiation Center (MNRC) (Choi et al., 2006).

## Accomplishments

The coatings discussed here were made with the high-velocity oxy-fuel (HVOF) process, which involves a combustion flame and is characterized by gas and particle velocities that are three to four times the speed of sound. This process is ideal for depositing metal and cermet coatings, which have typical bond strengths of 5,000 to

10,000 lbs per square inch, porosities of less than one percent, and extreme hardness. The cooling rate that can be achieved in a typical thermal spray process such as HVOF are on the order of  $10^4$  Kelvin per second (K/s), and is high enough to enable many alloy compositions to be deposited above their respective critical cooling rate, thereby maintaining the vitreous state.

Type 316L stainless-steel cylinders and plates were coated with SAM2X5, and served as half-scale models of containers and baskets for the storage of SNF. Figure 1 shows a prototypical 1/2 scale 1/2 length basket assembly, sized to fit inside a 1/2 scale container. The photographs shown here, the left shows the 1/2 scale basket assembly after fabrication by water-jet cutting. A thermal spray coating of SAM2X5 was subsequently applied to the 1/2 scale basket.

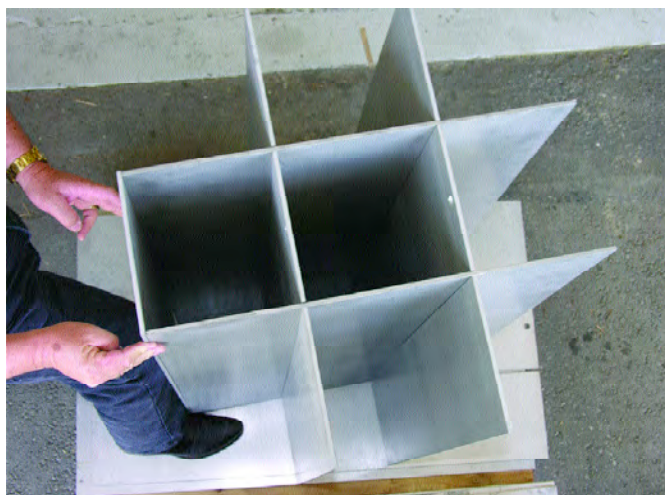


Figure 1. Half-scale criticality-control modules (basket assemblies).

Computational criticality evaluations at Lawrence Livermore National Laboratory showed the high boron content of SAM2X5 makes it an effective neutron absorber, lowering  $k$ -effective by at least 10% with the application of a 1 mm thick coating of SAM2X5 to SNF support structures (baskets) in a 21-PWR container.

Average measured values of the transmission neutron absorption cross section ( $\Sigma_t$ ) for Type 316L stainless steel, Alloy 22 (UNS N06022), borated stainless steel, a Ni-Cr-Mo-Gd alloy, and SAM2X5 have been determined to be approximately 1.1, 1.3, 2.3, 3.8 and 7.1  $\text{cm}^{-1}$ , respectively (Choi et al., 2006; Farmer et al., 2007 [submitted]). Data are shown in Figure 2. There remains potential to further increase performance through the use of enriched boron

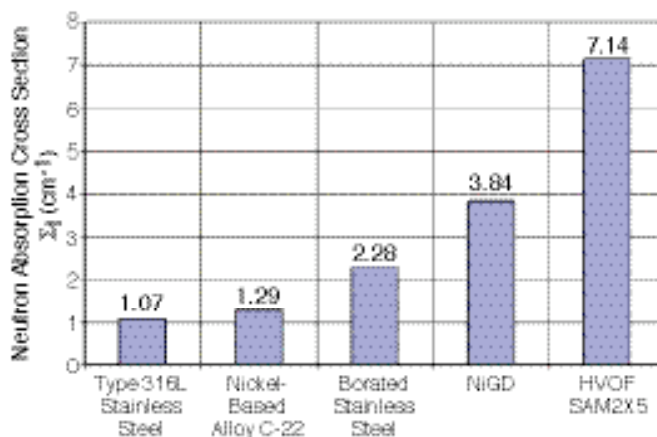


Figure 2. Average measured values of the thermal-neutron-absorption cross section in various alloys related to SNF storage. Measured at MNRC.

in the synthesis of the Fe-based amorphous metal. It has been shown that these Fe-based amorphous metals can be produced in large quantities for reasonable cost.

This material and its parent alloy have been shown to maintain corrosion resistance up to the glass transition temperature (see "Applications in the Nuclear Industry for Corrosion-Resistant Amorphous-Metal Thermal-Spray Coatings" in this volume) and to remain in the amorphous state after receiving relatively high neutron doses. At MNRC, SAM samples were exposed to a neutron flux of  $1.6 \times 10^{10} \text{ n cm}^{-2} \text{ sec}^{-1}$ . Samples were irradiated for three different time durations: The first irradiation was 44 minutes, the second 132 minutes, and the third 263 minutes. The corresponding neutron doses per duration were  $4.3 \times 10^{13} \text{ n cm}^{-2}$ ,  $1.3 \times 10^{14} \text{ n cm}^{-2}$ , and  $2.6 \times 10^{14} \text{ n cm}^{-2}$ , respectively.

These doses are respectively equivalent to ~ 670 years, 2,000 years, and 4,000 years inside the waste packages designed for emplacement at Yucca Mountain. X-ray diffraction measurements displayed in Figure 3 confirm the amorphous structure is retained for an exposure corresponding to a 4,000-year service life.

These new iron-based amorphous metals have exceptional neutron absorption characteristics and are stable at high doses. SAM2X5 may thus have applications in the safe disposal of SNF. The thermal neutron transmission absorption cross section for SAM2X5 coatings is three to four times greater than that of borated stainless steel, which is often used to store SNF for long periods of time (Lian et al., 2006; Choi et al., 2006; Farmer et al. 2007 [submitted]). These materials are extremely hard

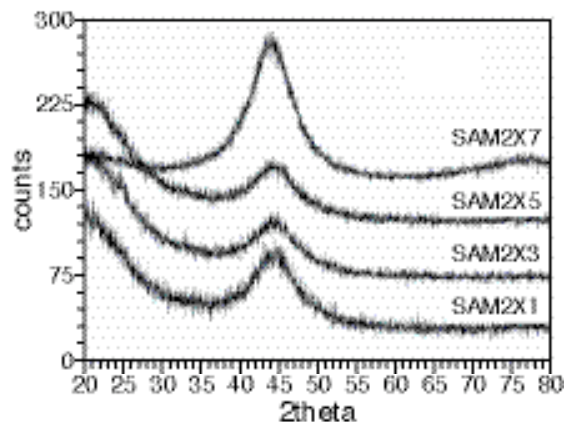


Figure 3. X-ray diffraction of high-boron SAM2X-series alloys after 3rd irradiation. The broad peaks confirm that the amorphous state is retained.

and provide enhanced resistance to abrasion and gouges. It may be possible to achieve substantial cost savings by substituting these new Fe-based materials for more expensive alloys used in criticality-control applications in the disposal of SNF.

## References

- Choi, J-S., C. Lee, J. Farmer, D. Day, M. Wall, C. Saw, M. Boussoufi, B. Liu, H. Egbert, D. Branagan, and A. D'Amato, Application of neutron-absorbing structural amorphous metal coatings for spent nuclear fuel container to enhance criticality safety controls. Scientific Basis for Nuclear Waste Management XXX, Symposium NN, MRS Symposium Series, Vol. 985, 2006.
- Farmer, J., J-S. Choi, C-K. Saw, R.H. Rebak, S.D. Day, T. Lian, P.D. Hailey, J.H. Payer, D.J. Branagan, and L.F. Aprigliano, Corrosion resistance of amorphous  $\text{Fe}_{49.7}\text{Cr}_{17.7}\text{Mn}_{1.9}\text{Mo}_{7.4}\text{W}_{1.6}\text{B}_{15.2}\text{C}_{3.8}\text{Si}_{2.4}$  coating, a new criticality-control material. UCRL-JRNL-229505, LLNL, Livermore, CA; J. Nuclear Technology, ANS, 2007 (submitted).
- Farmer, J., J. Haslam, S. Day, T. Lian, C. Saw, P. Hailey, J. Choi, R. Rebak, N. Yang, J. Payer, J. Perepezko, K. Hildal, E. Lavernia, L. Ajdelsztajn, D. Branagan, Corrosion resistance of thermally sprayed high-boron iron-based amorphous-metal coatings:  $\text{Fe}_{49.7}\text{Cr}_{17.7}\text{Mn}_{1.9}\text{Mo}_{7.4}\text{W}_{1.6}\text{B}_{15.2}\text{C}_{3.8}\text{Si}_{2.4}$ . UCRL-TR-227111 Rev. 1, LLNL, Livermore, CA; 2007; JMR-2007-0058, MRS, 2007 (in press).
- Farmer, J., J. Haslam, S. Day, T. Lian, C. Saw, P. Hailey, J. Choi, N. Yang, C. Blue, W. Peter, J. Payer, and D. Branagan, Corrosion resistances of iron-based amorphous metals with yttrium and tungsten additions in hot calcium chloride brine and natural seawater,  $\text{Fe}_{48}\text{Mo}_{14}\text{Cr}_{15}\text{Y}_2\text{C}_{15}\text{B}_6$  and W-containing variants. Critical Factors in Localized Corrosion 5, A Symposium in Honor of Hugh Issacs, 210th ECS Meeting, N. Missert, ed., ECS Transactions, Vol. 3, ECS, 2006.
- Farmer, J., J. Haslam, S. Day, T. Lian, C. Saw, P. Hailey, J. Choi, R. Rebak, N. Yang, R. Bayles, L. Aprigliano, J. Payer, J. Perepezko, K. Hildal, E. Lavernia, L. Ajdelsztajn, D. J. Branagan, and M. B. Beardsley, A high-performance corrosion-resistant iron-based amorphous metal – The effects of composition, structure and environment on corrosion resistance. Scientific Basis for Nuclear Waste Management XXX, Symposium NN, MRS Symposium Series, Vol. 985, 2006.
- Farmer, J., J. Haslam, S. Day, T. Lian, R. Rebak, N. Yang, and L. Aprigliano, Corrosion resistance of iron-based amorphous metal coatings. PVP2006-ICPVT11-93835, ASME, New York, NY, 2006.
- Farmer, J., J. Haslam, S. Day, D. Branagan, C. Blue, J. Rivard, L. Aprigliano, N. Yang, J. Perepezko, and M. Beardsley, Corrosion characterization of iron-based high-performance amorphous-metal thermal-spray coatings. PVP2005-71664, ASME, New York, NY, 2005.
- Lian, T., D. Day, P. Hailey, J-S. Choi, and J. Farmer, Comparative study on the corrosion resistance of Fe-based amorphous metal, borated stainless steel and Ni-Cr-Mo-Gd alloy. Scientific Basis for Nuclear Waste Management XXX, Symposium NN, MRS Series, Vol. 985, 2006.
- Polk, D., and B. Giessen, Overview of principles and applications. Metallic Glasses, Chapter 1, J. Gilman and H. Leamy, eds., ASME, pp. 2–35, 1978.
- Sorensen, N., and R. Diegle, Corrosion of amorphous metals. Corrosion, Metals Handbook, 9th Ed., Vol. 13, J.R. Davis and J.D. Destefani, eds., ASME, pp. 864–870, 1987.
- Telford, M., The case for bulk metallic glass. Materials Today, 3, 36–43, 2004.

---

This page intentionally left blank.



# Evaluation of Structurally Amorphous Materials to Improve Tunnel Boring Machine Disc Cutters

Frank Wong<sup>1</sup> and Craig Blue<sup>2</sup>

<sup>1</sup>Lawrence Livermore National Laboratory (LLNL) | <sup>2</sup>Oak Ridge National Laboratory (ORNL)

## Research Objectives

The objective of this project is to leverage the recent development of structural amorphous metals (SAMs) and to develop them for use as wear/impact-resistant coatings on the disc cutters of the Tunnel Boring Machine (TBM) machine (Figure 1) to be used at Yucca Mountain (41 miles of emplacement drifts are planned at Yucca Mountain).



Figure 1. Photo of a TBM.

The TBM has a 5 m diameter rotating face with multiple disc cutters (17-inch-diameter tool steel discs). As the machine advances into the tunnel, the “crown” area of the disc cutters compresses and pulverizes the host rock, which causes the disc cutters to wear out. During the excavation of the Exploratory Studies Facility (ESF) at Yucca Mountain, the disc cutters were moved (from the outer to the inner radii) approximately every two days, and the disc cutters were discarded after approximately 7 days, or 500 ft, of drift excavation. With the current state of the art in disc cutter technology, excavating an emplacement drift (600 m / 2,000 ft) would require approximately 3 to 4 changes of the entire set of disc cutters. The ultimate goal of this project is to improve the operational life of TBM disc cutters so that a 2,000 ft long emplacement drift can be excavated on a single set of TBM disc cutters.

## Approach

In FY 06/07, several sets of disc cutter wheels were coated

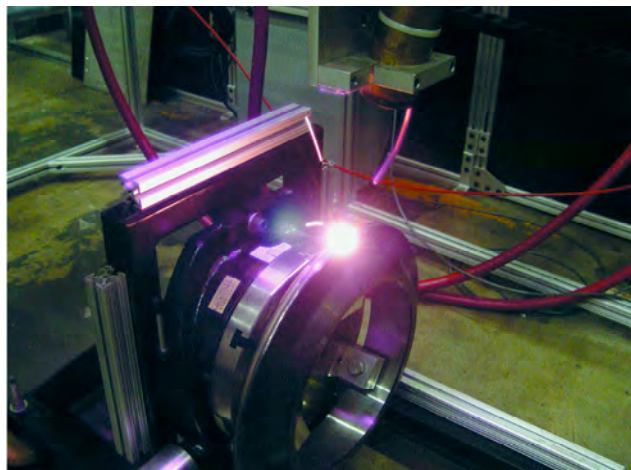


Figure 2. Laser coating of a disc cutter.

with structurally amorphous metal (SAM) alloys by laser fusing (Figure 2) at Oak Ridge National Laboratory (ORNL) and tested at the Colorado School of Mines in their Linear Cutting Machine.

The coatings were tested with patterns of stripes and dots. The coatings are a devitrified form of original SAM compositions. A disc cutter with a striped coating pattern on its cutting edge is shown in Figure 3.

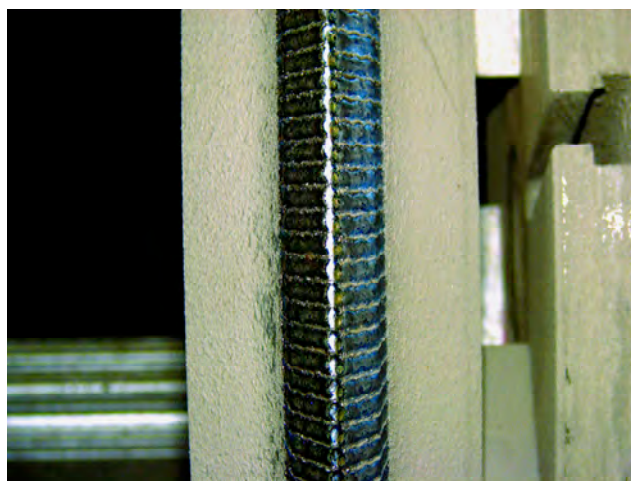


Figure 3. Close-up of the cutting edge of a coated disc cutter.



Figure 4. Coating disc cutters ready for shipping to TBM in Atlanta.



Figure 5. A coated disc cutter after multiple “pushes” in Atlanta TBM.

## Accomplishments

Tests of the coated disc cutters at the Colorado School of Mines (CSM) have shown these coatings to be extremely resistant to spallation, even at loads as high as 105,000 lbs. They were the first coatings, in over twenty five years of testing disc cutter coatings at CSM, to survive more than one pass of rock cutting. These results indicated that a full-scale field test was warranted. Coated disc cutters ready for field testing are shown in Figure 4.

The field test was performed on the TBM being used at the Combined Sewer Overflow Project in Atlanta, GA. Four of the 52 disc cutters on the 32 ft diameter TBM were replaced with the SAM coated discs. This TBM advances in the tunnel in 5' increments called “pushes”. The SAM coated discs survived 13 pushes without cracking or spalling and resulted in a 10 to 28% improvement in cutter wear rate in the very hard and abrasive rock of

the Atlanta Tunnel (which is considered to be harder than Topapah Spring welded tuff). Even more significantly, the SAM coating did not fail by spallation or peeling, which had occurred in all previous attempts to use hard facing coatings with disc cutters. The SAM coating enabled the disc cutters to maintain their initial wedge-tip profile longer (Figure 5), which reduces dust generation. Lower dust generation will be of significant benefit to the construction of the proposed Yucca Mountain repository.

The project has demonstrated that it is possible to extend the life of TBM disc cutters by using SAM coatings. This will result in less down time, more rapid excavation rates, and potentially less dust generation, which will all result in significant savings in excavation costs. In addition, this technology may allow for the excavation of a 2,000 ft emplacement drift using a single set of disc cutters.



# Extreme Ground Motions

Lloyd Cluff

Pacific Gas & Electric Company

## Research Objectives

The extreme ground motions from the 1998 probabilistic seismic hazard analysis (PSHA) present exceptional challenges to the design of underground facilities. Many experts consider these ground motions to be physically unrealizable, as they may exceed the strength of the rock units underlying Yucca Mountain. In addition, the mean hazard curve is inconsistent with the existence of fragile geologic features that have existed for up to 12 million years at Yucca Mountain. Initial modifications to the PSHA have been made by the Yucca Mountain Project, but they lack a strong technical basis and face difficulties in licensing. Limits on the extreme ground motions with a strong technical basis are needed to improve and support the revisions to the ground motion hazard.

## Approach

There are three types of information that can be used to constrain the extreme ground motions at Yucca Mountain: physical limits, unexceeded ground motions, and event frequencies.

### Physical Limits

The physical limits approach evaluates the largest possible ground motion that could occur at Yucca Mountain. There are two parts to the physical limits: (1) the limits of the amplitudes of the seismic waves that can be generated by the faulting, and (2) the limits of seismic waves that can be propagated through the rocks underlying the repository. For example, this could be a limit on the stress-drop of an earthquake in the region, or it could be a limit of the maximum strain that a weak rock unit could sustain before it fails. This is the most technically difficult approach, but it has the potential to provide the strongest constraints.

### Unexceeded Ground Motions

The unexceeded ground motion approach evaluates the limits that can be put on ground motions that have occurred at Yucca Mountain over the past hundreds of thousands to millions of years, based on observations of undamaged geologic features. There are two parts to the unexceeded ground motion: the strength of shaking that

would cause damage to the geologic feature, and the age of the geologic feature. By using geologic features with varying ages, we can greatly extend the time period of our observations and provide some checks on the hazard at low probability levels.

### Event Frequencies

The event frequencies approach evaluates the rates at which extreme ground motions occur, based on studies of large numbers of earthquakes around the world.

## Accomplishments

In FY06, initial numerical calculations for the physical limits for peak ground velocity (PGV) were conducted. Unexceeded ground motions for precarious rocks, precipitous slopes, unshattered cliffs and rocks, and lithophysae were compiled from previous studies. Estimates of uncertainties in the failure ground-motion levels and the ages for the geologic features were estimated. Event frequencies were estimated using global earthquake catalogs, and new ground motion models were developed.

The main accomplishment for FY07 has been to compile all of the research to date within a single points-in-hazard-space plot (Figure 1). The key findings are as follows:

1. The estimates from the unexceeded ground motions (symbols in Figure 1) lie well below the mean hazard from the 1998 PSHA. As these points represent ground motions that have not been observed in a specific time period, they should lie above or near the hazard curve. The 1998 PSHA (shown by the black lines) is overestimating the hazard even at the  $10^{-4}$  hazard level.
2. The event frequencies have been modeled using new empirical ground motion attenuation relations (called NGA). These models were developed through the Pacific Earthquake Engineering Research (PEER) Center as part of the cooperative agreement between PG&E and the DOE. The hazard curves from these new ground motion models



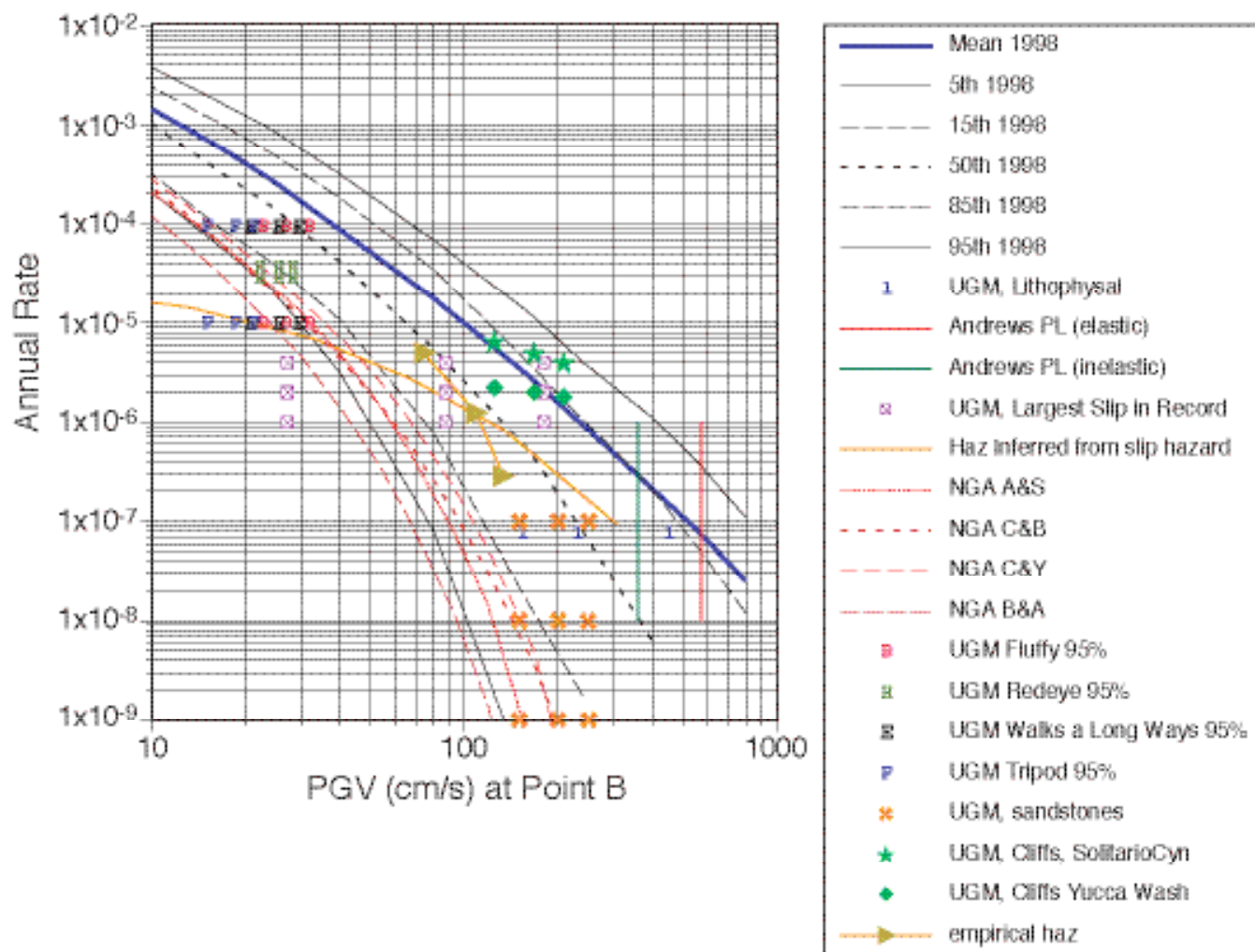


Figure 1. Compilation of the research results in hazard space.

are shown by the red curves in Figure 1 and are representative of the median hazard. These new ground-motion models lead to a large reduction in the median hazard as compared to the 1998 PSHA results, even at the  $10^{-4}$  level. In addition, the hazard computed using these new ground-motion models are now consistent with unexceeded ground motions.

3. The physical limits are shown in Figure 1 as vertical lines. The hazard curve should not extend to ground motions higher than given

by the physical limits. The estimated physical limits are violated by the 1998 PSHA results, but not by the updated results using the NGA ground motion models.

The preliminary results show that there is a clear indication from multiple data sources that the 1998 hazard significantly overestimated the ground-motion hazard at Yucca Mountain. We are building the strong technical basis that will be required to reduce the ground motions from the extreme values currently being used for design at Yucca Mountain.

# Reduced Pressure Electron Beam Closure Welding of Nuclear Waste Containers

T. James Dorsch<sup>1</sup> and Christopher Punshon<sup>2</sup>

<sup>1</sup>BAE Systems | <sup>2</sup>The Welding Institute (TWI—United Kingdom)

## Research Objectives

BAE Systems and TWI (The Welding Institute, UK) have teamed to develop an alternative welding process, Reduced Pressure Electron Beam (RPEB), for making the closure welds on nuclear waste packages. Although RPEB has been applied to the Swedish nuclear waste program canisters, the Yucca Mountain design uses different material. The expected results will provide a more robust closure weld in terms of quality and throughput, but mainly provide lower surface residual stresses via the single-pass weld process and an integral low-temperature thermal process that redistributes and substantially reduces the surface residual tensile stress. This will eliminate the need for additional mechanical peening or burnishing in the closure cell to prevent stress corrosion cracking of the outer waste package.

RPEB welding is an alternative welding technology that was developed at TWI. The RPEB process offers numerous advantages over conventional high vacuum electron beam (EB) welding processes and the baseline gas tungsten arc welding (GTAW) process—including vastly reducing the time required for welding, by 20 fold over GTAW, eliminating the need for filler wire, simplifying weld joint preparation, providing comparable or improved weld quality, reducing repairs, and reducing distortion and residual stress. These advantages, which translate into significant cost savings during closure welding and fabrication, are described below.

Traditionally, the successful application of EB welding requires enveloping the components to be joined in a vacuum chamber, which has to be pumped to a pressure of approximately  $10^{-3}$  mbar. To a large extent, this requirement has inhibited its use in fabricating large structures in thick materials—where the process benefits are potentially greatest—because of the prohibitive capital investment necessary for the construction of large vacuum chambers and the attendant cost of pumps. In addition, the high vacuum EB process is intolerant of poor surface condition and demands extraordinary care in preparation of joint details on large parts. However, for production of large quantities of precision components, such as for the Yucca Mountain Project, the use of a customized chamber may be justified.



Figure 1. Reduced pressure electron beam (RPEB) welding system and remote lid handling arrangement for closure welding of Swedish high-level nuclear waste containers.

Swedish authorities have already approved the RPEB process for fabrication of nuclear waste containers. Figure 1 shows the RPEB welding system and remote lid handling arrangement used for Swedish high-level nuclear waste containers.

For a variety of reasons outlined below, the RPEB process is particularly attractive when considering both the fabrication and closure of high-level nuclear waste containers:

- The process is ideally suited to remote operation and is a true noncontact process.
- The system is fully automatic with on-line seam



tracking and no operator dependence.

- The components and elements of the system are radiation-hard and are not degraded by extended exposure to high radiation flux levels.
- The operation lends itself to rigorous quality control via a combination of in-process monitoring and post-weld inspection.
- The welding speed is high, thereby minimizing the need for several expensive hot cell welding stations to achieve the desired production rate.
- The weld quality is consistently high and reproducible, minimizing the need for rework and/or repair.

## Approach

With the RPEB system, it is possible to establish a welding vacuum ('reduced pressure') using a simple mechanical vacuum pump and crude seals that permit the use of local sealing and pumping. This process variable represents a step change and could obviate the need for large vacuum chambers. Furthermore, in this pressure regime, the RPEB system was tolerant of many variations that had previously hindered the application of EB welding for large structures. This research program will demonstrate and define the following parameters to validate the range of tolerance within which the RPEB welding process is successful.

### Component Cleanliness

Welding at high vacuum requires that both the immediate joint area and the entire assembly are relatively clean; otherwise, out-gassing can occur, leading to welding difficulties. Working at "reduced pressure" greatly increases tolerance to component cleanliness, and only the immediate joint area needs to be cleaned.

### Gun Stand-Off Distance

Traditional high vacuum EB welding requires that the gun-to-work distance be controlled to  $\pm 2$  mm to maintain an appropriate beam focus position. In contrast, the RPEB is essentially parallel and has no well-defined focus position. As a consequence, the gun-to-work distance can vary by more than 400 mm without detriment to weld quality.

### Pumping Time and Use of Rough Seals

Operation at 1 mbar pressure, in contrast to  $10^{-3}$  mbar in traditional EB welding, significantly reduces pumping time for a given volume. Even for large volumes, pumping times are measured in minutes as opposed to hours. Additionally, local seals will be demonstrated to be capable of maintaining the reduced pressure environment.

### Material Tolerances

Surface roughness, gaps, and mismatch will be quantified to define the fit-up and machining characteristics required by RPEB. The increased attenuation of the beam caused by the scattering effect of the reduced pressure atmosphere results in a "softer" beam, which results in wider weld profiles, in turn offering greater tolerance to joint gaps and better weld termination behavior.

### Residual Stress Mitigation

The narrow-beam, full-penetration, single-pass weld characteristic of RPEB gives reduced weld distortion, but also places the maximum tensile residual stress at the center of the weld depth. This reduces the opportunity for tensile residual stresses on the surface that could lead to initiation of stress corrosion cracking. Finite element analysis (FEA) modeling with validation will demonstrate this effect. In addition, techniques for further reducing residual stresses using low temperature application in the weld vicinity via electron beam scanning will be evaluated.

### Increased Throughput

The single pass, full penetration capability, even in 50 mm thick stainless steel, gives RPEB a substantially higher welding speed than the baseline GTAW. In addition, no filler metal is needed, simplified weld joints are used, and the need for interpass cooldown, inspection, and repair is eliminated. This can lead to significant cost savings by increasing production throughput.

## Accomplishments

This research program:

- Developed welding parameters for 19–30 mm thick Alloy 22 and 50 mm thick 316 NG stainless steel, with gaps, offset, and varying levels of cleanliness.
- Performed nondestructive mechanical and corrosion tests on Alloy 22 RPEB welds, demonstrating

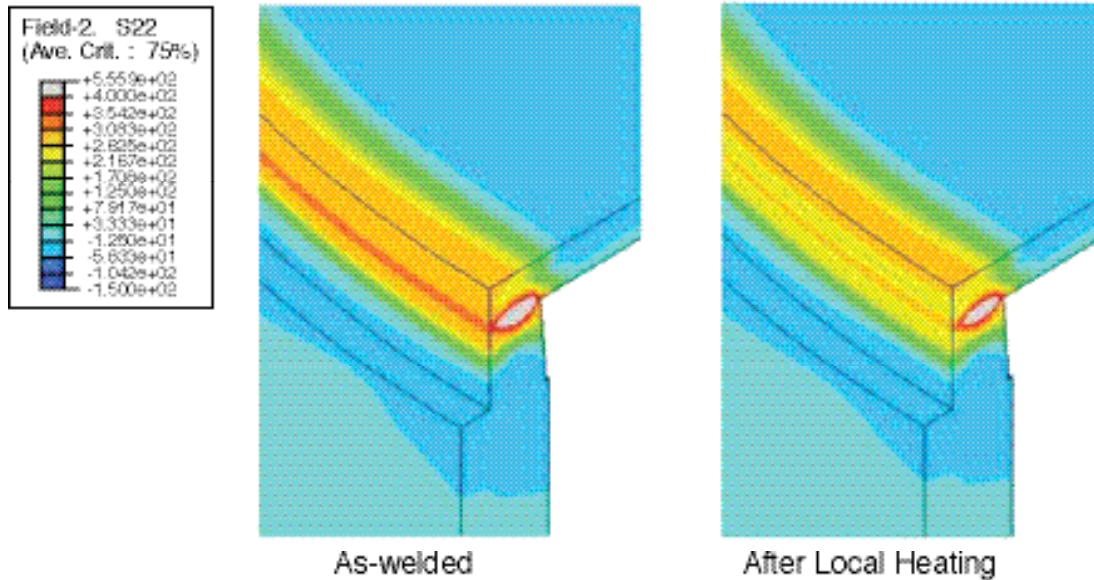


Figure 2. Temperature distributions as-welded and after local heating.

equivalent performance to the baseline welding process.

- Demonstrated that residual stress and distortion in RPEB welds are less than GTAW, but tensile residual stresses (which can cause stress corrosion cracking) are below the surface.
- Developed and validated a robust analytical FEA model to accurately predict temperatures during welding, weld pool solidification, distortion, and postweld residual stress.
- Developed methods for improving residual stress by reducing or even eliminating weld-zone surface tensile stresses have been modeled and validated empirically. A localized post-weld thermal treatment at less than 500°F can achieve this. A thermal treatment using a defocused electron beam scanned along a precise path after welding can produce this effect, eliminating the need for additional mechanical stress mitigation processes, such as peening or burnishing. The initial beam scanning results showed an 80% reduction of surface stresses. Further analysis of the stress distribution indicates that, with more optimization of the location and intensity of the EB heating, there is opportunity for further improvements in stress

relief. Figure 2 demonstrates this effect.

- Fabricated (Figure 3) and welded full diameter and thickness coupons to demonstrate the RPEB capability in stainless steel. Alloy 22 full diameter samples will be welded in the near future. Samples will be removed for additional metallurgical and corrosion testing.
- Developed concepts for adapting the RPEB weld system to the closure cell.

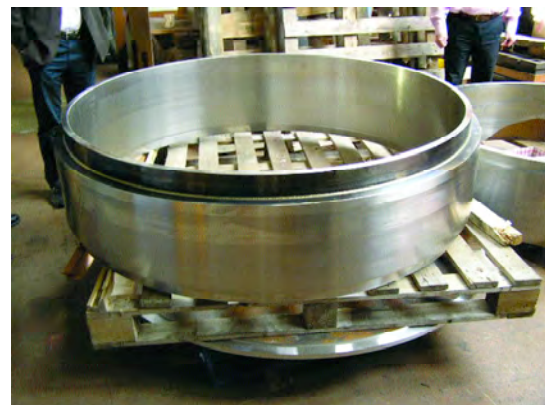


Figure 3. Half-meter long stainless steel inner waste package coupon with inner lid being readied for RPEB welding.

---

This page intentionally left blank.

---

## APPENDIX A

# OCRWM S&T PARTICIPATING ORGANIZATIONS

**Argonne National Laboratory**

**Arizona State University**

**Atomic Energy of Canada Limited**

**Auburn University**

**BAE Systems**

**Case Western Reserve University**

**Clemson University**

**Desert Research Institute**

**Idaho National Laboratory**

**Iowa State University**

**Joseph Oat Corporation**

**Lawrence Berkeley National Laboratory**

**Lawrence Livermore National Laboratory**

**Los Alamos National Laboratory**

**Northern Illinois University**

**Nye County Nuclear Waste Repository Office,  
Nye County, NV**

**Oak Ridge National Laboratory**

**Ohio State University**

**OLI Systems, Inc.**

**Pacific Gas and Electric**

**Pacific Northwest National Laboratory**

**Pennsylvania State University**

**Rice University**

**Sandia National Laboratories**

**United States Department of Energy, Office of Civilian  
Radioactive Waste Management**

**United States Geological Survey**

**University of California, Berkeley**

**University of California, Davis**

**University of Manchester, Great Britain**

**University of Manitoba**

**University of Michigan**

**University of Minnesota**

**University of Missouri-Columbia**

**University of Nevada-Las Vegas**

**University of Nevada-Reno**

**University of Notre Dame**

**University of Southern California**

**University of Tennessee-Knoxville**

**University of Texas-Arlington**

**University of Texas-El Paso**

**University of Toronto**

**University of Virginia**

**University of Western Ontario**

**Washington State University**

**The Welding Institute-United Kingdom**

#### OCRWM Disclaimer

This report was prepared by Ernest Orlando Lawrence Berkeley National Laboratory pursuant to Contract No. DE-AC02-05CH11231, funded by the United States Department of Energy (DOE), Office of Civilian Radioactive Waste Management (OCRWM), and neither Ernest Orlando Lawrence Berkeley National Laboratory, nor any of its contractors or subcontractors, nor the DOE/OCRWM, nor any person acting on behalf of either:

- Makes any warranty or representation, express or implied, with respect to the accuracy, completeness, or usefulness of the information contained in this report, or that the use of any information, apparatus, method, or process disclosed in this report may not infringe privately-owned rights; or
- Assumes any liabilities with respect to the use of, or for damages resulting from the use of, any information, apparatus, method, or process disclosed in this report. Reference herein to any specific commercial product, process, or service by trade name, trademark, manufacturer, or otherwise, does not necessarily constitute or imply its endorsement, recommendation, or favoring by DOE/OCRWM.

The views, opinions, findings, and conclusions or recommendations of authors expressed herein do not necessarily state or reflect those of the DOE/OCRWM.

#### Ernest Orlando Lawrence Berkeley National Laboratory Disclaimer

This document was prepared as an account of work sponsored by the United States Government. While this document is believed to contain correct information, neither the United States Government nor any agency thereof, nor The Regents of the University of California, nor any of their employees, makes any warranty, express or implied, or assumes any legal responsibility for the accuracy, completeness, or usefulness of any information, apparatus, product, or process disclosed, or represents that its use would not infringe privately owned rights. Reference herein to any specific commercial product, process, or service by its trade name, trademark, manufacturer, or otherwise, does not necessarily constitute or imply its endorsement, recommendation, or favoring by the United States Government or any agency thereof, or The Regents of the University of California. The views and opinions of authors expressed herein do not necessarily state or reflect those of the United States Government or any agency thereof, or The Regents of the University of California.

Ernest Orlando Lawrence Berkeley National Laboratory is an equal opportunity employer.



